Investigation on Fatigue Failure in Tyres

Thomas Louis Marie Baumard

A thesis submitted for the award of Doctor of Philosophy

The School of Engineering and Materials Science
Queen Mary University of London
Mile End Road,
LONDON E1 4NS
June 2016

Declaration

I, Thomas Louis Marie Baumard, confirm that the research included within this thesis is my own work or that where it has been carried out in collaboration with, or supported by others, that this is duly acknowledged below and my contribution indicated. Previously published material is also acknowledged below.

I attest that I have exercised reasonable care to ensure that the work is original, and does not to the best of my knowledge break any UK law, infringe any third party's copyright or other Intellectual Property Right, or contain any confidential material.

I accept that the College has the right to use plagiarism detection software to check the electronic version of the thesis.

I confirm that this thesis has not been previously submitted for the award of a degree by this or any other university.

Signature:

Date:

Details of collaboration and publications:

Publications:

Baumard T.L.M.,, Thomas A.G., Busfield J.J.C. (2013). «Evaluation of the tearing energy in a radial tyre » in *Constitutive Models For Rubber Viii - Proceedings of The 8th European Conference On Constitutive Models For Rubbers*, ECCMR p 377-382.

Baumard T.L.M., Thomas A.G., Busfield J.J.C (2012). « Fatigue peeling at rubber interfaces » Plastics, Rubber and Composites **41**: 296.

Baumard T.L.M, Thomas A.G., Ding. W. and Busfield J.J.C. (2012). «Fatigue peeling of rubber» *in Constitutive Models For Rubber Vii - Proceedings of The 7th European Conference On Constitutive Models For Rubber*, ECCMR p 293-297.

Conferences

8th European Conference on Constitutive Models for Rubber, San Sebastian 25th-28th June 2013 *Predicting fatigue life in radial tyre*

International Rubber Conference, Paris 20th-22nd March 2013 *Fatigue peeling at interfaces in tyres; Role of moulding pressure.*

Tire Technology International, Cologne 7th-9th March 2013 *Role of moulding pressure on the resulting interfacial strength of rubber.*

Tire Technology International, Cologne 14th-16th February 2012 *Investigations on the fatigue life at rubber interfaces in tires.*

7th European Conference on Constitutive Models for Rubber, Dublin 20th-23rd December 2011 *Fatigue peeling of rubber*

Tire Technology International, Cologne 15th-17th February 2011 *Fatigue type peeling at rubber interlayers in tires.*

Abstract

Tyres are highly engineered complex rubber composite products. They are constructed from a wide range of different materials in addition to the rubber. In different parts of the tyre's construction, the rubber elements are expected to perform different functions and as a consequence many different types of rubber are used, each of which will have its own specific detailed compound formulation. These different regions of a tyre's construction are joined together by different types of molecular bonding. This variety of materials introduces potential sources of failure both in the homogenous regions within the tyre's construction but also at the interfaces between them. This thesis investigates the crack growth resistance of the rubber materials used in different regions of a tyre's construction as well as the interfaces that are found between the different parts of the tyre. A fracture mechanics framework was used to investigate the fatigue behaviour of bulk rubber and some of the interfaces.

The loading of a tyre is periodic in nature as a consequence of the wheel's rotation therefore the materials were characterised over a range of loading conditions. The effect of cyclical loading frequency on the fatigue behavior of the bulk rubber was also investigated. This work discovered that the amount of crack growth per cycle was comprised from two different crack growth contributions. The first is related to the steady tear which is related to the length of time the load is applied. The second resulted from additional damage caused by the repeated loading and unloading of the material. Potential reasons for this additional crack growth contribution are discussed. The interfacial fatigue properties between adjoining and potentially dissimilar rubber compounds were examined using a fatigue peeling experiment. A novel test piece geometry was developed to evaluate the fatigue properties of interfaces in tyres and it was also used to investigate how different processing parameters such as the pressure at the interface during vulcanisation alter the interfacial strength. A significant effect was observed and this was related to the different phenomena occurring when two rubbery polymers are brought into contact. Finally, a fracture mechanics approach was also used to derive the value of the tearing energy, the variable governing crack growth propagation in the rubber materials found in tyres, using submodelling technique in finite element analysis. The tearing energy values at different locations within a tyre

were calculated and are shown not to exceed the minimum energy criteria for crack propagation under normal service conditions.

Acknowledgements

I would like to express my deepest gratitude to my supervisors, Dr. James Busfield and Professor Alan Thomas, for their guidance, tremendous help, patience and encouragement throughout the course of this programme.

I also express my gratitude to all the members of the Soft Matter Group for the interesting discussions both on rubber and life. I would like to thank the support staff in SEMS which provided tremendous help to manufacture the different parts necessary for this project as well as the funding partners for this work; EPSRC and Dunlop Aircraft Tyres Ltd - in particular the support of Dr Wei Ding and Mr Andrew Turner.

Finally, special thanks go to my family and friends for their support and encouragements which helped tremendously in the writing of this thesis.

Table of content

Declaration **2**
Abstract **4**
Acknowledgements **6**
Table of content **7**
List of figures **10**
List of Tables **15**
List of symbols and abbrevations **16**

Chapter 1 - Introduction **21**

Chapter 2 - Review of the relevant literature **25**

2-1. Rubber elasticity *25*
2-1-1. General observations for rubber elasticity 25
2-1-2. Statistical theory of rubber elasticity 26
2-1-3. Phenomenological treatment of rubber elasticity 34
2-1-4. Alternative forms of strain energy function 40
2-1-5. Inelastic phenomenon encountered with rubbers 44

2-2. Tearing of rubbery materials *51*
2-2-1. Rupture of rubber 53
2-2-2. Types of crack growth 62
2-2-3. Factors influencing the crack growth 63

2-3. Cyclic crack growth, fatigue of rubbery materials *69*
2-3-1. Fatigue initiation and crack growth 69
2-3-2. Typical fatigue behaviour 70
2-3-3. Fatigue life prediction 73
2-3-4. Influence of composition on the fatigue behaviour 73
2-3-5. Effect of fillers 75
2-3-6. Influence of environmental parameters on fatigue behaviour 75
2-3-7. Roughness measurements on fractured surfaces 80

2-4. Polymer interactions at an interface *82*
2-4-1. Formation of an interface 82
2-4-2. Strength of interface 85

2-5. Fracture mechanics in FEA *88*
2-5-1. Introduction on FEA 88
2-5-2. Modelling of tyres 94
2-5-3. Evaluation of T using Finite element techniques 97

2-6. Summary *99*

Chapter 3 - Materials and experimental techniques **101**

3-1. Materials used in this study *101*
3-1-1. Polymer materials 101
3-1-2. Vulcanisation 102
3-1-3. Sample preparation procedure 104
3-1-4. Evaluation of curing time 105

3-2. Material analysis *106*
3-2-1. Determination of the crosslink density 106
3-2-2. Crosslink density using the stress-strain behaviour 108

3-3. Mechanical testing *109*
3-3-1. Tensile test 109
3-3-2. Additional mechanical tests for validation of FEA parameters 110
3-3-3. Dynamic mechanical analysis 111

3-4. Fracture of elastomers *113*
3-4-1. Fatigue crack growth test 113
3-4-2. Peeling test 118

3-5. Optical measurements *121*
3-5-1. Optical microscopy 121
3-5-2. Scanning electron microscope (SEM) 122

3-6. Roughness measurements *122*

3-7. Material characterisation for FEA analysis *124*

Chapter 4 - Fatigue of Non strain crystallsing elastomers 132

4-1. Introduction *132*

4-2. Frequency effect on the fatigue behaviour of SBR *133*
4-2-1. Evolution of fatigue behaviour with frequency 133
4-2-2. Theoretical time dependent contribution 135
4-2-3. Static crack growth 136
4-2-4. Time dependent and cyclic contributions for SBR0 139

4-3. Effect of the type of waveform *143*
4-3-1. Waveforms used 143
4-3-2. Effect of frequency with different waveforms 144
Square signal 145
4-3-3. Comparison of the different waveforms 148

4-4. Summary of the results and discussion *151*
4-4-1. Conclusions 151
4-4-2. Prediction based on static crack growth 151
4-4-3. Possible origins and phenomena affecting the cyclic contribution 154

Chapter 5 - Peeling at interfaces 156

5-1. Introduction *156*

5-2. Experimental arrangement *162*
5-2-1. Modification of the geometry 162
5-2-2. Validation of the preparation method 165

5-3. Strength of interfaces between different materials *166*

5-4. Influence of vulcanising pressure on strength of interface *167*
5-4-1. Observation of peeled off surfaces 172
5-4-2. Resulting roughness 176
5-4-3. Investigations on contact area 178

5-5. Conclusion *184*

Chapter 6 - Predicting Tearing Energy in a tyre using a submodeling approach 186

6-1. Introduction *186*

6-2. Comparison of FEA techniques to obtain the tearing energy in a component on typical specimens *187*
6-2-1. Pure shear specimen 187

6-2-2. Edge crack specimen 191

6-3. Submodelling technique for common geometries *193*
6-3-1. A working example: the pure shear geometry 194
6-3-2. Limitations of the method: edge crack specimen 196

6-4. Tyre model used in this study *200*
6-4-1. Presentation of the model 200
6-4-2. Selection of the driven nodes in the submodel 202

6-5. Evaluation of the tearing energy for various cases *204*
6-5-1. Crack in the vicinity of the clinch 204
6-5-2. Crack growth in the perpendicular direction 208

6-6. Conclusion on using submodelling to calculate energy *210*

Chapter 7 - Conclusion and future work 212

7-1. Conclusions *212*

7-2. Proposition for future work *213*

References 216

List of figures

Figure 2-1. Trend of force-displacement curve for a single random chain. Adapted from Treloar (1975) 30
Figure 2-2. The Neo-Hookean SEF poorly fits experimental data in tension for natural rubber. 33
Figure 2-3. Mooney plot for an unfilled NR vulcanisate. Left part of the graph is tension, right side is compression. Adapted from Rivlin and Saunders (1951)..... 37
Figure 2-4. Biaxial setup used by Rivlin and Saunders (1951) to determine the variation of $\partial W/\partial I_1$ and $\partial W/\partial I_2$ with I_1 and I_2..... 39
Figure 2-5. Schematic of network structures in the undeformed state, uniaxial tension and equibiaxial extension. (a) 3-chain model (b) 4-chain model (c) 8-chain model and (d) full network model..... 42
Figure 2-6. Hysteresis exhibited in rubbers and energy dissipated..... 45
Figure 2-7. Time Temperature Superposition principle applied to storage modulus E'. Adapted from Gent and Walker (2005). 47
Figure 2-8. Cyclic stress softening and Mullins' effect. From Diani et al. (2009)..... 48
Figure 2-9. Stress softening effect occurs mainly over the first cycles. Redrawn from Asare et al. (2009). 49
Figure 2-10. Evolution of the maximum stress with the number of cycles for NR60 subjected to a combination of tension and torsion. Adapted from Mars and Fatemi (2004)..... 50
Figure 2-11. J-integral contour. The J-integral value is independent of the path G chosen for the calculation. 53
Figure 2-12. (a) Trouser test piece, (b) Pure shear specimen..... 54
Figure 2-13. (a) Split tear test piece, (b) Angled test piece..... 55
Figure 2-14. Edge crack specimen..... 56
Figure 2-15. The tearing energy T as a function of crack growth rate r for an unfilled SBR using a variety of test piece geometries. Plot based on data from Lake (1995)..... 57
Figure 2-16. Crack tip strain state model used by Thomas (1955). 57
Figure 2-17. The tearing energy calculated from consideration of the strain field at the crack tip and from the overall forces applied to a trouser test specimen are similar. From Thomas (1955). 59
Figure 2-18. Similar trends for W_c and $T/(2r_t)$ for (a) unfilled SBR and (b) a carbon black filled SBR vulcanizates. Adapted from Greensmith (1960). 60
Figure 2-19. Hysteresis loop for a volume element going through the high strain region close to the crack tip as the crack advances..... 62
Figure 2-20. Crack growth types regarding their force vs time curves. (a) and (b) steady tearing, (c) stick-slip tearing. Taken from Greensmith and Thomas (1955). 63
Figure 2-21. Evolution between crack growth rate with tearing energy for a non strain crystallising material (logarithmic scale). 64
Figure 2-22. Temperature and rate effects on the tear behaviour of (a) an unfilled SBR (b) an unfilled NR and (c) an filled SBR vulcanisates. From Greensmith (1960)..... 65
Figure 2-23. Master curve for the tearing of unfilled SBR measured over a wide range of rates and temperatures. Taken from Mullins (1959)..... 66

Figure 2-24. Tear strength of NR and IR against rate of crack growth. Taken from Gent et al. (1998). 68
Figure 2-25. Critical tearing energy against time derivative of the tearing energy for a highly crosslinked natural rubber. Adapted from Sakulkaew et al. (2010). 68
Figure 2-26. Regimes of crack growth in fatigue for unfilled SBR and NR. The inset is showing threshold tearing energy and linear relationship at low tearing energies. From Lake (1983). 72
Figure 2-27. Crack growth rate per cycle for various types of base polymer and loading(o) unfilled (+) filled with 50phr of MT carbon black and (•) filled with 50 phr of HAF carbon black. Based on Lake and Lindley (1964a) 74
Figure 2-28. The steady crack growth rate can be fitted with a powerlaw relationship with respect to T in both slow and fast region. Taken from Busfield et al. (2002) 77
Figure 2-29. Effect of temperature on the fatigue life of (•) an unfilled SBR and (+) an unfilled NR. Adapted from Lake and Lindley (1964b). 78
Figure 2-30. Effect of temperature on the fatigue behaviour of (a) CIIR (Young (1986)) and (b) NR (Young (1994)). 78
Figure 2-31. Influence of R-ratio on the fatigue behaviour of unfilled NR. Taken from Lindley (1973) 80
Figure 2-32. Four regimes of interfacial broadening. Taken from Karim et al. (1990). 85
Figure 2-33. Strength of the interface interpenetration depth for polybutadiene bonded with different elastomers. Taken from Schach et al. (2007). 87
Figure 2-34. Strength of interface of SBR versus contact time for three molecular weights (80, 160 and 240kg.mol^{-1}). Reptation times are respectively 13, 140 and 1140 seconds. Adapted from Schach and Creton (2008). 87
Figure 2-35. Symmetries commonly adopted to simplify the model in FEA. The dotted regions suffice to model the entire geometry. Taken from Busfield (2000). 91
Figure 2-36. Components of a tyre. From Gent and Walker (2005). 95
Figure 2-37. Mixed Lagrangian/Eulerian method 97

Figure 3-1. Chemical formula of the elastomers used in this study. 101
Figure 3-2.Mould used in the hot press to vulcanise 240mm x 200mm x 2mm sheets 104
Figure 3-3. Moving die rheometer employed and Torque vs Time curve obtained for the SBR0 compound (plateau cure behaviour). Reversion and creeping cure behaviour are also shown respectively as dashed and dotted lines. 105
Figure 3-4. Mooney plot for SBR0, the dashed line shows the fit in the linear region of the graph. 109
Figure 3-5. Instron 5567 used for the tensile testing fitted with video extensometer. Two dots are drawn on the sample to measure the strain in the gauge length of the specimen. 110
Figure 3-6. Dimensions of the tensile specimen. $L1$ = 65mm, $L0$ = 30mm, width = 3.1mm with dots for video-extensometer. 110
Figure 3-7. Dimensions of samples used compression and pure shear testing. 111
Figure 3-8. Phase shift between the displacement and force signal. Dynamic mechanical analysis equipment can measure the phase shift and can identify the elastic and the viscous contributions of the behaviour. 112

Figure 3-9. Temperature dependence of the viscoelatic parameters for SBR0 showing three methods to determine T_g. 113
Figure 3-10. Four regions of the pure shear test specimen. 114
Figure 3-11. Evaluation of crack growth rate during the fatigue testing. 117
Figure 3-12. Peeling specimen 118
Figure 3-13. Measurement of crack growth during the peeling tests. 120
Figure 3-14.Comparison of crack growth obtained from maximum displacement of the crosshead and silver marks at the crack tip. 120
Figure 3-15. Optical microscopy of crack surface at different peeling energies 121
Figure 3-16. SEM images of crack surface (a) from the top (b) from the side. 122
Figure 3-17. Profile of crack surface obtained with topography analysis. 123
Figure 3-18 . Models used for comparison with FEA of mechanical behaviour with SEF. 125
Figure 3-19. Mooney-Rivlin SEF fitted to tensile experimental data for unfilled materials. ... 126
Figure 3-20. The data fitted in tension to the Mooney SEF used to predict the behaviour in pure shear 126
3-21. Fitting the Yeoh strain energy function to experimental data (DC005) in tension. 127
Figure 3-22. Simulated and experimental results in tension for DC005. 128
Figure 3-23. Comparison of FEA results and experimental data in pure shear for DC005. 129
Figure 3-24. Comparison of FEA results and experimental data in compression for DC005. . 129

Figure 4-1. Fatigue behaviour of SBR0 subjected to frequencies ranging from 0.01 to 10 Hz. 134
Figure 4-2. Calculation of the time dependent contribution to fatigue crack growth based on static crack growth behaviour. 137
Figure 4-3. Static crack growth setup. 138
Figure 4-4. Crack growth rate versus tearing energy graph with the different regions of crack growth. 139
Figure 4-5. Time dependent contribution to the crack growth in fatigue for SBR0. Time dependent contributions are represented as dashed lines. 140
Figure 4-6. Time dependent (TDC) and cyclic components (CC) of the fatigue behaviour at 0.1 and 10 Hz. 142
Figure 4-7. Waveforms used to characterise the fatigue behaviour of SBR0. 144
Figure 4-8. Triangle waveform 145
Figure 4-9. Square waveform. 146
Figure 4-10. Trapezoidal waveform. 147
Figure 4-11. The fatigue behaviour of SBR0 subjected to various waveforms at 0.01Hz. 149
Figure 4-12. The fatigue behaviour of SBR0 subjected to various waveforms at 0.1Hz. 149
Figure 4-13. The fatigue behaviour of SBR0 subjected to various waveforms at 1Hz. 150
Figure 4-14. Time dependent contribution predicted with static steady crack growth for 0.01 Hz. 150
Figure 4-15. The effect of a tearing energy dependent cyclic factor on the total crack growth rate per cycle for the different waveforms. The total crack growth rate per cycle is equal to the area under the curve 153

Figure 5-1. Schematic diagram of an interface between two rubbery materials showing partial contact and flaws. Taken from Hamed (1981). 158
Figure 5-2. Evolution of work of adhesion at short times of contact. Adapted from Davis et al. (2014). 160
Figure 5-3. Reduction of the surface of contact with a 25μm thick PTFE film. The PTFE is shown as hatched on the drawing. 162
Figure 5-4. Schematic drawing of the process to obtain peeling specimen with reduced bonded area. 164
Figure 5-5. Peeled off specimen. 164
Figure 5-6. Fatigue behaviour of (a)SBR50 and (b)NR50 with different geometries. 166
Figure 5-7. Interfaces tested under cyclic loading shows similar behaviour as the weaker material. 168
Figure 5-8. Cure curve for SBR70 showing time available for interdiffusion. 170
Figure 5-9. Compressive pressure during vulcanisation changes the resistance to crack growth of SBR70. 171
Figure 5-10. Influence of pressure on the adhesion strength of an unvulcanised SBR. Adapted from Gent and Kim (1990). 172
Figure 5-11. SEM images of the separated surfaces magnified (a) 300 times and (b) 5000 times 175
Figure 5-12. SEM images of the sides of the specimen after separation for higher vulcanising pressure. The crack propagates from left to right. 175
Figure 5-13. Surface topography of the specimen at the same peeling energy. The height is expressed in μm. 176
Figure 5-14. Profile lines of the resulting surface after crack growth taken at the same peeling energy. 177
Figure 5-15. Evolution of roughness. 178
Figure 5-16. Contact area between glass and the rubber under (a) 0.2 MPa, (b) 0.5MPa and (c) 1 MPa. 179
Figure 5-17. Microscope pictures of the cracked surface for the 0.2 MPa specimen. Magnification: (a) and (b) 300x and (c) 5000x. 180
Figure 5-18. Compensated peeling energy at 0.2 MPa 182
Figure 5-19. Virtual change in surface of contact with pressure to reach bulk properties. 183

Figure 6-1. Pure shear specimen model. 188
Figure 6-2. Convergence of the tearing energy obtained using the Rice J-Integral method. 188
Figure 6-3. The results for the different methods are in agreement with theoretical calculations and in reasonable agreement with experimental data for (a) SBR0 and (b) SBR50. 190
Figure 6-4. Tearing energy calculated for the edge crack sample deviates from theory for higher crack length. 192
Figure 6-5. Results of simulation are in a reasonable agreement with theory and experimental data for (a) SBR0 and (b) SBR50. 193
Figure 6-6. The region chosen to assess the submodelling technique. 194
Figure 6-7. Submodelling technique calculates similar tearing energies to the global cracked model of pure shear geometry (a) SBR0 (b) SBR50. 195

Figure 6-8. The tearing energy deviates from the whole geometry results as the crack approaches the edges. 196
Figure 6-9. Submodelling the edge crack specimen. 196
Figure 6-10. Submodelling approach compared with a global crack model. 197
Figure 6-11. The displacements of the driven nodes are modified by the presence of the crack. 199
Figure 6-12. Evolution of the tearing energy with size of the submodel. The dashed lines represent the values for the simulations with the whole specimen, the red line is the distance at which the results in Figure 6-10 were obtained. 199
Figure 6-13. Axisymmetric model of the tyre. The materials are rubber compounds unless otherwise stated. 200
Figure 6-14. The region chosen for the submodel is significantly refined and a crack is introduced. 201
Figure 6-15. Comparison of the position of the nodes in an axisymmetric model with a large crack and 1MN load. The error bars represent the change in the displacement of the nodes amplified by a factor 50 for clarity. 202
Figure 6-16. Nodes chosen for the submodel of the region close to the bead in the tyre. 203
Figure 6-17. Locations of the cracks in the tyre. 205
Figure 6-18. Crack growth in the model. The front surface is the surface of the body plies (clinch and sidewall have been removed for clarity). 205
Figure 6-19. Tearing energy for a crack between the clinch and the body plies growing (a) in the radial direction (b) in the circumferential direction. 207
Figure 6-20. Tearing energy obtained through the revolution of the submodel. 208
Figure 6-21. Evolution of the tearing energy with crack length for a crack in the clinch. 209
Figure 6-22. Effect of cornering on the tearing energy in the clinch region. 210

Figure 7-1. Loading of the rubber is (a) slower in the static crack growth tests than in the (b) fatigue tests. 215

List of Tables

Table 3-1. Formulations of the rubbers compounded at QMUL given in parts per hundred rubber in mass. 103
Table 3-2. Formulation of the compounds supplied by DATL. 103
Table 3-3. Glass transition temperature of the compounds used in this study determined with dynamic mechanical analaysis. 112
Table 3-4. Mooney-Rivlin coefficients for FEA implementation 125
Table 3-5. Yeoh SEF coefficients measured for each of the filled materials used in this thesis. 127

Table 4-1. Characteristics B and β of SBR0 at different frequencies. 134
Table 4-2. Coefficients of static crack growth for SBR0. 139

Table 5-1. Compensated peeling energies for 0.2 MPa pressure. 182
Table 5-2. Change in the contact area to fit the bulk material behaviour. 183

List of symbols and abbreviations

Arabic letters

$[K]$	Stiffness matrix
$[X]_{cb}$	Crosslinks and physical entanglements density in a carbon black filled rubber
$[X]_{phys}$	Crosslinks and physical entanglements density
$[x_i]$	Concentration of species i
$\{F\}$	Nodal force vector
$\{U\}$	Nodal displacements vector
A	Helmholtz free energy
A_0	Coefficient for mechanical contribution in chemico mechanical fatigue crack growth
A_{app}	Surface at full contact
A_c	Crack surface area
A_{comp}	Compensated surface area including flaws in contact
A_D	Coefficient for Davies SEF
A_{static}	Constant in powerlaw relationship T vs r
a_T	WLF function frequency shift factor
b	Statistical theory variable
B	Constant for powerlaw relationship of fatigue crack growth
B_s	Constant for powerlaw relationship of static steady state crack growth
c	Crack length
c_0	Initial crack length
c_{crit}	Critical crack length for catastrophic failure
C_D	Coefficient for Davies SEF
$C_{i,\ i=1,2}$	Coefficients for Mooney-Rivlin SEF
$C_{ijk,\ i,j,k=1...\infty}$	Coefficient for Rivlin formulation of SEF
C_{NG}	Constant for Non-Gaussian distribution of chains
C_S	Constant for entropy of a chain in statistical theory
$C_{wi,\ i=1,2}$	TTS shift coefficients
D	Distance between crack and nodes in submodel
D_{hyst}	Diameter of the region subjected to high strains at the crack tip
D_M	Coefficient of mutual diffusion
D_{Rouse}	Coefficient of diffusion for Rouse model
D_s	Coefficient of self diffusion
E'	Storage modulus
E''	Loss modulus
E^*	Complex elastic modulus
F	Force

f	Frequency
F_A, F_B	Force applied in region A and B of the split tear specimen
f_{sc}	Force on a single molecular chain
G	Shear modulus
h	Thickness of a specimen
i	Complex number defined by $i^2=-1$
$I_{i,\ i=1..3}$	Strain invariants of the left Cauchy strain tensor
J	Value of the J-integral
J_i	Flux of migration of species in diffusion
K	Bulk modulus
k	Function in calculation of the tearing energy for edge crack specimen
K_c	Fracture toughness
K_D	Coefficient for Davies SEF
k_z	Coefficient of reaction of ozone attack on polymer
L	Length of deformed specimen
l	Displacement
L_0	Original length of a specimen
l_0	Original height of a specimen
l_l	Length of a Kuhn segment
L_m	Contour length of a macromolecule
M_0	Mass of dried rubber
M_r	Total mass of the compound
M_{rn}	Mass of elastomer network and sulfur
N	Number of cycles
n	Number of Kuhn segments in a chain
P	Peeling energy
P_{app}	Peeling energy calculated from external force
P_{comp}	Peeling energy compensated for the lower contact area
r	Crack growth rate
$\boldsymbol{R}$	Gas constant
R	Ratio of the minimum T to maximum T in cyclic loading
R_a	Roughness
r_c	End-to-end distance of a chain
R_q	Root mean square roughness
r_t	radius of the crack tip
S	Entropy
T	Tearing energy
$\boldsymbol{T}$	Traction vector
t	Time
T_0	Threshold tearing energy

t_{90}	Optimal cure time
T_c	Critical tearing energy
T_g	Glass transition temperature
t_i	True stresses
T_m	Maximum tearing energy achieved during one loading cycle
U	Elastically stored strain energy
$\boldsymbol{u}$	Displacement vector
U_{lost}	Energy lost as hysteresis in the high strain region at the crack tip
V	Volume
v_0	Molar volume of the solvent
V_{cb}	Volume fraction of carbon black
V_{rn}	Volume of elastomer in network
V_s	Volume of solvent absorbed at equilibrium
w	Width of a specimen
W	Strain energy density
w_0	Original width of a specimen
W_A, W_B	Strain energy density in region A and B of the split tear specimen
w_{air}	Weight of network in air
W_c	Strain energy density at the crack tip at break
w_c	Reduced width of peel specimen
W_{cr}	Strain energy density due to the crosslinked network
W_d	Energy dissipated per unit volume
$W_{\square}$	Strain energy density at an angle $\square$ at the crack tip
W_{ht}	Hysteretic loss per unit volume in the region around the crack
W_{ph}	Strain energy density due to other contributions
W_{ps}	Strain energy density in pure shear
W_t	Strain energy density in tension
w_{water}	Weight of network in water
X	Number of chains per unit volume
x_i	Cartesian coordinates

Greek letters

α	Angle in angled test piece
α_i	Exponent for Ogden SEF
α_{static}	Exponent powerlaw relationship T vs r
β	Constant for powerlaw relationship of fatigue crack growth
β_s	Constant for powerlaw relationship of static steady state crack growth
χ	Flory-Rehner interaction parameter between polymer and solvent
χ_{FH}	Flory-Huggins interaction parameter
δ	Angle at the crack tip with respect to the direction of growth
γ	Shear strain
Γ	Path for the J-integral calculation
γ_s	Surface free energy per unit area
φ	Coefficient for Davies SEF
λ	Extension ratio
λ_A, λ_B	Extension ratios in region A and B of the split tear test piece
μ_i	Coefficients for Ogden SEF
ν_r	Volume fraction of elastomer in a swollen network
θ	Absolute temperature
θ_g	Glass transition temperature in Kelvin
ρ_{rn}	Density of the rubber network
ρ_{water}	Density of water
σ	Stress
σ^*	Reduced stress
τ	Shear stress
$\tan\delta$	Damping
τ_{load}	Time of loading
ξ	Inverse Langevin function of $r_c n/l_l$
ψ	Angle in the split tear test piece
ζ_f	Coefficient of friction in Rouse model for diffusion of molecular chains

Abbreviations

BR	Polybutadiene Rubber
DMA	Dynamic Mechanical Analysis
FEA	Finite Element Analysis
HAF	High Abrasion Furnace
IR	PolyIsoprene Rubber
MT	Medium Thermal
NR	Natural Rubber
phr	per hundred rubber
SBR	Styrene Butadiene Rubber
SEF	Strain Energy Function
SEM	Scanning Electron Microscope
SIC	Strain Induced Crystallisation
TTS	Time Temperature Superposition
WLF	Williams, Landel, Ferry
VCE	Virtual Crack Extension
VCCT	Virtual Crack Closure Technique
PTFE	Polytetrafluoroethene

CHAPTER 1 - INTRODUCTION

The large extensibility without breaking, the ability to dissipate or absorb energy and the flexibility of rubbery materials give rise to a wide range of different engineering applications including rubber seals, earthquake bearings, shock absorbers and anti vibration devices. While many applications rely on a single rubber compound, tyres are complex multilayered structures of different rubber materials, some layers being reinforced with fibres. The wide range of properties achievable for a particular rubber compound depend upon the base polymer, its detailed formulation and the curing conditions. This is particularly true for the different rubber compounds utilised in the design of tyres in which each material is carefully selected and optimised to fulfil specific requirements related to their location in the structure. Manufacturers are today under growing pressure from legislation and consumers to reduce the environmental impact and increase the performance of the tyre. Research efforts are mainly focused on the optimisation of the design, the materials selection and formulation to decrease fuel consumption of the entire vehicle. Rolling resistance of tyres can account for up to 15% of fuel consumption for a passenger vehicle. Car tyre manufacturers therefore currently aim to develop low rolling resistance tyres while maintaining good adherence to the road surface and wear resistance. In the aircraft industry, the problem is entirely different as the tyres are only in operation sporadically whilst taxiing on the ground. The main concern is therefore to reduce the size and the weight of the tyre to save on fuel in flight whilst getting similar or higher number of landings out of each tyre. Changes to aircraft tyre design have already been made in pursuit of this objective, one significant change has been the transition from bias-ply tyres to radial-ply tyres which require less body plies for a similar weight bearing loading capacity. For low duty aircraft, the radial-ply design also demonstrates increased lifetime. However, for high duty airplanes, the transition to radial-ply design has not been fully achieved yet as failure of the tyre often occurs prematurely and/or it does not yet present sufficient reduction in weight to be financially viable for airlines.

The evaluation of the mechanical properties of the materials surrounding the crack in a burst radial tyre does not show significant variation from the virgin tyre materials. This observation combined with the sudden and relatively rapid fracture of the tyre during

rolling road type tyre testing suggests that the lifetime of the structure is mostly determined by fracture processes rather than a progressive degradation or ageing of the physical properties of the materials. Although catastrophic failure might occur under a single loading due to inherent flaws, it is more typical to see an initial flaw in the rubber network growing progressively under repeated loading until its size becomes critical whereupon a rapid fracture occurs. This fatigue process may be accelerated by a combination of poor material selection, environmental degradation, significant overloading operating conditions, loading history, materials and tyre manufacturing processes.

The research presented in this thesis is part of the work carried out to investigate the potential causes of failure of radial tyres used in high duty aircraft such as a wide bodied passenger plane. The aspiration at the start of this programme of work was to use a fracture mechanics framework to examine a wide range of different potential failure modes in a tyre. The different aspects that were of interest to the sponsor included:

- Evaluating the fatigue performance of typical tyre compounds under repeated loading. This included how different compounds used in different parts of the tyre construction have different fracture or fatigue behaviour and how these results could be compared to existing published data of similar compounds.

- Developing a novel test to characterise the fatigue peeling behaviour at the interface between similar and dissimilar rubber materials.

- Identifying the key parameters that may lead to premature failure of the tyre and understand how they affect resistance to crack growth of tyre compounds and interfaces under cyclic loading.

- Developing a whole tyre model that included fracture modelling capabilities to predict which parameters affect the lifetime of the whole structure under normal loading conditions.

- Understanding how the initial design and detailed manufacturing specification for the tyre build and construction might be enhanced to increase the robustness of a radial tyre.

This thesis is divided into 7 chapters. Chapter 2 summarises the existing literature relating to fatigue failure and lifetime prediction using finite element analysis. It details the approach necessary to understand the failure of rubbery materials and to develop reliable tests to characterise it using a fracture mechanics approach. The physics of rubbery materials and the models available to describe the mechanical behaviour for use in finite element analysis are also reviewed. The key parameters influencing the crack growth are highlighted to help identify potential sources of failure in tyres. Chapter 2 ends with a brief review of the previous work done to predict fatigue failure using finite element analysis in engineered components with an emphasis on tyres.

Chapter 3 describes the materials and the experimental techniques used in this study to characterise the materials and implement their behaviour in a FEA model. It also presents the experimental setup and equipment used to evaluate the fatigue properties of rubber materials and interfaces and to analyse the results.

Whilst the initiation of fatigue failure seems to depend on the size of the inherent flaws which does not vary much from one rubber material to another, the propagation of the crack under cyclic loading depends significantly on the mechanical and intrinsic properties of the compound. Different processes are involved in toughening rubbers such as hysteresis, strain induced crystallisation, and crack tip blunting. In the absence of those processes, the behaviour should only relate to the rubber's ability to dissipate energy. In fatigue, this should result in an entirely time dependent crack growth but an additional component has been observed to contribute to the crack growth under repeated loading. An objective of this thesis is the quantification of this additional component and the understanding of its origin. Chapter 4 presents the results on the fatigue of non-strain crystallising compounds and tries to identify the origin of this additional crack growth contribution.

A tyre is a multi-layered structure made of various rubber compounds. Failure of the whole structure can arise from poor bonding or adhesion between the different layers which might result from less than optimal manufacturing or vulcanisation processes. So far, few results are available for interfaces between vulcanised compounds due to a lack of reliable testing method. Chapter 5 focuses on the fatigue behaviour of rubber interfaces with the development of a novel peeling test able to constrain the crack growth path in the interface region. The results obtained on the fatigue behaviour of

interfaces are discussed and the effect of compressive pressure during the moulding process is investigated.

Finally, the fracture mechanics approach leads to the formulation of crack growth criteria in terms of the strain energy release rate often known in the rubber research community as the tearing energy. The calculation of the tearing energy relies on the variation of stored energy in the component. Whilst for some simple components and loading conditions, the variation of energy can be calculated analytically, the complex design of the tyre prevents such an energy balance approach being used on an arbitrary crack geometry. However, the advent of finite element analysis has now facilitated the calculation of the tearing energy in a loaded component. A finite element analysis fracture mechanics framework is used in Chapter 6 which presents the finite element submodelling method adopted and the results obtained from the finite element analysis of an aircraft tyre under a range of typical loading conditions.

Finally, Chapter 7 presents the conclusions and suggestions for future work for this research project.

CHAPTER 2 - REVIEW OF THE RELEVANT LITERATURE

This chapter reviews the theories, concepts and experimental observations significant to the work undertaken in this study. In Section 2-1, the theories of rubber elasticity, their limitations and applicability are reviewed as they are essential to the analysis of experimental work in this thesis and to the analysis of components made of rubber. The general fracture mechanics approach adopted for the treatment of crack growth is then presented in Section 2-2 with an emphasis on the fracture of rubber. The concept is then extended to fatigue and cyclic crack growth in Section 2-3. A brief review of the fundamentals of interfacial interactions between polymer materials is then given in Section 2-4 along with remarks on strength of interface between rubbery materials. Finally, Finite Element Analysis is described in Section 2-5 with particular attention to tyre models and lifetime prediction in rubbery components.

2-1. **Rubber elasticity**

2-1-1. General observations for rubber elasticity

Elastomers exist in natural and synthetic form. As pointed out by Treloar (1975), the term rubber is not limited to Natural Rubber (NR) which is most commonly extracted from the sap of the Hevea Braziliensis but is a general term for materials exhibiting similar properties regardless of their chemical constitution. The most obvious characteristic of elastomers is their high extensibility even under the application of relatively small stresses. Long chain molecules are a common property of all polymers including elastomers. They consist of a repeated short chemical unit called monomer linked together through polymerisation. In elastomers, these freely rotating chains are bound in a network thanks to the entanglement of the polymer chains and weak intermolecular forces. However, these networks are of limited use in industrial applications as they will flow under even modest load over a prolonged period of time. They behave like a high viscosity fluid and can also be dissolved in a suitable solvent. In most industrial applications including tyres, crosslinks are added chemically between the macromolecules along their length through a process called vulcanisation to create a

three dimensional network. The chains may orient easily in the direction of the load when stressed and rotate freely so that the network can easily be extended several hundred percent. When the stress is released, the chains rearrange back to their original state and the rubber comes back to its original shape. To exhibit this behaviour, a polymer has to fulfil three requirements:

- It has to be made of long chain and flexible molecules in an amorphous state with weak forces between the molecules which are only lightly crosslinked together.
- It has to be above the glass transition temperature T_g which can be considered as the temperature at which the polymer goes from a glassy to a rubbery state.
- It must not be highly crystalline.

The introduction of crosslinks converts the free chains into a single coherent network in which all the molecules are connected and therefore can no longer move independently as in a liquid. The elastomer is transformed into an elastic solid, a rubber material that can no longer be dissolved in a solvent or be reprocessed. Different theories attempt to describe the elasticity of such rubbery materials based on statistical treatment of polymer chain or empirical observations. The different approaches lead to the derivation of a strain energy function (SEF) (sometimes referred to as the elastic stored energy function) which is an evaluation of the elastic energy stored in a unit volume of material that can be used to determine the stress-strain behaviour of the material subjected to a variety of modes of loading. Both statistical and phenomenological theories are explained in the following paragraphs.

2-1-2. Statistical theory of rubber elasticity

Elasticity of a single chain

The statistical theory follows the work carried out by Kuhn (1936) and by Guth and Mark (1934) on the random joint chain. They showed that for a random chain made out of freely rotating n links of length l_l and assuming one end of the chain was at the origin of a spherical coordinate system, the probability that the other end lies in a volume $\mathrm{d}\tau$ is expressed by equation (2-1) as a Gaussian error function which is only a function of the end-to-end distance of the chain r_c.

$$p(r_c)\mathrm{d}\tau = \frac{b^3}{\pi^{3/2}} e^{(-b^2 r_c^2)} \mathrm{d}\tau \tag{2-1}$$

where b is a constant depending only on the number of links in the chain and their length.

$$b^2 = \frac{3}{2nl_l^2} \tag{2-2}$$

It has to be noted that this distribution is only valid as long as the end-to-end distance is not comparable with the fully extended length of the chain.

$$r_c << nl_l \tag{2-3}$$

Equation (2-1) has a maximum for r_c=0 which means that the most probable conformation of the chain is where both ends of the chain are at the same position. However, it does not mean that the most probable end-to-end distance is zero. Equation (2-1) only considers one direction for the chain. To obtain the probability of any given r_c value, all the possible directions have to be taken into account which is done by taking the volume $\mathrm{d}\tau$ as a spherical shell centred on the origin of the coordinates system. The probability becomes

$$p(r_c)\mathrm{d}\tau = p(r_c)4\pi r_c^2 \mathrm{d}r_c = \frac{4b^3}{\pi^{1/2}} r_c^2 e^{(-b^2 r_c^2)} \mathrm{d}r_c = P(r_c)\mathrm{d}r_c \tag{2-4}$$

The function $P(r_c)$ represents the distribution of end-to end distance for a set of chains such as in a crosslinked rubber. The end-to-end distance is then taken as the distance between two successive crosslinks. From equation (2-4), the root mean square value of the end-to-end distance can be obtained as

$$\overline{r_c^2} = nl_l^2 \tag{2-5}$$

The work for a reversible deformation of this type of polymer chain is given by the variation in the Helmholtz free energy A.

$$W = \Delta A \tag{2-6}$$

where

$$A = U - \theta S \tag{2-7}$$

U is the internal energy of the system, S its entropy and θ the absolute temperature. As the rotation of the links in the chain is unrestricted, the internal energy of all the molecules is the same and the variation of A is equal to the variation of the second term in equation (2-7). Therefore, for an isothermal deformation

$$W = -\theta \Delta S \tag{2-8}$$

For a single chain in a network, it can be shown that the entropy is given as

$$S = C_s - \mathbf{k}\, b^2 {r_c}^2 \tag{2-9}$$

Where C_s is an arbitrary constant and $\mathbf{k}$ is the Boltzmann constant. Combining equation (2-8) and (2-9) gives the work of deformation for a single chain in a network.

$$W = \mathbf{k}\, \theta b^2 {r_c}^2 \tag{2-10}$$

This deformation results in a tension force at the ends of the chain necessary to create the displacement of one end. The force f_{sc} is given by equation (2-11).

$$f_{sc} = \frac{\mathrm{d}W}{\mathrm{d}r_c} = 2\mathbf{k}\, \theta b^2 r_c \tag{2-11}$$

The validity of this equation is limited to the range of end-to-end distance where the Gaussian distribution function is valid which means r_c must be small compared to the chain length and is not valid anymore once r_c approach the fully extended length of the chain where an upturn in the force-displacement response of a chain is expected. For higher deformation and therefore higher r_c, a non-Gaussian distribution function has to be used. Kuhn and Grun (1942) derived the probability density in a logarithmic form shown in equation (2-12) for a macromolecular chain by obtaining the most probable distribution of angles between the freely rotating links.

$$\ln\left(p(r_c)\right) = C_{NG} - n\left(\frac{r_c}{n l_l}\right)\zeta + \ln\left(\frac{\zeta}{\sinh\zeta}\right) \tag{2-12}$$

where ζ is the inverse Langevin function.

$$\zeta = \mathscr{L}^{-1}\left(\frac{r_c}{nl_l}\right) \tag{2-13}$$

The probability density $p(r_c)$ can also be expressed as a series expansion of equation (2-12) as given by Kuhn and Kuhn (1946).

$$\ln\left(p(r_c)\right) = C_{NG} - n\left[\frac{3}{2}\left(\frac{r_c}{nl_l}\right)^2 + \frac{9}{20}\left(\frac{r_c}{nl_l}\right)^4 + \frac{99}{350}\left(\frac{r_c}{nl_l}\right)^6 + \ldots\right] \tag{2-14}$$

The first term in equation (2-14) corresponds to the Gaussian distribution described above. As in the theory stated earlier in this chapter, the probability for a chain to present an end-to-end distance r_c irrespective of the direction in space is obtained by multiplying the probability density in equation (2-14) by the volume of a spherical shell $4\pi r_c^2 dr_c$. The tension force in the chain as it is being stretched is obtained as in the Gaussian distribution case by differentiation of the entropy term in the Helmholtz free energy.

$$f_{sc} = \left(\frac{\mathbf{k}\theta}{l_l}\right) \times \zeta \tag{2-15}$$

or expanded in series form

$$f_{sc} = \left(\frac{\mathbf{k}\theta}{l_l}\right)\left[3\left(\frac{r_c}{nl_l}\right) + \frac{9}{5}\left(\frac{r_c}{nl_l}\right)^3 + \frac{297}{175}\left(\frac{r_c}{nl_l}\right)^5 + \frac{1539}{875}\left(\frac{r_c}{nl_l}\right)^7 + \ldots\right] \tag{2-16}$$

The force-displacement curve for both Gaussian and non-Gaussian distribution are shown on Figure 2-1. The inverse Langevin function cannot be represented in a closed form. Several methods have been proposed and compared in a study by Itskov et al. (2012) either by a series expansion method or by rational functions (Cohen (1991), Treloar (1975)) to approximate the function. The Taylor expansion method fits the real function accurately except in the neighbourhood of the asymptotic behaviour when r_c/nl_l approaches 1 while the rational function describes this behaviour quite well. However the error in the lower range of r_c/nl_l is much higher for rational functions. The force-displacement curve for both Gaussian and non-Gaussian distribution are shown in Figure 2-1 using the Treloar approximation and a 59 terms Taylor expansion series of

the inverse Langevin function. The inverse Langevin follows the linear behaviour of the Gaussian distribution for value of chain extension ratio less than 1/3.

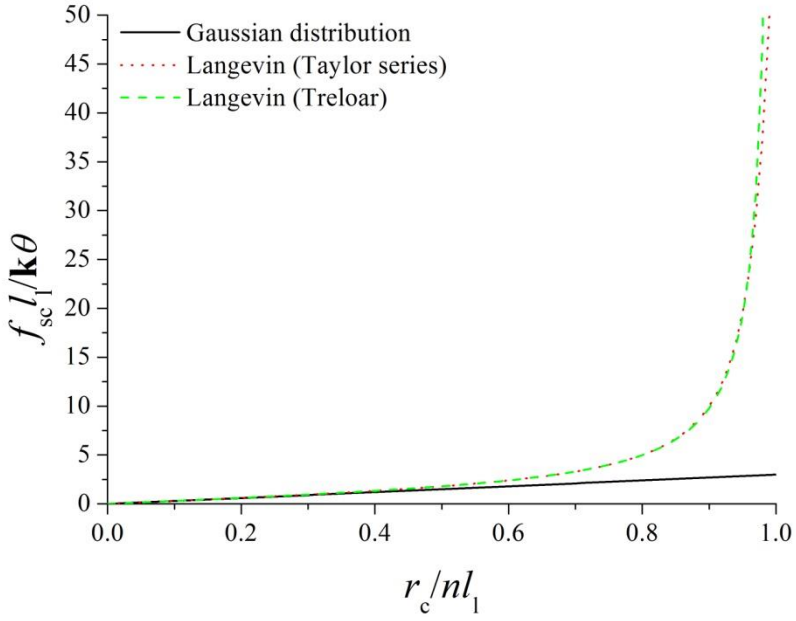

Figure 2-1. Trend of force-displacement curve for a single random chain. Adapted from Treloar (1975).

Incompressibility

Two fundamental constants *K* and *G* can be used to describe the behaviour of isotropic elastic materials at small strains. The bulk modulus *K* is the ratio of the variation of pressure due to a relative change of volume. It measures the resistance of a material to a hydrostatic pressure. The shear modulus *G* is defined as the ratio of the shear stress to the shear strain and measures the resistance of a material to a simple shear deformation. All the other elastic constants such as the Young's modulus *E* or the Poisson's ratio ν can be calculated from these two material characteristics through simple relationships such as those shown in equations (2-17) and (2-18).

$$E = \frac{9KG}{3K + G} \tag{2-17}$$

$$\nu = \frac{3K - 2G}{2(3K + G)} \tag{2-18}$$

For typical rubbers, the shear modulus is low (0.1 to 10MPa) compared to the bulk modulus (about 1GPa). Therefore, for rubbery materials, incompressibility is often

assumed as the Poisson's ratio approximates to 0.5 and the Young's modulus is taken as 3*G*. The behaviour of the material at strains in the linear region can thus be obtained from a single constant *G*. At larger strains however, the non-linear behaviour of the material is not accounted for by a single linear elastic constant and another theory is required.

Elasticity of a rubber network at large strains

By considering a rubber network of X chains per unit volume, it is possible to explore the behaviour of a network at large strain. Here, a chain is defined as the segment of the molecule between two crosslinks. Like a single chain, the work of deformation for a network of chains can be obtained through equation (2-8). The change of entropy on deformation can be calculated as follows. A unit cube under deformation presents extension ratios in the principal directions equal to λ_i (i=1,2,3). If affine deformation in the material is assumed (the components of length of a chain change in the same ratio as the whole network), a chain in the original position (x_{0i}, i-1,2,3) is subjected to a transformation so that its deformed coordinates (x_i, i=1,2,3) are given by equation (2-19).

$$x_i = \lambda_i x_{0i} \tag{2-19}$$

The entropy of a chain in the deformed state, as given by (2-9) is now

$$S = C_s - \mathbf{k} b^2 \sum_{i=1}^{3} {\lambda_i}^2 {x_{0i}}^2 \tag{2-20}$$

Therefore, the change of entropy for a single chain in the network is

$$\Delta S = -\mathbf{k} b^2 \sum_{i=1}^{3} (\lambda_i^2 - 1) {x_{0i}}^2 \tag{2-21}$$

The total entropy of deformation for the network is obtained by the summation of the entropy for each chain.

$$\Delta S_{network} = -\mathbf{k} b^2 \sum \left(\sum_{i=1}^{3} (\lambda_i^2 - 1) {x_{0i}}^2 \right) \tag{2-22}$$

Since there is no preferential direction for the principal directions, we may write for i=1,2,3.

$$\sum x_{0i}{}^2 = \frac{1}{3}\sum r_{c0}{}^2 = X\overline{r_{c0}{}^2} \tag{2-23}$$

where $\overline{r_{c0}{}^2}$ is the mean square length of the chain in the unstrained state. Therefore, combination of (2-2), (2-5), (2-22) and (2-23) gives

$$\Delta S_{network} = -\frac{1}{2} X \mathbf{k}(\lambda_1{}^2 + \lambda_2{}^2 + \lambda_3{}^2 - 3) \tag{2-24}$$

Therefore, the work of deformation otherwise known as the strain energy function is expressed as

$$W = \frac{1}{2} X \mathbf{k}\theta(\lambda_1{}^2 + \lambda_2{}^2 + \lambda_3{}^2 - 3) \tag{2-25}$$

It follows from equation (2-25) that, apart from temperature, the elastic properties of the network depend only on the number of chains per unit volume which is directly related to the degree of crosslinking and which is independent of the chemical nature of the polymer. By considering the state of stress of a unit volume of rubber under simple shear, it can be shown that the first factor in the strain energy function is equal to the shear modulus *G* of the material. The relationship between the shear stress and the shear strain is therefore linear according to the statistical theory similar to Hooke's law. Hence equation (2-25) is called the Neo-Hookean strain energy function.

$$G = X \mathbf{k}\theta \tag{2-26}$$

More generally, the SEF can be transformed into stress-strain relationship for a variety of modes of loading. Treloar (1944) compared the results of the SEF to stress strain data obtained experimentally for an unfilled NR with high sulphur content. The main graph on Figure 2-2 shows the comparison in tension but in general Treloar showed the theoretical behaviour only approximately fits the experimental data for specific homogenous isotropic deformation modes. The main deviation is explained by the finite extensibility of the chains which causes an upturn in the stress at strains typically above 300% which the statistical theory does not predict. Treloar (1975) points out that this deviation is not a failure of the statistical theory but rather a mathematical simplification related to the assumption of a Gaussian distribution of the probability density in the development of the theory. Moreover, Flory (1944) observed that, at strains lower than

100%, the material is stiffer than predicted by the statistical theory. He proposed this discrepancy originates from the ideal model failing to incorporate three main network defects all of which have an influence on the modulus. On one hand, loose ends which are chains connected to the network by only one end do not contribute to the stiffness; neither does a chain obtained from a molecule curled around and crosslinked with itself. On the other hand, physical entanglements of molecules similar to those present in an unvulcanised elastomer are not taken into account in the theory and may increase significantly the shear modulus especially at high strains.

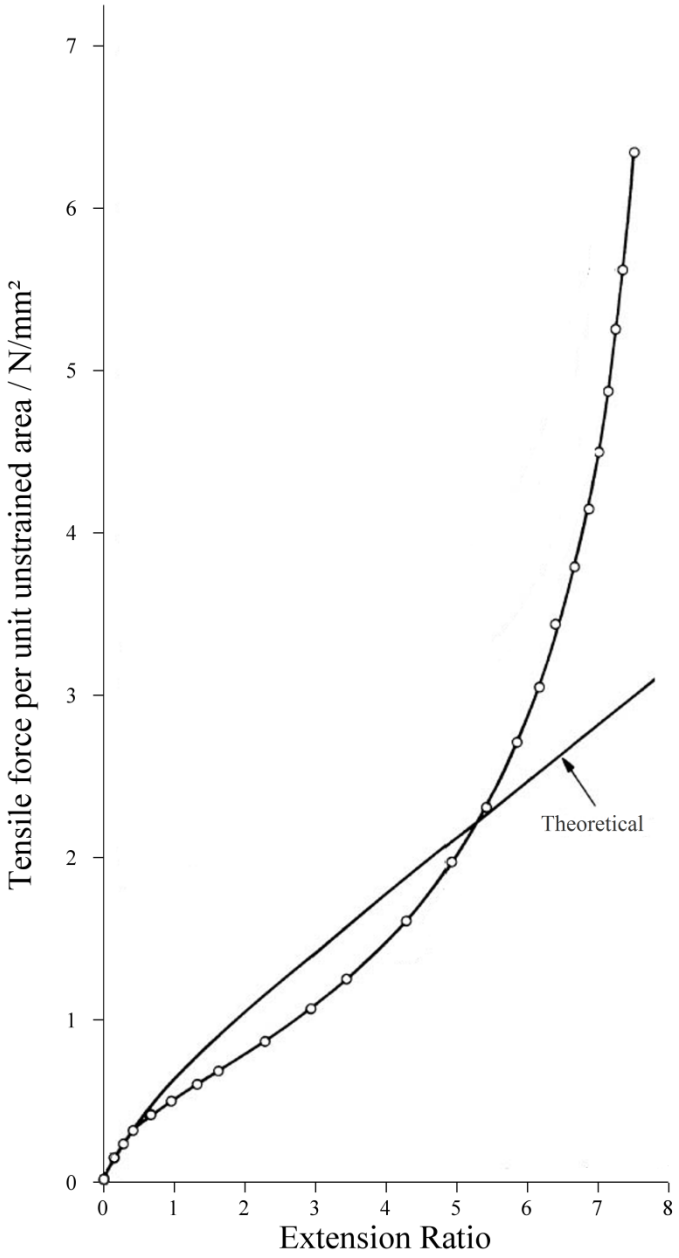

Figure 2-2. The Neo-Hookean SEF poorly fits experimental data in tension for natural rubber.

2-1-3. Phenomenological treatment of rubber elasticity

The theory presented in the previous paragraph is based on physical arguments about the polymer chains in a rubbery material. Alternatively, strain energy functions have been derived from pure mathematical reasoning to fit the experimentally obtained mechanical behaviour of rubbers. This approach focuses on finding the most general way of describing the stress-strain relationship without being concerned by the physical and molecular explanation of the expressions used in the theory. The first significant work using this approach was made by Mooney (1940). He derived the form of the work of deformation of a cylinder subjected to combination of tension/compression and shear based on the following assumptions.

- The rubber is incompressible and isotropic in the deformed state.
- Hooke's law is obeyed in simple shear or in shear superimposed in a plane transverse to uniaxial tension or compression which allowed him to express the work of deformation directly proportional to the squared shear strain.

Using purely mathematical arguments involving symmetry, Mooney derived the following strain energy function depending on the principal extension ratios λ_i.

$$W = C_1(\lambda_1^{\,2} + \lambda_2^{\,2} + \lambda_3^{\,2} - 3) + C_2\left(\frac{1}{\lambda_1^{\,2}} + \frac{1}{\lambda_2^{\,2}} + \frac{1}{\lambda_3^{\,2}} - 3\right) \tag{2-27}$$

Although derived before the statistical theory, this SEF simplifies to the Neo-Hookean SEF if constants C_1 and C_2 are taken respectively to equal to G/2 and 0 respectively. It can also be noted that in a simple shear mode, the stress-strain relationship corresponds again to Hooke's law with a shear modulus equal to $2(C_1+C_2)$. Following Mooney and assuming similar assertions, Rivlin (1948c) argued that the SEF should be symmetrical with respect to the three principal extension ratios and that, since a rotation of a body through 180° must not affect the SEF, it must only depend on even powers of the extension ratios. He concluded the SEF can be expressed as a function of the strain invariants I_1, I_2 and I_3 defined as

$$I_1 = \lambda_1^{\,2} + \lambda_2^{\,2} + \lambda_3^{\,2}$$
$$I_2 = \lambda_1^{\,2}\lambda_2^{\,2} + \lambda_2^{\,2}\lambda_3^{\,2} + \lambda_1^{\,2}\lambda_3^{\,2}$$
$$I_3 = \lambda_1^{\,2}\lambda_2^{\,2}\lambda_3^{\,2}$$

(2-28)

A direct consequence of the incompressibility assumption is expressed as

$$\lambda_1\lambda_2\lambda_3 = 1 \tag{2-29}$$

That implies that the Mooney SEF can be expressed in terms of the strain invariants I_1 and I_2.

$$W = C_1(I_1 - 3) + C_2(I_2 - 3) \tag{2-30}$$

In the late 40's, Rivlin (1948a) and (1948b) examined the stress-strain relationship, the equations of motion and the boundary conditions of different deformation mode for specific geometries. More generally, he showed that the principal extension λ_i ratios and the true stresses t_i could be related to the derivatives of the strain energy function W with respect to the strain invariants I_1 and I_2. The relationship is shown in equations (2-31) where the left hand side is referred to as the reduced stress σ^*.

$$\begin{aligned}
\frac{t_1 - t_2}{{\lambda_1}^2 - {\lambda_2}^2} &= 2\left(\frac{\partial W}{\partial I_1} + {\lambda_3}^2 \frac{\partial W}{\partial I_2}\right) \\
\frac{t_1 - t_3}{{\lambda_1}^2 - {\lambda_3}^2} &= 2\left(\frac{\partial W}{\partial I_1} + {\lambda_2}^2 \frac{\partial W}{\partial I_2}\right) \\
\frac{t_2 - t_3}{{\lambda_2}^2 - {\lambda_3}^2} &= 2\left(\frac{\partial W}{\partial I_1} + {\lambda_1}^2 \frac{\partial W}{\partial I_2}\right)
\end{aligned} \tag{2-31}$$

The commonly used engineering stresses σ_i which relate to the undeformed geometry can be calculated from the true stresses through equation (2-32).

$$\sigma_i = \frac{t_i}{\lambda_i} \tag{2-32}$$

The relationships in equation (2-31) can be used to derive the reduced stress σ^* in a variety of simple deformation modes. For example, in uniaxial tension or compression, the reduced stress term is given as

$$\sigma^* = \frac{\sigma}{\lambda - \lambda^{-2}} = 2\left(\frac{\partial W}{\partial I_1} + \lambda^{-1}\frac{\partial W}{\partial I_2}\right) \tag{2-33}$$

An example of the plot of the reduced stress against the inverse of the extension ratio is given in Figure 2-3 for an unfilled NR vulcanisate under uniaxial tension ($1/\lambda<1$) and compression ($1/\lambda>1$). Although it has been pointed out by Rivlin and Saunders (1951) that in simple extension I_1 and I_2 are not independent and therefore, for the Mooney SEF, $\partial W/\partial I_2$ is not equal to C_2, it is common to identify the partial derivatives $\partial W/I_1$ and $\partial W/I_2$ to the coefficients C_1 and C_2 in the case of the Mooney SEF. This approach to obtain the coefficients presumes an approximate linear relationship (despite the deviations pointed out later in this section) between the reduced stress and the inverse of the extension ratio found experimentally that is explained by identification of the partial derivatives of the strain energy function with respect to the strain invariants to the coefficients of the Mooney SEF. Rivlin and Saunders attribute this shape to the variation of $\partial W/I_1$ and $\partial W/I_2$ with the strain (and therefore with I_1 and I_2).

Despite these observations, in the case of the Mooney SEF, the partial derivatives $\partial W/I_1$ and $\partial W/I_2$ are commonly equalled to the coefficients C_1 and C_2. A plot of the reduced stress against the inverse of the extension ratio in any of the two modes of deformation is therefore known as a Mooney plot and should create a straight line with a slope equal to $2C_2$ and an intercept of $2C_1$. The experimental results however deviate somewhat from the linear relationship obtained from the Mooney SEF. The standard method to circumvent this deviation is to find the best fit line a very wide range of strains covered experimentally. The deviations can be explained in a similar manner as those for the Neo-Hookean function. The Mooney SEF does not account for the upturn of the stress-strain relationship and the effect of the finite extensibility of the network. For unfilled rubbers, the Mooney SEF describes the behaviour well until relatively large strains (about 500%) in tension. Conversely, filled rubbers behaviour exhibit a much earlier upturn due to the effect of strain amplification described by Mullins and Tobin (1965) and the samll strain behaviour is much more non-linear. Therefore, the Mooney SEF fails to predict reliably the behaviour of reinforced rubber materials.

Moreover, theoretically, C_1 and C_2 should be identical independently of the mode of deformation. However, Rivlin and Saunders showed that if the data derived from a tensile test were extrapolated to the compression region, then it would predict a significantly different response than the experimentally measured behaviour. This is further supported by the study of Fukahori and Seki (1992) on unfilled and filled elastomers and is a direct consequence of equating the coefficient C_1 and C_2 to $\partial W/\partial I_1$

and $\partial W/\partial I_2$. Clearly, the procedure for obtaining the coefficient C_1 and C_2 leads to inappropriate coefficients to predict the stress versus strain in different modes of loading especially for filled rubbers. However, for the unfilled materials used in this study, the Mooney SEF (thereafter referred to as the Mooney-Rivlin SEF) fits the experimental data in other modes of deformation relatively well as will be discussed in Chapter 3.

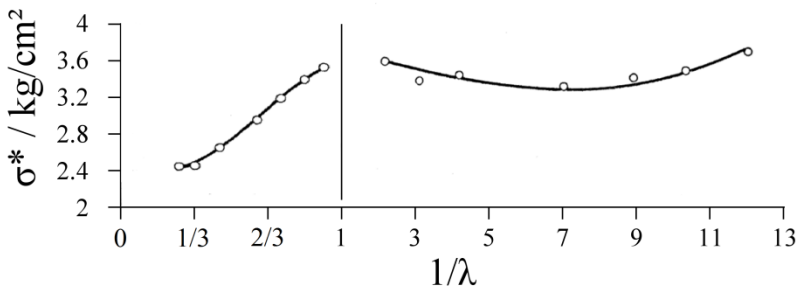

Figure 2-3. Mooney plot for an unfilled NR vulcanisate. Left part of the graph is tension, right side is compression. Adapted from Rivlin and Saunders (1951).

Since the early work of Mooney on strain energy functions with phenomenological approach, many SEF have been developed to describe rubber-like elasticity. Rivlin (1956) based on mathematical reasoning concluded the strain energy density in a rubbery material to be a symmetric function of the extension ratios in the principal directions. Therefore, Rivlin proposed it can be expressed as a function of the three strain invariants such as in equation (2-34).

$$W = \sum_{i,j,k=0}^{\infty} C_{ijk} (I_1 - 3)^i (I_2 - 3)^j (I_3 - 3)^k \tag{2-34}$$

For an incompressible material, I_3=0 and equation (2-34) reduces to

$$W = \sum_{i,j=0}^{\infty} C_{ij} (I_1 - 3)^i (I_2 - 3)^j \tag{2-35}$$

The first coefficient C_{00} has to be fixed to zero to ensure there is zero strain energy density in the unstrained state. Equation (2-35) reduces to the Neo-Hookean and the Mooney-Rivlin SEFs given earlier in equations (2-25) and (2-30) if appropriate coefficients are selected and the others are all equalled to zero. Many researchers proposed strain energy functions based on Rivlin's formula such as Isihara et al. (1951),

Bernstein et al. (1965), Van Der Hoff and Buckler (1967), Alexander (1968) or Tschoegl (1971). The SEF they proposed add higher degree terms of (I_1-3) and (I_2-3) to the Mooney-Rivlin formulation based on a non-Gaussian distribution of the chains in the network or mathematical reasoning. Those theories were successful to predict the behaviour in one mode of deformation or another and were also able to account for the deviation from the linear behaviour in Mooney plots. However, Alexander also showed that they often fail to predict the behaviour in other modes of deformation and especially in biaxial extension. Treloar (1975) pointed out one of the reasons for this failure was the same as for the Mooney-Rivlin SEF and that fitting experimental data in uniaxial extension only could not lead to good agreement in other modes of deformation. James et al. (1975) investigated the expansion of the Rivlin formula to higher degree and evaluated their ability to predict the mechanical response for both unfilled and filled NR (James and Green (1975)). They concluded that an expansion to the third order of deformation of the SEF given in equation (2-36) with five coefficients fitted the stress-strain behaviour accurately enough for most engineering applications.

$$W = C_{10}(I_1 - 3) + C_{01}(I_2 - 3) + C_{11}(I_1 - 3)(I_2 - 3) + C_{20}(I_1 - 3)^2 + C_{30}(I_1 - 3)^3 \quad (2\text{-}36)$$

They also pointed out it was not necessarily more precise to develop the Rivlin formula further. In fact, as Busfield (2000) emphasized, the introduction of more terms often leads to unstable functions that fit the experimental data well in the range of obtained results but predict inaccurate mechanical behaviour outside of the range of strains tested. They are therefore not very reliable for modelling components under complex modes of deformation. Moreover, the derivation of the coefficients for a Rivlin function including I_1 and I_2 necessitates measurements of the stress terms independently in two orthogonal directions which is not a straightforward procedure. The use of equation (2-31) in specific deformation state allows the calculation of $\partial W/\partial I_1$ and $\partial W/\partial I_2$ and therefore the identification of the coefficients of the SEF. However, the variation of these two functions has to be measured over a wide range of values of I_1 and I_2 to obtain appropriate coefficients. This requires the most general homogeneous strain possible. Biaxial tests have originally been proposed by Treloar (1948) and further developed by Rivlin and Saunders (1951) to control I_1 and I_2 independently. They used a series of strings attached to a thin sheet of rubber and with a system of springs they were able to control the strains in both directions in the middle part of the specimen (see Figure 2-4).

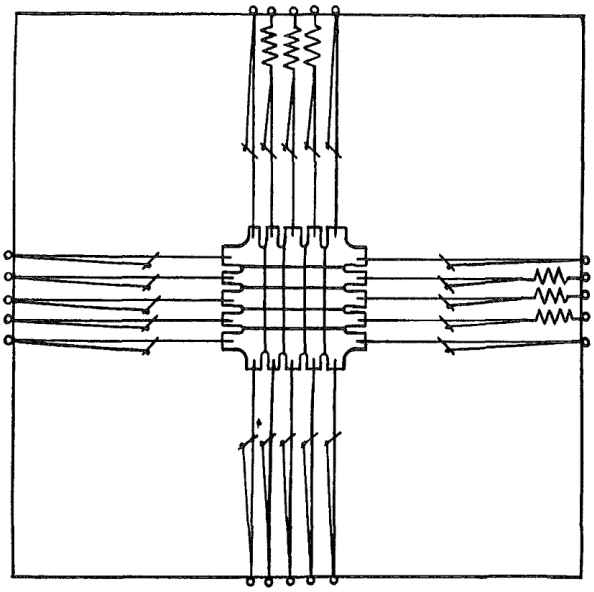

Figure 2-4. Biaxial setup used by Rivlin and Saunders (1951) to determine the variation of $\partial W/\partial I_1$ and $\partial W/\partial I_2$ with I_1 and I_2.

Many researchers used to same approach both with unfilled and filled elastomers (Hart-Smith (1966), Obata et al. (1970), Kawabata et al. (1981)). However, because of imperfect elasticity, hysteresis and stress relaxation, reliable and repeatable measurements are often difficult to obtain especially for filled rubbers for which all those effects are more pronounced. Moreover, it has been pointed out by Criscione (2003) that experimental errors in biaxial deformation are amplified and that an accurate measurement of the dependence of W on I_1 and I_2 could not be achieved in biaxial extension especially at moderate strains below 400%. Alternative setups have been proposed in order to derive the coefficients of the Rivlin series in other combined modes of loading such as pure shear (Gough et al. (1998)) and tension-torsion (Lectez et al. (2014)). Nevertheless, using biaxial extension, a general trend has been observed. The variation of W with I_1 is much larger than its variation with respect to I_2. Moreover, James et al. (1975) went further and showed for filled elastomers that $\partial W/\partial I_2$ was numerically close to zero which was later supported by the study of Fukahori and Seki (1992) on filled NR. A SEF independent of I_2 would significantly simplify the characterisation of filled elastomer as measurement of the relationships for I_2 would not be required. This idea was originally examined by Gregory (1979) who plotted the reduced stress against (I_1-3) for experimental data obtained with carbon black filled rubber under tension, compression and simple shear. He showed that the results obtained from the different deformation modes all lie on the same curve suggesting the

influence of (I_2-3) could be ignored for this type of rubbers. This observation was confirmed later by Davies et al. (1994) who extended the results of Gregory to pure shear on Natural Rubber filled with different carbon black volume fractions. This observed dependence only on (I_1-3) is possible when the strain energy density W is a function of I_1 and not significantly changed by a variation of I_2 or in other words $\partial W/\partial I_1 >> \partial W/\partial I_2$. It also requires the variation of W with respect to I_1 not to be a function of I_2. The first proposition is valid for both filled and unfilled elastomers as stated earlier in this chapter but the second assertion is only true for filled elastomers. Therefore a simple relationship exists between the reduced stress and the first strain invariant for this type of rubbers. Yeoh (1990) based his approach on this observation and proposed a strain energy function including the first three terms in (I_1-3) of the Rivlin formulation.

$$W = C_{10}(I_1 - 3) + C_{20}(I_1 - 3)^2 + C_{30}(I_1 - 3)^3 \tag{2-37}$$

He reported the mechanical behaviour of filled elastomers could be predicted accurately at large strains and in different modes of deformation but departed from the experimental data at low strain levels, lower than 1.3.

Based on the same observation, Davies et al. (1994) proposed the expression of the strain energy density under deformation given in equation (2-38) for small strains (1 to 100%) where A_D, φ, C_D and K_D are material constants. The first term comes from the observation that the shear stress-strain behaviour could be fitted with a power-law while the second term is added to account for the deviation at higher strains retaining the assumption the SEF is only a function of (I_1-3). This formulation of the strain energy proved to work well over a wide range of general strains.

$$W = \frac{A_D}{2(1-\varphi/2)}(I_1 - 3 + C_D)^{(1-\varphi/2)} + K_D(I_1 - 3)^2 \tag{2-38}$$

2-1-4. Alternative forms of strain energy function

Alternative forms of SEF for hyperelasticity have been proposed by many researchers over the years. An extensive review and comparison of various models has been published by Marckmann and Verron (2006) for use in Finite Element Analysis. Like the theories presented earlier in this chapter, they can be classified in two main categories depending on the approach adopted to derive them. The first are motivated by physical considerations and are based on the physics of the polymer network, the

second approach being phenomenological in origin. Attempts have been made to extend the statistical theory of Treloar (1943) to account for non-Gaussian distributions and broaden the domain of validity of the SEF to account for the finite extensibility of the polymer chains. Based on the non-Gaussian probability distribution derived by Kuhn and Grun (1942) and given in equation (2-12), a relationship between the stretch of the single chain and the applied deformation has to be established by assuming a representative network structure. James and Guth (1943) derived a constitutive equation for the behaviour of rubbery materials by assuming affine deformation in the network and considering that chains were distributed with equal density upon the three principal strain axes. In the undeformed state, the chains are along the three edges of a cube and are stretched uniformly to the applied deformation. This 3-chain model was later taken as a basis for development of other SEFs such as the 4-chain model by Flory (1944) where the junction point of four chains lies in a regular tetrahedron formed by the other ends of the chains connected together at the junction point and the 8-chain model by Arruda and Boyce (1993) where the chains lie on the diagonals of a cubic cell in the undeformed state. A general theory where the chains are assumed to be randomly distributed in space and to deform in an affine manner can also be developed. The strain energy density is found by integrating the stress-strain response of all the chains. Representations of the network structures are given in Figure 2-5. While the 3- and 4-chain models fit experimental data well in uniaxial tension, they fail to predict the stress-strain behaviour in other modes of deformation especially biaxial extension. The 8-chain model predicts the biaxial deformation reasonably well and in fact it is better than the full network model whose affine deformation assumption is no longer valid once the polymer chains approach finite extensibility (Boyce and Arruda (2000)).

The theories described above capture the finite extensibility of the network but present the same deviation from experimental results at small strains as the Neo-Hookean model. Flory (1944) attributed this discrepancy to the fact the statistical theory only considers crosslinks and ignores the contribution of the surrounding network such as physical entanglements. This idea has been developed by several researchers (Flory and Erman (1982), Kilian (1981) amongst others) who proposed the strain energy density at small strains is the sum of the crosslinked network contribution W_{cr} and a phantom network contribution W_{ph} accounting for interactions between interlocking polymer chains so that the strain energy W is given as

$$W = W_{\text{ph}} + W_{\text{cr}} \tag{2-39}$$

The resulting SEFs predict the behaviour at strains lower than 50% well.

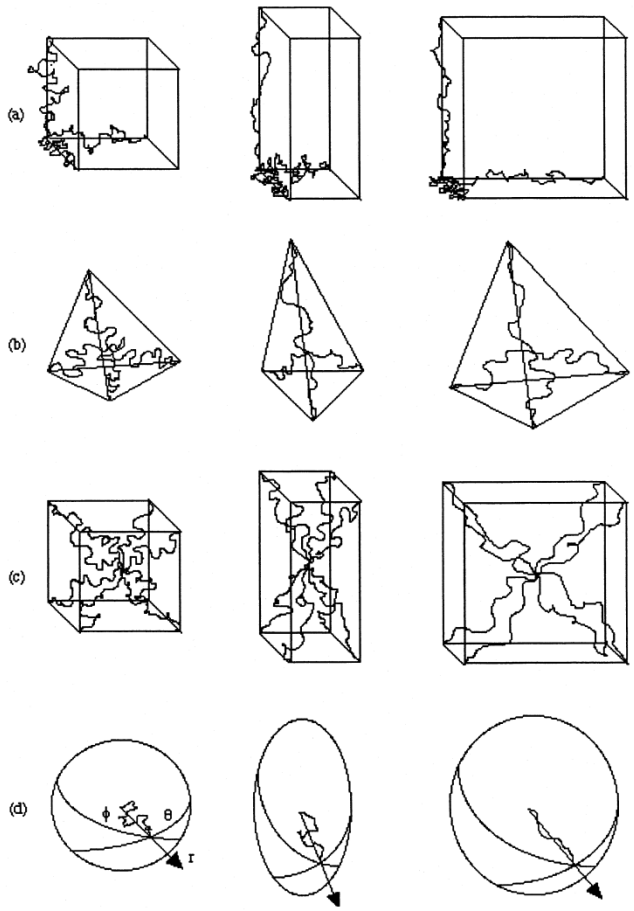

Figure 2-5. Schematic of network structures in the undeformed state, uniaxial tension and equibiaxial extension. (a) 3-chain model (b) 4-chain model (c) 8-chain model and (d) full network model.

Other phenomenological approaches have also been proposed. Based on equation (2-31) and on the variations of $\partial W/\partial I_1$ and $\partial W/\partial I_2$ with I_1 and I_2 measured by Rivlin and Saunders (1951), Gent and Thomas (1958) proposed a logarithmic variation of the strain energy function with regards to I_2.

$$W = C_1(I_1 - 3) + C_2 \ln(I_2 / 3) \tag{2-40}$$

Adopting a similar approach, Hart-Smith (1966) fitted the curve he obtained for $\partial W/\partial I_1$ and $\partial W/\partial I_2$ with an exponential function of the first invariant and an inverse function of the second strain invariant respectively. Both models do not give satisfying prediction of the behaviour of rubbers which is partly explained by the difficulty in measuring the variation of W with I_1 and I_2 accurately.

Strain energy functions based on the stretch ratio rather than the strain invariants have also been proposed with the basic claim the energy density should be a symmetric function of the extension ratios but does not necessarily depend only on even function of the stretch ratio. Following this idea, Valanis and Landel (1967) proposed the strain energy density could be expressed as a sum of functions of the different extension ratios λ_i. A similar approach was adopted by Ogden (1972) to derive the SEF shown in equation (2-41) with a stability condition defined in equation (2-42) where α_i can take any real values. Ogden showed than when $i \geq 3$, good fit of the stress-strain behaviour can be achieved in tension, pure shear and equibiaxial extension.

$$W = \sum_i \frac{\mu_i}{\alpha_i} (\lambda_1^{\alpha_i} + \lambda_2^{\alpha_i} + \lambda_3^{\alpha_i} - 3) \tag{2-41}$$

$$\mu_i \alpha_i > 0 \tag{2-42}$$

This review shows that there is not a single unique solution for the strain energy function. The choice of SEF for modelling rubbery materials behaviour depends on the loading the component is subjected to and the desired results from the model. The selection might be different to model the stiffness of an engine mount which requires a good fit in the low strain region and a fracture analysis where high strains and the upturn in the behaviour have to be predicted accurately. Many discussions about the range of validity of the functions and their ability to predict the stress-strain response of rubbery materials have been published over the years (Treloar (1975), Boyce and Arruda (2000), Marckmann and Verron (2006), Rickaby and Scott (2014)) sometimes with the emphasis being on using a FEA model (Ali et al. (2010)). Most SEFs commonly used in engineering applications are incorporated into FEA software packages but some models necessitate the development of user subroutine that defines the constitutive equation in a separate file to be applied to the simulation which is not a trivial task. The selection has also to consider the number of parameters in the function and especially the type of test it requires to obtain the coefficients. For the phenomenological approach, it is sometimes necessary to perform biaxial extensions to obtain a good fit of the SEF to experimental data in other modes of loading. For physical approaches, obtaining physical constants such as n or λ_{chain} might not be straightforward. In that regard, Mooney-Rivlin and Yeoh SEF have been considered in Chapter 3 for unfilled and filled rubbers respectively as they show a good fit to

experimental data at high strains and constants are relatively easy to determine experimentally.

2-1-5. Inelastic phenomenon encountered with rubbers

The theories described above rely on the fundamental assumption that rubbers exhibit a perfectly elastic behaviour. In reality, various phenomena cause the mechanical properties to deviate from this assumption. Despite this observation, a specific loading curve can always be fitted by a SEF chosen but the consequences of the phenomena described below have to be considered when trying to explain the deviations from the behaviour obtained for a component using a specific SEF.

Hysteresis

Hysteresis is the amount of energy dissipated when a piece of rubber is stretched. Upon relaxing, the path of the unloading curve in a stress-strain plot is lower than the loading curve as the energy the material can restore is lower than the work necessary to deform it. A hysteresis loop is shown in Figure 2-6 for a stress-strain curve measured in tension. The energy dissipated per unit volume W_d can be evaluated by the area between the loading and the unloading curve. The magnitude of the energy loss is related to the composition of the rubber and phenomenon at the microscopic scale dissipating energy such as friction between polymer chains and the breakdown of the filler structure. The presence of crosslinks reduces the hysteresis as elasticity of the rubber network is increased (Mark and Erman (1994)). Hysteresis is quite small for unfilled elastomers but becomes larger as the fraction of particulate fillers in the compound is increased (Lindley (1974)). Payne (1962) attributed this to breakdown and reformation of agglomerates of filler particles. Another contribution to energy loss comes from strain induced crystallisation (SIC). Larger dissipation is observed at higher strains once the threshold for formation and dissolution of crystals in materials exhibiting strain crystallisation has been reached (Choi and Roland (1997)).

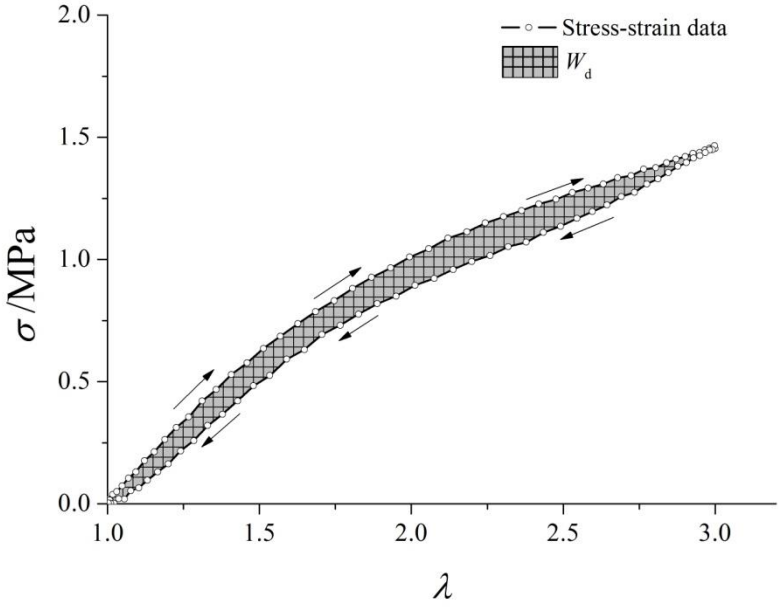

Figure 2-6. Hysteresis exhibited in rubbers and energy dissipated.

Dynamic behaviour

Application of a force on a piece of rubber does not result in an immediate deformation. The strain always lags somewhat behind the applied stress. A phase shift called the loss angle exists between the applied loading and the resulting strain when the rubber is subjected to a cyclic load. The magnitude of this angle depends upon the rubber formulation, the frequency of the oscillation, the temperature and the magnitude of the force applied (Gent (2001)). This behaviour is commonly described by the definition of a complex modulus summing the contribution of the in-phase elastic and the out-of-phase viscous responses of the material. In tension, this results in the expression of a complex modulus E^* given as

$$E^* = E' + iE'' \tag{2-43}$$

E' is usually termed the elastic modulus and E'' the loss modulus. The ratio of these values gives an estimate of the damping in the material and is a measure of the loss angle δ.

$$\tan\delta = \frac{E''}{E'} \tag{2-44}$$

An example of the typical variation of those quantities with temperature is given in Chapter 3 (Figure 3-9) for a constant strain rate. A full analysis of these properties might prove difficult to obtain as the ranges of temperature and frequency are limited experimentally. Williams et al. (1955) proposed an empirical relationship to express mechanical relaxation processes such as viscosity as a single function of temperature. They suggested the ratios of relaxation process at a temperature θ and at a reference temperature θ_s were similar and could be expressed as a single shift function a_T given by equation (2-45).

$$\log a_T = \frac{-C_{w1}(\theta - \theta_s)}{C_{w2} + (\theta - \theta_s)} \tag{2-45}$$

The choice of the reference temperature depends on the polymer the formula is applied to. Originally, Williams et al. (1955) suggested the coefficients C_{w1} and C_{w2} were not changed by the polymer type and were respectively equal to 8.86 and 101.6K and that a suitable choice of the reference temperature was sufficient to fit experimental data. Williams et al. (1955) recommended using an approximate value of θ_s.

$$\theta_s = \theta_g + 50 \tag{2-46}$$

where θ_g is the glass transition temperature in Kelvin. However, it has been shown case by case later that C_{w1} and C_{w2} vary from polymer to polymer. Ferry (1980) indicated values of θ_g, C_{w1} and C_{w2} to obtain a good fit for various polymers and elastomers. For example, for SBR, C_{w1} and C_{w2} are equal to 4.57 and 113.6K for a reference temperature of 298K. Using this equation at different temperatures, it is possible to draw a mastercurve of the variation of one quantity related to relaxation process in the material such as E' or E''. This process, called Time Temperature Superposition (TTS) is depicted in Figure 2-7 (Gent and Walker (2005)).

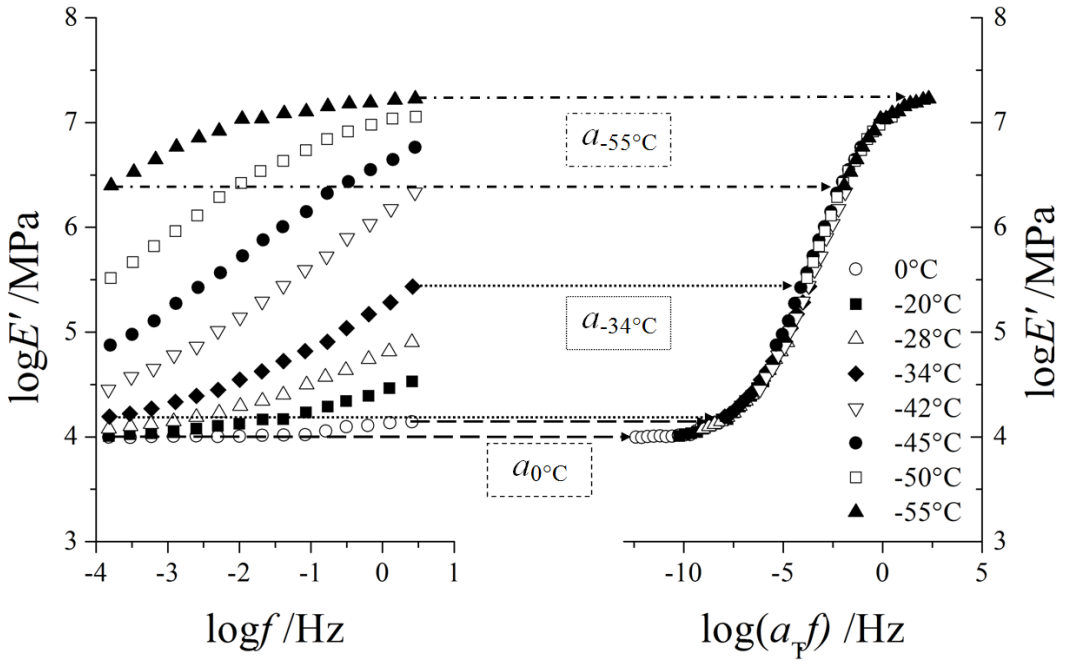

Figure 2-7. Time Temperature Superposition principle applied to storage modulus E'. Adapted from Gent and Walker (2005).

The change in temperature corresponds to a variation of time (here represented by the frequency) associated with the function a_T. The mastercurve is obtained for the reference temperature of -50°C and shows the variation of storage modulus with the frequency at this temperature. The behaviour at other temperatures can be obtained by a shift of the curve along the frequency axis using equation (2-47) so that the behaviour over a wide range of frequency at one particular temperature is accessible with experimentation over a restricted range of frequency at different temperatures. However, the use of the TTS principle is restricted to quantities for which the temperature dependence is solely controlled by the rate of molecular motion in the polymer. For example, it cannot be applied to filled rubbers as the presence of fillers also contributes to their temperature dependence by changing the filler-rubber matrix interactions.

$$\log(f_{\theta 2}) = \log(f_{\theta 1}) + \frac{C_{w1}C_{w2}(\theta_2 - \theta_1)}{(C_{w2} + \theta_2 - \theta_s)(C_{w2} + \theta_1 - \theta_s)} \tag{2-47}$$

Stress relaxation-Creep

When subjected to a constant load, the deformation in the rubber keeps on increasing with time. This phenomenon is known as creep and originates from the same mechanism as stress relaxation, the process by which the stress necessary to maintain a

defined strain in a material decreases with time. Friction forces exist between the chains in an elastomer. When a macromolecular chains network is deformed, these frictional forces have to be overcome in order for the chains to slide past each other. This introduces a time delay and a gradual approach to an equilibrium position corresponding to a reorganisation of the chains towards the minimum entropy. If chemical effects are not encountered then the rate of creep and stress relaxation follow an approximate linear relationship with the logarithm of time (Gent (2001)).

Cyclic stress softening and Mullins effect

When a rubber is subjected to cyclic loading, its stiffness decreases progressively with each loading cycle. This behaviour has been observed very early in the science of rubber materials (Bouasse and Carriere (1903)) and is termed cyclic stress softening. Mullins (1948) was one of the first to investigate this phenomenon and therefore cyclic stress softening is often mistakenly referred to as Mullins' effect in the literature. The stress-strain behaviour for a SBR filed with 50 parts per weight of carbon black is shown in Figure 2-8 for a series of increasing maximum strain cycles. For a series of loading and unloading at the same maximum strain, the maximum stress measured decreases with the number of cycles.

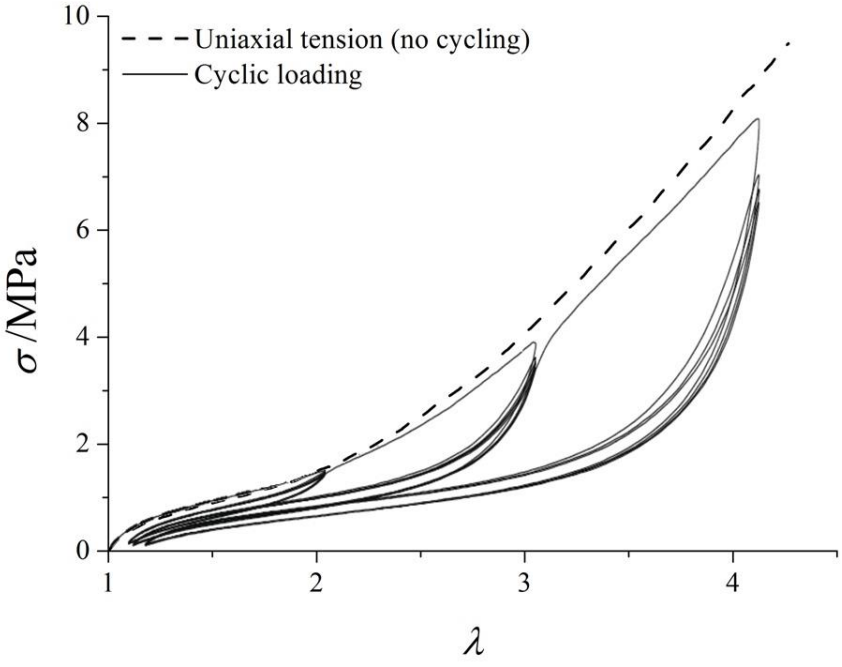

Figure 2-8. Cyclic stress softening and Mullins' effect. From Diani et al. (2009).

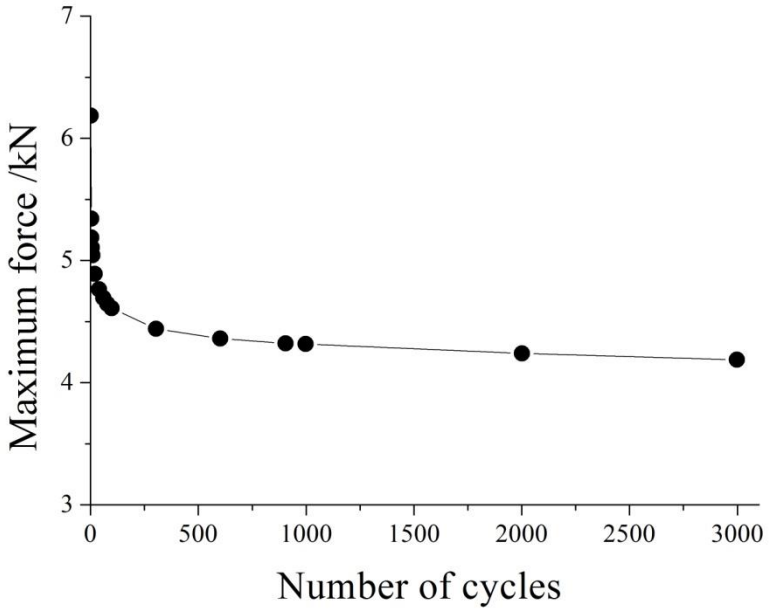

Figure 2-9. Stress softening effect occurs mainly over the first cycles. Redrawn from Asare et al. (2009).

This softening is much more pronounced in the first cycles (Harwood et al. (1966)). In fact, it is often considered most of the softening occurs in the 10 first cycles. A plot of the maximum force against the number of cycles such as given by Asare et al. (2009) confirms this observation (see Figure 2-9). Davies C. K et al. (1996) noticed the maximum force evolves linearly with the logarithm of the number of cycles except for the first few cycles. This observation was further supported by data from Asare et al. (2009) and Mars and Fatemi (2004) on different materials and with different strains although the establishment of the semi logarithmic behaviour is delayed with increasing maximum strains. An example is given in Figure 2-10 for a NR compound filled with 60 phr of carbon black under a combination of tension and torsion. The steeper slope as the peak strain increases in Figure 2-10 indicates the stress softening effect increases progressively with increasing strain, an observation Mullins (1948) made early in his work and which has been confirmed by many authors since. Figure 2-8 also shows that the softening appears for levels of strain equal to or lower than to the maximum stretch ever applied. When the strain exceeds the maximum extension applied previously then the stress-strain response approximately returns to the path of the virgin material under monotonic loading through a transition phase which gets wider in term of strain as the

maximum stretch is increased. This phenomenon is called correctly the Mullins' effect and should not be confused with cyclic stress softening.

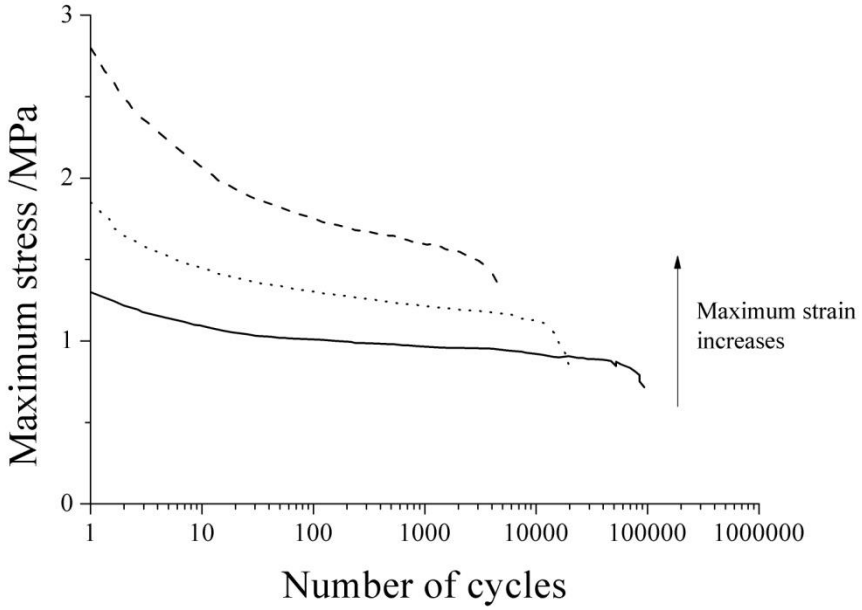

Figure 2-10. Evolution of the maximum stress with the number of cycles for NR60 subjected to a combination of tension and torsion. Adapted from Mars and Fatemi (2004).

In conclusion, imperfect elasticity is exhibited in many ways in rubbery materials. Under cyclic loading, rubbers show different mechanical behaviour in each cycle. Moreover, strain rate, frequency and temperature have a significant influence on these phenomena as well as on the elastic properties. The SEFs described earlier in this chapter (at least the phenomenological approaches) necessitate fitting the function to experimental data in order to obtain coefficients. Models taking into account those phenomena especially cyclic stress softening and Mullins' effect have been proposed (Diani et al. (2009)) but still fail to correctly predict the behaviour in all modes of deformation. It would also be extremely difficult and time consuming to obtain coefficients for every single cycle and for all environmental conditions. Because the stress-strain curves reach a steady state after a certain number of cycles, the strain energy function can be derived after a defined number of cycles and considered stable with further repeated loading. This approach is called conditioning and has been used widely (Yeoh (1990), Busfield (2000), Papadopoulos et al. (2003)). Moreover, great care has to be taken in the choice of environmental conditions for experimental investigations and the effect of imperfect elasticity on SEFs has to be carefully analysed

especially for long lasting cyclic loading experiments such as fatigue crack growth testing.

2-2. **Tearing of rubbery materials**

Different approaches can be used to characterise the fracture of materials namely the stress intensity factor, the energy release rate and the J-integral. The first approach is based on the higher stress experienced by a material containing a crack when subjected to a load far away from the crack. A relationship must be established between this load and the distribution of the stresses and strains in the region around the crack tip. The stress distribution in the neighbourhood of the crack tip has been successfully calculated for a perfectly linear elastic material by Westergaard (1939) and led to the critical stress intensity factor or fracture toughness K_c which when exceeded results in the growth of the crack through the material. Thomas (1994) pointed out that to apply this theory to rubber, an evaluation of the stress field around the crack tip was necessary for elastomers. The complexity of the calculation involved due to non-linear viscoelastic behaviour and uncertain crack tip geometry results in the common treatment of fracture of rubbery materials with an energy criterion such as the *J*-integral approach by Rice (1968) or an extended theory of Griffith (1921) using a strain energy release rate.

In 1921, Griffith (1921) proposed a criterion for fracture based on an energy balance. The foundation of his theory is that there is a driving force for crack extension working against a resistance to crack growth. He proposed this resistance was directly associated to the creation of surface energy when the crack grows. Therefore, he suggested that a crack would propagate of a length d*c* only if the stored strain energy decrease d*U* caused by the crack growth is higher than the increase in surface free-energy γ_s created as the crack is extended. It can be expressed as

$$-\left(\frac{\mathrm{d}U}{\mathrm{d}A_c}\right)_l \geq 2\gamma_s \tag{2-48}$$

where U is the strain energy stored in the material, A_c is the surface of the crack, γ_s is the surface free energy per unit area and l denotes that the differentiation is carried out at constant extension so that the external forces do no work. In the case of a thin sheet of material, equation (2-48) is reduced to

$$-\frac{1}{h}\left(\frac{\mathrm{d}U}{\mathrm{d}c}\right)_{\mathrm{l}} \geq 2\gamma_{\mathrm{s}} \tag{2-49}$$

where h is the thickness of the sheet. The first terms in equations (2-48) and (2-49) are commonly referred to as the energy release rate. For brittle materials, Griffith proposed the critical energy release rate at which crack propagation occurs is equal to the surface energy created and he successfully applied this theory to thin sheets of glass in which he introduced small flaws in the form of elliptical holes. He was able to derive the differential adopting the linear elastic theory by Inglis (1913) for holes of different sizes and found reasonable agreement with the surface energy for glass. However for elastomers, the magnitude of the critical energy release rate is orders of magnitude higher than predicted by the surface energy criterion. As Thomas (1994) pointed out, the relaxation of large volumes of material near the crack tip as the crack grows suggests the strain energy is dissipated over a large volume of rubber and is therefore greater than just the surface energy term.

The expression of the J-integral defined by Rice (1968) is given in equation (2-50). It is based on a field theory for elasticity that can be derived from the SEFs seen in Section 2-1 of this chapter to evaluate the different terms in the equation. The J-integral was originally developed for 2-D non linear elastic materials at small displacement gradients.

$$J = \int_{\Gamma} \left(W\mathrm{d}x_2 - \boldsymbol{T}.\frac{\partial \boldsymbol{u}}{\partial x_1}\mathrm{d}s\right) \tag{2-50}$$

where Γ is a curve that surrounds the crack tip, $\boldsymbol{u}$ is the displacement vector, x_1 and x_2 are the coordinates parallel and normal to the direction of the crack, $\boldsymbol{T}$ is the traction vector defined by $T_{\mathrm{i}}=\sigma_{\mathrm{ij}}n_{\mathrm{j}}$ with n_{j} the component of the outward normal to the path Γ and W is the SEF used to characterise the elastic material (see Figure 2-11). Rice (1968) showed the J-integral is equivalent to the energy release rate and could be related to the fracture toughness K_{c}. Later, the theory was extended to large displacement gradients and highly extensible materials. In this case, the J-integral was found equal to the tearing energy T described later in this section.

$$J = -\frac{1}{h}\left(\frac{\mathrm{d}U}{\mathrm{d}c}\right)_{\mathrm{l}} = T \tag{2-51}$$

where h is the thickness of the sheet, U is the strain energy stored, c is the crack length and T is the tearing energy.

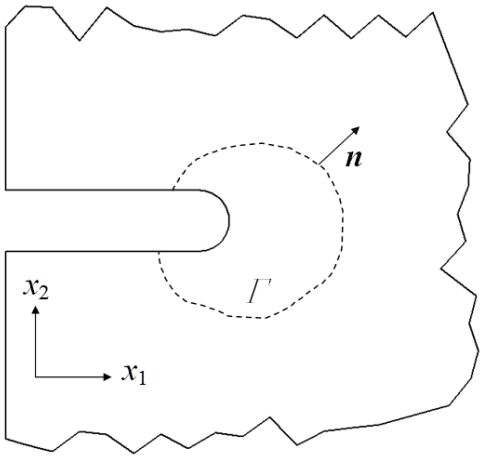

Figure 2-11. J-integral contour. The J-integral value is independent of the path Γ chosen for the calculation.

2-2-1. Rupture of rubber

Tearing energy concept

Rivlin and Thomas (1953) extended Griffith's theory to rubbery materials including the irreversible dissipative phenomena occurring in the highly strained region of the crack tip due to viscoelastic nature of elastomers. They defined the tearing energy T as the total energy release as a new surface is created. This tearing energy thus takes into account the surface energy but also all the energy dissipation processes as the crack grows. The main objective of this treatment is to find a parameter that depends only on the physical properties of the material tested and which is independent of the geometry. The magnitude of the energy dissipation should only depend on the viscoelastic properties and the strain of the material at the crack tip of a given radius. The mechanism at the crack tip responsible for the release of energy is localised and T should hence be independent of the geometry and the way the forces are applied.

$$T = -\left(\frac{\mathrm{d}U}{\mathrm{d}A_\mathrm{c}}\right)_\mathrm{l} \tag{2-52}$$

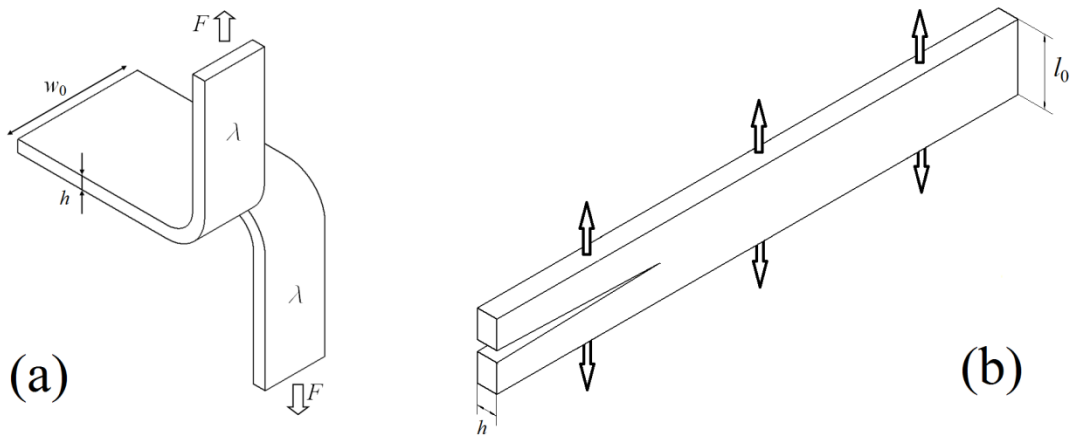

Figure 2-12. (a) Trouser test piece, (b) Pure shear specimen

Measurement of tearing energy

Rivlin and Thomas (1953) developed several different specimen geometries to check the validity of their energy based criterion. The pure shear crack growth test piece and the simple extension test piece also referred to as "trouser specimen" are shown in Figure 2-12 allow the derivation of the tearing energy from the measured force and strains using very simple relationships. For the pure shear crack growth test geometry, the tearing energy can be obtained as

$$T = W_{\mathrm{ps}} l_0 \tag{2-53}$$

where W_{ps} is the strain energy density in the pure shear central region and l_0 is the original height of the specimen. This geometry is the most commonly used for crack growth studies as the tearing energy is independent of the crack length and constant for an applied strain if inelastic phenomena are ignored. In the case of the trouser test piece the tearing energy is given as

$$T = \frac{2\lambda F}{h} - w_0 W_{\mathrm{t}} \tag{2-54}$$

where λ is the extension ratio in the legs, F is the force applied to the specimen, h is the thickness in the undeformed state, w_0 is the width of the legs and W_{t} is the strain energy density in tension stored in the legs in simple extension. Further investigations used other geometries such as split tear test piece (Thomas (1960)) and angled test piece (Lake et al. (1969)) shown in Figure 2-13. The tearing energy is calculated using equation (2-55) in the case of the split tear test piece.

$$T = \frac{F_A \lambda_A \sin\psi}{h} + \frac{F_B(\lambda_A \cos\psi - \lambda_B)}{h} - w(W_A - W_B) \tag{2-55}$$

where λ_A and λ_B are the extension ratios in region A and B, W_A and W_B the strain energy densities in those regions, ψ is the angle of splitting with $\tan\psi = F_A/F_B$ and w is the width. For the angled specimen, the tearing energy is calculated using equation (2-56).

$$T = \frac{2F}{h}\sin\alpha \tag{2-56}$$

where α is the angle between the clamps.

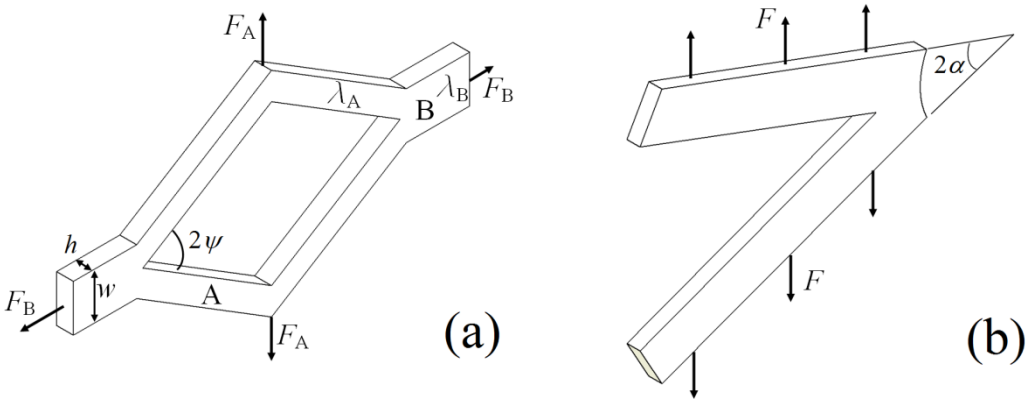

Figure 2-13. (a) Split tear test piece, (b) Angled test piece.

An additional test piece that has been widely used for fracture of rubbery materials is the edge crack specimen shown in Figure 2-14. With an energy balance approach, Rivlin and Thomas (1953) showed that the tearing energy could be obtained using equation (2-57) where W_t is the stored energy density in tension in a region remote from the crack and k is a function of the extension ratio in this region. The calculation is valid only if the length of the crack is small compared to the other in-plane dimensions. Lindley (1972) evaluated the dependence of k on the extension ratio using FEA and derived equation (2-58). The numerator is also often approximated by π to lead to equation (2-59).

$$T = 2kW_t c \tag{2-57}$$

$$k = \frac{3.03 - 0.08\lambda}{\sqrt{\lambda}} \tag{2-58}$$

$$k = \frac{\pi}{\sqrt{\lambda}} \tag{2-59}$$

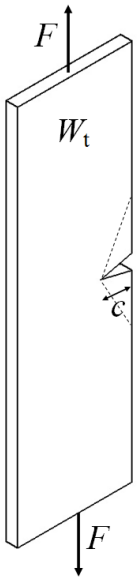

Figure 2-14. Edge crack specimen.

Lake et al. (1969) evaluated the relationship between the tearing energy and the crack growth rate *r* for four of the geometries described above and discovered that the different geometries all give similar results as can be seen on Figure 2-15 for an unfilled SBR hence confirming the tearing energy concept is suitable for the evaluation of the toughness of elastomers and its value is a fundamental material characteristic for a given rubber. Moreover, over the range of tearing rate tested, the tearing energy varies by two orders of magnitude and greatly exceeds the surface energy approximately equal to 0.1 $J.m^{-2}$ therefore proving dissipative processes play a significant role in controlling the crack growth and the strength of rubbery materials.

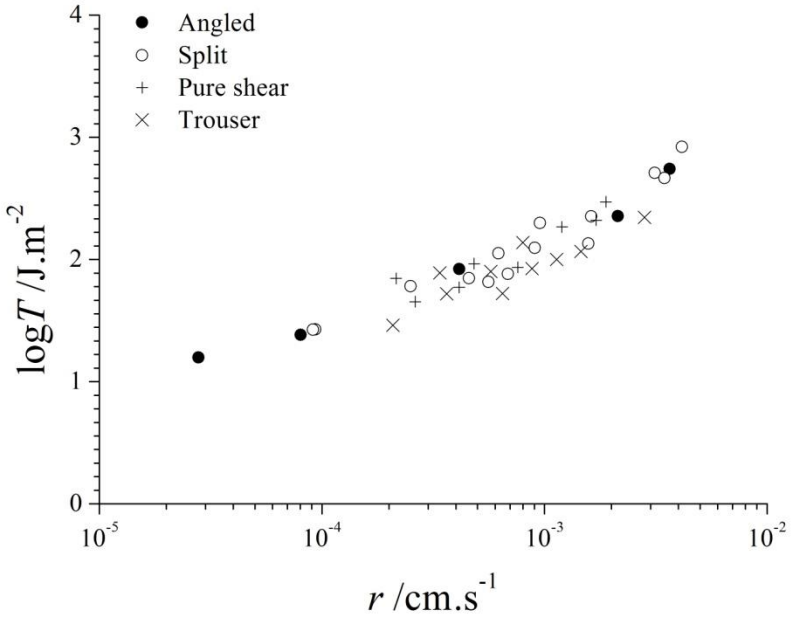

Figure 2-15. The tearing energy T as a function of crack growth rate r for an unfilled SBR using a variety of test piece geometries. Plot based on data from Lake (1995).

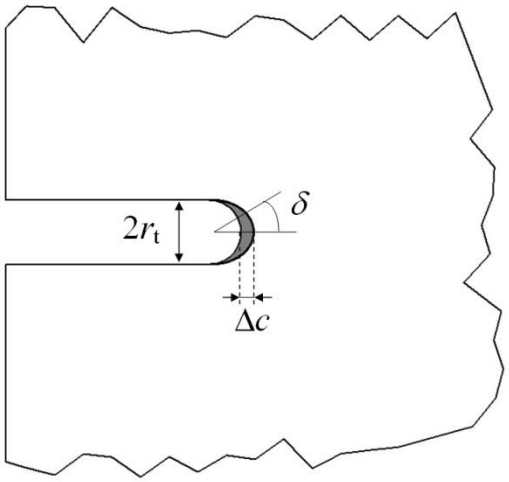

Figure 2-16. Crack tip strain state model used by Thomas (1955).

The tearing energy concept was extended by Thomas (1955) by analysing the strain distribution around the crack tip. He modelled the crack as parallel-sided slit finished by a semi-circle as can be seen on Figure 2-16 and related the tearing energy to the state of the crack tip. As the crack is growing by an amount Δc referred to the unstrained state, the stored energy loss ΔU in the shaded area is equal to

$$-\Delta U = \int_{-\frac{\pi}{2}}^{\frac{\pi}{2}} W_\delta h r_t \cos\delta \mathrm{d}\delta \tag{2-60}$$

where W_δ is the strain energy density in the direction at an angle δ with the direction of the crack, h is the thickness of the sample and r_t is the crack tip radius. Taking W as a suitable average of W_δ, the relationship to the tearing energy can be established as follows.

$$T = -\frac{1}{h}\left(\frac{\mathrm{d}U}{\mathrm{d}c}\right)_l = r_t \int_{-\frac{\pi}{2}}^{\frac{\pi}{2}} W_\delta \cos\delta \mathrm{d}\delta = 2Wr_t \tag{2-61}$$

If a specimen is brought to catastrophic failure, equation (2-61) becomes

$$T_c = 2r_t W_c \tag{2-62}$$

where W_c is the work to break per unit volume of material. Thomas (1955) compared the magnitudes of the tearing energies obtained from equations (2-54) and (2-62) using trouser test specimens with model tip diameter ranging from 1mm to 3mm. Clearly a good agreement was observed as can be seen on Figure 2-17. Moreover he found the ratio $T_c/(2r_t)$ to be fairly constant and approximately equal to the strain energy density at break in a tensile test. Further work has been made by Greensmith (1960) following the same approach. He compared the tearing energy obtained with crack growth specimen to the work at break for tensile specimen at different rates. Figure 2-18 shows the results of the two experiments together comparing $T_c/(2r_t)$ and W_c at different rates of extension given by the reciprocal of time to stretch the samples to breaking point. The values are of the same order of magnitude and show a similar dependence on time. The theory of flaws has been proposed to account for the difference. It states that more and larger flaws are present as the size of the specimen is increased as a matter of probability. Therefore the tensile strength decreases as the volume of the test piece increases. The tensile specimen therefore shows higher probability of breaking early as the number of flaws is larger than in a crack growth test where location of the rupture is imposed by the notch.

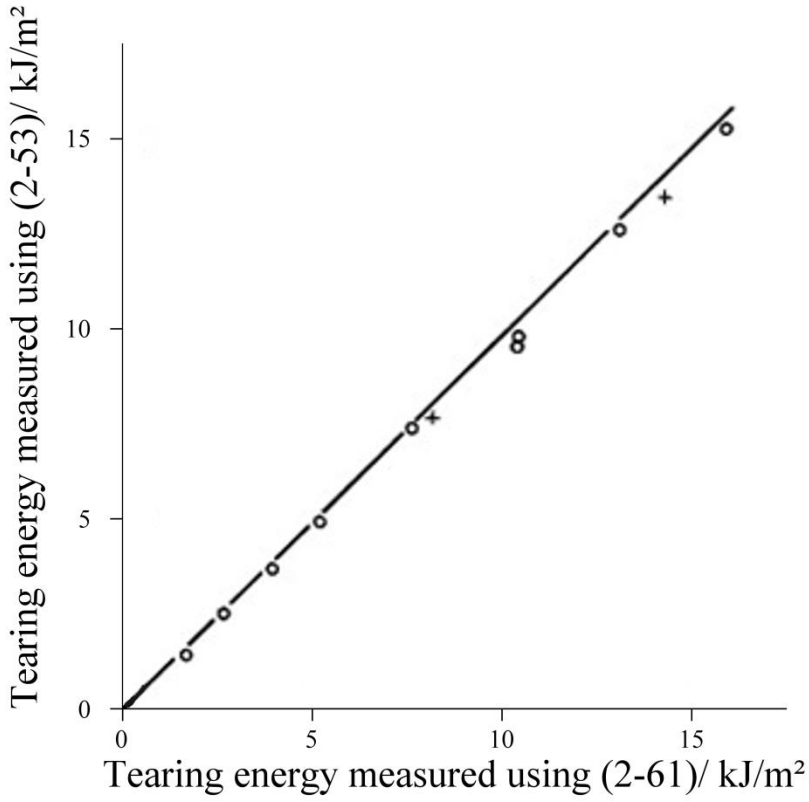

Figure 2-17. The tearing energy calculated from consideration of the strain field at the crack tip and from the overall forces applied to a trouser test specimen are similar. From Thomas (1955).

Thomas also suggested that the crack tip diameter could be related to the tearing energy through the hysteretic losses in the region ahead of the crack tip. Indeed as the crack grows, an element ahead of the crack tip is submitted to a strain cycle (see Figure 2-19). If the crack grows of a length Δc, then a volume $hD_{hyst}\Delta c$ goes through this cycle with h the thickness of the sample and D_{hyst} the diameter of the high strain region which is related to the radius of the crack tip r_t. The energy lost in this region can be calculated as

$$U_{lost} = hD_{hyst}\Delta c W_{ht} \tag{2-63}$$

Where W_{ht} is the hysteretic energy loss per unit volume. This energy loss has to be compensated by a decrease in the stored elastic energy in the material, hence

$$\Delta U = U_{lost} \tag{2-64}$$

Putting together equations (2-63) and (2-64), the tearing energy can be given by

$$T = D_{hyst} W_{ht} \tag{2-65}$$

As the hysteretic energy loss is highly rate dependent, the hysteretic loss must be evaluated at the right frequency. Considering the rate of strain in the transverse direction is similar to that in the direction of the crack growth, the time of loading τ_{load} is approximately equal to

$$\tau_{load} = \frac{D_{hyst}}{r} \tag{2-66}$$

Hence the frequency is given by

$$f = \frac{2r}{D_{hyst}} \tag{2-67}$$

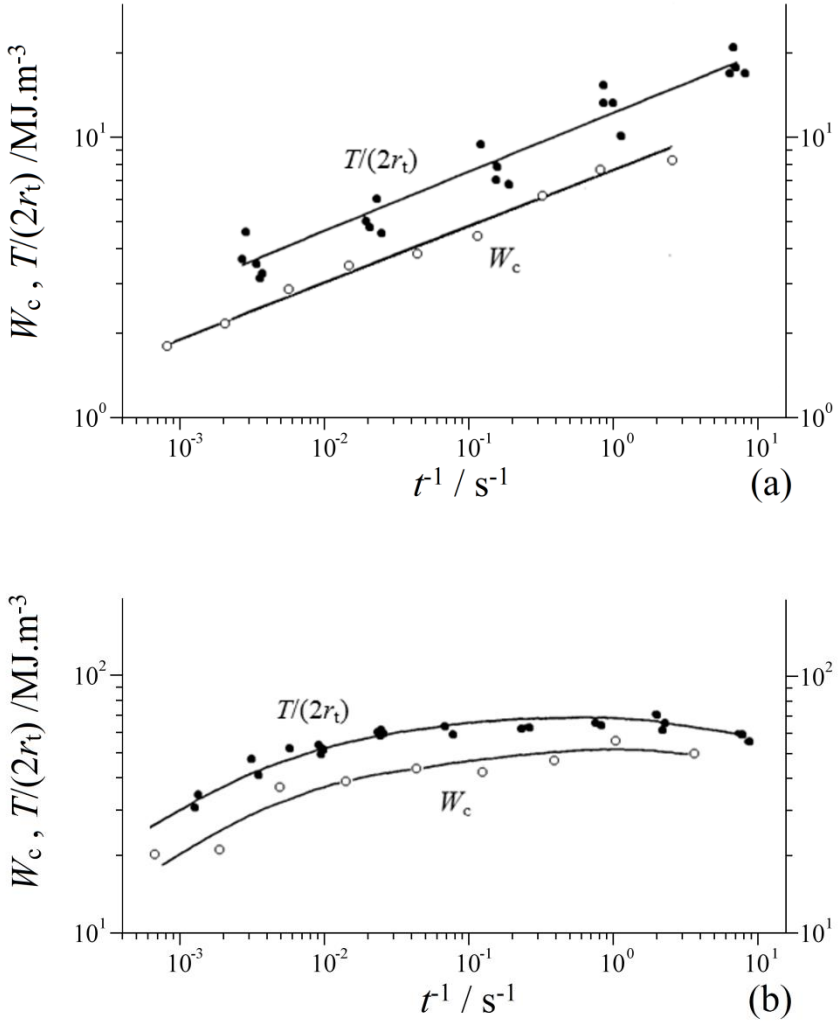

Figure 2-18. Similar trends for W_c and $T/(2r_t)$ for (a) unfilled SBR and (b) a carbon black filled SBR vulcanizates. Adapted from Greensmith (1960).

Both theories presented in this paragraph require either the measurement of the crack tip radius or the diameter of the high strain region ahead of the crack tip. Accessing those values is not straightforward as various phenomena such as crack tip branching and blunting may cause changes to the crack tip geometry. These phenomena are explained in more detail later in this chapter. Crack tip radius influence on strength has been investigated by Lake and Yeoh (1980) and (1987). They used a sharp razor blade to cut through a rubber piece subjected to various degrees of strain and thus to different tearing energy values. The additional effect of the force applied at the crack tip by the razor blade was taken into account. From observation of the roughness profile, the crack tip radius is estimated to be in the range of 0.1mm to 1mm during a crack growth test whereas when introduced by the razor blade the sharpness is much less at about 100nm. At low tearing energies (calculated from the contributions of the stretching and the blade), they observed the total energy is constant suggesting the intrinsic strength of rubber is relatively unaffected by the crack growth rate but that the crack tip diameter may be a function of the propagation rate. This was further supported by the behaviour at higher values of T for which the crack growth was a mix of cutting and tearing. The razor blade made the tip so sharp that the propagation was going faster than the razor blade. However, shortly after the initial growth, the crack stopped due to a change in crack tip geometry. Thomas (1959) observed that an initial sharp cut roughened as the crack propagated during cyclic loading of a pure shear test piece changing considerably the crack growth rate. This roughening was proposed to result from an increase of the radius of curvature of the crack tip which causes a decrease of the stress concentration in the region around the tip. Thomas suggested the roughening caused the creation of a certain number of small sharp cracks whose radii are smaller than the initial sharp tip made with the razor blade, hence dividing the value of the tearing energy for each small crack by a certain factor with regards to the tip as a whole. The energy that has to be supplied to the test piece as a whole is therefore significantly increased when roughening appears.

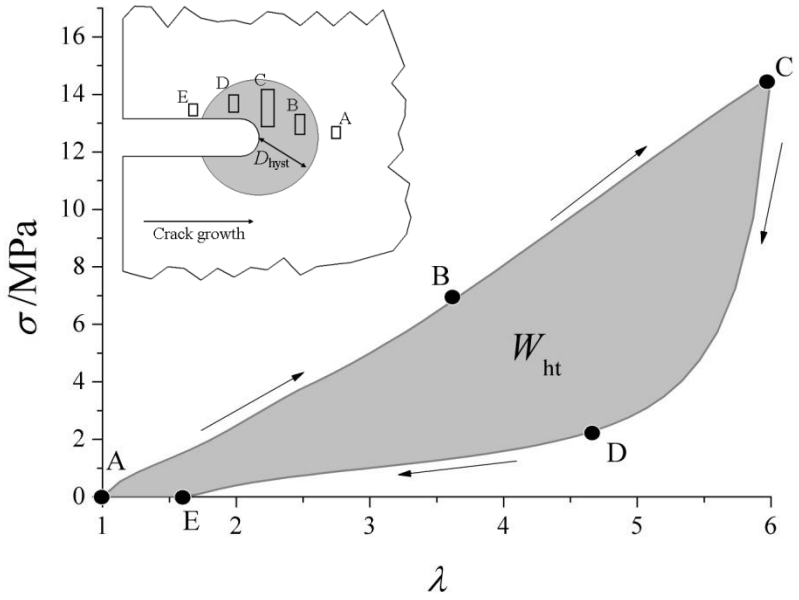

Figure 2-19. Hysteresis loop for a volume element going through the high strain region close to the crack tip as the crack advances.

2-2-2. Types of crack growth

Figure 2-20 shows the force versus time curve for different types of crack growth in a rubber, the most common way to distinguish the types of crack growth is to carry out trouser tear experiment at a constant rate of grip separation and to measure the fluctuations of the force (Greensmith and Thomas (1955)). Two main behaviours can be observed. If the force remains constant or fluctuates only by a small magnitude, the crack growth is qualified to be steady. It is noteworthy to point out the relationship between the type of crack growth and the morphology of the torn surface. If steady tearing occurs the fracture surface is essentially smooth or regularly rough with a straight crack path. A second type of tearing occurs if the force versus time curve shows a succession of peaks in the force. This behaviour corresponds to alternate periods of slow growth (even null) where the force increases continually followed by rapid and significant crack propagation causing a sudden drop of the load. Due to similarity with a phenomenon observed in friction of rubbery materials, this crack growth type is often referred to as stick-slip behaviour. A rough pattern corresponding to the stick period of the propagation alternates with a smooth fracture surface corresponding to the slip period. Knotty tearing is a special case of stick-slip behaviour where the crack deviates from its original direction and propagates at a right angle. The force increases as the

crack grows sideways until a new crack front is created corresponding to an abrupt decrease in the force. The knotty tearing is thought to be due to the development of strength anisotropy perpendicular to the direction of the crack which acts as a barrier and leads to the deviation of a crack growth path.

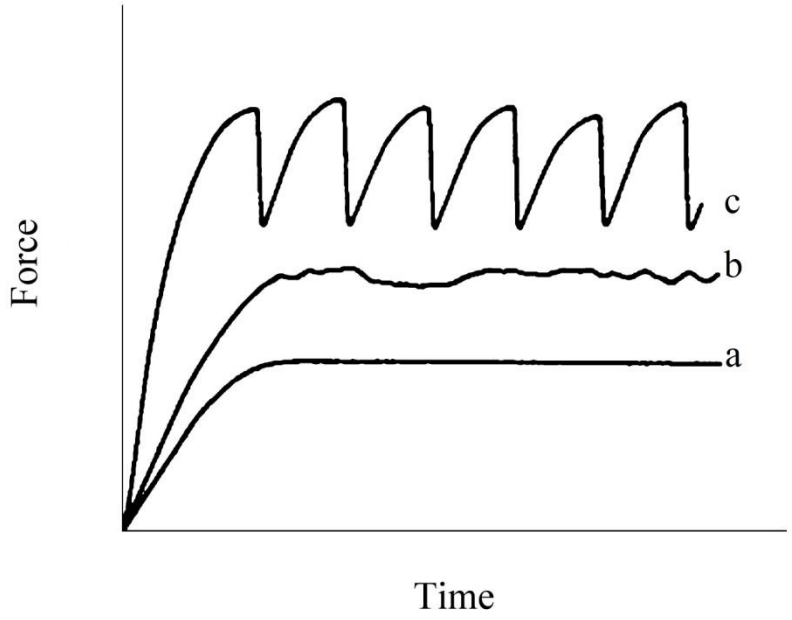

Figure 2-20. Crack growth types regarding their force vs time curves. (a) and (b) steady tearing, (c) stick-slip tearing. Taken from Greensmith and Thomas (1955).

2-2-3. Factors influencing the crack growth

The magnitude of the tearing energy *T* depends mainly on the energy dissipation processes reducing the stored energy available to drive the crack or remove the stress concentration present at the crack tip. Those processes are greatly affected by various factors detailed in the next paragraphs.

Influence of rate and temperature for non-strain crystallising elastomers

The dependence of the critical tearing energy on the rate of crack growth has been widely investigated. Kadir and Thomas (1981) investigated the behaviour of unfilled styrene butadiene rubber over a wide range of rates. They observed three regions for the crack growth behaviour using pure shear test pieces (see Figure 2-21). The rate of crack growth was calculated using the time to pass through regularly spaced marks on the rubber sample. Each region is related to a specific fracture surface pattern. In region A, the fracture surface is rough and the propagation is steady with small fluctuations. The magnitude of the energy release rate in this region slightly depends on the thickness of

the test piece suggesting the process at the origin of the fracture surface is influenced by a geometric factor. In region B, a stick slip phenomenon was identified and the rate has been taken as the average of the rate of crack growth. In region C, the crack propagates smoothly at a constant rate. The surface roughness in region A has been reportedly associated with cavitation phenomena at the crack tip (Kadir and Thomas (1981), Lake et al. (1992)). Roughness is the result of the intersection of the advancing crack with the cavities formed ahead of the crack tip. This hypothesis is further supported by the thickness effects observed by Tsunoda et al. (2000) suggesting the tearing energy and roughness over the range of rate in region A is related to the magnitude of the dilatational stresses ahead of the crack and thus to the propensity to cavitate.

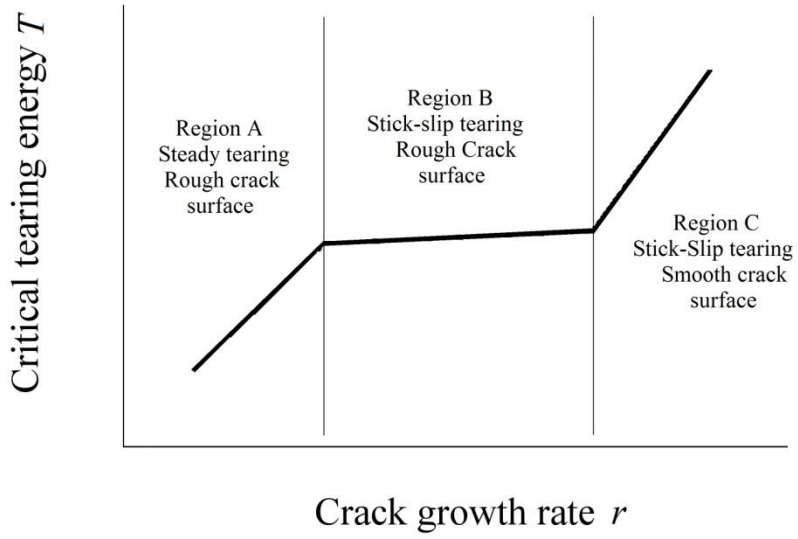

Figure 2-21. Evolution between crack growth rate with tearing energy for a non strain crystallising material (logarithmic scale).

Figure 2-22 presents the variation of the critical tearing energy with rate and temperature on a 3D plot as obtained by Greensmith et al. (1960). There is a significant increase of the strain energy release rate as the tearing rate increases and the temperature decreases. This evolution of the tearing energy is directly associated with the amount of viscoelastic dissipation. In the case of a non-strain crystallising and unfilled material (Figure 2-22 (a)), the magnitude of the energy dissipation can be related to the internal viscosity of the elastomer. The WLF shift relationship has been used later by Mullins (1959) or Tsunoda et al. (2000) to correlate the fracture data at different temperatures and a good agreement between the internal viscosity and the fracture behaviour has been found. Mullins conducted a series of experiment on

different unfilled amorphous elastomers and compared the tearing energy with the shear loss modulus used as a measure of the viscous energy dissipation. He found a close relationship between them concluding the magnitude of the tearing energy was solely due to the segmental mobility of the chains in the material (see Figure 2-23).

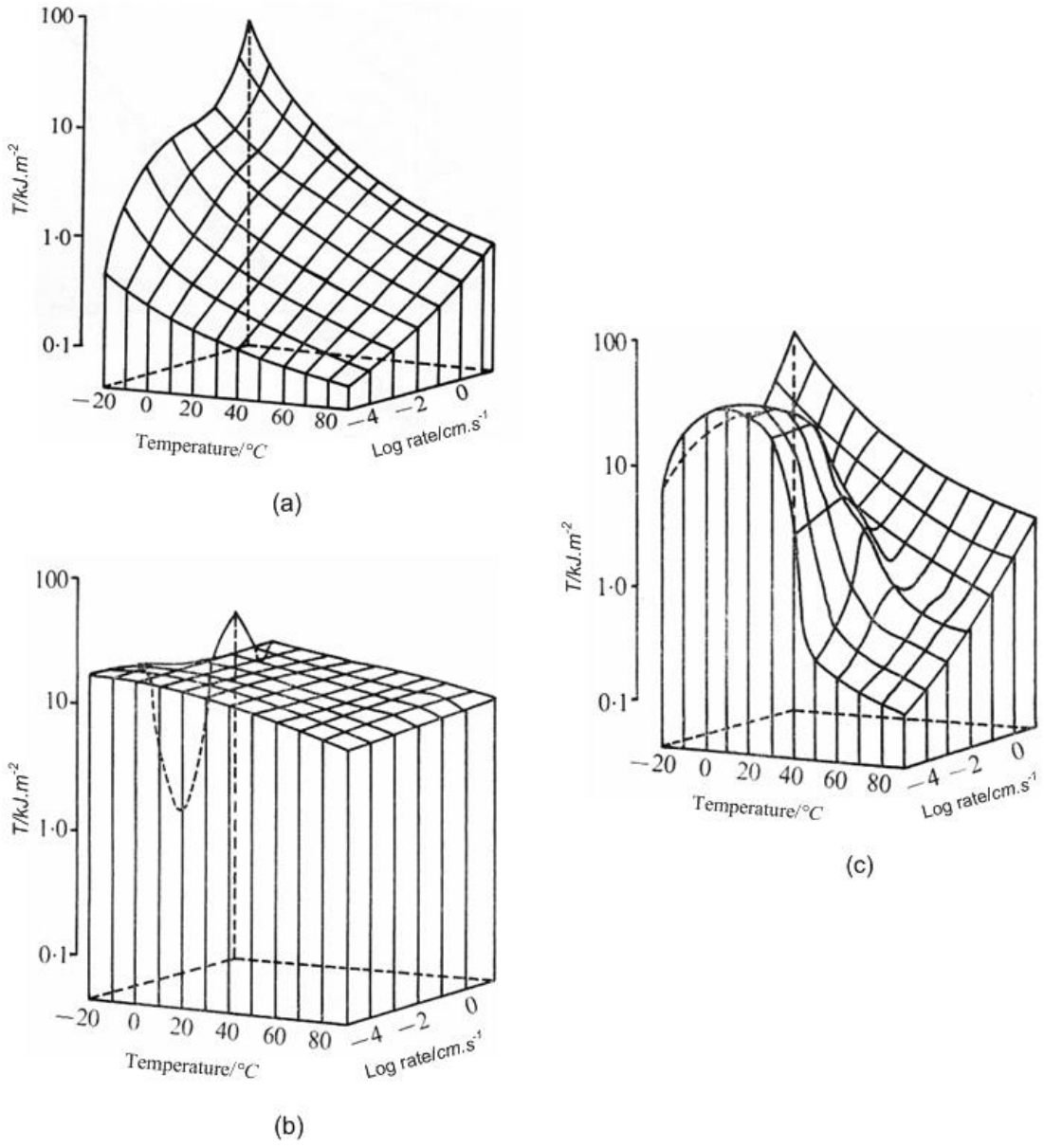

Figure 2-22. Temperature and rate effects on the tear behaviour of (a) an unfilled SBR (b) an unfilled NR and (c) an filled SBR vulcanisates. From Greensmith (1960).

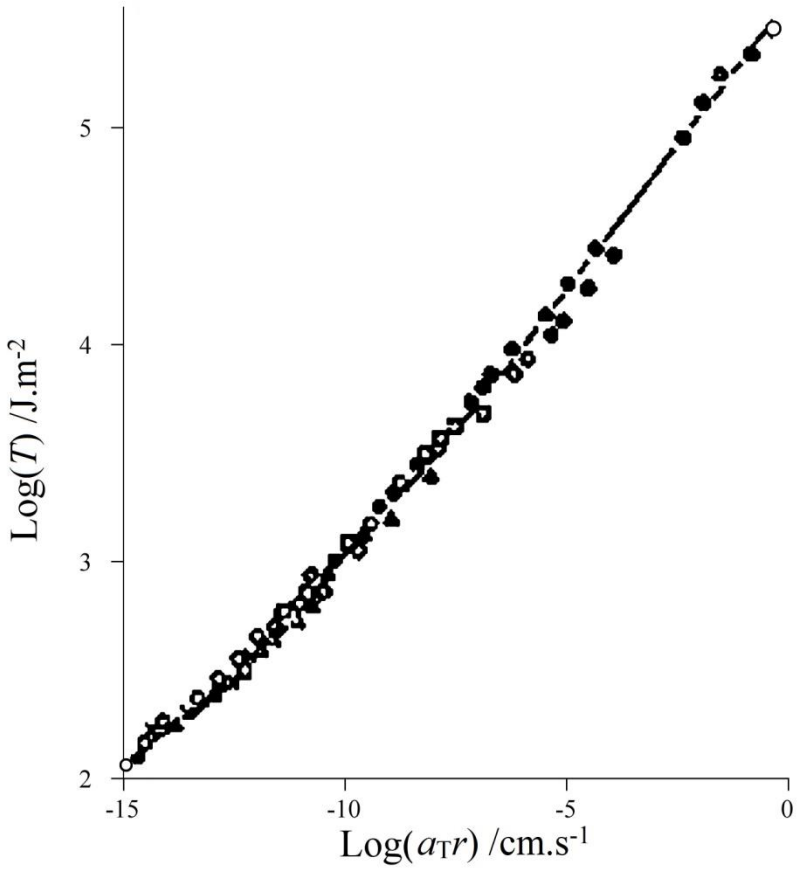

Figure 2-23. Master curve for the tearing of unfilled SBR measured over a wide range of rates and temperatures. Taken from Mullins (1959).

The addition of fillers such as carbon black causes a significant increase in the tear energy at low crack growth rates and temperatures as can be seen on Figure 2-22 (b). This change in the tearing energy has been attributed to the development of strength anisotropy at the crack tip and the occurrence of reinforcing mechanisms such as crack tip blunting and knotty tearing. Outside of this region the fracture data follow the dependence of the viscous energy dissipation increasing with higher rate and decreasing temperature. Moreover Gent and Henry (1967) showed a smaller increase in the tearing energy if the crack is prevented from deviating and that a WLF could be used to predict the temperature dependence of the tearing behaviour in the absence of the reinforcing process at the crack tip suggesting the viscoelastic dissipation in the bulk rubber still determines the tear resistance for carbon black filled rubbers.

Strain induced crystallisation

Some elastomers such as Natural Rubber because of the structure of their main chain can show a certain degree of reorientation under strain and reorganise hence forming crystals that melt once the strain is removed. This exothermic process is called strain induced crystallinity (SIC) and has been shown to significantly impact the fracture behaviour of certain elastomers. The origin of the reinforcement can be attributed to two factors. First a substantial amount of energy is dissipated in the formation of the crystals that form preferentially in the high strain region of the crack tip. Strain crystallising elastomers are significantly more resistant to tearing due to a higher hysteresis in the crack tip region. In addition, strain crystallisation is thought to be at the origin of the crack deviation phenomenon occurring over a wide range of rates and temperatures which represent a major strengthening mechanism in rubbers resulting in a fracture behaviour insensitive under certain test conditions to the crack growth rate and temperature as can be seen on Figure 2-22 (c). Moreover it has been proposed that as soon as a crystal forms in the crack tip, the crack growth is arrested until a new catastrophic threshold is exceeded when the stresses are high enough to produce a catastrophic rupture across several chains simultaneously (Persson et al. (2005)). Gent et al. (1998) evaluated the influence of tear rate on Natural (NR) and polyIsoprene Rubber (IR). Results are shown on Figure 2-24. As it has been shown before the natural rubber compound shows a plateau over the range of rates tested but a sudden decrease in the tearing energy can be seen for IR at rates over 0.01 $m.s^{-1}$. This was attributed to the time dependent nature of the strain crystallisation and to the fact that IR is crystallising more slowly than NR resulting in a decrease of the tear strain at the fastest tear rate. Furthermore, Sakulkaew et al. (2010) conducted experiments where they related the rate of strain at the crack tip (related to the time derivative of the tearing energy dT/dt) to the critical tearing energy for strain crystallising materials which were highly crosslinked to reduce the rate of crystallization and found out a significant decrease in the strength of the material at high rates. The strength reached a minimum. Sakulkaew explained this minimum by considering the tear strength to be the addition of two factors, the first due to strain crystallisation and the second to viscoelastic dissipation within the rubber. As the rate increases the effect of the former decreases because of a decrease in the rate of formation of the crystal at the crack tip while the viscoelastic dissipation gets increases with tear rate (see Figure 2-25).

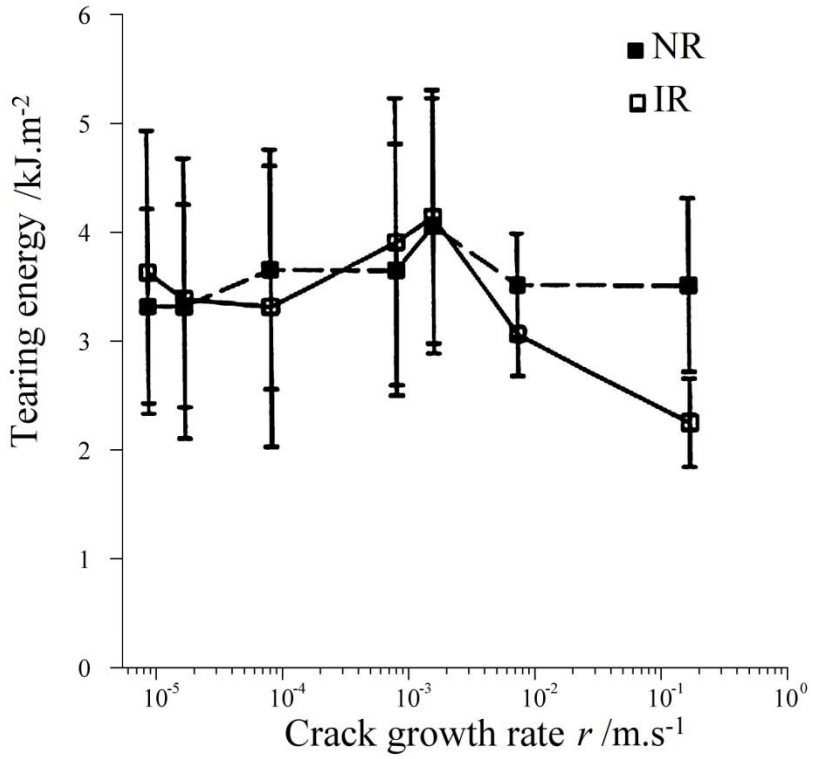

Figure 2-24. Tear strength of NR and IR against rate of crack growth. Taken from Gent et al. (1998).

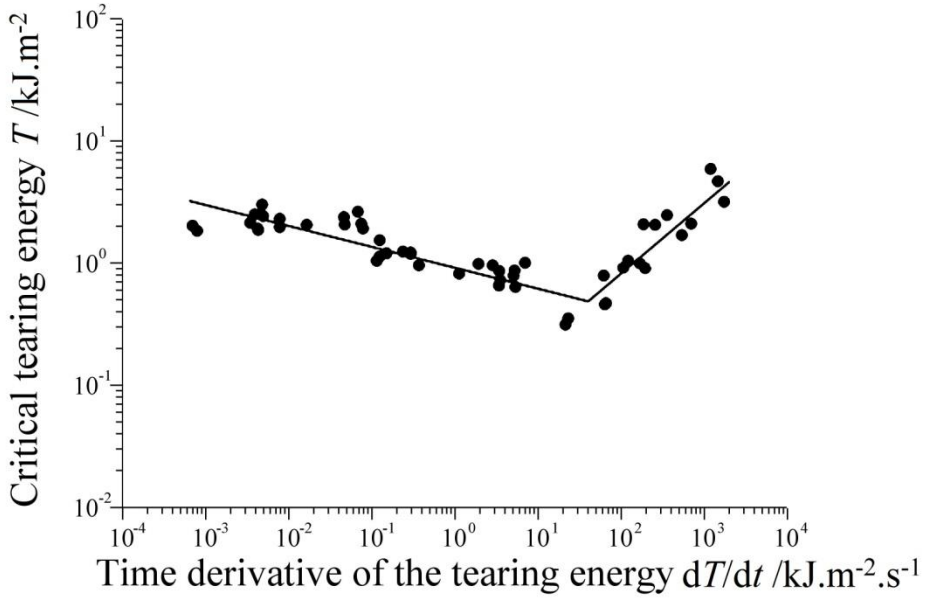

Figure 2-25. Critical tearing energy against time derivative of the tearing energy for a highly crosslinked natural rubber. Adapted from Sakulkaew et al. (2010).

Knotty tearing

Another reinforcing mechanism occurring at the crack tip is called knotty tearing. It is thought to result from the development of strength anisotropy in the high strained region at the crack tip leading to the deviation of the crack from its path. The presence of filler and strain crystallisation are known to promote this process. Figure 2-20 presents a typical force-time curve observed for knotty tearing. The force increases until a new crack breaks ahead and drops suddenly as the crack grows. This results in a discontinuous stick-slip crack growth characterised by a lateral growth or even a crack circling around (Glucklich and Landel (1976)). This propagation pattern is only seen over a range of rates and temperature depending on the filler used and the type of elastomer (De (1996), Greensmith (1956)). Several explanations for the occurrence of knotty tearing have been put forward by researchers such as crystallization which could create anisotropy at the front of the crack and result in lower strength to the direction of crack growth (Andrews (1961)). Other researchers pointed out that chain alignment could take place in the highly strained region of the crack. The addition of filler could cause a higher anisotropy by the orientation of the carbon black particles or agglomerates (Greensmith (1956)). This would lead to the creation of a laminar type of structure and the crack would propagate in between the layers such as in fibre reinforced composites and produce a deviation of the crack.

2-3. **Cyclic crack growth, fatigue of rubbery materials**

For most rubber components, failure does not occur under a single loading producing a catastrophic crack growth but rather because of a relatively low repeated stressing. The theory described in the previous section was initially intended to describe fracture under static conditions. However, a fracture mechanics approach has also been used to describe dynamic and fatigue related problems for rubbers.

2-3-1. Fatigue initiation and crack growth

Two phases can be distinguished in the fatigue failure process. The first is a nucleation phase during which cracks appear in regions that were originally thought free of cracks. The second one is a growing phase: the initial crack grows until rupture occurs (Mars and Fatemi (2002)). Rubber compounds contain various sorts of inhomogeneities that can act as a weak point or local stress raiser for the crack to initiate. A rubber compound is made of various products such as curatives and fillers that are embedded in a rubber

matrix. Their size and quantity vary from one compound to another causing a source of inhomogeneities from the nanometric to the microscopic scale. Flaws at the origin of a crack can also result from poor process or design features such as voids, dust, embedded particles, sharp edges, corners and holes. Different approaches have been adopted to examine and predict the fatigue life of rubber components. One is based on a crack nucleation approach based on the history of the quantities that are defined at one point such as strain, stress or strain energy density (Beatty (1964)). The other is based on the fracture mechanics theory. When a virgin rubber component is submitted to cyclic loading, a certain number of cycles is necessary before the appearance of any visible crack. Whether this initiation stage should be considered as part of the propagation stage is a topic of controversy among researchers. As for most of the engineering purposes, what matters is how fast a crack of a certain size is going to grow to catastrophic rupture, the problem is tackled by assuming a distribution of cracks in the test piece so that all non-material related features do not influence the fatigue behaviour. Moreover, it has been shown that the intrinsic initial flaw size in rubbery materials is of the order of tens of microns (Lake and Lindley (1965)) hence giving an idea for the initial size of crack in virgin rubber components. The focus of fatigue life determination for rubbery materials is thus shifted to an analysis of cyclic crack growth.

2-3-2. Typical fatigue behaviour

As it has been seen in the previous section, Rivlin and Thomas (1953) established that the energy required to drive a crack was a material characteristic. Later in the decade, Thomas (1959) found the extent of crack growth during one cycle could be related to the maximum energy release rate achieved during one cycle.

$$\frac{\mathrm{d}c}{\mathrm{d}N} = f(T_{\mathrm{m}}) \tag{2-68}$$

where c is the crack length, N is the number of cycles and T_{m} is the maximum tearing energy during a cycle.

Thomas (1959) also proposed the cyclic crack growth rate follows a power law relationship with the maximum tearing energy during one cycle which is also independent of the test piece geometry which was supported by many studies later such as Gent et al. (1964). Lake and Lindley (1965) later studied the fatigue behaviour of rubbers over a wider range of tearing energy and identified three other regimes in the

fatigue crack growth of rubbery materials. These regimes can be seen on Figure 2-26 and can be described using the following empirical relations (Lake (1972)).

In region I, the tearing energy is lower than a threshold energy T_0 and the whole crack growth is solely due to chemical mechanisms such as ozone degradation. The chemical reaction between ozone and carbon-carbon double bonds constitutive of the rubber molecules results in chain scission. The crack growth rate per cycle is related to the kinetics of the chemical reaction in the form

$$\frac{\mathrm{d}c}{\mathrm{d}N} = k_z[\mathrm{O}_3] \tag{2-69}$$

where k_z is the reaction constant and $[O_3]$ is the concentration of ozone. In this region, the crack growth rate is thus independent of the tearing energy and constant provided the concentration of oxidative components does not change.

In region II, the crack growth is governed by chemical and mechanical processes that approximately add up.

$$\frac{\mathrm{d}c}{\mathrm{d}N} = k_z[\mathrm{O}_3] + A_0(T_\mathrm{m} - T_0) \tag{2-70}$$

where A_0 is a constant for region II and T_0 is the threshold tearing energy to see additional non oxidative fracture process occurring.

In region III, a power law relationship has been established following Thomas's work (Thomas (1959)).

$$\frac{\mathrm{d}c}{\mathrm{d}N} = BT_\mathrm{m}{}^{\beta} \tag{2-71}$$

where B and β are material constants. β approximately takes a value of 2 to 6 for most rubbers and is mainly dependent on the base polymer and to a lower extent on the formulation of the compound. β is approximately equal to 2 for Natural Rubber and 4 for Styrene Butadiene Rubber.

At higher tearing energies, the crack growth is unstable and the crack growth rate is essentially infinite. The transition from mechanical fatigue damage to catastrophic growth is often associated with a large change of crack growth rate over a narrow range of tearing energy and a variation in the fracture surface. For strain crystallising

compounds, this usually coincides with the critical tearing energy observed in a monotonic loading (Mars and Fatemi (2003)).

$$\frac{\mathrm{d}c}{\mathrm{d}N} = \infty \tag{2-72}$$

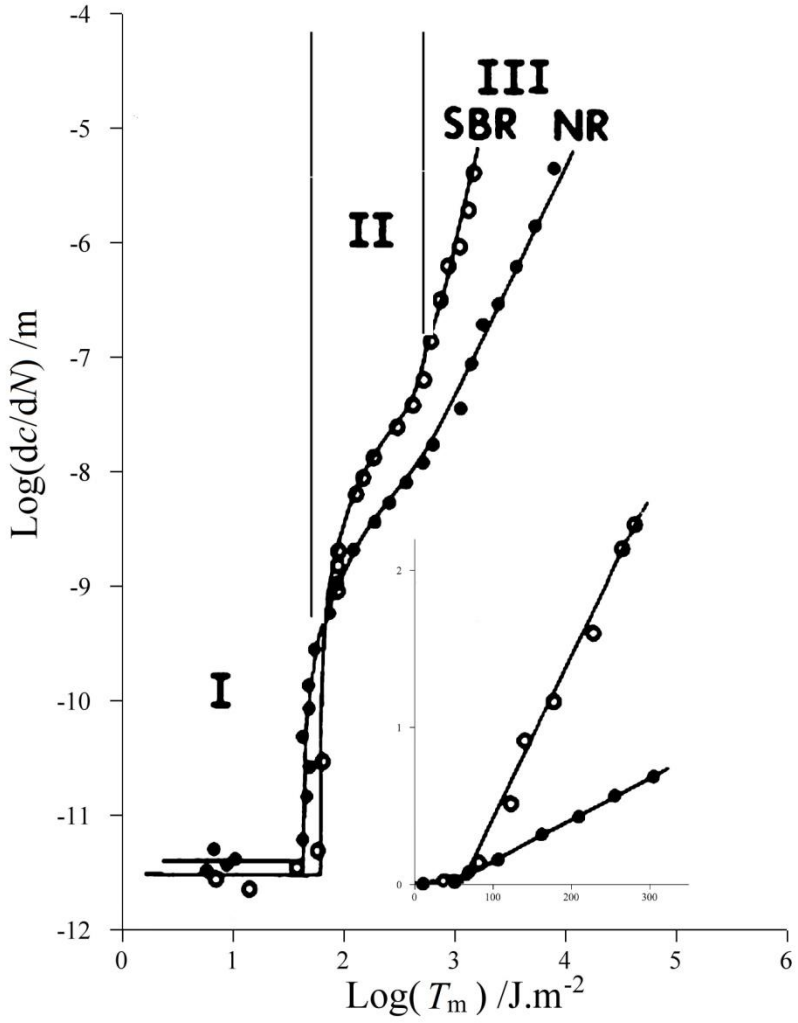

Figure 2-26. Regimes of crack growth in fatigue for unfilled SBR and NR. The inset is showing threshold tearing energy and linear relationship at low tearing energies. From Lake (1983).

2-3-3. Fatigue life prediction

The crack growth rate in regions of the graph where mechanical damage has an effect (II and III on Figure 2-26) is related directly to the maximum tearing energy during one cycle until catastrophic failure occurs. Therefore, it is possible to estimate the number of cycles necessary for the crack to grow from a length c_1 to a length c_2 using equation (2-73).

$$N = \int_{c_1}^{c_2} \frac{dc}{f(T_m)} \tag{2-73}$$

If an analytical relationship can be found between T_m and the crack length c, equation (2-73) becomes

$$N = \int_{c_1}^{c_2} \frac{dc}{g(c)} \tag{2-74}$$

This approach was used by Gent et al. (1964) and Lake and Lindley (1965) using a edge cut test specimen described on Figure 2-14. Combining equations (2-57) and (2-74), taking c_0 as the initial crack length and c_{crit} as the length at which the critical tearing energy is reached, and integrating from c_0 to c_{crit}, the number of cycles to rupture can be expressed as

$$N = \frac{1}{B(2k_t W_t)^{\beta}(\beta - 1)} \left(\frac{1}{{c_0}^{\beta-1}} - \frac{1}{{c_{crit}}^{\beta-1}} \right) \tag{2-75}$$

If $c_{crit} >> c_0$, the second term in the bracket can be neglected. In the case of uncut sample, the evaluation of N allows an estimation of the apparent initial flaw size which has been found to lie in the range of 25 to 50μm.

2-3-4. Influence of composition on the fatigue behaviour

Effect of the nature of the polymer

The nature of rubber influences the fatigue crack growth behaviour in several aspects (Lake and Lindley (1964c)). SIC is of primary concern and enhances the fatigue behaviour by the same process as monotonic tearing (see section 2-2-3 b). Performance of a particular material can be analysed through the coefficient B and β. The value of β

can vary from 2 to 6 approximately and is said to reflect the mechanical hysteresis of the material. Lake and Lindley (1964a) examined 7 different polymer types as shown in Figure 2-27. It can be seen that it is difficult to rank the polymer type according to their fatigue behaviour as it depends on the range of tearing energy encountered in the specific application. For example, it shows that Polybutadiene Rubber (BR) exhibits better fatigue life at low tearing energies but it performs less well than almost any other rubber at higher tearing energies.

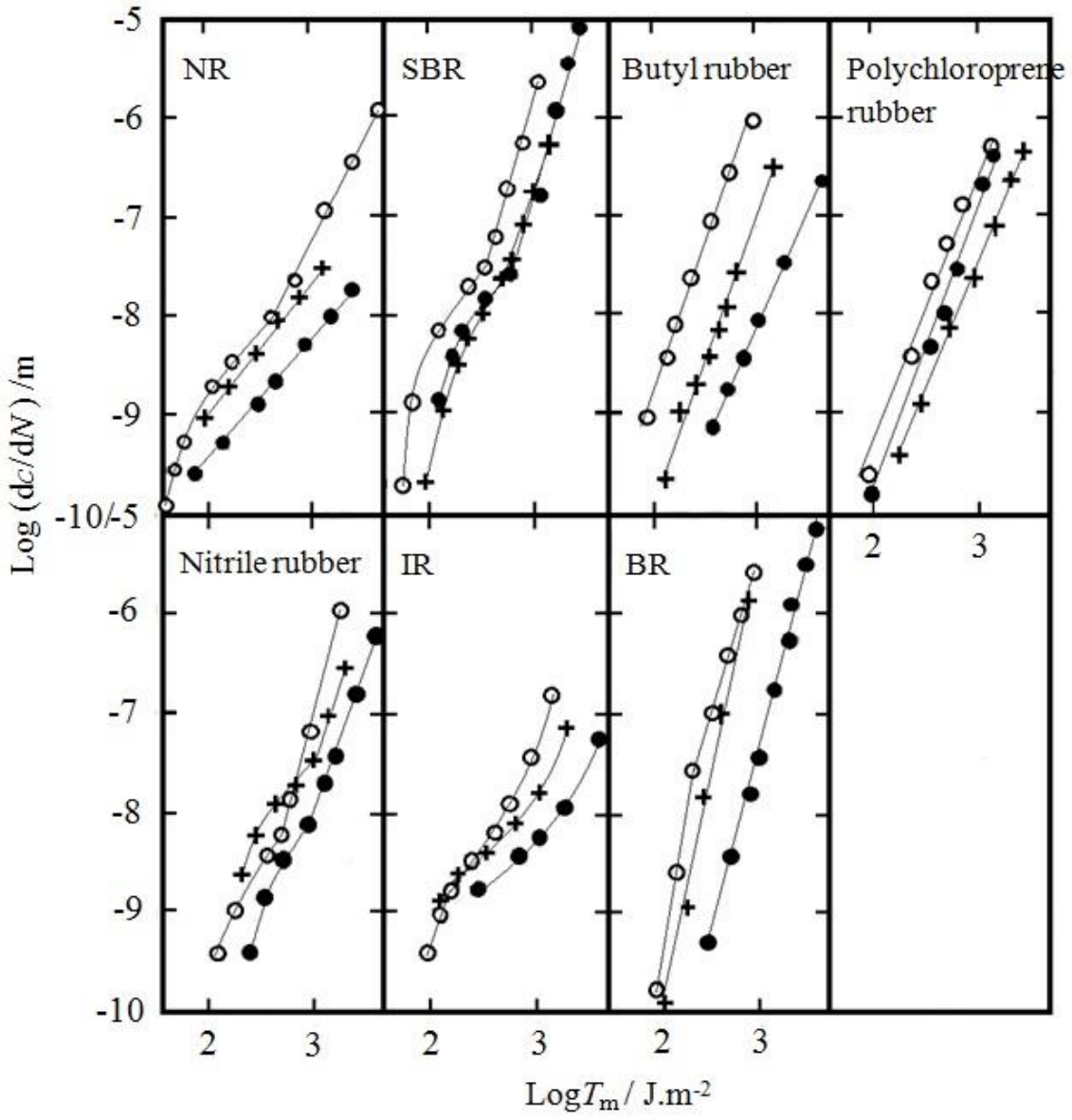

Figure 2-27. Crack growth rate per cycle for various types of base polymer and loading(o) unfilled (+) filled with 50phr of MT carbon black and (•) filled with 50 phr of HAF carbon black. Based on Lake and Lindley (1964a)

2-3-5. Effect of fillers

The addition of fillers to the compound can enhance the fatigue performance. Lake and Lindley (1964a) studied the effect of the addition of different grades of carbon black on the fatigue behaviour of several elastomers. Results can be seen on Figure 2-27. They mixed 50 phr (parts per hundred rubber by weight) of two types of carbon black into various elastomer matrix: MT (Medium Thermal) and HAF (High Abrasion Furnace) which differ significantly in their reinforcing properties. HAF carbon black is known to be reinforcing filler as the interactions with the rubber matrix are high due to low particle size and a high specific surface area per unit volume. MT carbon black presents a larger particle size that significantly diminishes its reinforcing power. In all cases presented for 7 different types of rubber, the insertion of carbon black particles reduces crack growth rate per cycle relative to the unfilled elastomer. Finer grades of carbon are seen to lead to larger improvements at the same volume fraction and tearing energy. This tendency has been confirmed by the evaluation of the fatigue life of rubber components (Dizon et al. (1974)). It has also been observed that the volume fraction had an important effect on the fatigue life with an optimum loading balancing energy dissipation and initial flaw size (Auer et al. (1958)). Addition of filler induces changes in the stiffness and the hysteresis properties which increase energy dissipation and can lead to anisotropy in the region ahead of the crack tip and hence promote blunting, branching and deviation of the crack similarly to monotonic tearing.

2-3-6. Influence of environmental parameters on fatigue behaviour

Effect of frequency

The effects of frequency and strain rate on the fatigue behaviour of elastomers have both been studied and have been found to be very different depending on the type of rubber tested (Lake and Lindley (1964b), Young (1986)). For strain-crystallising compounds, very little effect has been observed over a wide range of frequency (Lake (1983)). Crack growth only occurs above a given tearing energy and therefore the fatigue behaviour does not appear to be time dependent.

Conversely, non strain crystallising rubbers demonstrate a significant effect of frequency. Lake and Lindley (1964b) proposed the fatigue behaviour is obtained by summation of two contributions. The first component is a time dependent contribution that only depends on the duration of the loading cycle, the inverse of the frequency and

the second is a cyclic contribution that only reflects the fact the material is subjected to repeated loading and unloading. Lake and Lindley (1964b) stated that the crack growth behaviour was dominated by the cyclic component at high frequencies (10 to 1000 cycles per minute) with a decrease of a factor three in the crack growth rate per cycle where it should have been a factor 100 providing the crack growth was mainly time dependent. However at low frequencies (below 10 cycles per minute), the crack growth has been found to be inversely proportional to frequency reflecting an entirely time dependent behaviour. Young (1986) later found that the strain rate also has an effect on a partially crystallising material. The crack growth rate at a fixed tearing energy decreases with an increase in the strain rate revealing a time dependent contribution.

Busfield et al. (2002) adopted the theory of Lake and Lindley and proposed an experimental approach to evaluate both contributions for a Styrene Butadiene Rubber. The total crack growth rate per cycle is taken as the sum of two contributions: a time dependent and a cyclic contribution. They calculated the time dependent contribution from the relationship between static crack growth behaviour and the constant applied tearing energy (see Figure 2.28).

$$\left(\frac{\mathrm{d}c}{\mathrm{d}N}\right)_{\mathrm{total}} = \left(\frac{\mathrm{d}c}{\mathrm{d}N}\right)_{\mathrm{time}} + \left(\frac{\mathrm{d}c}{\mathrm{d}N}\right)_{\mathrm{cycle}} \tag{2-76}$$

Busfield et al. (2002) found out similar results as Lake and Lindley (1964b). The time dependent contribution dominates the behaviour at low frequencies whereas the behaviour is mainly due to the additional cyclic contribution at higher frequencies. They also pointed out an effect of the maximum tearing energy. The behaviour is entirely time dependent at high tearing energies but the cyclic contribution must be considered at lower T. They explained this cyclic contribution by a strain crystallisation type phenomenon of the butadiene component occurring at the crack tip that would not have time to occur at greater tearing energies.

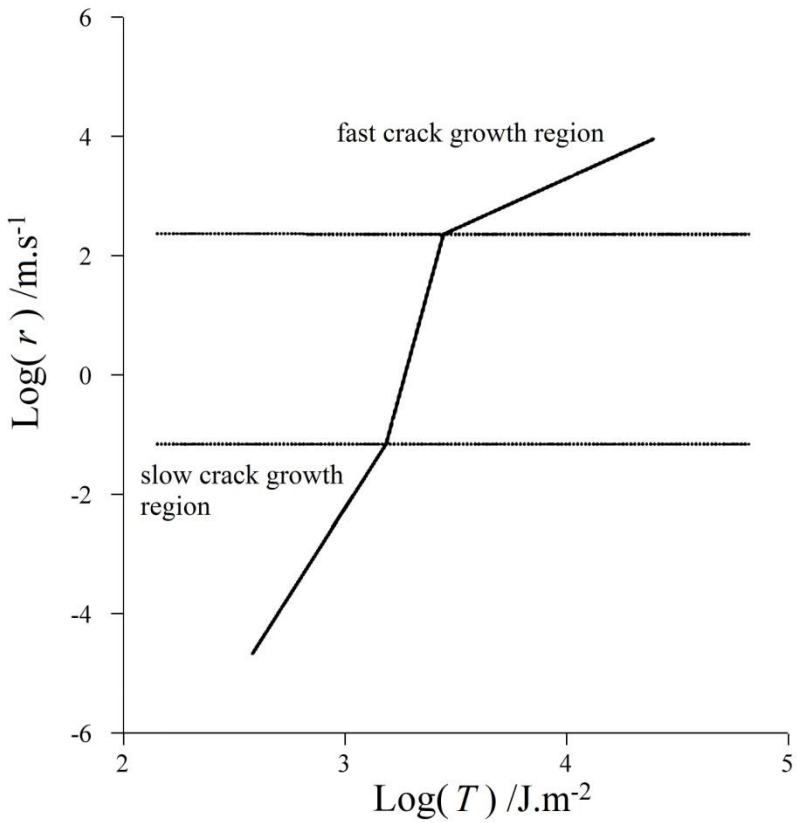

Figure 2-28. The steady crack growth rate can be fitted with a powerlaw relationship with respect to T in both slow and fast region. Taken from Busfield et al. (2002)

Effect of temperature

The effect of temperature on crack growth is higher for non strain crystallising rubbers. For SBR, fatigue life decreases by four orders of magnitude as the temperature increases from 0°C to 100°C (Lake and Lindley (1964b)) while the fatigue life of natural rubber only drops by a factor of 4 as can be seen on Figure 2-29. As for the monotonic tearing, the fatigue behaviour is mainly affected by the energy dissipation in the highly strain region around the crack tip (Lake (1972)). For non strain crystallising materials, the dissipation results from the mechanical hysteresis of the rubber and hence the internal viscosity of the elastomer which is reduced as the temperature moves away from T_g and therefore by an increase in the temperature. Conversely for a strain crystallising elastomer, hysteresis is primarily due to strain induced crystallisation. This process is only slightly affected by a change in temperature according to Gent (1978) so that the fatigue behaviour remains similar as the temperature increases as can be seen in Figure 2-30.

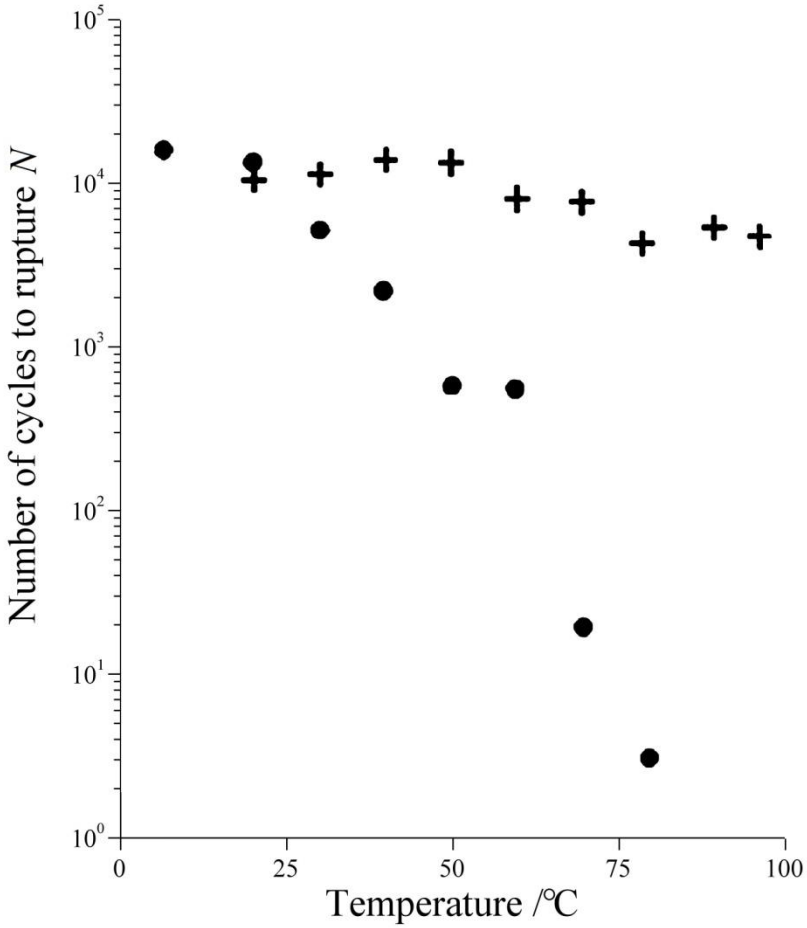

Figure 2-29. Effect of temperature on the fatigue life of (•) an unfilled SBR and (+) an unfilled NR. Adapted from Lake and Lindley (1964b).

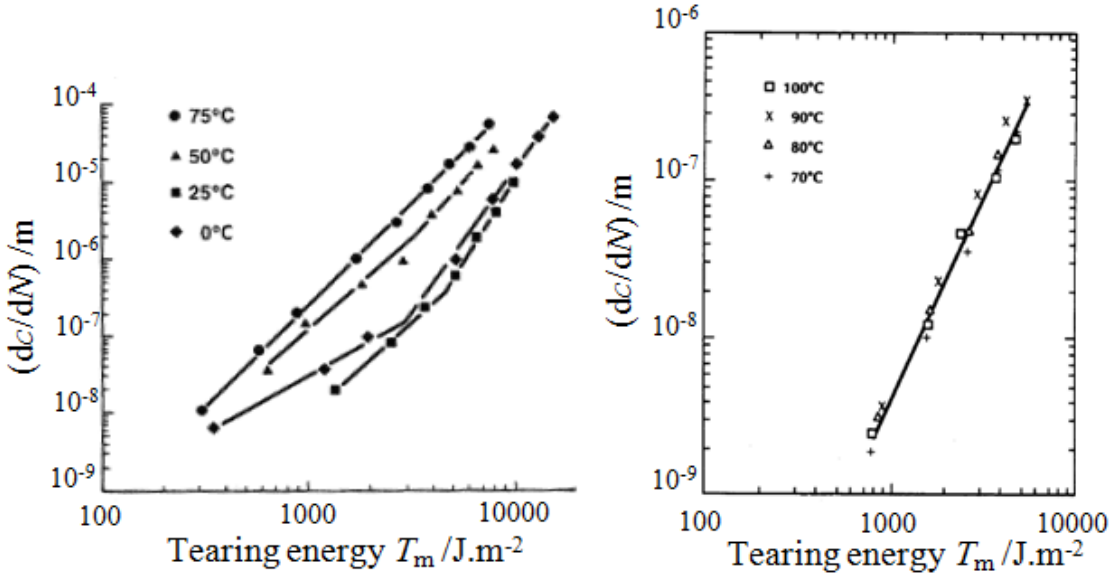

Figure 2-30. Effect of temperature on the fatigue behaviour of (a) CIIR (Young (1986)) and (b) NR (Young (1994)).

Effect of the mechanical load history

The effect of non zero minimum loading on fatigue crack growth was discussed by Lindley (1973) on natural rubber vulcanisates. He introduced a variable *R* equal to the ratio of the minimum to the maximum tearing energy achieved during one cycle (equation 2-77) and studied its influence on the crack growth behaviour.

$$R = \frac{T_{\min}}{T_{\mathrm{m}}} \tag{2-77}$$

The results are shown in Figure 2-31 and reveal a significant drop in the crack growth rate even with very small *R* ratios. An *R* ratio as little as 0.06 can lead to a decrease of two orders of magnitude in the crack growth rate compared with the *R*=0 case (Legorju-Jago and Bathias (2002)). This drop was attributed to strain crystallisation taking place at the crack tip as the strain increases and to the melting of the crystal upon relaxing. If fully relaxing conditions are achieved further crack growth can occur upon reloading whereas crystals are still present if the *R* ratio is sufficiently high. An empirical relationship to account for the effect of the *R* ratio on fatigue behaviour has been proposed by Mars and Fatemi (2003) based on the observation than the fatigue behaviour for different *R* ratios tends towards the same value at high tearing energy.

The loading sequence has also been studied by Sun et al. (2000). They submitted filled elastomer samples to both increasing and decreasing maximum stress values and concluded that increasing load had a deleterious effect on the crack growth compared with decreasing the load. This has been related to cyclic stress softening.

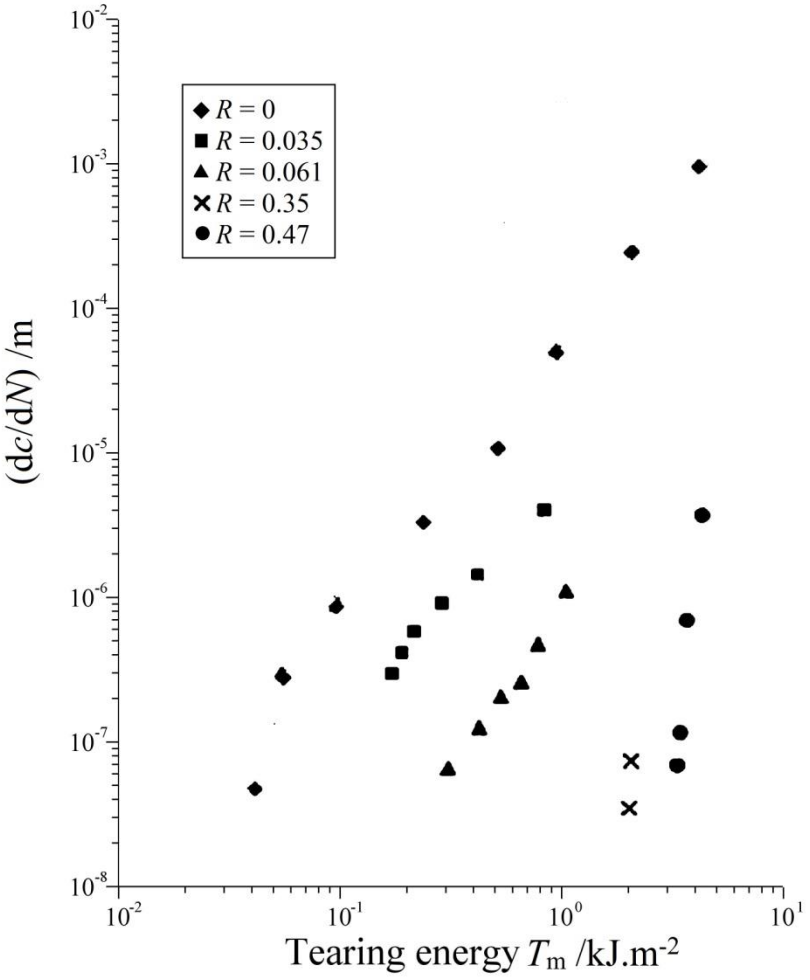

Figure 2-31. Influence of R-ratio on the fatigue behaviour of unfilled NR. Taken from Lindley (1973)

2-3-7. Roughness measurements on fractured surfaces

The surfaces resulting from fracture of rubbers present different roughness depending on the tearing energy and the crack growth rate (see Section 2-2-2). The establishment of a relationship between the resulting crack surface morphology and tearing parameters or conditions can therefore potentially bring more information on the fracture process. Moreover, analysis of fracture surface could also indicate if reinforcing processes have occurred at the crack tip. Most studies of fracture surface have been qualitative because of the lack of intrinsic parameters able to describe the roughness and the limitations of measuring techniques. Nevertheless, some attempts have been made to relate the fracture surface to the tearing behaviour both qualitatively and quantitively.

Pandey et al. (2003) used SEM to observe fracture surface of polychloroprene rubber filled with different fillers and correlated the measured increase in both tensile strength and tear resistance to the apparent change in fracture surface. The surface of the unfilled material presented smooth patterns with apparent tear paths whereas the crack surface of filled materials showed deep cracks and grooves they attributed to filler particles being pulled out. They also observed extensive tear branching and hindrance of smooth crack paths by filler particles.

Fukahori and Andrews (1978) evaluated the roughness of fracture surface obtained through steady state tearing using microscopic images by counting the number of steps crossing a line. To assess the roughness of the surface, they assumed that the broader the step lines are, the deeper the steps are. They observed that an increase in the tearing energy (corresponding to an increase in the tear rate) led to smoother crack surface. They attributed this change to a variation of the hysteretic losses at the crack tip. Higher hysteresis would cause higher stress decay as we move away from the crack tip and therefore only the flaws closest to the crack tip would be involved in crack propagation hence reducing the apparent roughness of the fracture surface. A similar approach was used by Gent and Pulford (1984). They measured the step spacing and found out they were larger in weaker materials. They also observed the height of the steps increased with the strength of the material. They attributed this increase in strength to a higher density of stress raisers and wider stress distribution at the crack tip that would allow more numerous second cracks to develop which creates higher roughness and strength. This is in contradiction with Fukahori and Andrews (1978) who proposed the larger the stress decay away from the crack tip the stronger the material. Clearly great care must be taken when analysing fracture surfaces and especially linking roughness profile to strength or crack growth rate. First, the crack growth rate measured is usually an average over a period of time and does not reflect the local fluctuations that may modify the surface pattern. Stick-slip behaviour for example presents two very different crack surfaces, one very rough over short distance for the stick period and one smoother over relatively long distance for the slip phase. Secondly, different phenomenon might be at the origin of the roughness profile and do not necessarily evolve in the same way with strength and crack growth rate. Crack tip reinforcement phenomena described earlier in this chapter are clearly related to the surface patterns of fracture surface and there is a general agreement that rough profile originates in the intersection of secondary cracks.

However, the influence of materials parameter and the mechanisms governing these phenomena are still unclear. The lack of universal roughness parameter is another problem when analysing fracture surface as it makes the comparison of different surfaces complicated. Kim and Jeong (2005) pointed out the scale of the roughness measurement should be taken into account when examining the relationship with toughness. They observed that for cyclic loading, the roughness at small scale increases with strength but that at large scale the roughness decreases with fatigue resistance meaning that in the cases they examined, the tougher materials presented large amounts of small peaks whereas weaker materials exhibited spaced high peaks with smooth surface in-between them. Despite all these difficulties, analysis of fracture surface can lead to information on the toughness and crack growth rate and their relationship to reinforcing mechanisms.

2-4. **Polymer interactions at an interface**

2-4-1. Formation of an interface

Miscibility of polymers

The miscibility of polymer mixture can be evaluated through the free energy of mixing ΔF_{mix} given by equation (2-78).

$$\Delta F_{mix} = \Delta U_{mix} - \theta \Delta S_{mix} \tag{2-78}$$

Essentially, ΔU_{mix} is a measure of the energy change associated with intermolecular interaction and is independent of the molecular weight (Ansarifar et al. (1993)) while ΔS_{mix} is associated with the change in molecular arrangements and is inversely proportional to the degree of polymerisation of the polymers (Jones and Richards (1999)). Due to long chain molecules, the entropy of mixing is likely to be small compared with the energy that becomes the main parameter when determining the miscibility of polymers. For non polar polymers, the internal energy of mixing is related to the solubility of the materials into each other or more fundamentally to their interactions at a molecular scale and has to be very small for miscibility to be possible which is rarely the case (Ansarifar et al. (1993)**)**. The interaction between the molecules can be summarised in the Flory-Huggins interaction parameter χ_{FH}. χ_{FH} is the energy change related to the swapping of a segment of each molecule into an environment of the other molecule. If χ_{FH} is positive then the interaction between the molecules is

unfavourable resulting in an increase of energy. Conversely, if χ_{FH} is negative the interaction is energetically favourable.

Molecular dynamics

Diffusion of polymers chains can be regarded as the motion of one molecule into an environment of similar or different polymers chains. The first case is called self-diffusion and the coefficient of diffusion D_s can be seen as the motion of the centre of mass of the molecule over a long period of time compared to any relaxation time of the molecule (Kausch and Tirrell (1989)).

$$D_s = \lim_{t\to\infty} \frac{<(r_{CM}(t+t_0) - r_{CM}(t_0))^2>}{6t} \tag{2-79}$$

It is possible to define a similar quantity for a segment of a long chain molecule. This quantity would give the self-diffusion at long time scales and account for the internal modes of motion the molecule is subjected to over shorter time periods. For mutual diffusion coefficient where molecules moves into a environment of a different nature, it is generally difficult to define the coefficient of diffusion D_M in terms of the motion of a single molecule and therefore the coefficient of diffusion is often defined by Fick's law.

$$-J_i = D_M \nabla[x_i] \tag{2-80}$$

Where J_i is the flux of species i and $[x_i]$ is its concentration. The environment of the diffusing species has a major influence on the coefficient through both frictional and thermodynamics effects that can lead to considerable changes in the magnitude of D_M. Additional interactions with the environment can also lead to significant changes in the coefficient of diffusion.

Polymer chains dynamics are significantly influenced by their configuration and connectivity. In bulk, the configuration of a chain can be represented by the random walk model. For a random walk model, the end to end distance which is representative of the configuration is given by equation (2-5).

The dynamics of a random chain have been modelled by Prince E. Rouse (1953) in order to model viscoelastic behaviour. He modelled the polymer chain as a series of beads connected to each other by springs. The interaction of the medium with the chain is represented by a friction coefficient ζ_f for the motion of the beads. Solving the set of

equations of the motions of the bead for a coupled oscillator gives a linear response of the motion of the centre of mass versus time. The coefficient of diffusion is thus given as

$$D_{Rouse} = \frac{\mathbf{k}\theta}{n_l \zeta_f} \tag{2-81}$$

Where **k** is Boltzmann's constant, θ is the absolute temperature and n_l is the number of segments in the polymer chain. In this model, the diffusion is related to the number of segments constitutive of the polymer chain that feel the same frictional interaction with other segments. The coefficient is inversely proportional to the number of segments or more generally to the molecular weight. This model gives representative results for relatively short chains but above a certain threshold the coefficient of diffusion becomes more dependent on the molecular weight. When the length of the macromolecules gets higher, they start to feel other interactions from other polymers chains that result in chain entanglements. Doi and Edwards (1978a), (1978b) and (1978c) were the first to argue these entanglements constrain the path of the molecule to a tube. Inside the tube the dynamics are similar to a Rouse model but confinement to the tube changes the motion of the whole chain and thus the coefficient of diffusion. (De Gennes (1971)) proposed a theory to account for the surrounding constraints called reptation. The chain would move by curvilinear motion along its tube and avoid lateral motion and crossing of the obstacles made by other chains. The diffusion coefficient D_{rep} is calculated from the time τ_{rep} the chain needs to escape its tube.

$$D_{rep} = \frac{{r_c}^2}{\tau_{rep}} \tag{2-82}$$

$$\tau_{rep} = \frac{1}{2}\frac{{L_m}^2}{D_{Rouse}} \tag{2-83}$$

where L_m is the contour length of the molecule. The coefficient of diffusion becomes inversely proportional to the square of the molecular weight because of the entanglements. For sufficiently long polymer chains, good agreement has been found between the diffusion coefficient and the molecular weight. This models leads to a series of regimes for the motion of chain. At very short times, the chain does not feel the constraint of the tube and moves as in free space proportionally to $t^{1/2}$. At longer times,

the chain begins to react to the environment of chains and the motion is constrained to a tube. As the tube is also submitted to a random path, the motion of the centre of mass is proportional to $t^{1/4}$. A third regime appears when the dynamics of the chain inside the tube are no longer significant and only the confinement of the chain to a path is significant. In this regime the motion is proportional to $t^{1/2}$ again. The fourth regime is observed when all monomers move with the centre of mass and the motion is proportional to t.

Those four regimes have been observed by (Karim et al. (1990)) and can be seen on Figure 2-32 even though the time exponents are not found in this work due to thermodynamic interactions that are still not fully understood.

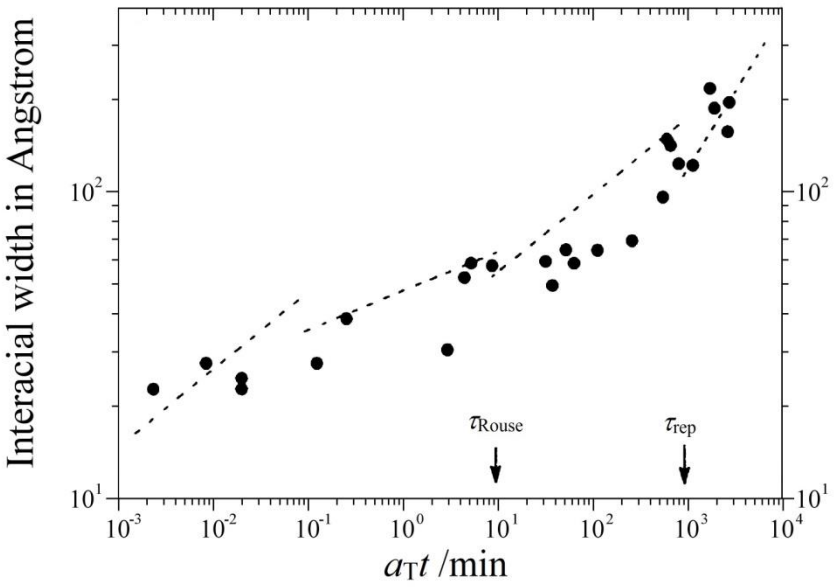

Figure 2-32. Four regimes of interfacial broadening. Taken from Karim et al. (1990).

2-4-2. Strength of interface

At an interface between rubbery materials, stress can be transferred across the interface by chemical bonds (crosslinks for example), physical bonds or entanglements. If the stress transferred is high enough, reinforcing process dissipating energy can yield significant increase in the strength of the interface. Generally, if these processes are activated by the bonding between the two layers, the energy involved to create the new surface can be orders of magnitude greater than the work of adhesion.

Two elastomers will interdiffuse until the strength of the interface reaches the bulk properties of one of the materials. Molecules near the interface do not necessarily have

to totally interpenetrate in the material in the vicinity of the interface to develop the full strength of the interface. Portions of the chain may be sufficient provided that they are able to resist mechanical separation (Kausch and Tirrell (1989)). Several studies have tried to relate the depth of interdiffusion to the strength of the resulting interface (Gent and Kim (1990), Hamed (1981), Schach et al. (2007)). They measured the energy necessary to separate the materials at very low rates and high temperatures to minimise the viscous energy dissipation. Even though the values of energy are still higher than what we could expect from strictly thermodynamic work of adhesion, they all showed that the strength of the interface greatly increases with the depth of interpenetration as can be seen on Figure 2-33. It has been shown a penetration depth of just a few entanglements was enough to fully recover the bulk properties.

The kinetics of the development of the interfacial strength has also been investigated in terms of time for similar materials at the interface. Schach and Creton (2008) showed that the time to recover the strength of the material scaled with the reptation relaxation time (the time for a molecule to completely leave its original tube). This effect can be seen on Figure 2-34. Schach and Creton examined interface between Styrene Butadiene Rubber of different molecular weights and observed a plateau was reached after contact times of the same order of magnitude as the relaxation time. It can also be seen on this figure that the time necessary for the chain to reptate is greater for higher molecular weight in accordance with the theory.

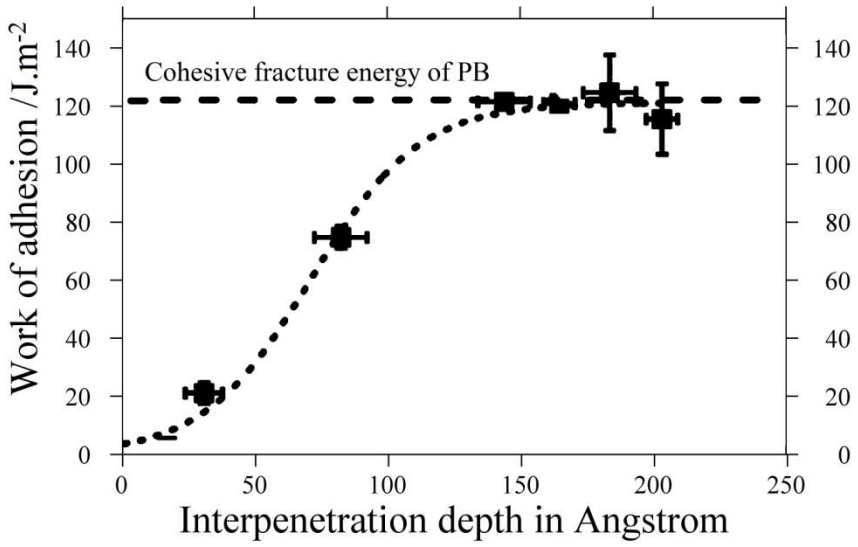

Figure 2-33. Strength of the interface interpenetration depth for polybutadiene bonded with different elastomers. Taken from Schach et al. (2007).

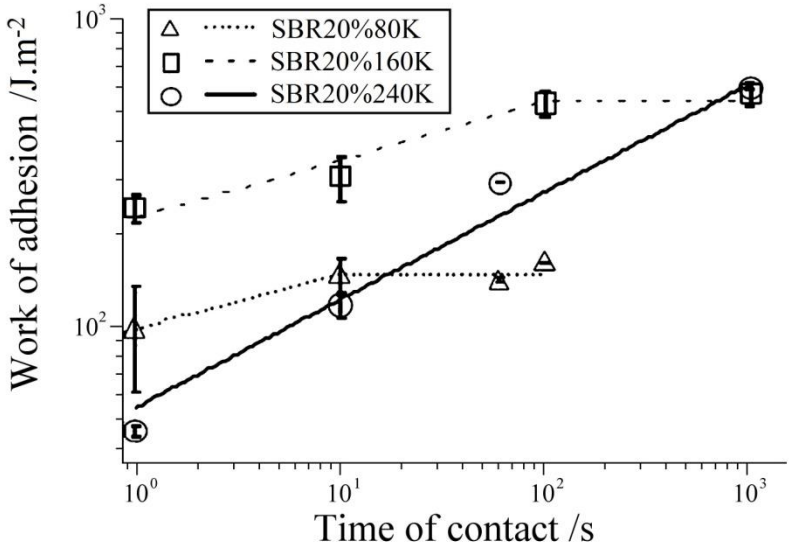

Figure 2-34. Strength of interface of SBR versus contact time for three molecular weights (80, 160 and 240kg.mol^{-1}). Reptation times are respectively 13, 140 and 1140 seconds. Adapted from Schach and Creton (2008).

2-5. **Fracture mechanics in FEA**

Since its initial development, Finite Element Analysis has increasingly been used in industry and progressively replaced prototyping in the development phase of products and components. It has been accepted widely as a tool to provide numerical solution for problems which are difficult or intractable to solve using classical analytical method. Over the last three decades, the solution methods and the options available in FEA software package have become numerous and complex and the mathematics behind the solution process is increasingly buried in the code. To be an effective user of FEA, it is preferable to understand the basis of the method and the calculations involved in the solving of an analysis in order to be able to interrogate the results of the modelling. The wide array of possibilities given by most FEA software package is above the scope of this thesis and only a basic introduction to FEA modelling will be given in this chapter with a particular attention to fracture in rubbery components and the modelling of tyres. Many books provide a full discussion of FEA with regards to the mathematical aspect Brenner and Scott (2008)), the different types of analysis (Fenner (1975), Quek and Liu (2003)) and the formulation of an analysis (Narasaiha (2009)).

2-5-1. Introduction on FEA

Basic concept

Finite Element Analysis is a numerical method seeking an approximate solution to the distribution of field variables such as displacement or temperature in a component. This is done by dividing the geometry under consideration into multiple elements each of a simple geometry. A continuous function of the unknown field variable is assumed for each element. Shape functions are defined in a local coordinate system to relate the unknown field variable value at any point of the element to the values at points connecting the elements, the nodes. For stress analysis, the preferred field variable is the displacement and therefore, only displacement based relationships will be considered in the rest of this thesis. The profile of the displacement in an element is therefore completely assumed by the form of the shape functions. Known physical laws are then applied to those elements. To derive the equations for the finite elements, the general system of partial differential equations with boundary conditions governing the deformation of the component has to be restated in an integral formulation. This is made using a mathematical tool such as the principle of virtual work or variational principles

such as the minimum potential energy theorem. The solution of the problem is therefore not exact but an approximation to the best solution. The system of equation is then expressed for one element by replacing the displacement in the integral formulation by the shape functions expression of the displacement. The FEA equations are basically a combination of the expression of the general system of equation at equilibrium and the assumed expression of the displacement with respect to the displacement of the nodes.

Once the equations for each element have been derived, they are combined together to obtain the system of equations for the whole structure by expressing them into a common coordinate system. They are rearranged into a matrix form where the unknown variables are the nodal displacements. For a static deformation where the inertial forces are not taken into account, this expression takes the form described in equation (2-84).

$$[K]\{U\} = \{F\} \tag{2-84}$$

[*K*] being the stiffness matrix for the entire model which includes the material constitutive equation. {*U*} is the vector of the unknown nodal displacements that has to be obtained for a certain vector {*F*} which represents the forces applied at the nodes of all the elements. The constraints on the displacement imposed by the boundary conditions are included in the {*U*}. Equation (2-84) could be considered analogous to the equation of a spring under deformation by a given force. The same approach is used to obtain the displacement in FEA. The stiffness matrix is inverted and the equation is solved for {*U*}. The stress and strain distribution and more generally any physical value related the displacement can be calculated from the solution of the displacement vector.

Inverting the stiffness matrix is the time consuming part of the FEA and requires most of the computation time. The stiffness matrix is a square matrix whose size increases rapidly with the complexity of the problem. The number of degrees of freedom, the shape of the elements or the number of nodes used to define an element (which relates to the function assumed for the displacement inside an element) are among the parameters defining the size of the stiffness matrix. Techniques to optimise the calculation time have been developed, such as wavefront minimisation techniques, so that solving of the equations requires fewer calculations. They are usually related to the way the problem is defined and are implemented directly in the FEA software pre-processor. Nonetheless, simulation of real components can be extremely demanding in computation resources to reliably simulate real components such as tyres. The analysis

procedure should therefore take advantage of any feature related to the loading and the geometry of the component that can potentially simplify the problem and reduce the number of unknown variables in the stiffness matrix.

Analysis steps

The numerical simulations conducted in this thesis were all implemented in the software Abaqus 6.12 supplied by Dassault Systemes. The development of a FEA model usually requires 5 steps described by Busfield (2000). In some steps, different possibilities are available to model the problem amongst which the FEA user should chose carefully to obtain realistic formulation of the problem, accuracy of the solution and efficiency of the calculations.

Determination of the most suitable model to describe the component:

Examination of the geometry and of the loading conditions applied to the component might lead to simplification in the formulation of the model. Combination of appropriate dimensions and loading can lead to the modelling of a 3D structure by a 2D model. In the case of a component where one dimension is much larger than the others with a uniform and constant loading along this direction, it can be considered the strain field remains constant along this direction. Therefore, only one plane perpendicular to the direction has to be modelled assuming plane strain conditions. Similarly, when a specimen presents one dimension small compared to the others, plane stress conditions can be applied to a 2D model. The pure shear tearing specimen shown in Figure 2-12 (c) can for example be modelled using this assumption. Another simplification and reduction of the number of degrees of freedom can arise from symmetries in the model. Types of symmetries are summarised in Figure 2-35. Axial symmetry occurs when the distribution of variables remains unchanged with a rotation around an axis. Only the radial and axial directions must be considered with this type of symmetry. An inflated tyre is an example where axisymmetry is found. When geometry and boundary conditions are symmetric with regards to a plane, symmetric boundary conditions can be applied to simplify the model. Additional boundary conditions are applied to nodes belonging to the plane of symmetry reflecting the restriction of their motion to a displacement in the plane of symmetry. When geometry and boundary conditions vary cyclically around an axis such as in Figure 2-35 (c), cyclic symmetry conditions can be applied. This type of symmetry is similar to planar symmetry but in a cylindrical rather

than a Cartesian coordinate system. The displacements of the nodes in the circumferential direction are constrained to account for this symmetry. Repetitive symmetry is present when a region of a structure is linearly repeated along an axis. Only one segment need to be modelled to model the whole structure. The boundary conditions resulting from the types of symmetries described above are implemented directly into Abaqus as long as the plane of symmetries can be identified in the general Cartesian coordinate system of the model. Dimension dependent output variables are scaled according to symmetries. Therefore, a scaling factor has to be applied to obtain the values of the variables for the whole structure.

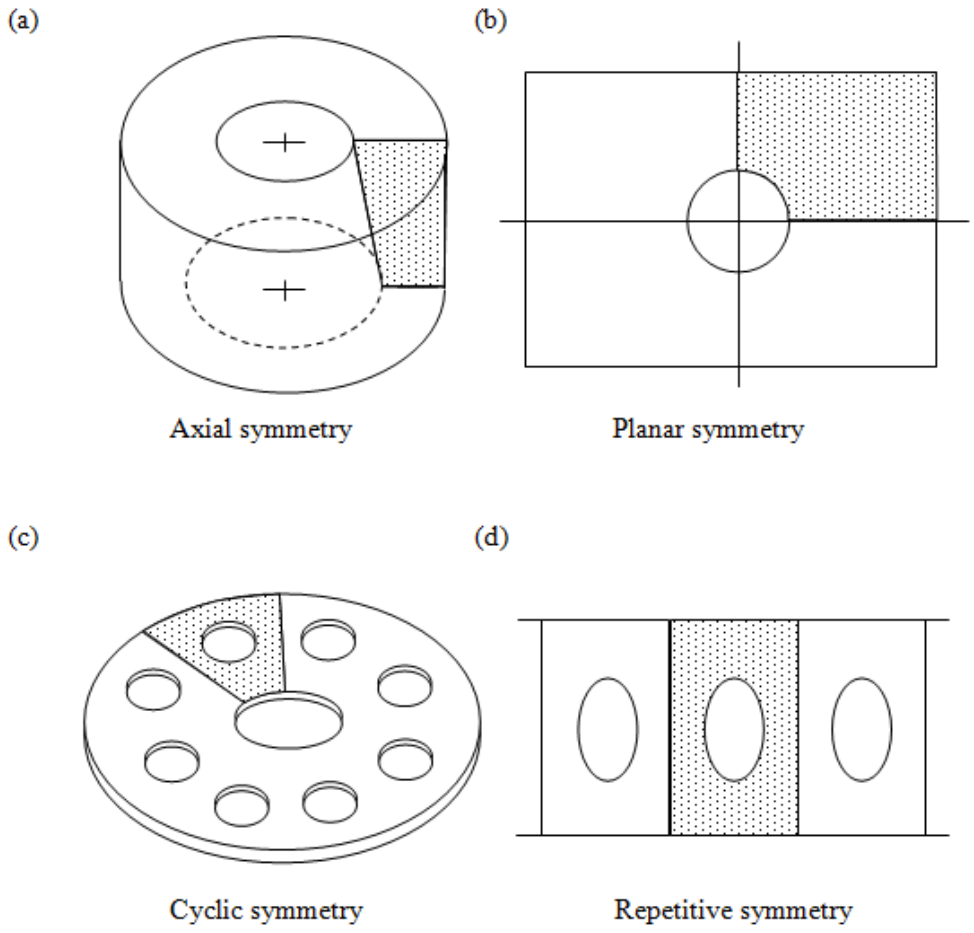

Figure 2-35. Symmetries commonly adopted to simplify the model in FEA. The dotted regions suffice to model the entire geometry. Taken from Busfield (2000).

The expected structural behaviour, typical loads and materials properties are other attributes that have to be considered. The main concern is whether dynamic non linear effects are significant in the behaviour of the structure. Static and quasi-static problems

where dynamic effects can be neglected are solved by only considering nodal forces applied by the external forces and therefore the formulation of the stiffness matrix is sufficient to solve the problem. For dynamic problems, an additional mass matrix must be defined and the system of equations modified to take the inertial effects into account.

Mesh generation:

The analysis of large components using FEA relies on the division of the structure into a finite number of entities to form a mesh of elements and nodes. The generation of this mesh plays an important role in both the accuracy and the efficiency of the simulation. Some of the attributes of the elements are a direct consequence of the type of simulation, the choices made in the determination of the model, the material behaviour and the expected behaviour of the component. The type of elements is directly dictated by the field variable of interest. Thermal, stress or fluid dynamics analyses therefore require different element formulation. The shape of the elements depends on the dimensionality of the model (truss for 1D, membrane or shell for 2D or 3D solids) and as well as the materials properties. The number of nodes per element is given by the shape functions chosen to intercept the field variable in an element with the values at the nodes. In Abaqus, two types of elements are available reflecting a linear and a quadratic form of the shape functions. Additional features of the elements can be related to the solution method and additional properties of the material such as incompressibility.

Boundary conditions and materials properties:

Boundary conditions have to be defined to reflect working conditions of the structure. Abaqus proposes various formulations of materials properties ranging from linear elastic behaviour to user defined properties. A suitable form has to be selected to account for the variation of the material behaviour over the range of strain and stress expected to be encountered in the simulation. Elastomers typically exhibit large strains and are modelled with SEF such as those described in Section 2-1. The SEF can be defined directly through an input of experimental data collected in typical modes of deformation or by the input of coefficients directly as explained in Chapter 3.

The geometry, the mesh, the boundary conditions and the materials properties are then assembled into a file that can be submitted to a solver.

Solving of the equation:

Abaqus offers different algorithms with different computational cost to solve non linear problems. A full Newton iterative method is used to solve static and long time dynamic problems. The variation of the boundary conditions or loading is divided into several time increments and approximate equilibrium conditions are found at the end of each. In an implicit method, the variation of the unknown variables for an increment is calculated by solving equations relating to the new state of the variables. The method is said to be unconditionally stable which means there is theoretically no limit to the size of the increment. However the accuracy of the method greatly depends on the time increment. Control parameters for the numerical solution have to be defined so that the solution obtained reflects the real behaviour of the component. It is usually done by checking the force equilibrium between the internal structural forces and the externally applied loads. By default, the software evaluates different parameters related to the field variables calculated such as residuals or corrections made by the method and accepts the solution if they sit in a predefined range. The model is said to converge towards a solution. If the solution is not acceptable with regards to these parameters, the stiffness and mass matrices are modified and a new iteration is carried out or the time increment is reduced to decrease the approximation. This method can fail to predict the behaviour in the sense that the approximate force equilibrium can sometimes not be obtained within predefined tolerance range. The calculations cannot reach an acceptable approximation of the field variables and is said to diverge. Severe discontinuities in the stiffness of the structure between two increments are an example of common source of divergence.

The explicit techniques are introduced to overcome the disadvantages of the implicit method. An explicit integration rule is implemented along with the use of diagonal element mass matrices (Dssimulia (2012)). The system of equations for the structure is integrated using an explicit central difference integration rule. The variations of the variables in the new state are calculated based on the solutions for the previous increments. Conversely to the implicit method, the maximum time increment is limited to the smallest transition time for a dilatational wave to cross an element in the mesh. Therefore the explicit method is conditionally stable. Because of this limit, the increment time is usually very small and a large number of increments are necessary for a simulation. Even though attempts have been made to increase the maximum time

increment, explicit methods are still limited to relatively short dynamic simulations. The computation time for each increment is significantly shorter than in the implicit method because the integration rule does not require the matrices to be reconstructed. Moreover, the force equilibrium in an explicit method does not have to be enforced. Therefore considerable computation time is saved and discontinuities such as buckling instabilities are handled more easily. The drawback is that the solution does not necessarily accurately reflect reality. When possible, the results obtained from explicit method should therefore be compared with the result from implicit method until the point the implicit method fails to converge.

Analysis of the results:

The solution of the equations introduces approximation of the field variables. Post-processing and analysis of field variables and quantities such as displacements, stress contours, contact forces should be done carefully to assess the quality of the numerical solution. Mesh convergence should be checked and the efficiency of the model questioned.

2-5-2. Modelling of tyres

Tyres are essential components regarding safety, handling and efficiency of a vehicle. They must as such fulfil fundamental functions:

- Road to vehicle interface
- Provide load-carrying capacity
- Ensure adequate friction to move the vehicle in any situation (cornering, wet and dry conditions)
- Absorb road irregularities
- Resist abrasion
- Durability
- Noise

Moreover, with the recent higher environmental demands, these requirements have to be optimised for best fuel efficiency without decreasing performance of the tyre itself. These basics requirements are achieved by engineering the right design for each application (car, truck or aircraft) and by suitable materials selection. A typical design of a radial tyre is given in Figure 2-36. The different parts of the tyre are designed to

fulfill specific functions related to their location and the loading conditions they are subjected to in service. Materials are selected to optimise performance of the different regions. The tread compound is, for example, chosen to optimise traction, rolling resistance and wear. The abrasion gum strip is highly resistant to abrasion as it is the part in contact with the rim. The innerliner is a compound with very low gas permeation to help retain the inflation pressure over time.

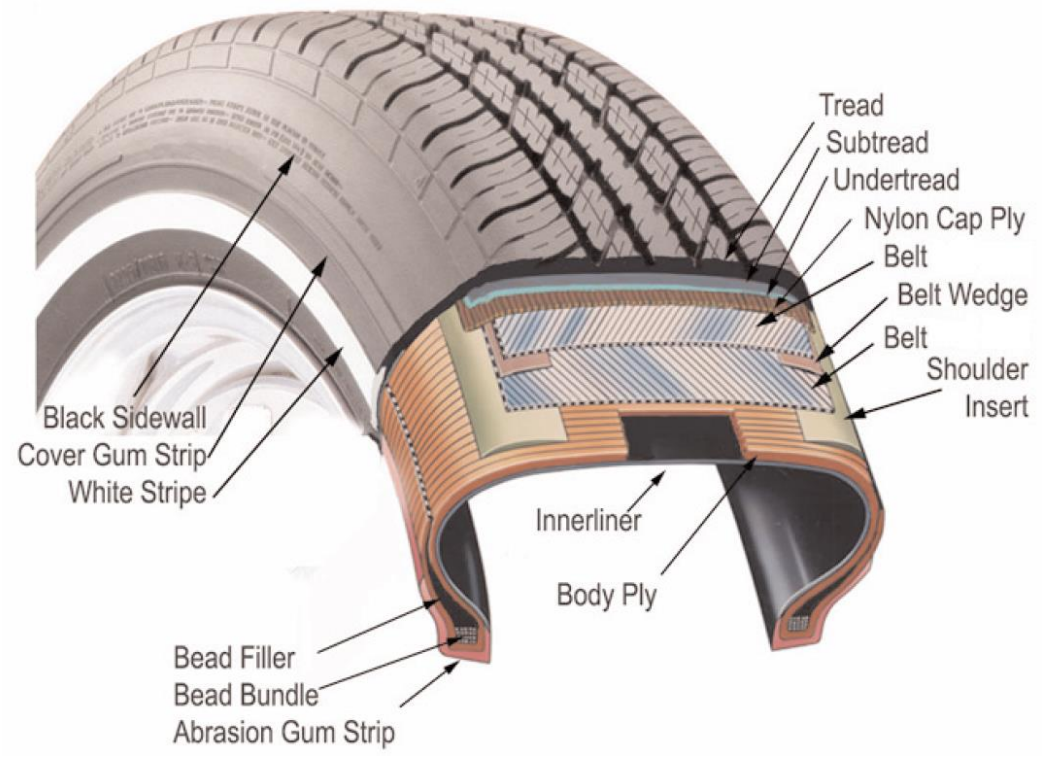

Figure 2-36. Components of a tyre. From Gent and Walker (2005).

Knowledge of how the tyre operates can give insight into design considerations. Therefore many investigators tried to develop mathematical or simulation schemes to model the kinematic and dynamic behaviour of a rolling tyre on a surface. The use of Finite Element technique has been widely accepted as a solution. The complexity of the problem prevents investigators to use a unique and standard approach for all the problems encountered and hence different models are developed depending on the main focus of the analysis. A model investigating rolling resistance will consider different attributes than a simulation investigating friction or failure. This section aims to introduce the general approach adopted to model a tyre. Approaches used to evaluate fracture properties are then also described later in this section.

Despite the apparent symmetries of a tyre that may permit the use of 2D models, 3D simulations are generally required to achieve accurate and complete results. 2D models are however useful to solve problems where the loads do not vary circumferentially such as the shrinkage upon moulding or the application of the inflating pressure. Assessing the effect of the loading and the rolling requires more advanced techniques. Generally, for stress analysis, a Lagrangian description of the problem is adopted. The material particles are followed when they move through space and time. Therefore the mesh moves with the material through rigid motion and deformation. The main benefits of this approach are easy tracking of surface and interface between materials and possibility to treat history dependent material behaviour. A rolling tyre is difficult to model using a Lagrangian description as it would require, because of the rotation, relatively fine mesh over the entire structure or systematic remeshing techniques that are highly costly in terms of computation. Conversely, an Eulerian approach where the nodes are fixed and the continuum moves with respect to the mesh gives poor interface definition and precision in the resolution of the flow details (Donea et al. (2004)). Because of these shortcomings, an alternative approach is used. The rolling tyre simulation is treated with a mixed Lagrangian/Eulerian approach. The rigid body rotation is described in an Eulerian manner and the deformation measured relative to the rotating rigid body in a Lagrangian manner. This is made possible by the creation of a reference frame linked to the axle of the wheel. In this frame, the tyre is seen as points that are not moving although the material is moving through those points. Therefore the finite element mesh does not undergo the large spinning motion of the tyre but deforms under load. The motion of a material particle is decomposed into a rigid rotation and the displacement resulting from the external loads (see Figure 2-37). The time dependence is removed and the problem is treated as purely spatially dependent which is convenient as it requires less computational resources and therefore less time for an analysis.

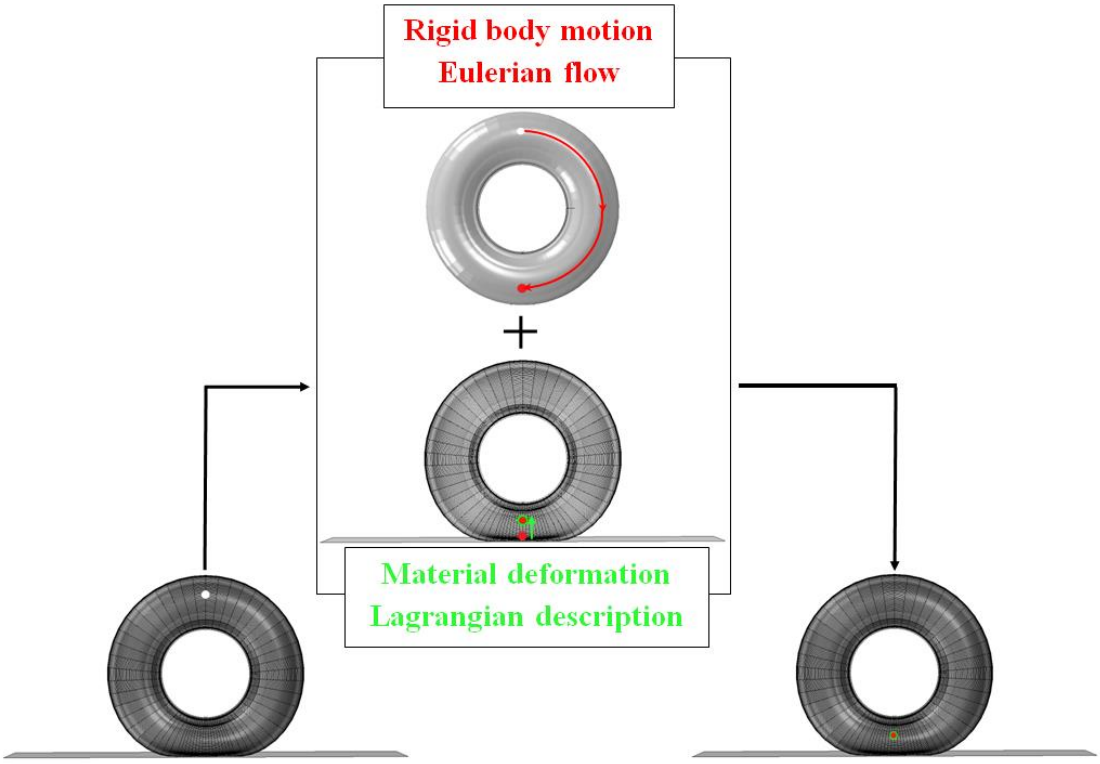

Figure 2-37. Mixed Lagrangian/Eulerian method.

This approach has been used by many researchers to investigate different characteristic of tyres such as cornering forces and moments (Kabe and Koishi (2000), Darnell et al. (2002)), temperature rise or rolling resistance. The mixed Lagrangian/Eulerian technique is limited to steady state rolling analysis. Therefore it is often used as a first step towards further analysis to simulate transient phenomena due to acceleration or braking phase of a tyre (Kabe and Koishi (2000)).

2-5-3. Evaluation of T using Finite element techniques

Rubber components subjected to deformations fail due to the initiation and propagation of initial flaws present in the material. Two main approaches have been adopted for theoretical investigations of fracture of rubber components, either based on the crack nucleation or crack growth phenomena. The crack nucleation approach follows the idea of Wohler curves to estimate the fatigue life. A continuum mechanics parameter is chosen or defined to relate the load to the number of cycles a component can sustain before crack initiation and eventually before failing. Those parameters have been compared and reviewed in a study by Previati and Kaliske (2012). An alternative way of predicting the fatigue life is based on the propagation of an initial crack adopting a

fracture mechanics approach such as the one adopted by Asare and Busfield (2011). In this approach the release of stored energy has to exceed a critical value for the crack to extend further into the material. Three main approaches have been derived to evaluate the tearing energy in a component using Finite Element Analysis (Busfield et al. (1999)). The Virtual Crack Extension (VCE) technique consists in evaluating the variation of the energy stored in the component dU between two models held at a fixed displacement as a crack surface is increased by a small amount dA_c. The tearing energy is calculated by the ratio of the two values. For relatively small crack growth, the energy change might be low. It is in this case essential to ensure the models are similar remote from the crack as the errors inherent to the Finite Element calculations might be significant in the calculation of the variation of the stored energy. This approach was used successfully by Busfield et al. (2005) to predict the lifetime of rubbery components. A finite element formulation of the *J*-Integral described in equation (2-48) has been developed. The contour is taken along the edges of successive element. The calculation of the *J*-integral value is readily available in Abaqus and can be done over different contours. The advantage of the technique is that it requires only a single analysis to derive the tearing energy. The last method that has been used in the past to obtain the tearing energy is the Virtual Crack Closure Technique (VCCT). The force required to close an element at the tip of the crack is integrated over the displacement applied to the nodes that have to be brought together to close the crack. The tearing energy is determined by dividing the resulting work by the area of the element (see equation 2-85).

$$T = \frac{1}{A_c}\int F_n \mathrm{d}u_n \tag{2-85}$$

The techniques described in the previous paragraph have been used to derive the tearing energy in tyres and require the crack to be geometrically present in the mesh representing the structure. Han et al. (2004) evaluated the influence of different loading conditions (acceleration, braking or free rolling) using a virtual crack extension method. They also used the *J*-integral method to predict the direction of the crack growth, the higher value of tearing energy being the privileged direction. A similar technique was used by Ozupek and Becker (2005) to predict the delamination of the truck tyres belts. The location to introduce the crack was taken as the highest stress region from a stress analysis of the tyre. They investigated the influence of the crack geometry on the

resulting tearing energy using rectangular crack of different width and length. They used the method described in Section 2-3-3 to derive the lifetime of the truck tyre and evaluated the influence of cornering conditions on the behaviour.

2-6. **Summary**

From the literature review presented in this chapter, it is clear that many effects can contribute to the fatigue failure of a tyre. The complex structure of the tyre and the variety of materials involved in its composition, although being necessary to achieve high performances, also introduce multiple interfaces and hence additional sources of failure. The harsh environmental conditions a tyre is subjected to may also contribute to the growth of a flaw inherent to the material and turn it into a crack leading to premature failure. The focus of this thesis is the investigation of potential sources of failure in a tyre. The effect of frequency on the fatigue behaviour of non-strain crystallising rubbers has been studied by many researchers previously. It is particularly interesting at the high loading frequencies that are reached in aircraft tyres during the takeoff and landing phases. The crack growth rate per cycle in fatigue appears to be the sum of two components, the first one being related to the length of time the rubber containing a crack is subjected to loading. The second additional contribution is thought to be related to the repeated cyclic loading. This cyclic contribution has been quantified for a range of rubbers under different loading conditions but its origin is still under debate. Additional tests are still required to help explain the underlying phenomena that generate this additional cyclic contribution.

A tyre is made of many different materials brought together in the unvulcanised state, stored and then vulcanized under pressure. Although thorough research has been conducted on the thermodynamics and the strength of adhesion of an interface between two unvulcanised elastomers, the resulting resistance to crack growth of the vulcanised structure as well as the influence of external variables has rarely been attempted. The main issue is the lack of a reliable method to test strong interfaces such as those encountered between two rubbers. In this thesis, a method is proposed to investigate the strength of interfaces between vulcanised materials and the influence of external parameters is discussed with an emphasis on the influence of compressive pressure during vulcanisation.

The complexity of the formulation of the compounds used in tyres often leads to difficulties when it comes to quantifying the effect of one particular parameter. The effect of additives and fillers also often hinders a detailed understanding of the basic mechanisms controlling the crack growth. Model materials have therefore mostly been used in this thesis to investigate the fundamental behaviour of rubbery materials subjected to cyclic loading. Both the model compounds and the industrial compounds used throughout this thesis are detailed and characterised in the next chapter.

CHAPTER 3 - MATERIALS AND EXPERIMENTAL TECHNIQUES

3-1. **Materials used in this study**

3-1-1. Polymer materials

Two different polymers were used in this study: Natural Rubber (NR) which is the common name for cis-1, 4-polyisoprene and Styrene Butadiene Rubber (SBR). The monomer unit of each of the material is given in Figure 3-1. SBR is a random copolymer of styrene and butadiene. Strain induced crystallisation is inhibited by the stearic hindrance of the phenyl unit on the backbone of the chain as the chains are stretched. SBR is therefore widely known as a non strain crystallising rubber although a small amount of crystallisation might take place at very large strain. The SBR used in this study consisted of a standard grade containing about 23% styrene with a balance of butadiene units.

Natural rubber is a product obtained from latex of the Hevea Brasiliensis tree. It consists of approximately 100% cis-1,4-polyisoprene which allows it to rapidly crystallise under strain resulting in high tear resistance and good fatigue properties. A standard Malaysian grade was used in this study (SMR CV60).

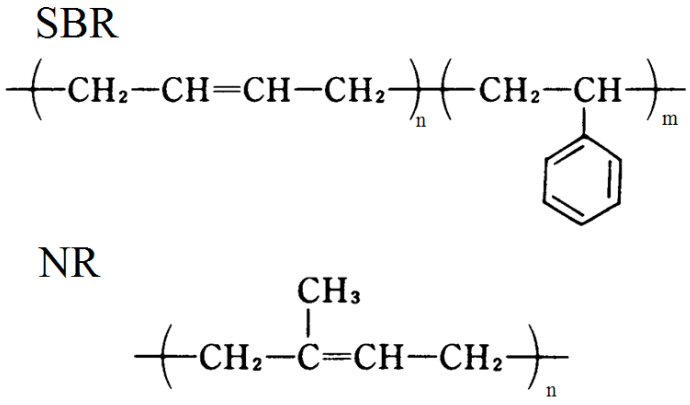

Figure 3-1. Chemical formula of the elastomers used in this study.

3-1-2. Vulcanisation

The raw forms of both polymers are poorly elastic and exhibit very low mechanical properties due to microscopic slippage of polymer chains over each other resulting in extensive flow. They behave like highly viscous liquids. To obtain typical features of rubbers such as large strain elasticity and high toughness, a 3D network has to be created to connect the long chains of the base polymer, transforming it into a viscoelastic solid. This process is known as vulcanisation and consists of forming mainly covalent bonds (crosslinks) between the chains. The most common vulcanising agent is sulphur that can form bridges between the long chain molecules only if they contain unsaturated double carbon-carbon bonds. Typically, various additives are mixed with the raw polymer to initiate and control the vulcanising reaction, modify the mechanical properties of the resulting rubber or to alter the processability of the material. These additives can be classified in five categories: curatives; activators; fillers and reinforcing agents; plasticisers and other additives. Curatives include vulcanising agent and accelerators which make the crosslinking reaction more efficient and faster. Different types of accelerators exist depending on the desired characteristics of the vulcanising reaction. They will have an influence on the nature and the density of the crosslinks and their choice determines the optimum curing time and temperature. Activators are also incorporated to initiate the sulphur vulcanisation and reduce vulcanisation time. Fillers are typically added to improve specific properties of the resulting rubber composite such as the modulus, the tensile strength and the fatigue properties. In this work, filled rubbers were obtained from masterbatches of premixed HAF carbon black N330 supplied by Tun Abdul Razak Research Centre. Formulations of the rubber used in this study are detailed in Tables 3-1 and 3-2. The amount of each component of the formulation is given per hundred rubber in mass units, the mass mixed with 100 mass units of base polymer. Additional rubber composites were supplied by Dunlop Aircraft Tyres. For confidentiality reasons, only the key ingredients of their commercial formulation are given.

Component / **Rubber**	**NR0**	**NR50**	**SBR0**	**SBR50**	**SBR70**
SMR CV60	100	100			
SBR 1500			100	100	100
Carbon black HAF N330	-	50	-	50	70
Stearic acid	2	2	2	2	2
Zinc oxide	5	5	5	5	5
6PPD	3	3	3	3	3
CBS	1.5	1.5	-	-	-
MBTS	-	-	1	1	1
DPG	-	-	1.3	1.3	1.3
Sulphur	1.5	1.5	1.5	1.5	1.5
Curing temperature /°C	150	150	140	140	140
Curing time /min	12.5	12	15	16	16

Table 3-1. Formulations of the rubbers compounded at QMUL given in parts per hundred rubber in mass.

	DC005	**DC005A**	**DC005B**	**DC005C**	**DC019**
SMR CV60	100	100	100	100	100
Carbon black HAF N330	40	40	40	50	37.5
Curatives and additives	Similar formulation for every material				
Sulphur			Higher than other industrial coumpounds		
Curing temperature /°C	150	150	150	150	150
Curing time /min	12	12	16	14	12

Table 3-2. Formulation of the compounds supplied by DATL.

In addition, two of the materials (DC018, DC029) were supplied for characterisation for Finite Element Modeling and interfacial fracture analysis; however their formulation was not released for publication in this thesis.

3-1-3. Sample preparation procedure

The composite materials were compounded using a two roll mill which consists of two rotating rolls separated by a narrow gap. As the rubber is carried through the gap it is submitted to high shear stresses that have the effect of mixing the different additives evenly through the raw material. The shear stresses are controlled by adjusting the gap width and the relative rotational speed of the rolls. The rubber strip is usually wound around one roll. Addition of the products is made gradually ensuring homogeneous mixing is achieved. Due to the viscous nature of the polymer, heat is generated and the temperature can reach values above 100°C especially for filled materials that exhibit high hysteresis. The temperature has thus to be checked before the addition of sulphur and other curing ingredients to ensure premature vulcanisation is avoided.

Unless otherwise stated, vulcanisation was then carried out in a hydraulic hot press adjusted to the desired curing temperature. The temperature of the platens was controlled with a precision of +/- 2°C. A compressive pressure of about 10 MPa was applied to obtain flat sheets of rubber using different moulds depending on the desired geometry and dimensions of the samples (Figure 3-2). Pressure was increased progressively and removed several times in the early stages of vulcanisation to ensure the diffusion and evacuation of any air trapped inside the mould and into the rubber.

Figure 3-2.Mould used in the hot press to vulcanise 240mm x 200mm x 2mm sheets

3-1-4. Evaluation of curing time

Curing time has been estimated using a moving die rheometer. A small amount of unvulcanised compound is compressed between two plates set at the curing temperature. One of them is oscillating and the torque necessary to rotate the disc is monitored against time. A typical torque-time response is given in Figure 3-3. As the disc touches the rubber, an initial large increase in the torque is seen. Then the rubber heats up and the torque goes down due to a decrease in viscosity. Eventually crosslinks start to form and the viscous liquid is transformed into a viscoelastic solid. Although chain scission might occur the torque increases reflecting the domination of the formation of crosslinks. The torque can then either reach a maximum followed by a reduction known as reversion, remain constant or keep increasing but at a much slower rate known as creeping cure depending on the nature of the crosslinks formed and the amount of chain and crosslink scission after vulcanisation. Typically the optimum curing time (t_{90}) is defined as the time required to reach 90% of the maximum torque for rubbers exhibiting reversion or plateau cure behaviour. For rubbers exhibiting creeping cure, the point at which the increase of the torque was less than 20% of the maximum slope during crosslink formation was taken as the reference torque for the optimum cure calculation. For rubber sheets with similar thickness as the rheometer cavity (about 2mm) the rheometer timings can be used as the curing time. However, if the dimensions of the sample are larger, longer curing time should be applied. Values of curing times for the compounds used in this study are given in Tables 3-1 and 3-2 alongside their formulations.

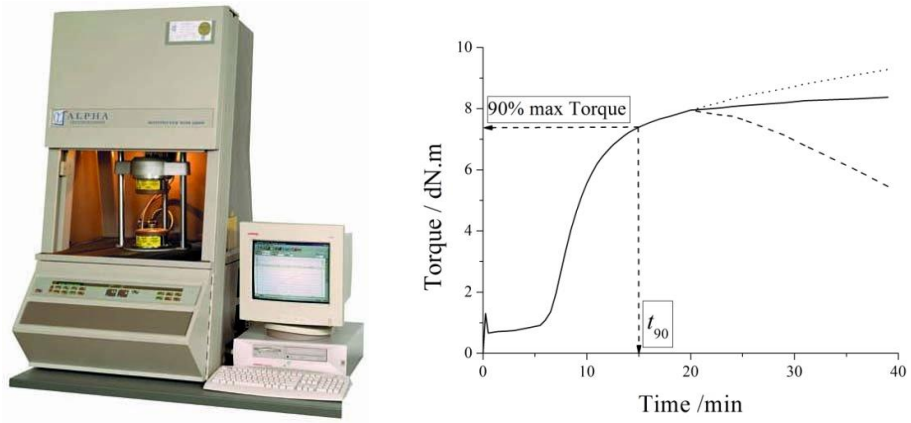

Figure 3-3. Moving die rheometer employed and Torque vs Time curve obtained for the SBR0 compound (plateau cure behaviour). Reversion and creeping cure behaviour are also shown respectively as dashed and dotted lines.

3-2. **Material analysis**

3-2-1. Determination of the crosslink density

Unfilled rubbers

An equilibrium swelling method was used to determine the crosslink density of unfilled rubbers to check whether samples prepared independently had a similar crosslink density, a factor which significantly affects the mechanical properties. This ensures a good consistency between compounds that might result from less than optimal mixing and moulding processes. Rubber samples of relatively small size (about 10mm x 10mm x 2 mm) were cut out from rubber sheets and immersed into toluene. The change in mass was monitored as a function of time for the first experiments which showed that equilibrium is reached in less than 24h. The samples were therefore left immersed in the solvent for 48h to ensure equilibrium was reached. The swollen samples were then evaporated fully in air for 48h. Their final mass was measured. This was done to evaluate the extraction of oils and other products soluble in toluene and also any residual rubber ripped away from a cut edge during swelling. The volume of toluene absorbed by the rubber network was calculated from the difference in the mass of the swollen and dried samples. The volume of elastomer in the dried network can be calculated using equation (3-1).

$$V_{\mathrm{rn}} = \frac{M_0}{\rho_{\mathrm{rn}}} \frac{M_{\mathrm{rn}}}{M_{\mathrm{t}}} \tag{3-1}$$

Where V_{rn} is the volume of the rubber network, M_0 is the mass of the dried specimen, M_{rn} is the mass of the rubber network and sulphur and M_{t} is the total mass of the compound formulation including fillers and additives. ρ_{rn} is the density of the elastomer network and was calculated using a simple experiment based on Archimedes' law. The weight of the network was measured in air (w_{air}) and in water (w_{water}). The density of the rubber network can be estimated with equation (3-2).

$$\rho_{\mathrm{rn}} = \frac{w_{\mathrm{air}} \rho_{\mathrm{water}}}{w_{\mathrm{air}} - w_{\mathrm{water}}} \tag{3-2}$$

Where ρ_{water} is the density of water. The densities of SBR and NR were respectively found to be about 0.93 and 0.94 g.cm^{-3}. The volume fraction of elastomer in the swollen network is then calculated using equation (3-3).

$$\upsilon_r = \frac{V_{rn}}{V_{rn} + V_s} \tag{3-3}$$

Where V_s is the volume of solvent absorbed at equilibrium. It was obtained from the mass difference between the swollen and the dried samples divided by the volume mass of the solvent which is about 0.867g/cm^3 for toluene. The crosslink density $[X]_{phys}$ is determined using the Flory and Rehner (1943) relationship (equation (3-4)).

$$\ln(1-\upsilon_r) + \upsilon_r + \chi\upsilon_r^{\,2} + 2\rho_{rn}v_0[X]_{phys}(\upsilon_r)^{\frac{1}{3}} = 0 \tag{3-4}$$

Where υ_r is the volume fraction of rubber at equilibrium, χ is the Flory-Rehner interaction parameter between the rubber and the swelling liquid and v_0 is the molar volume of the solvent equal to 106.29 cm^3/mol for toluene. The density $[X]_{phys}$ obtained from this experiment is the sum of the chemical crosslinks (covalent bonds) and the physical crosslinks such a chain entanglements or physical bonds.

Filled rubbers

For carbon black filled rubbers, the presence of fillers reduces the mobility of the polymer chain during the swelling process. Use of equation (3-4) would give higher crosslink density than the actual values. Porter Porter (1967) developed an empirical relationship to adjust the measurement of crosslink density by equilibrium swelling to account for the additional constraints found in a carbon black filled rubber. He proposed that the crosslink density $[X]_{cb}$ is given as:

$$[X]_{cb} = \frac{[X]_{phys}}{1 + K_f V_{cb}} \tag{3-5}$$

Where K_f is a constant characteristic of a given filler and V_{cb} is the volume fraction of carbon black in the rubber.

3-2-2. Crosslink density using the stress-strain behaviour

For an unfilled rubber the crosslink density can also be evaluated by tensile testing using Mooney-Rivlin constant C_1. From the statistical theory of elasticity, the crosslink density can be expressed as:

$$[X]_{\text{phys}} = \frac{C_1}{\mathbf{R}\,\theta} \tag{3-6}$$

Where $[X]_{\text{phys}}$ is the crosslink density, θ is the absolute temperature and **R** is the gas constant. In uniaxial tension, the Mooney-Rivlin equation is given as

$$\sigma = 2\left(\lambda - \frac{1}{\lambda^2}\right)\left(C_1 + \frac{C_2}{\lambda}\right) \tag{3-7}$$

Which is sometimes expressed as the reduced stress σ^*

$$\sigma^* = \frac{\sigma}{2\left(\lambda - \frac{1}{\lambda^2}\right)} = C_1 + \frac{C_2}{\lambda} \tag{3-8}$$

Where σ is the engineering stress, λ is the extension ratio. From of a plot of the reduced stress versus the inverse of the extension ratio, the constants C_1 and C_2 can be obtained as the slope and the intersection of the curve with the Y-axis as can be seen on Figure 3-4. The tensile tests to get C_1 and C_2 were carried out at a rate of 5 mm/min to be near equilibrium conditions. Details of the tensile tests are given in the next paragraph.

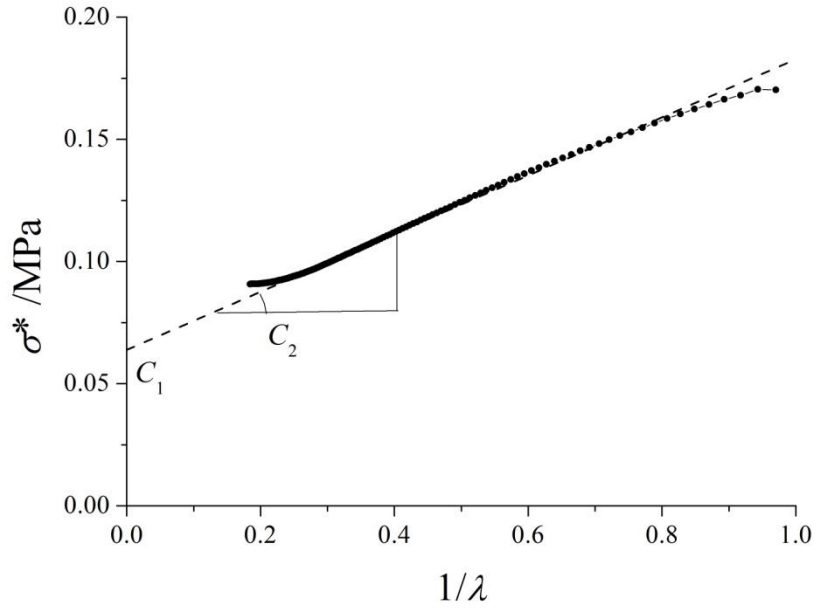

Figure 3-4. Mooney plot for SBR0, the dashed line shows the fit in the linear region of the graph.

3-3. **Mechanical testing**

3-3-1. Tensile test

Tensile tests were carried out on an Instron 5567 screw driven machine fitted with a video-extensometer (Figure 3-5). Dumbbell specimens ASTM D412 type D were cut out of flat rubber sheets. Dimensions of the dumbbell specimen can be seen on Figure 3-6. The thickness was measured using a micrometer on both ends of the reduced section and in the centre of the specimen. The average was used to calculate the cross-section and thus the stress. The extension ratio λ is calculated using equation (3-9).

$$\lambda = \frac{L}{L_0} \tag{3-9}$$

Where L is the length of the stretched sample at a given load and L_0 is the undeformed length. This can be evaluated either by the displacement of the crosshead or a non-contact video-extensometer. The latter case is more reliable and was used here, in this case two dots were drawn in the reduced width region and each was followed during deformation using a video-extensometer. Due to the large potential strains in the samples prior to breaking, the deformation of the dots creates a difficulty as they

become highly stretched at extension ratios greater than 5 and the video-extensometer is not able to distinguish them from the rubber anymore.

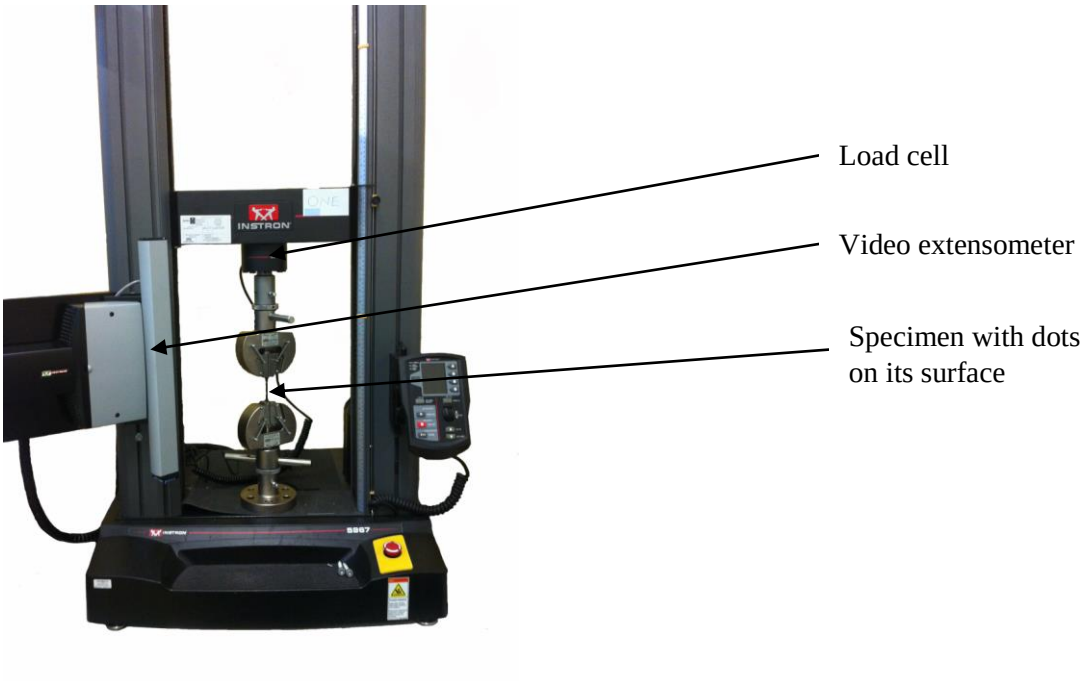

Figure 3-5. Instron 5567 used for the tensile testing fitted with video extensometer. Two dots are drawn on the sample to measure the strain in the gauge length of the specimen.

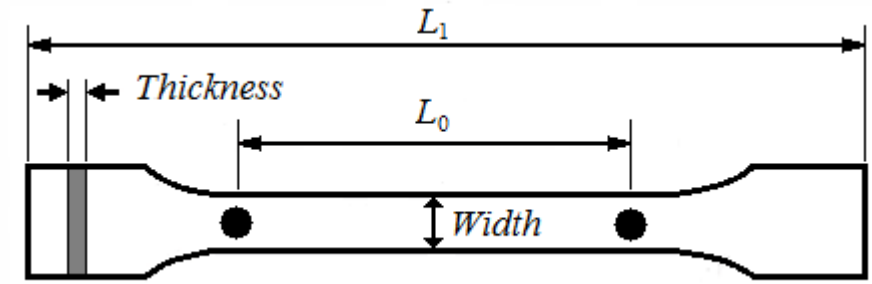

Figure 3-6. Dimensions of the tensile specimen. L1 = 65mm, L0 = 30mm, width = 3.1mm with dots for video-extensometer.

3-3-2.Additional mechanical tests for validation of FEA parameters

Other deformation modes have been used in addition to tension. Compression and pure shear tests were carried out on an Instron 5567. Dimensions of the specimen are given in Figure 3-7 in mm. Displacement was evaluated using the displacement of the crosshead and divided by the original length to obtain the strain. To reduce the barrelling effect, lubricant was applied on both compression plates and a tiny pin was

glued to one of them to prevent the sliding of the sample. Tests were conducted at a slow strain rate of 0.01 s^{-1} in order to be close to equilibrium conditions.

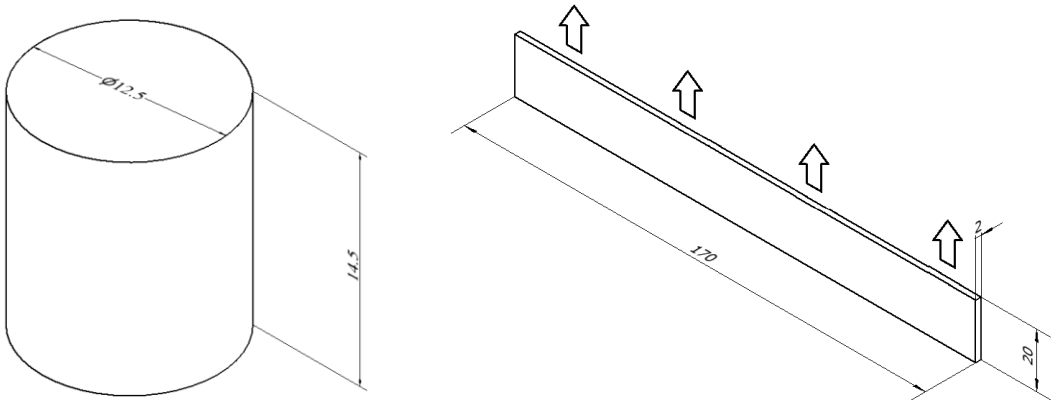

Figure 3-7. Dimensions of samples used compression and pure shear testing.

3-3-3. Dynamic mechanical analysis

The influence of glass transition temperature on the fracture behaviour of elastomers has been widely researched by many researchers. It is clear that the energy dissipation mechanisms at the crack tip are significantly influenced by the temperature. The further the ambient temperature is above T_g, the lower the dissipation and thus the magnitude of the critical tearing energy. In this work, Dynamic Mechanical Analysis was not only used to determine the glass transition temperature but also the stiffness (storage modulus) and damping properties (loss modulus) of a material subjected to an oscillatory loading over a range of frequencies and temperatures. A uniaxial tension setup was adopted for the experiment. A rectangular shaped specimen of about 15mm in length was attached at both ends to clamps and subjected to an oscillating signal either in terms of deformation or force. The response of the material was measured and decomposed into an in-phase signal (see Figure 3-8) which accounts for the elastic part and an out-of phase component representing the viscous part of the behaviour. Those components are expressed as the storage modulus *E'*, the loss modulus *E''* and the phase shift between them is tanδ (the ratio of the loss and the storage modulus) which is a measure of the damping of the material.

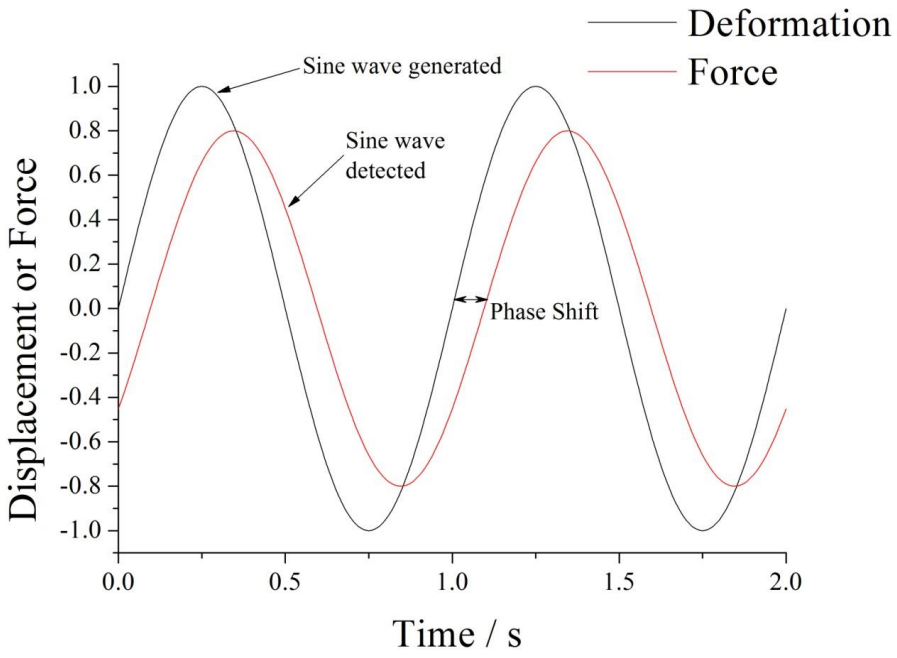

Figure 3-8. Phase shift between the displacement and force signal. Dynamic mechanical analysis equipment can measure the phase shift and can identify the elastic and the viscous contributions of the behaviour.

Determination of T_g was made through a temperature sweep from -120°C to 100°C at a fixed frequency of 1Hz. A plot of the typical variation of the viscoelastic properties of an elastomer is shown on Figure 3-9. As the rubber is heated up, it goes from a glassy region to a rubbery region through a transition state. The storage modulus *E'* drops by several order of magnitude while the loss modulus *E''* and tanδ present a peak in the transition region (Mark and Erman (1994)). The glass transition temperature is usually obtained from the intersection of the two tangents to the storage modulus curve in the glassy and the transition region (Mark and Erman (1994). The temperatures of the peaks in loss modulus and tanδ are also sometimes used to determine T_g. Values obtained for the elastomers used in this study are given in Table 3-3.

	NR0	**NR50**	**SBR0**	**SBR50**	**SBR70**
T_g *Storage Modulus /°C*	-50	-46	-40	-36	-36
T_g *Loss Modulus /°C*	-46	-41	-33	-31	-31
T_g tanδ */°C*	-39	-36	-25	-27	-26

Table 3-3. Glass transition temperature of the compounds used in this study determined with dynamic mechanical analaysis.

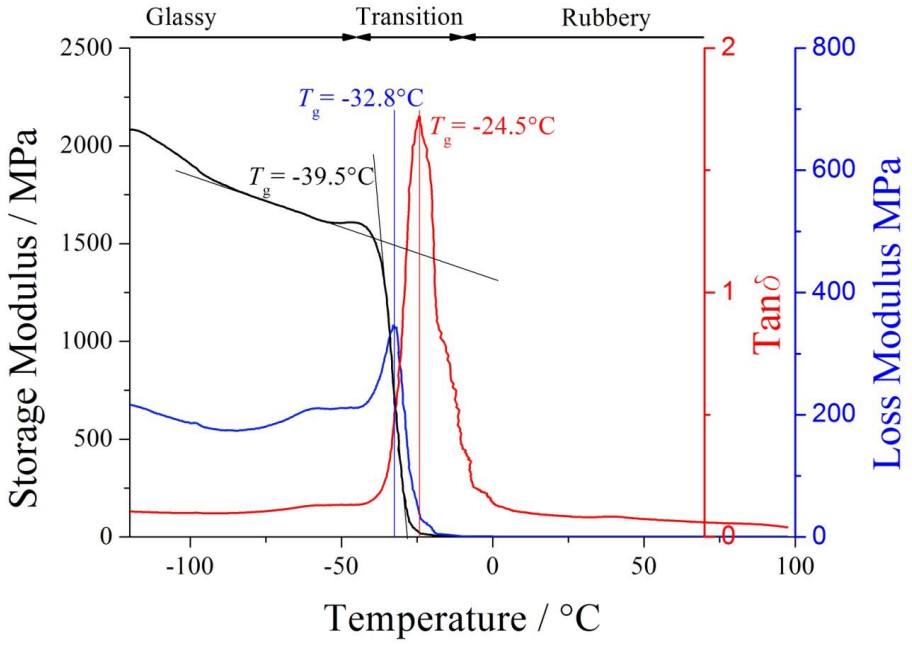

Figure 3-9. Temperature dependence of the viscoelatic parameters for SBR0 showing three methods to determine T_g.

Dynamic mechanical analysis was also used for time temperature superposition and determination of mastercurves as described in Chapter 2 section 2-1-5. Frequency sweeps were typically performed in isothermal steps ranging from T_g -10°C to T_g +100°C approximately.

3-4. **Fracture of elastomers**

3-4-1. Fatigue crack growth test

A pure shear crack growth test geometry was used for the fatigue crack growth tests. The specimens were 170 +/- 5mm long, about 2mm thick and about 20 mm high. For test at the highest frequencies this height was reduced to 12mm. For this geometry, the tearing energy can be obtained from two different methods. Both methods are based on different modes of loading depending on the region of the sample. Figure 3-10 shows the four different region of the sample (Greensmith and Thomas (1955)). Region 1 is undeformed and the strain energy stored in this region is null. As the crack grows, region 2 translates by the same amount as the crack front. Regions 2 and 4 exhibit complicated states of stress and strain but they are only dependent on the crack tip geometry and the dimensions of the samples and hence independent of the crack length. Region 3 is in pure shear as long as the thickness of the sample is small enough

compared with its height and its length at least 8 times its height. As the crack grows, the length of this region is reduced by the same amount as crack growth. Thus there is an energy transfer from the region in pure shear to the undeformed region equal to the strain energy density in pure shear multiplied by the volume involved in the crack growth. This allows an energy release rate to be derived which is equal to:

$$T = W_{ps} l_0 \tag{3-11}$$

Where W_{ps} is the strain energy density in pure shear (region 3) and l_0 the original height of the specimen. The strain energy density is obtained from an independent test at the same maximum strain on a sample of similar dimensions but with no crack so that the whole sample is considered to be in pure shear.

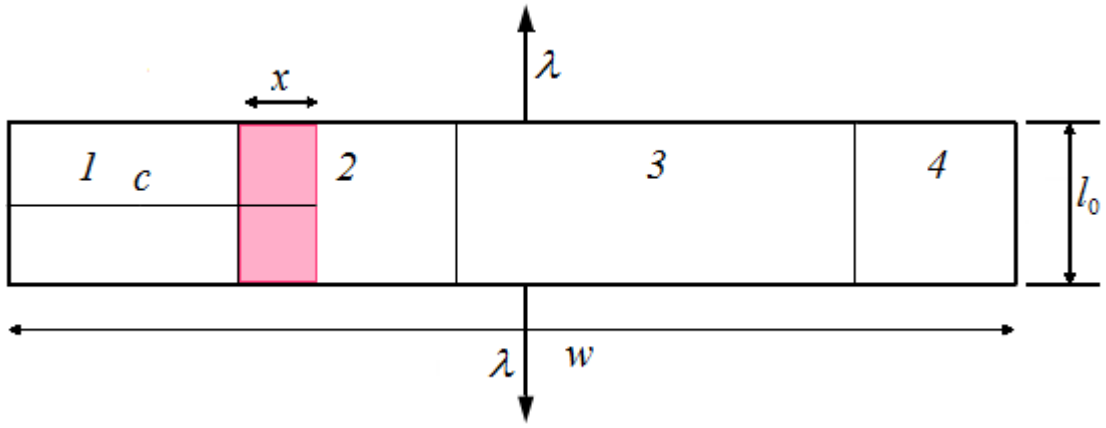

Figure 3-10. Four regions of the pure shear test specimen.

The tearing energy can also be calculated from the direct measurement of force and displacement in the material using a method described by Busfield (1997).

$$T = \frac{U}{h(w - c + x)} \tag{3-12}$$

Where U is the strain energy density calculated from the integral of the stress strain curve, h and w are the thickness and width of the material, c is the crack length and x is an additional length due to the strain state at the crack tip estimated to be about 28% of the height of the sample. In order to minimise the influence of the Mullins effect and the cyclic stress softening on the measurement, the calculations were made for the 1000th cycle as suggested by Busfield et al. (2002). The softening effect is then sufficiently low to be considered as null. The strain energy density method shows limitations especially

at low tearing energy due to the viscoelastic nature of the rubber and the permanent set resulting from stretching the rubber, as the extent of the permanent set depends on the maximum strain. The evaluation of the strain energy density should ideally be done at the same maximum strain and frequency as the crack growth tests but this would be extremely time and material consuming. The effect of the permanent set on the strain in the crack growth samples has been neglected but the tearing energy is thus underestimated as the permanent set is larger at higher strains. Another source of error results from using the loading curve to calculate the tearing energy. This curve also depends on the maximum strain achieved during the test. It has thus been chosen to evaluate the tearing energy from the measured force-displacement curves even though they require an evaluation of the strain energy in the region around the crack tip.

Generally, crack growth was monitored using a fixed camera taking a picture of the area around the crack tip at the maximum displacement in the test. A reference capture with a ruler in the plane of the specimen surface was taken once the camera had been positioned and optical parameters adjusted to give best resolution, contrast and focus. A picture was then captured at regular time intervals which combined with the frequency of the test was used to determine the specific loading number for any captured image. Using an image processing Matlab method, each picture was transformed into a black and white array of pixels and the length between the edge of the picture and the furthest white dot determined as the crack length in pixels. The latter was converted into a distance using the pixels/distance ratio calculated from a reference picture. Figure 3-11 illustrates the process. Gent and Thomas (1958) observed that the crack length increases more quickly in the earlier stages of the experiment. It is thought to be due to the initial sharp crack tip radius cut with a razor blade (Papadopoulos et al. (2008)). The crack growth rate per cycle was determined in the steady region of the crack growth. At frequencies above 1Hz, the time of capture of the camera was too long to obtain a good image. Also when testing at elevated temperatures, some ambient light was reflected by the temperature chamber window which resulted in overexposed pictures. In both of these cases, the tip of the crack was hardly discernable from the rest of the sample or poor contrast did not allow the crack tip to be easily identified using the method described above. The cyclic signal was therefore interrupted at constant interval, the crosshead was moved to a constant value to be able to locate the crack tip and a picture was taken. The length of the crack was then determined manually on each picture by

locating the tip of the crack. A minimum of eight points were acquired to monitor the crack growth and ensure that steady state crack growth rate had been attained.

Fatigue tests were carried out on a servohydraulic Instron 8871 and an Instron 8801 equipped with a 1kN dynamic load cell or an Instron Electropuls E10000 fitted with a 10kN load cell. The maximum frequency available on the machines is 100Hz but the large displacements necessary to see the crack propagating during the fatigue experiments for an elastomeric material in a reasonable time frame restricted the maximum frequency to a much lower 10Hz.

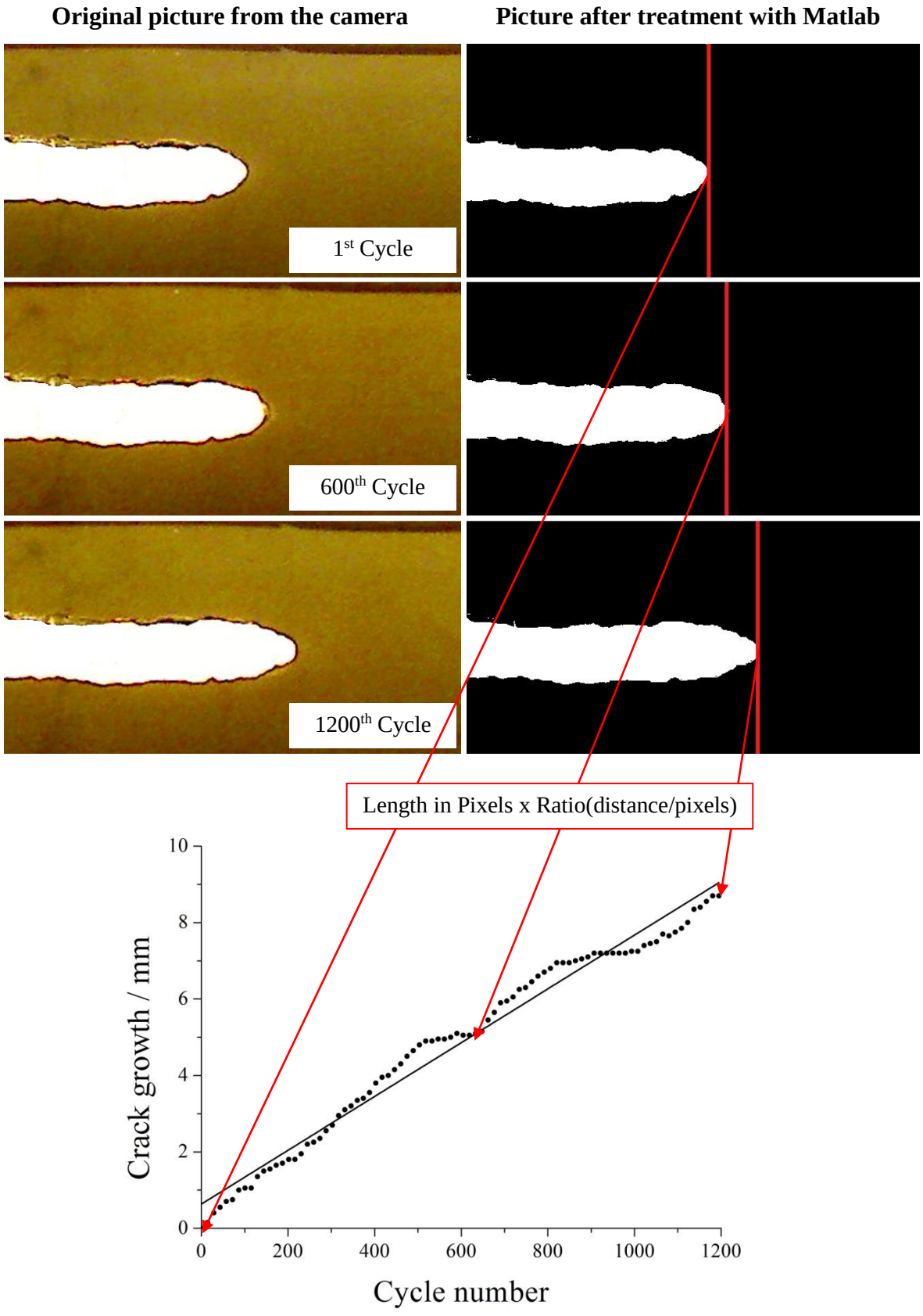

Figure 3-11. Evaluation of crack growth rate during the fatigue testing.

3-4-2. Peeling test

A common geometry (Igarashi (1975), Gent and Tobias (1984)) to evaluate the strength at the interface between flexible layers is the peeling test (Figure 3-12). The tearing energy in this particular geometry referred to as the peeling energy from now on in this work is given by the difference of the work done on the sample and the stored energy dissipated in the legs as the crack grows. It can be expressed as

$$P = \frac{2F\lambda}{w} - 2hW \tag{3-13}$$

Where F is the force applied to the legs, λ is the extension ratio in the legs in uniaxial tension, h is the thickness of one leg and W is the stored energy density in the legs. W can be estimated by a tensile test at the same maximum force encountered during the peeling test.

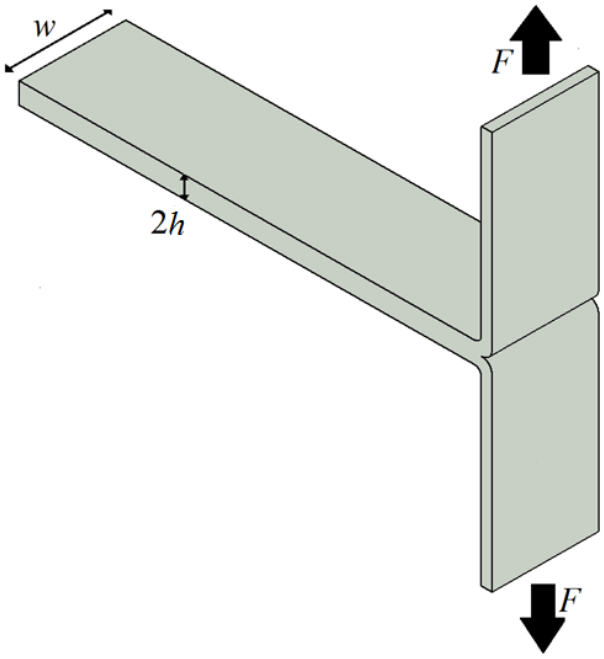

Figure 3-12. Peeling specimen

The peeling experiments were carried out on a servohydraulic Instron 8871 or an electrically driven Instron Electropuls under advanced amplitude control which allows a constant maximum load to be applied. This control mode results in a ramped transition during the start of the test until the desired maximum load is achieved.

The fatigue crack growth can be evaluated using the maximum displacement of the crosshead, see Figure 3-13. The crack growth rate per cycle is given as:

$$\frac{\mathrm{d}c}{\mathrm{d}N} = \frac{1}{2\lambda}\frac{\mathrm{d}l}{\mathrm{d}N} \tag{3-14}$$

Where l is the maximum displacement of the crosshead achieved during each cycle. Silver marks have been drawn at the crack tip at the start and at the end of each phase of the crack growth experiment. On Figure 3-14, each rectangle marked with a silver pen corresponds to a precise peeling energy. Between two separate cyclic tests, the crack was grown manually to facilitate the identification of the zone and the observation of the crack surface as described later in this chapter. The crack growth rates obtained from the displacement of the crosshead using equation (3-14) and from the drawing of marks using the ratio of the length in the crack growth direction of the rectangles by the number of cycles are also compared on Figure 3-14 to evaluate the influence of stress softening on the apparent crack growth rate. As the crack growth rate is measured after 1000 cycles for most of the loads, the results are similar for both methods as the stress softening effect is low after this number of cycles. The difference can be attributed to the establishment of the steady crack growth rate in the early stage of the testing. Equations (3-13) and (3-14) have to be modified to account for an interface between dissimilar materials so that the different mechanical properties on either side of the interface can be considered.

$$P = \frac{F(\lambda_1 + \lambda_2)}{w} - h_1 W_1 - h_2 W_2 \tag{3-15}$$

$$\frac{\mathrm{d}c}{\mathrm{d}N} = \frac{1}{\lambda_1 + \lambda_2}\frac{\mathrm{d}l}{\mathrm{d}N} \tag{3-16}$$

Where λ_1, λ_2, h_1, h_2, W_1 and W_2 are respectively the extension ratio, the thickness and the stored energy density in legs 1 and 2.

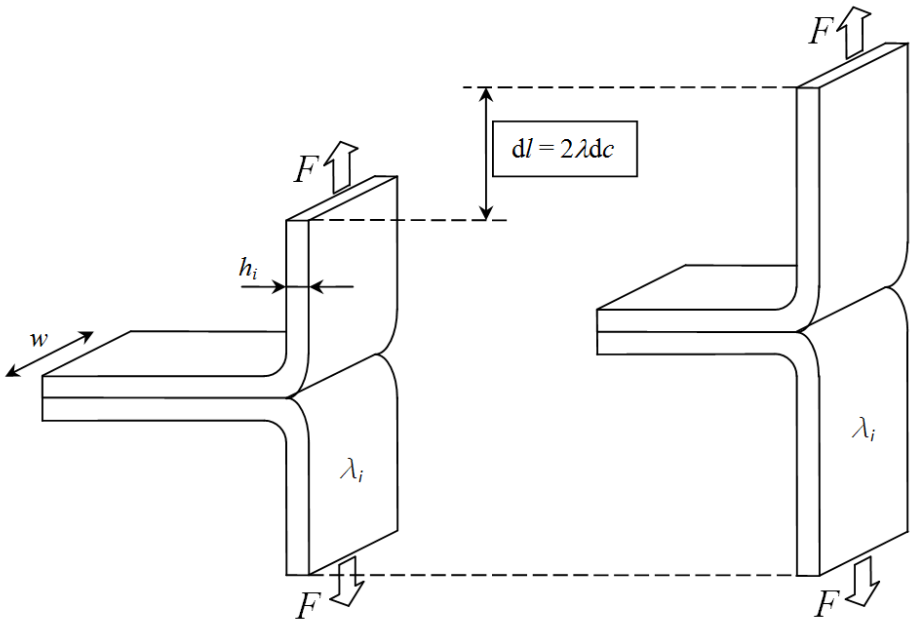

Figure 3-13. Measurement of crack growth during the peeling tests.

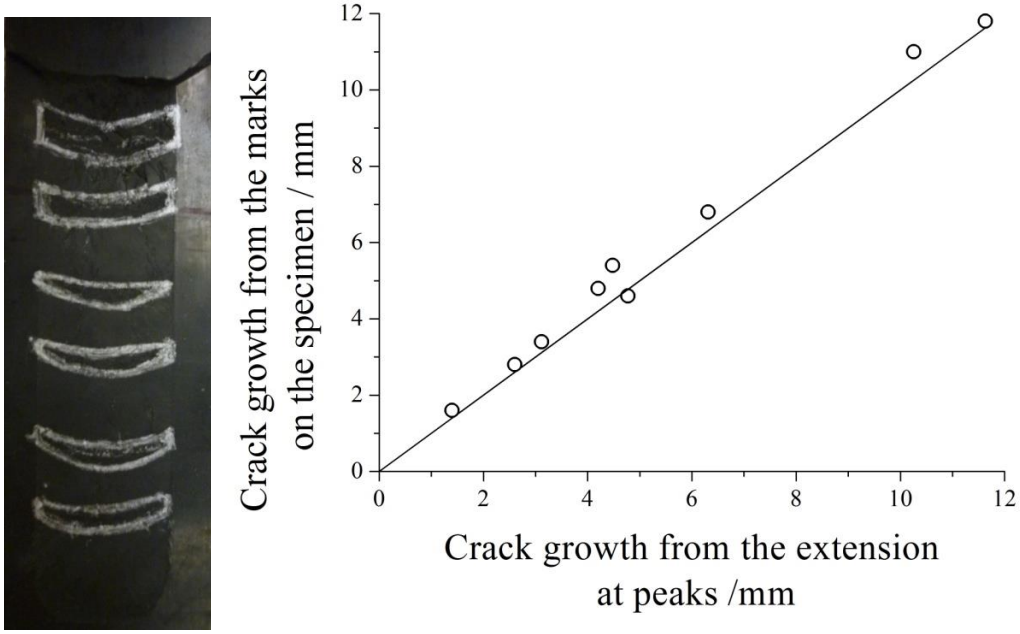

Figure 3-14.Comparison of crack growth obtained from maximum displacement of the crosshead and silver marks at the crack tip.

3-5. **Optical measurements**

Fukahori and Andrews (1978) observed the patterns on the crack surface changed depending on the maximum tearing energy. Inspection of surfaces resulting from fatigue crack growth in elastomers was performed using microscopes of different magnification.

3-5-1. Optical microscopy

Optical microscopes magnify a surface through a system of lenses. A beam of light is sent on the surface of the sample and the reflected light travels through two lenses, the objective and the ocular. The magnification of the microscope is the product of the magnifying power of the lenses and is generally no more than 1000 times. Resolution and depth of field represents the main limitations of optical microscopy and decrease with the magnification of the objective. Observation of the profile is thus limited to relatively small magnification due to the roughness of the surface preventing focus on a large enough observed area. The microscope used in this study was fitted with a camera. The maximum magnification used with acceptable resolution and depth of field was 100. Observation using the optical microscope allows detection of relatively big flaws such as air trapped at the interface during the vulcanisation and qualitative comparison of roughness. In Figure 3-15, two profiles are shown for surfaces obtained at different peeling energies. In the example below, the surface obtained at P=10kJ.m^{-2} appears to be rougher than in the P=5kJ.m^{-2} case.

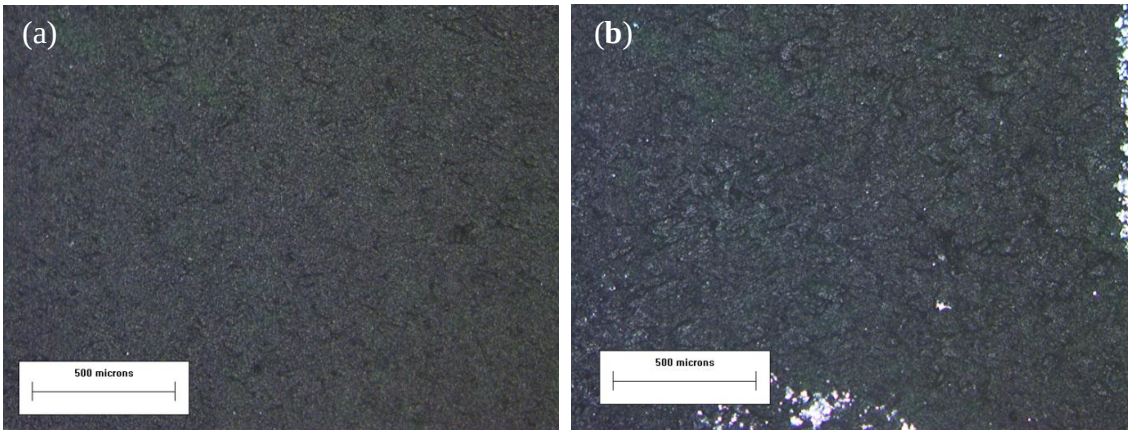

Figure 3-15. Optical microscopy of crack surface at different peeling energies

(a) P= 5kJ.m^{-2} (b) P=10kJ.m^{-2}

3-5-2. Scanning electron microscope (SEM)

A scanning electron microscope was also used to observe fracture surfaces at higher magnification. SEM projects a beam of electron on the surface of the sample. Atoms at the surface interact with the electron beam and various signals are produced. In this thesis, secondary electrons emitted by atoms excited by the electron beam were detected. This signal contains information about the topography of the surface which is transformed into an image of the surface by scanning the sample.

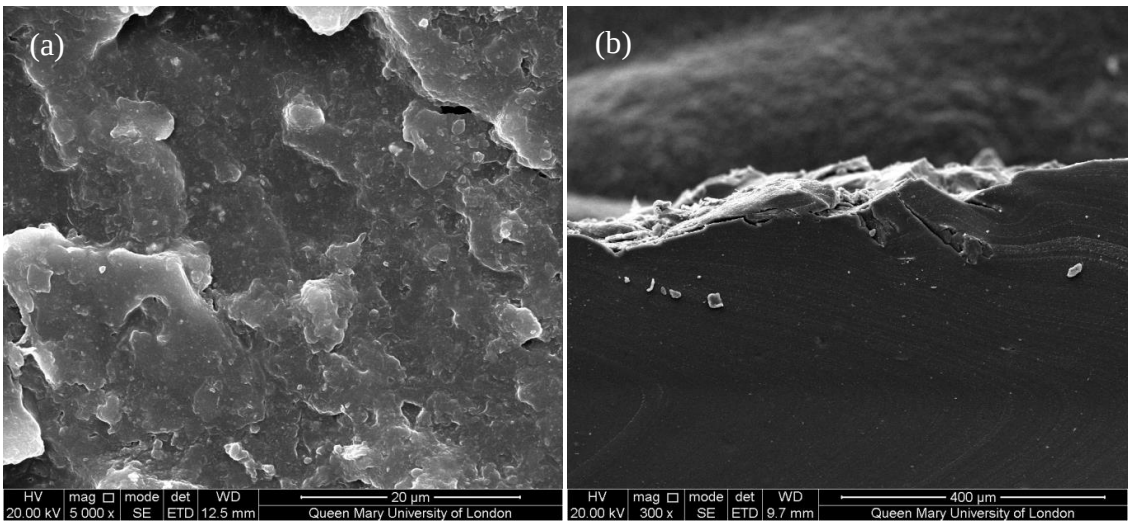

Figure 3-16. SEM images of crack surface (a) from the top (b) from the side.

Samples (about 4mm x 4mm) were cut from the cracked specimen using a sharp scalpel and then glued to a metallic support using conductive glue. To avoid the accumulation of charges on the surface of the specimen, the surface of the specimen has to be conductive. The elastomeric samples were therefore coated with a thin layer of carbon. The surfaces were observed from a view perpendicular to the torn surface as well as edge on using the SEM as can be seen on Figure 3-16.

3-6. **Roughness measurements**

Quantitative evaluation of the crack surface roughness was obtained using a non contact topography measurement instrument (Scantron Proscan). A focused 50µm diameter beam of light is sent to the surface of the sample. The intensity of the light reflected is measured by an optical head and relates to the distance between the detector and the sample. The scan consists of an array of points, each defined by their Cartesian coordinates. The specimen is scanned backwards and forwards in the X direction over a

predefined number of lines. Between each line the head is moved in the Y direction by a predefined distance. Data acquired are converted into a 3D chart (see Figure 3.17) of the surface from which different parameters can be calculated. 2mm x 2mm surfaces were analysed with a displacement of 10µm between two points in the X direction and 10µm in the Y direction between two lines. The optical head used (designation L35/10H) presents a nominal resolution of 0.5µm in the Z direction. The X axis direction was chosen parallel to the crack growth. The array of data was then transformed to a surface chart using Excel. Different roughness parameters can be calculated from the data with the Proscan software and are generally calculated by the deviation of the profiles from a mean line. In this study two parameters are used: the roughness average R_a and the root mean square roughness average R_q, sometimes also abbreviated to RMS. Definitions of R_a and R_q are given in equations (3.17) and (3.18) respectively for a line of length Z. While R_a gives an idea of the distance to the mean line, R_q represents the distribution of the peaks and valleys of the surface.

$$R_a = \frac{1}{Z}\int_0^Z |h(x)|\,dx \tag{3.17}$$

$$R_q = \sqrt{\frac{1}{Z}\int_0^Z h(x)^2\,dx} \tag{3.18}$$

Where the function *h* gives the distance of the point to the mean line of the profile.

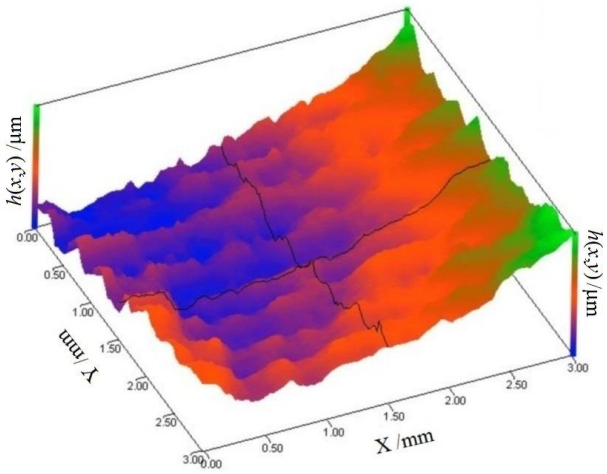

Figure 3-17. Profile of crack surface obtained with topography analysis.

3-7. **Material characterisation for FEA analysis**

In order to model a component made of elastomers and estimate its lifetime, it is necessary to model the elastic properties accurately. Commonly, the mechanical properties of an elastomer are given by a Strain Energy Function (SEF) such as those described in Section 2-1 which can relate the strain energy density in the material to the strain invariants of the Cauchy Green deformation tensor. They have to be carefully chosen to reflect the behaviour of the elastomer over the range of strains investigated in the simulation. Unfilled materials can be accurately described by the Mooney-Rivlin SEF Treloar (1975) while filled materials are better described by a Yeoh SEF especially at high strains (Yeoh (1990)). Expressions of both SEFs are given in equations (3.19) and (3.20) where I_1 and I_2 are the first and second strain invariants whose expressions are given in Chapter 2. Both of them are included in Abaqus 6.12 software package.

$$W = C_1(I_1 - 3) + C_2(I_2 - 3) \tag{3.19}$$

$$W = C_{10}(I_1 - 3) + C_{20}(I_1 - 3)^2 + C_{30}(I_1 - 3)^3 \tag{3.20}$$

Coefficients C_i and C_{i0} are material properties and have to be determined by fitting the SEF to experimental data. The loading history and environmental dependence of the mechanical properties have to be taken into consideration. Material behaviour has to be obtained in similar conditions the components are subjected to in service. Davies et al. (1996) showed that cyclic stress softening, the process by which the stiffness of an elastomer decreases when it is subjected to a cyclic loading, becomes small enough to be considered as approximately constant after a thousand cycles. Therefore, the test specimens were precycled a 1000 times before recording the stress-strain data. C_1 and C_2 can be obtained from the Mooney plot as explained previously. The coefficients for the unfilled materials used in this study are given in Table 3-4.

To validate the coefficients, the experimental behaviour of the materials has been compared to results obtained with finite element analysis under different modes of loading. The models are shown in Figure 3-18 for tension, compression and pure shear (or planar tension). Plane stress elements have been used for tension and pure shear as the thickness of the sheet is small compared to the other dimensions. Axisymmetric elements have been used to simulate a cylinder under compression. In tension, simulated results are in good agreement with experimental data for both materials as can

be seen on Figure 3-19. The drawbacks of using Mooney plots in uniaxial tension to obtain the SEF coefficients have been pointed out in Chapter 2. The main concern is the relative failure to predict behaviour in other modes of deformation. Figure 3-20 shows a comparison of experimental and simulated data for pure shear. A good fit is obtained over the range of strains typically encountered in tyre usage and in the region of the crack tip and therefore used throughout this investigation.

Materials	**C_1 / MPa**	**C_2 / MPa**
SBR0	0.064	0.120
NR0	0.114	0.087

Table 3-4. Mooney-Rivlin coefficients for FEA implementation

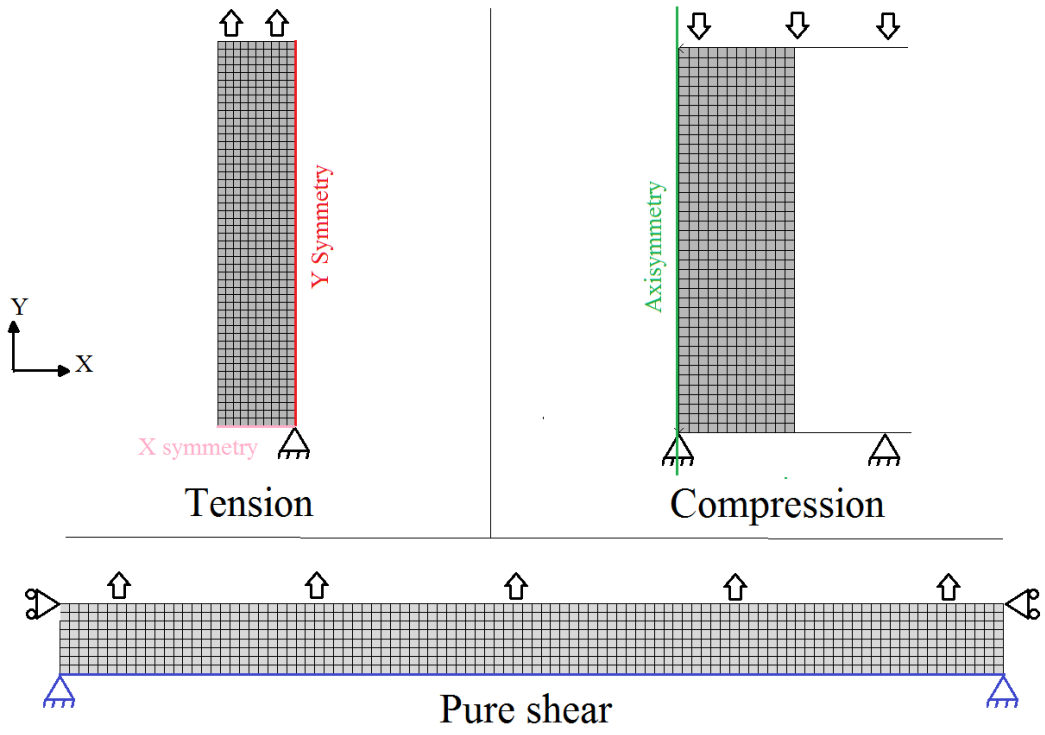

Figure 3-18. Models used for comparison with FEA of mechanical behaviour with SEF.

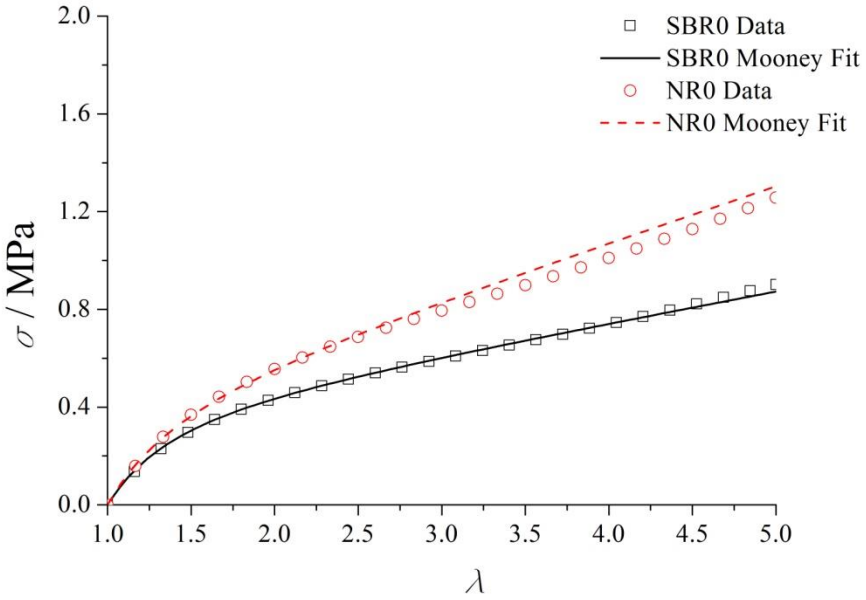

Figure 3-19. Mooney-Rivlin SEF fitted to tensile experimental data for unfilled materials.

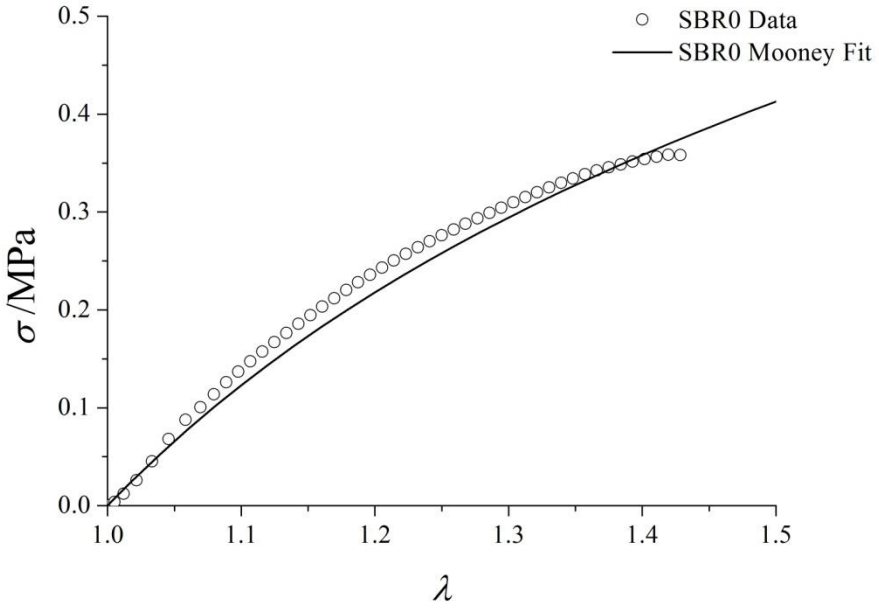

Figure 3-20. The data fitted in tension to the Mooney SEF used to predict the behaviour in pure shear.

The Yeoh strain energy function was used for filled elastomers as it is able to model the upturn in the strain-stress behaviour (Yeoh (1990)). Equation (3.20) can be differentiated regarding I_1 to express the reduced stress σ^* as a function of the first strain invariant (see equation (3.21)). The reduced stress is plotted against (I_1-3) to obtain the coefficients. An example is given in Figure 3-21 for DC005 compound. The coefficients for the filled materials used in FEA simulations are given in Table 3-5.

$$\sigma^* = \frac{\partial W}{\partial I_1} = C_{10} + 2C_{20}(I_1 - 3) + 3C_{30}(I_1 - 3) \tag{3.21}$$

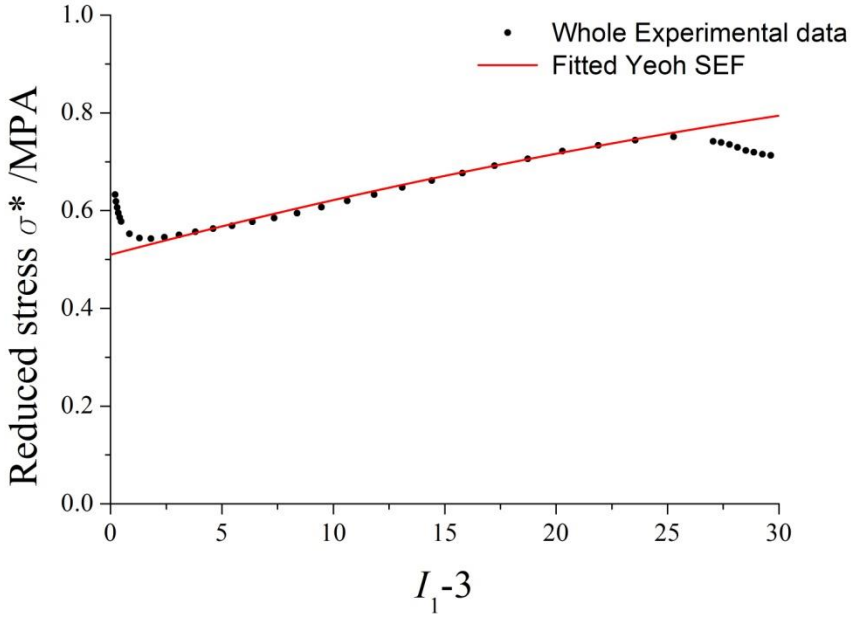

3-21. Fitting the Yeoh strain energy function to experimental data (DC005) in tension.

Material	C_{10} **/MPa**	C_{20} **/MPa**	C_{30} **/MPa**
SBR50	0.43	0.059	-0.00089
NR50	0.61	0.078	-0.0012
DC005	0.51	0.0060	-0.00028
DC018	1.215	-0.33	0.0987
DC019	0.795	-0.14	0.0227
DC029	0.647	-0.005	0.003

Table 3-5. Yeoh SEF coefficients measured for each of the filled materials used in this thesis.

On Figure 3-22, a comparison is drawn between the real behaviour and the simulated response in tension. It can be seen that over a wide range of strains, both curves are identical. At low strains, a slight deviation occurs. Coefficients are obtained at strains above 100% as we are mostly interested in a good fit in tension at high strains when investigating fracture in elastomers due to the high strains exhibited at the crack tip. This discrepancy at lower strains can therefore also be found in the tensile response in the simulation.

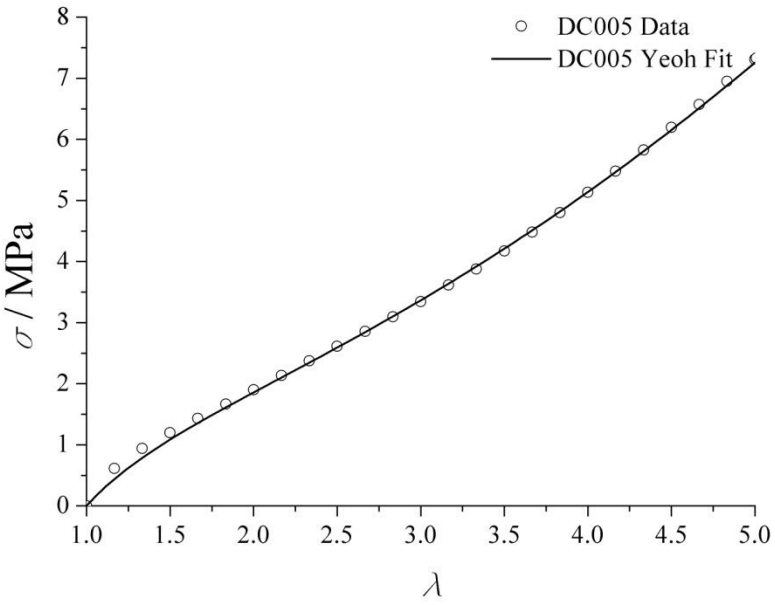

Figure 3-22. Simulated and experimental results in tension for DC005.

Compression and pure shear tests have also been performed with the materials to check the response of the fitted Yeoh function in tension to other modes of loading. On Figures 3-23 and 3-24, the results obtained from the FEA are compared with results obtained from experiments for DC005 compound. The same deviation at lower strains observed in tension is again seen in pure shear. The range of strains in the experimental data is limited by slippage of the sample but it can be seen that the simulation results get closer to the experimental data at as we approach an extension ratio equal to 1.6. Simulations in compression are in good agreement with experimental data. The deviation at high strain can be explained by additional friction that might occur in the experiment despite lubrication of the plates while a frictionless contact was used in the

simulations. This effect is more significant at higher strains and causes a higher average stress in the experiment.

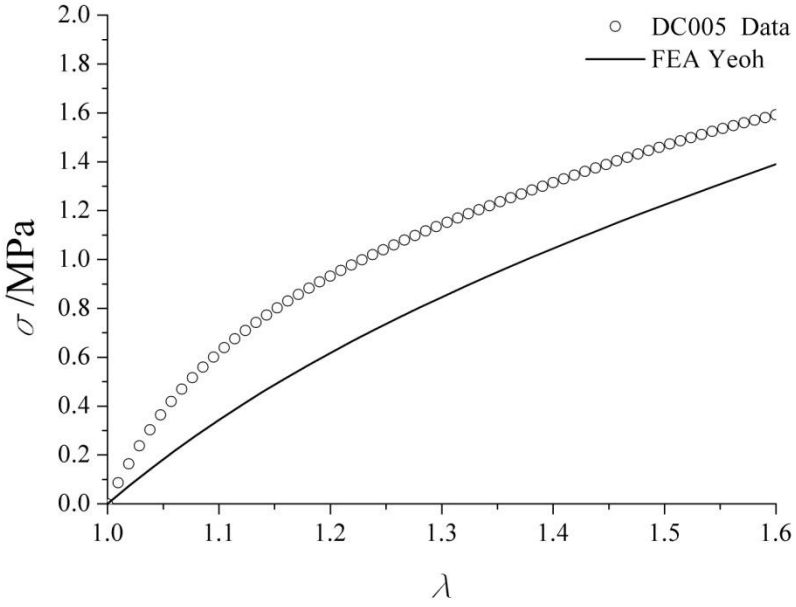

Figure 3-23. Comparison of FEA results and experimental data in pure shear for DC005.

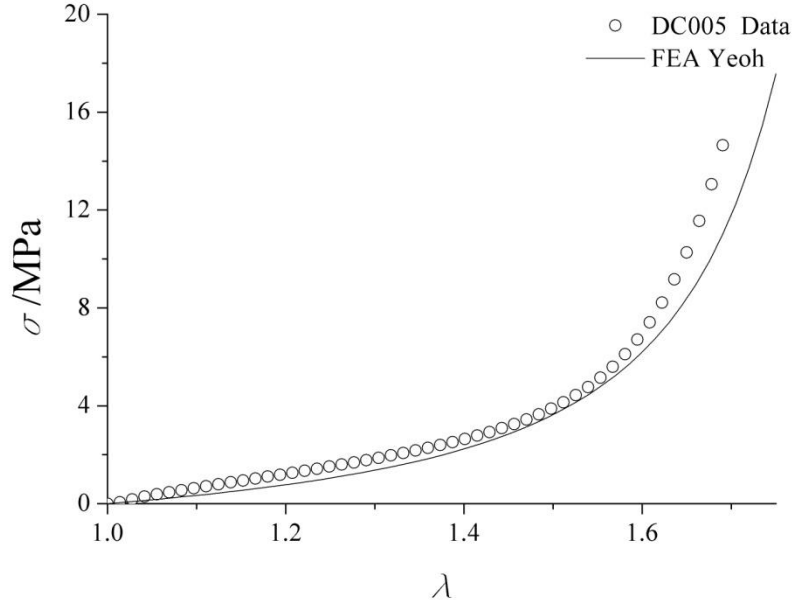

Figure 3-24. Comparison of FEA results and experimental data in compression for DC005.

3-8. **Summary**

The fatigue crack growth behaviour of rubber compounds is characterised later in this thesis using the pure shear crack growth test specimen. It offers the benefit that the loading is relatively simple to analyse and that the displacement required to reach high values of tearing energy are relatively small. This means that a high level of accuracy and precision using existing instrumentation available in the laboratory was possible compared to other crack growth geometries described in Chapter 2. Moreover, the crack growth can be monitored using a camera facing the sample which increases the number of points acquired to calculate the crack growth rate while avoiding complications in these calculations due to cycling stress softening encountered with other geometries. Equation (3-12) has been chosen over equation (3-11) as it relates the tearing energy to the force displacement curve of the current test and therefore significantly simplifies the experimental arrangement and number of tests necessary to obtain the tearing energy. This also reduces the experimental error by removing errors related to cyclic stress softening in the tearing energy calculations.

However, the pure shear crack growth specimen might show some limitations when the load is maintained for a long period such as in static crack growth experiment (see Chapter 4). The tearing energy being calculated with the loading force-displacement curve, it masks the viscoelastic effects such as stress softening in a specimen subjected to a constant displacement. Another geometry such as the trouser test piece might be more suitable for prolonged steady crack growth tests.

The peeling specimen has been widely used to test interfaces between soft materials but presents limitations when the adhesion between the two sides of the interface is high. The crack indeed tears through the arms of the specimen. A modification of the test is proposed to test stronger interface later in this chapter. The calculation of the peeling energy will be shown to be only slightly modified to reflect the modification of geometry.

Strain energy functions described in chapter 2 are shown to fit experimental data in different modes of loading and can therefore be implemented into commercial software Abaqus to evaluate the tearing energy in real components. Overall the Mooney-Rivlin and Yeoh SEFs present good correlation with the experimental data for the materials considered in this thesis. The use of these SEFs also limits the number of tests to be

carried out to determine the coefficients of the SEF as a single tension test is sufficient to derive them. For other SEFs, it would be necessary to gather biaxial tensile data.

CHAPTER 4 -FATIGUE OF NON STRAIN CRYSTALLISING ELASTOMERS

4-1. **Introduction**

In Chapter 2, the fatigue crack growth behaviour of rubbers is described including the identification of the key parameters. The tearing energy concept proposed by Rivlin and Thomas (1953) has been extended to describe the behaviour of rubbers under cyclic fatigue type of loading. The relationship between the maximum tearing energy T_m reached during a loading cycle and the crack growth rate per cycle dc/dN is material characteristic which is independent of the specimen geometry (Lake and Lindley (1964b)). The crack growth rate per cycle in the purely mechanical damage region of the fatigue behaviour may be related to the maximum tearing energy by adopting a simple power law relationship.

$$\frac{\mathrm{d}c}{\mathrm{d}N} = BT_m{}^{\beta} \tag{4-1}$$

where B and β are material characteristics. The value of β ranges from 2 to 6 for most rubbery materials, depending mainly on the nature of the polymer and the value is seen to be also affected by the crosslink density and the type of crosslink. As the crack growth of rubbery material is mainly governed by the energy dissipation phenomena at the crack tip, β is also known to depend upon the material hysteresis and any strain induced crystallisation the material might exhibit.

Cracks propagating in tyres may be subjected to extreme conditions in terms of the rate of loading. The effect on the fatigue properties of the loading frequency or the strain rate has been studied by many researchers previously. It is widely accepted that the variation of the crack growth resistance of strain crystallising rubbers with rate and frequency is small. This is attributed to the rapid development of crystals at the tip of the crack early in each loading cycle that quickly blocks fatigue crack propagation. This

assertion is corroborated by the significant decrease in fatigue crack growth rate when the load is not completely removed at the minimum of the loading cycle preventing the melting of the crystals at the crack tip. The most dramatic variations in the resistance to crack growth in strain crystallising materials are therefore often related to processes that affect the rate and extent of crystallisation at the crack tip.

Conversely, non-strain crystallising materials exhibit significant time dependence fatigue crack growth behavior with variations of several orders of magnitude in tearing rate with a change of frequency. Considering just the region of the tyre containing a potential physical crack then the time frame for this cracked region to pass say through the contact patch in order to undergo a complete loading cycle might be very short indeed. This is much shorter than the already rapid rotation period for the tyre when a vehicle is travelling at high speed. This short time frame results in relatively high rates of loading at a high frequency for any cracks present in the rubber. In the present chapter, an attempt is made to understand the origin of this fatigue behaviour.

4-2. **Frequency effect on the fatigue behaviour of SBR**

4-2-1. Evolution of fatigue behaviour with frequency

The fatigue behaviour of an unfilled SBR was measured using the pure shear test geometry. The experimental setup and approach to calculate the tearing energy (equation (3-12)) are described in Section 3-4-1. The frequency of the sinusoidal loading ranged from 0.01 Hz to 10 Hz. Figure 4-1 shows the relationship between crack growth and the maximum tearing energy achieved during one cycle for each frequency. The solid lines illustrate the power law relationship fitted to the experimental fatigue behaviours at each frequency. The materials characteristics B and β obtained are given in Table 4-1 for each frequency.

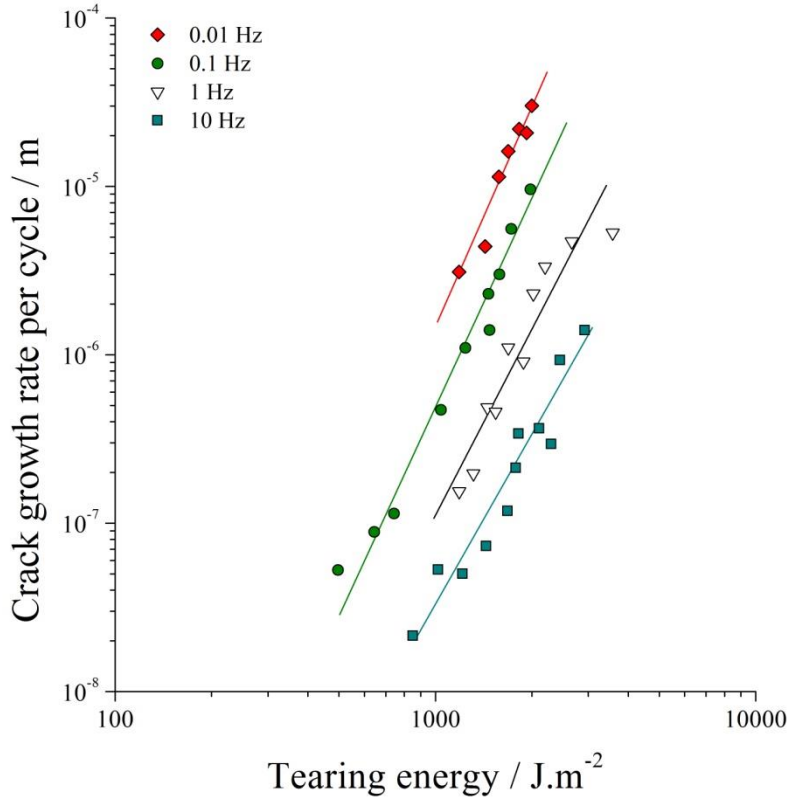

Figure 4-1. Fatigue behaviour of SBR0 subjected to frequencies ranging from 0.01 to 10 Hz.

Frequency /Hz	**log(*B*)**	***β***
0.01	-19.5	4.54
0.1	-18.28	3.86
1	-17.64	3.56
10	-17.29	3.27

Table 4-1. Characteristics B and β of SBR0 at different frequencies.

Clearly a significant frequency effect was observed and the variation of the crack growth rate per cycle between the different frequencies was found to be less than the change expected for a totally time dependent behaviour. In that case, the variation of crack growth rate would be proportional to the variation of the inverse of the fatigue test frequency at any given maximum tearing energy. Moreover β would be constant over

the range of frequency and B would scale with the inverse of the frequency being divided by 10 as the frequency is multiplied by 10. Here, the crack growth rate was only multiplied by a factor of 5 to 8 while the frequency decreased by an order of magnitude.

4-2-2. Theoretical time dependent contribution

Lake and Lindley (1964b) observed that at low frequencies (less than 0.2 Hz), the crack growth rate per cycle at a given tearing energy was proportional to the inverse of the frequency and concluded that the behaviour was therefore entirely time dependent. It was later suggested the fatigue growth was the sum of a time dependent and a cyclic contribution (equation (4-2)). The former would only depend on the length of time the material was subjected to loading and the maximum tearing energy T_m. The latter reflects the additional crack growth the loading and unloading cycle causes.

$$\left(\frac{dc}{dN}\right)_{total} = \left(\frac{dc}{dN}\right)_{time} + \left(\frac{dc}{dN}\right)_{cycle} \tag{4-2}$$

Busfield et al. (2002) proposed an experimental approach to evaluate both contributions. The time dependent component can be evaluated using a static steady state crack growth test at constant tearing energy. The crack growth rate was evaluated over a wide range of tearing energy values which were maintained constant over each experiment. Therefore the crack growth obtained is only due to the length of time the load is applied and is hence purely time dependent. A linear logarithmic relationship is found between the steady state crack growth rate and the tearing energy as shown in Figure 2-28. Therefore, a power law relationship can be fitted to the curve in both the slow and fast crack growth regions.

$$r = B_s T^{\beta_s} \tag{4-3}$$

where B_s and β_s are static crack growth constants depending on the material used.

Using the relationship between the tearing energy and the forces and strains away from the crack for typical crack growth geometries (equations (2-53) to (2-57)), the tearing energy over one cycle can be calculated as a function of time as shown in Figure 4-2.

$$T = f(t) \tag{4-4}$$

Combining equations (4-3) and (4-4) it is possible to deduce the rate of crack growth at each point throughout a single fatigue cycle resulting from the time dependent contribution alone. Integration of the crack growth rate over the length of time of one cycle equal to the inverse of the frequency yields the time dependent contribution to the fatigue behaviour. The cyclic contribution can then be deduced as the difference between the experimental data and the calculated time dependent contribution.

$$\left(\frac{\mathrm{d}c}{\mathrm{d}N}\right)_{\text{time}} = \int_0^{1/f} B_s T^{\beta_s} \mathrm{d}t \tag{4-5}$$

$$\left(\frac{\mathrm{d}c}{\mathrm{d}N}\right)_{\text{cycle}} = \left(\frac{\mathrm{d}c}{\mathrm{d}N}\right)_{\text{total}} - \left(\frac{\mathrm{d}c}{\mathrm{d}N}\right)_{\text{time}} \tag{4-6}$$

4-2-3. Static crack growth

A simple setup (Figure 4-3) was used to determine the crack growth rate under constant tearing energy for SBR0. The trousers tear test specimens (Figure 2-12a) were cut from cured 2mm thick rubber sheets. Dimensions were 50mm in length by 30mm in width. A crack was introduced with a razor blade and the crack initiated manually to remove the initial artificially rapid crack growth that arises due to the initial sharpness of the crack tip in such circumstances. The resulting crack tip is then much closer to the steady state crack tip radius encountered during tearing. The initial length of the crack was about 25mm so that even when a relatively small load was applied, a region of the legs was in tension to ensure sensible calculation of the tearing energy.

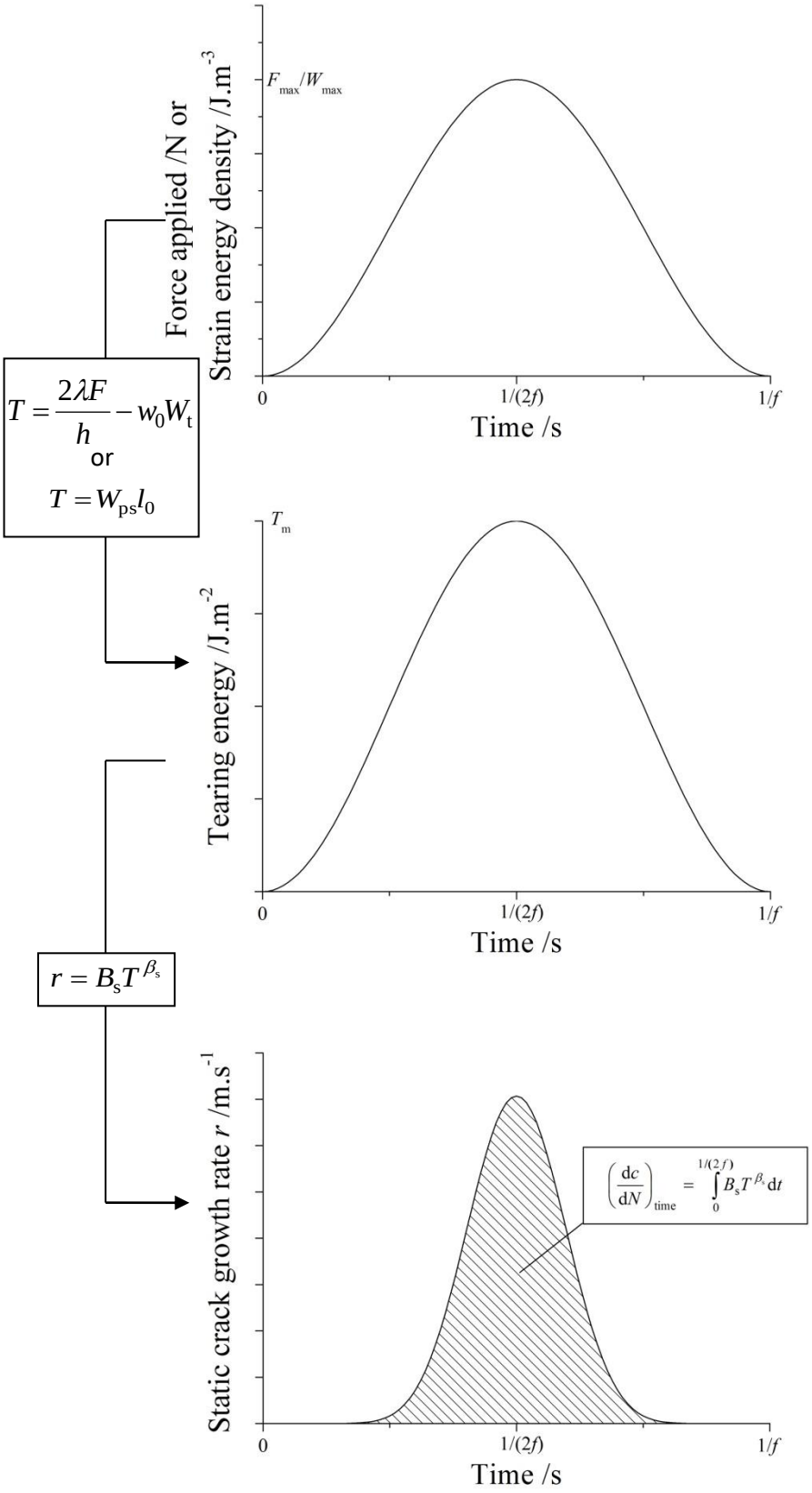

Figure 4-2. Calculation of the time dependent contribution to fatigue crack growth based on static crack growth behaviour.

Marks were regularly and carefully made on the crack tip to help identify specific crack growth rate post fracture avoiding any deformation of the samples capable of altering the results in order to monitor the crack growth rate. When significant crack growth was achieved or when the specimen was fully torn apart, the crack growth rate was determined by the ratio of the length of the crack growth in a specified time taken as measured using a stop watch.

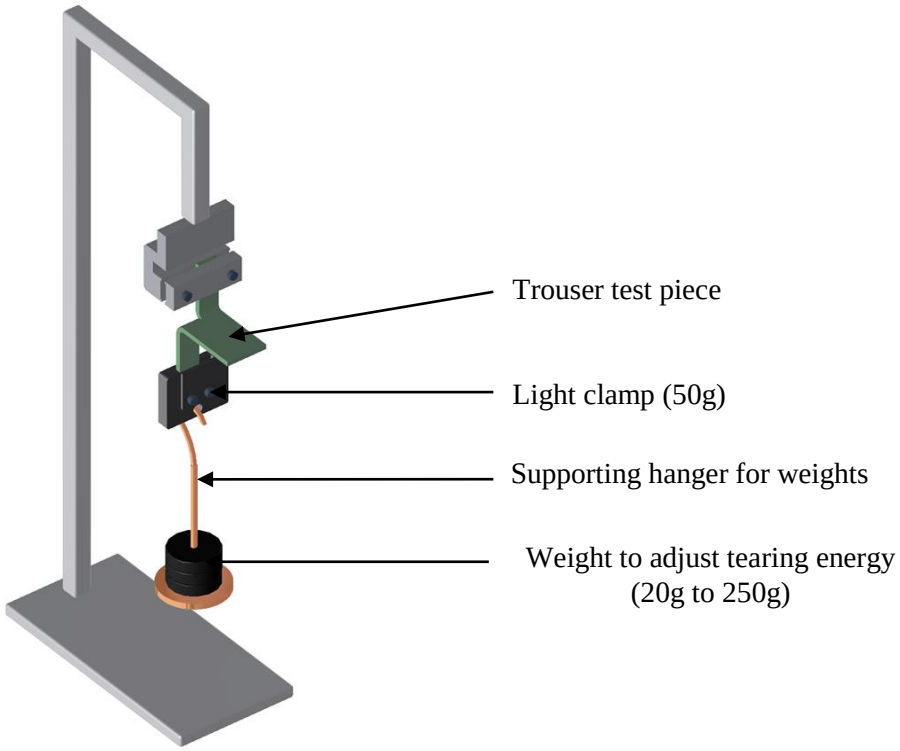

Figure 4-3. Static crack growth setup.

For faster crack growth rates where the crack growth occurred over a very short period of time, pure shear crack growth test specimens were used as they present a greater length for the crack to grow. Crack free samples were extended to a determined prestrain value to achieve a defined tearing energy and a notch was cut at one edge. The crack propagation was recorded using a high speed camera with a known high speed frame rate which was used to calculate the crack growth rate.

The fracture tearing energy is commonly plotted against the crack growth rate (Rivlin and Thomas (1953), Greensmith (1960), Lake (1995),Tsunoda et al. (2000)). In this study, the rate was plotted versus the tearing energy to obtain the required relationship in equation (4-3). The three regions of crack growth mentioned in Section 2-2-3 were observed. Slow and fast crack growth regions were fitted with a power law relationship

to calculate the materials parameter B_{static} and β_{static} for SBR0. Coefficients for both regions are given in Table 4-2.

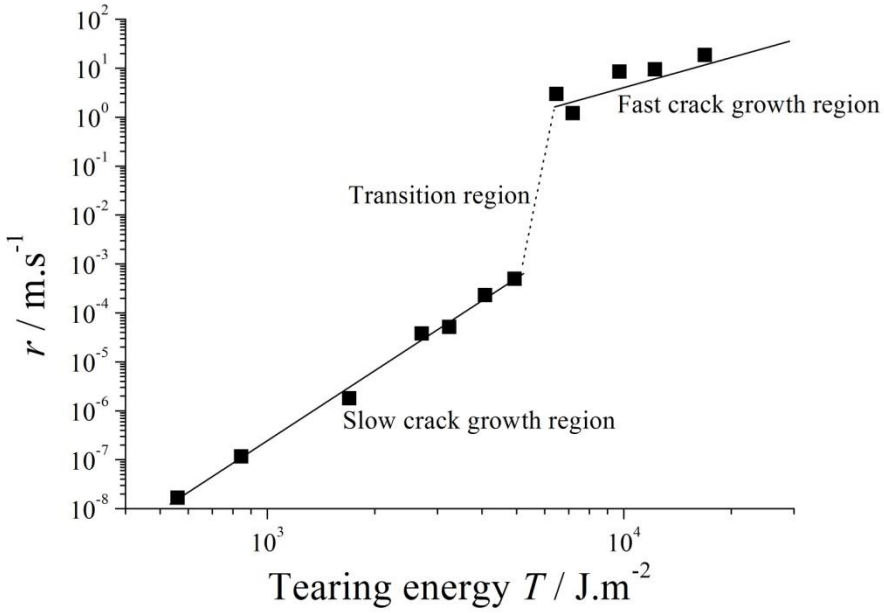

Figure 4-4. Crack growth rate versus tearing energy graph with the different regions of crack growth.

	log(B_s)	**β_s**
Slow region	-20.97	4.78
Fast region	-9.05	2.45

Table 4-2. Coefficients of static crack growth for SBR0.

4-2-4. Time dependent and cyclic contributions for SBR0

Based on the approach described earlier, the time dependent contribution to the total crack growth rate was calculated using the force versus displacement tests for a single cycle at each frequency. The range of tearing energy applied to the pure shear tests specimen remained in the slow crack growth region shown in Figure 4-4 therefore B_s and β_s were assumed to be constant and equal to $10^{-20.97}$ and 4.78 respectively. The time dependent component is represented as dashed line for each frequency in Figure 4-5. At low frequency, it tended to approach the total crack growth per cycle at the higher tearing energies and was also seen to contribute significantly over the entire range of

tearing energy tested. At 0.01 Hz, the calculated time dependent component slightly exceeded the value of the crack growth rate per cycle measured experimentally. The trend and the order of magnitude of the time dependent component were however very similar to the values measured under fatigue cyclic loading. This suggests that over the range of tearing energies tested at 0.01 Hz, the fatigue behaviour of SBR0 may be entirely described by the time dependent component. When the frequency was increased, the time dependent contribution clearly failed to account for the entire fatigue crack growth rate. The additional contribution due to cyclic loading became increasingly dominant and it was this cyclic component that contributed the most to the crack growth particularly at small tearing energy values.

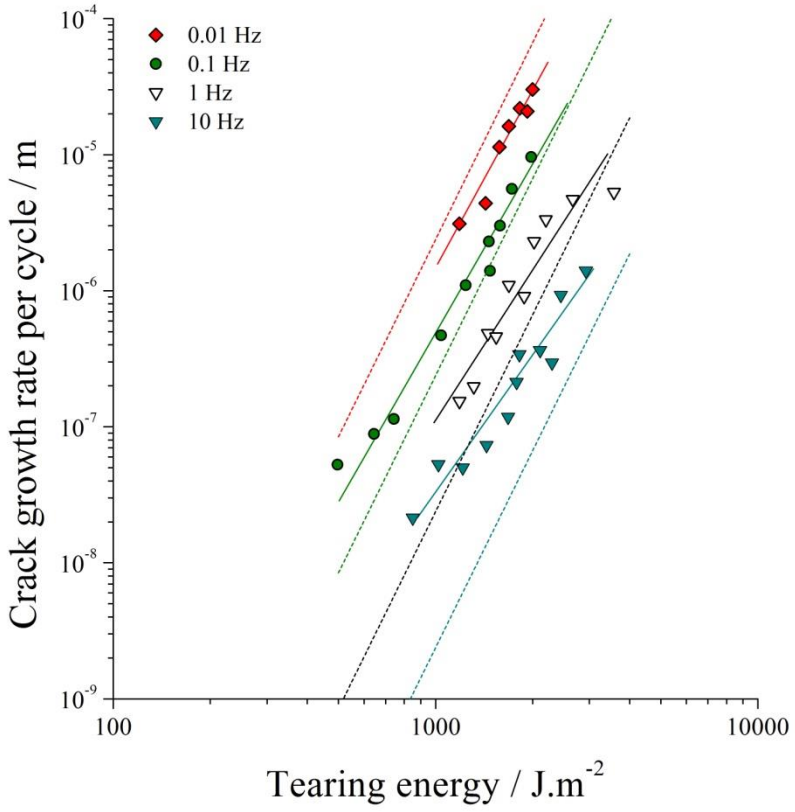

Figure 4-5. Time dependent contribution to the crack growth in fatigue for SBR0. Time dependent contributions are represented as dashed lines.

The cyclic contributions were calculated from equation (4-6) and are shown along with the time dependent contribution for 0.1 Hz and 10 Hz in Figure 4-6. The cyclic contribution accounted for most of the crack growth at 10 Hz while at 0.1 Hz it remained significant and approximately equal to the time dependent contribution for the

lowest tearing energy tested. Clearly the time dependent component to fatigue crack growth plays a significant role in the behaviour at low frequency and high tearing energy while the cyclic contribution completely dominates at higher frequencies and lower tearing energy. It is also worth noting that the magnitude of both contributions increases with the tearing energy and decreasing frequency. One may expect the cyclic component not to depend on the length of time of a cycle but only on the magnitude of the loading applied.

The total crack growth per cycle being taken as the sum of the two contributions:

- The behaviour is dominated by the time dependent contribution at low frequency and high tearing energy.
- The behaviour is dominated by the additional cyclic component at high frequency and low tearing energy.
- The cyclic component nonetheless increases with tearing energy and with the inverse of the frequency.

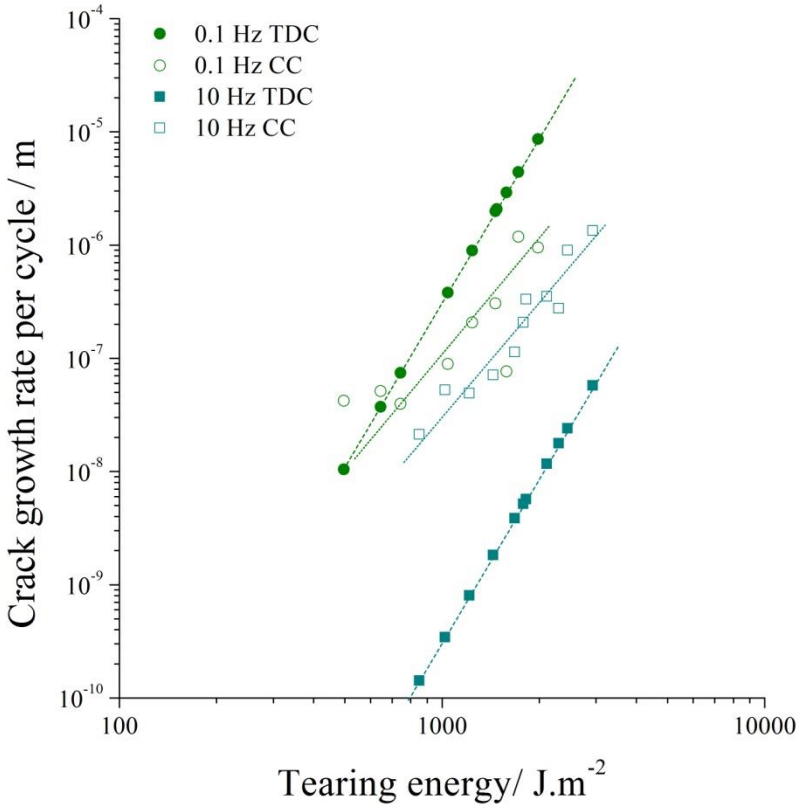

Figure 4-6. Time dependent (TDC) and cyclic components (CC) of the fatigue behaviour at 0.1 and 10 Hz.

The mechanism at the origin of the additional cyclic component remains unclear. Why does the cyclic contribution dominate the fatigue behaviour at low values of the tearing energy and high frequency while the behaviour is completely time dependent at large values of T_m and low frequency? Clearly this additional damage results from the unloading as for low values of the tearing energy and high frequency, the crack growth rate per cycle is only due to repeated loading and unloading the rubber is subjected to. The evolution of the cyclic component with the tearing energy suggests a mechanism occurring in the highly strained region of the crack tip when the rubber is subjected to a load which weakens the material locally under cyclic loading when compared to static crack growth. A reinforcement phenomenon might be activated during the static crack growth. Under cycling loading, the process would have sufficient time to develop at low frequency causing the crack to grow at the same rate as under static loading. Conversely, this process would not have time to occur at higher frequency and therefore additional crack growth would occur. It may also be the result of a progressive

weakening of the material in the region of the crack tip due to repeated loading. The rubber in the region of the crack being loaded only once in static crack growth may be more tear resistant than its counterpart in the fatigue specimen. This additional strength would result in a faster crack growth in the fatigue tests than predicted with the results of the static experiments.

4-3.**Effect of the type of waveform**

Clearly, the evolution of the fatigue behaviour with frequency is not entirely accounted for by the time dependent component. It appears that the material characteristics B and β depend on the nature of the polymer and some phenomena occurring at the crack tip which are influenced by the way the maximum tearing is reached during cyclic loading. The variation of the cyclic component with frequency suggests that using the static crack growth rate as a direct measure of the time dependent contribution might be inaccurate and might require an adjustment based on the history of the loading. Additional waveforms were therefore used to observe how the loading history affects the fatigue behaviour and how calculations based on the static crack growth account for the variations.

4-3-1. Waveforms used

Four different shapes of signal were used to characterise the fatigue behaviour of SBR0 and are shown on Figure 4-7. The waveforms were chosen to have a significant effect on the time dependent contribution while changing the path taken to achieve maximum tearing energy. The powerlaw relationship used to calculate the rate of crack growth during one cycle magnifies the influence of high tearing energies. Therefore, introducing plateau should clearly increase the crack growth rate per cycle when the behaviour is dominated by the time dependent component. The different path to the maximum tearing energy in terms of rate and shape may also play a role in the total and cyclic crack growth by affecting the rubber present in the region of the crack tip. The machine used being limited in terms of celerity; the tests were performed at frequencies ranging from 0.01 to 1 Hz.

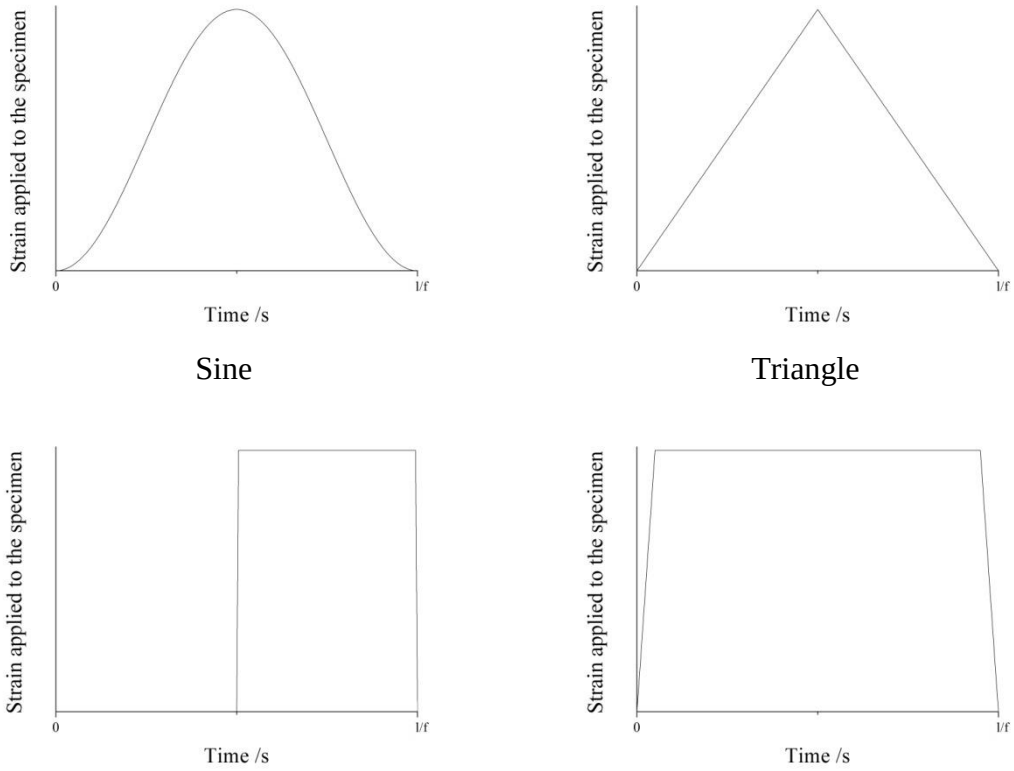

Figure 4-7. Waveforms used to characterise the fatigue behaviour of SBR0.

4-3-2. Effect of frequency with different waveforms

The time dependent component of the crack growth per cycle was calculated using the same method as in Section 4-3-1. The results are shown on Figures 4-8 to 4-10 for the different signal shapes used. The dashed lines represent the time dependent contribution for each loading configuration.

Triangle

The fatigue behaviour shown in Figure 4-8 is very similar to the results obtained with the sinusoidal waveform. Clearly, time dependency is not sufficient to describe the fatigue behaviour when the frequency is increased. At high tearing energy and low frequency, the behaviour is dominated by the time dependent contribution whilst the cyclic component plays a significant role at higher frequency and low tearing energy.

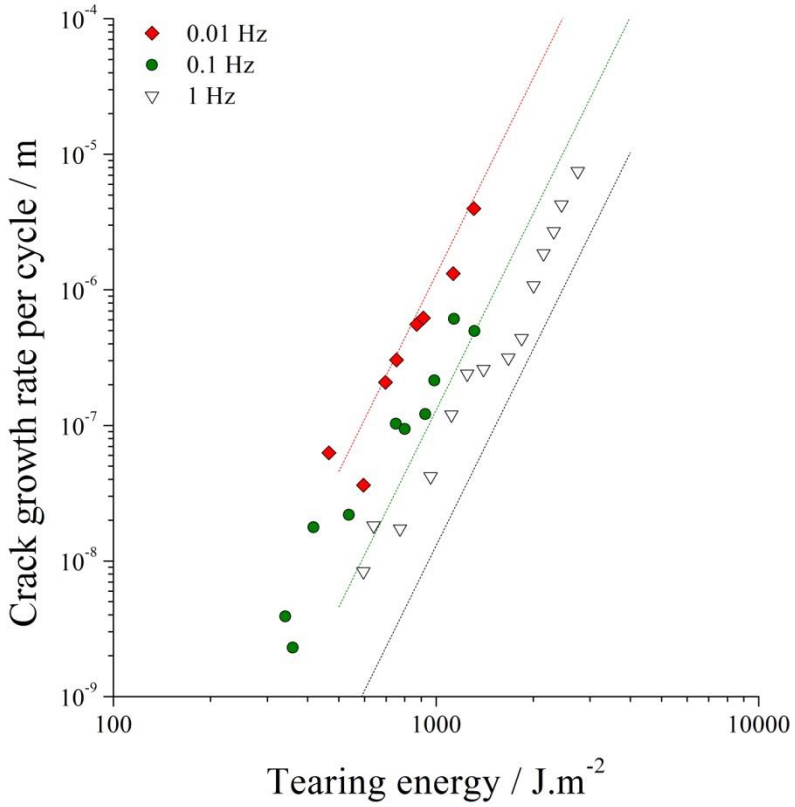

Figure 4-8. Triangle waveform

Square signal

The results for the square shaped signals are shown on Figure 4-9. It can be seen the behaviour approaches a purely time dependent as the crack growth rate per cycle scales with the inverse of the frequency.

With regards to time dependent and cyclic contributions based on the static crack growth, the total crack growth behaviour is mainly due to the time dependent contribution over the range of frequency and tearing energy tested. As the frequency increases, the range of tearing energy where this assertion is valid broadens. The cyclic contribution to the crack growth remains small over the range of frequencies and tearing energy tested. By definition, the square signal is similar to a static crack growth where rest periods are imposed to the specimen, static crack growth being virtually a square cycle with an infinitely small frequency. In this case the rubber is loaded and unloaded so fast that the time dependent contribution to the crack growth occurring during loading and unloading is very small and most of it is due to the fact the rubber is

maintained at a constant maximum tearing energy just as in the static crack growth experiments. In this case, the cyclic contribution appears to be smaller and the rubber fatigue crack growth resistance almost obeys a purely time dependent behaviour predicted by the static crack growth.

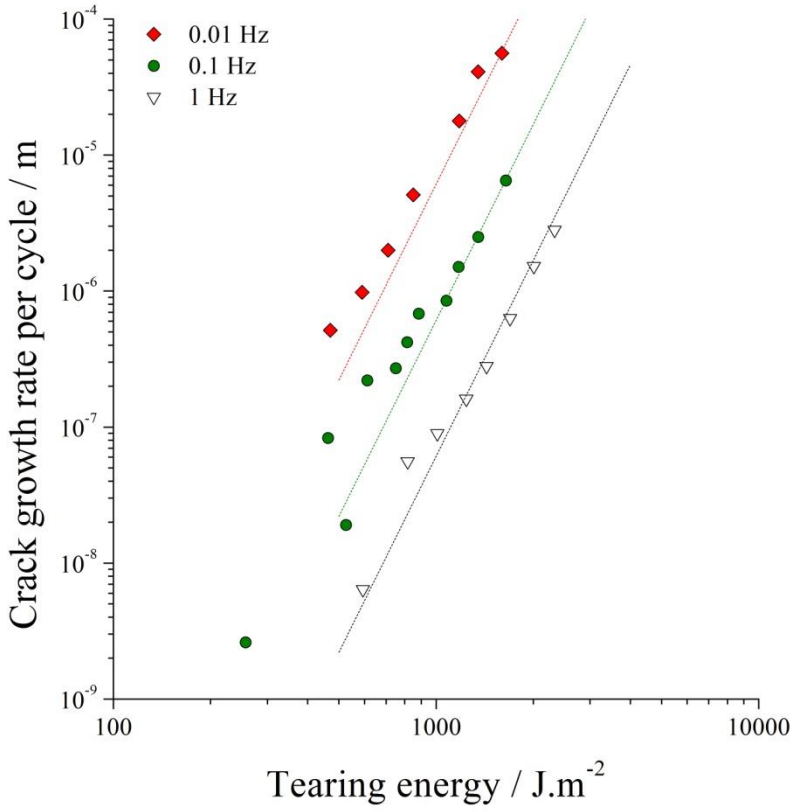

Figure 4-9. Square waveform.

Trapezoidal waveform

The results obtained using the trapezoidal waveform are shown on Figure 4-10. It appears the behaviour approaches a pure time dependent behaviour. The slopes of the curves at different frequencies are similar and a factor 10 relates the crack growth rate per cycle at the same tearing energy.

However, when both contributions are calculated based on the static crack growth rate, the cyclic contribution is significant over a large range of tearing energies. This range appears narrower as the frequency increases similarly to results obtained with the square waveform. The duration to load or unload the rubber is only $1/10^{th}$ of the period of the waveform and therefore small compared to the time the rubber is subjected to the

maximum loading. The additional cyclic contribution however represents a significant part of the crack growth.

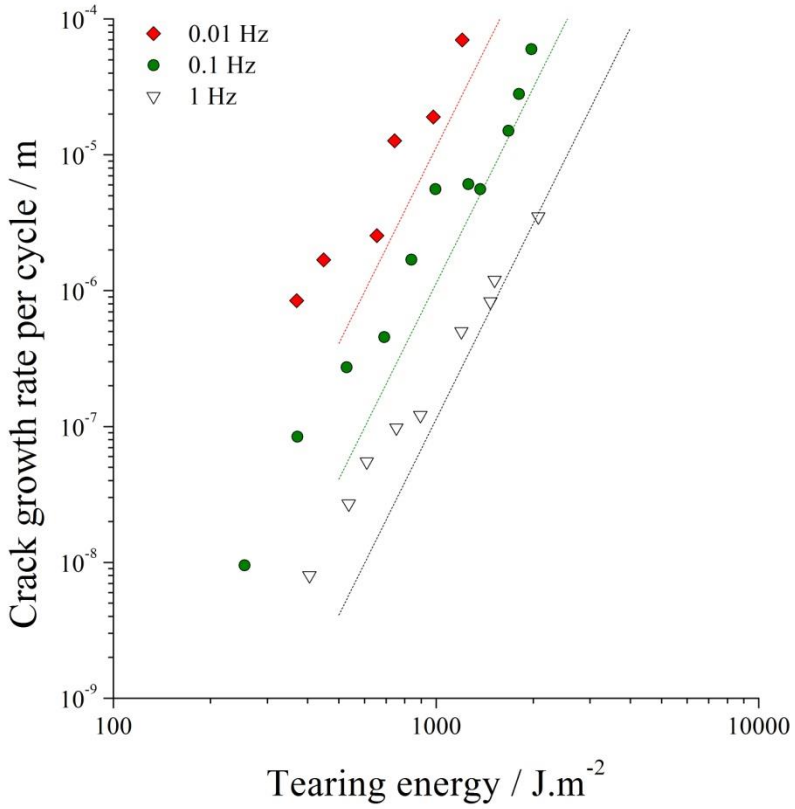

Figure 4-10. Trapezoidal waveform.

The observations made with the sinusoidal loading are also valid for the triangle waveform. The fatigue behaviour can not be only described by time dependence. The fatigue crack growth gets closer to a purely time dependent behaviour when the waveform includes a plateau at the maximum tearing energy even though calculations show the cyclic component exists and contributes significantly to the behaviour. This observation combined with the frequency dependence of the cyclic contribution suggests the approach to calculate the time dependent contribution might leave out some phenomena influencing the crack growth. It appears that taking the static crack growth behaviour and ignoring the loading conditions does not predict fully the time dependent contribution to the crack growth.

4-3-3.Comparison of the different waveforms

Figure 4-11 to 4-13 show the behaviour of SBR0 subjected to the four waveforms at different frequencies. The relationship between crack growth rate per cycle and maximum tearing energy is represented as solid lines on the figures. At 0.01 Hz, the square and trapezoidal waveforms clearly result in a much higher total crack growth. The presence of a plateau at T_m in these waveforms clearly affects the behaviour significantly allowing more time for the crack growth at the maximum tearing energy. The slopes of the curves at 0.01 Hz are similar which indicates the material parameter β is nearly unchanged by the modification of the waveform. These observations suggests that at this frequency, the time dependent component accounts for most of the total crack growth rate per cycle and masks the effect of a potential cyclic crack growth. The approach using the static crack growth rate (shown in Figure 4-14 for 0.01 Hz) predicts the variation of the behaviour between the waveforms although the magnitude of the change between the different waveform is clearly underestimated and the characteristic β higher than the real values.

As the frequency increases the influence of the plateau at high tearing energy diminishes. At 0.1 Hz, the time dependence remains significant although the difference between the waveforms is less marked and approaches what can be expected from the static crack growth approach. At 1 Hz, the time dependence is not observed except for the trapezoidal waveform which results in a slightly higher crack growth rate per cycle at the same maximum tearing energy. At this frequency, the crack growth is mainly governed by the maximum energy achieved during one cycle and not the shape of the signal.

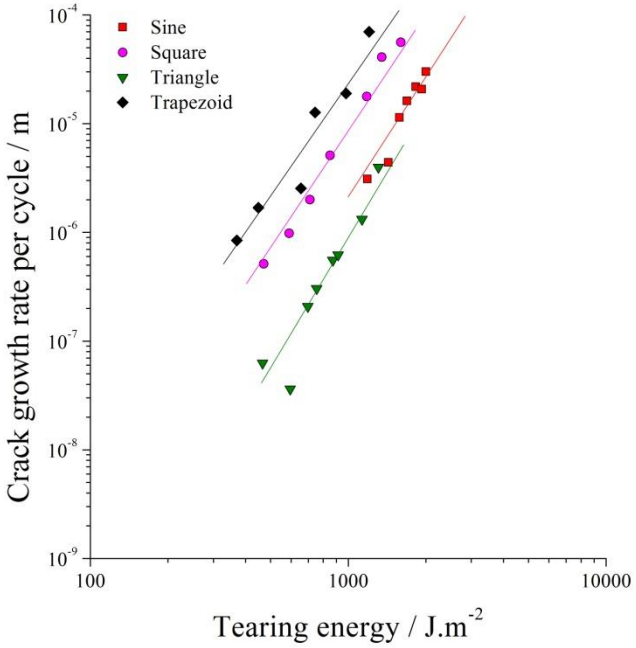

Figure 4-11. The fatigue behaviour of SBR0 subjected to various waveforms at 0.01Hz.

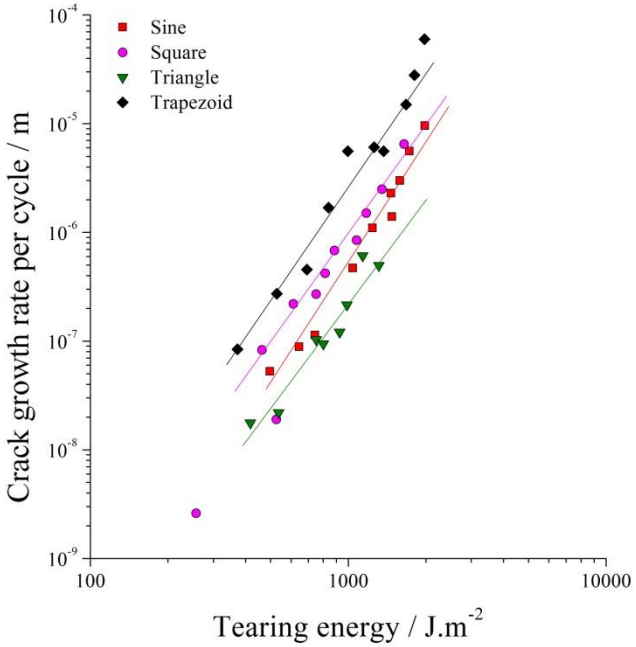

Figure 4-12. The fatigue behaviour of SBR0 subjected to various waveforms at 0.1Hz.

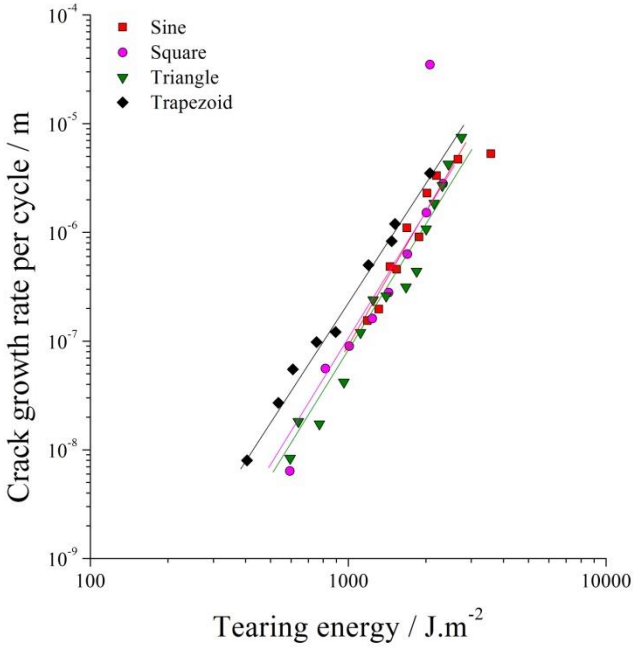

Figure 4-13. The fatigue behaviour of SBR0 subjected to various waveforms at 1Hz.

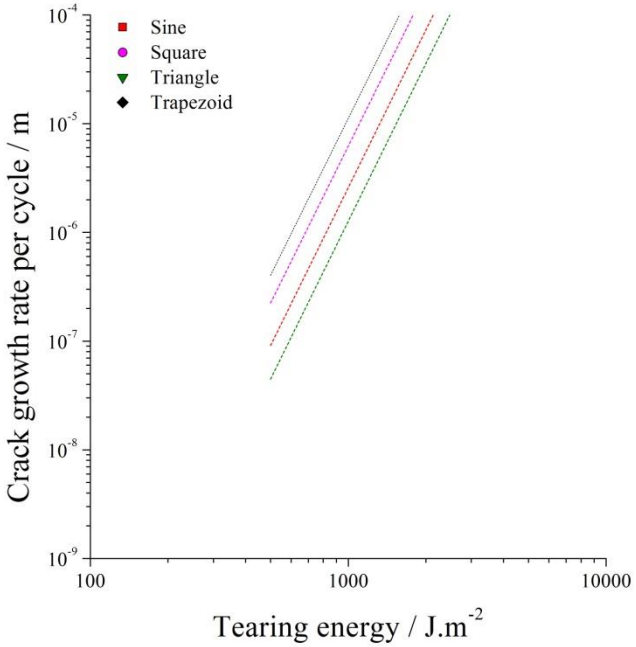

Figure 4-14. Time dependent contribution predicted with static steady crack growth for 0.01 Hz.

4-4. **Summary of the results and discussion**

4-4-1. Conclusions

When SBR0 is subjected to increasing frequencies, the material does not behave as a purely time dependent material. An additional component contributes to the crack growth and originates in the cyclic loading of the material. The magnitude of this additional contribution is affected by the maximum tearing energy and the frequency. The frequency dependence may indicate that the cyclic component is somehow also "time dependent".

The application of a long period of time at the maximum tearing energy results in an apparent time dependent crack growth behaviour that cannot however be completely predicted using the steady state crack growth measured under static loading component alone, the resulting prediction being less than the actual crack growth rate.

The application of different waveforms to an unfilled material leads to a variation in the fatigue crack growth behaviours conforming with the time dependence imposed by the signal shape although the ratios between the results with the various waveforms do not fit the expected theoretical values based on the steady state static crack growth behaviour.

The characteristic β, given by the slope of the crack growth versus T_m, for the sine and the triangle waveform changes with frequency and tends towards the static steady state crack growth β_s value when the frequency decreases. The value of β for the square and trapezoidal waveforms remains constant with frequency although it is not equal to β_s.

At frequency exceeding 1 Hz, the behaviour is still affected by the frequency but also shows less dependence on the length of time the rubber is subjected to the maximum load during one cycle.

4-4-2. Prediction based on static crack growth

The observations made in the last section suggest the effect of the frequency on the fatigue behaviour of SBR0 obeys an apparent time dependence amplified by a factor f_{cyclic} due to the cyclic loading and which depends on the tearing energy applied instantly rather than a constant additional component independent of the frequency and only influenced by the change in the maximum tearing energy achieved during the

cycle. The cyclic component appears to create a higher crack growth rate at any time of the cycle than expected from the steady state crack growth. At low tearing energy f_{cyclic} may have high values leading to a much higher crack growth than expected from the approach based on the static crack growth experiment. At high tearing energy f_{cyclic} decreases and the total crack growth is approximately equal to the theoretical values for the time dependent component expected from the static crack growth. The effect of such a factor on the rate of crack growth at any time during a cycle is shown in Figure 4-15 for the different waveforms used. The total crack growth per cycle obtained would be the sum of both the static crack growth base time dependent contribution and the additional crack growth induced by f_{cyclic}.

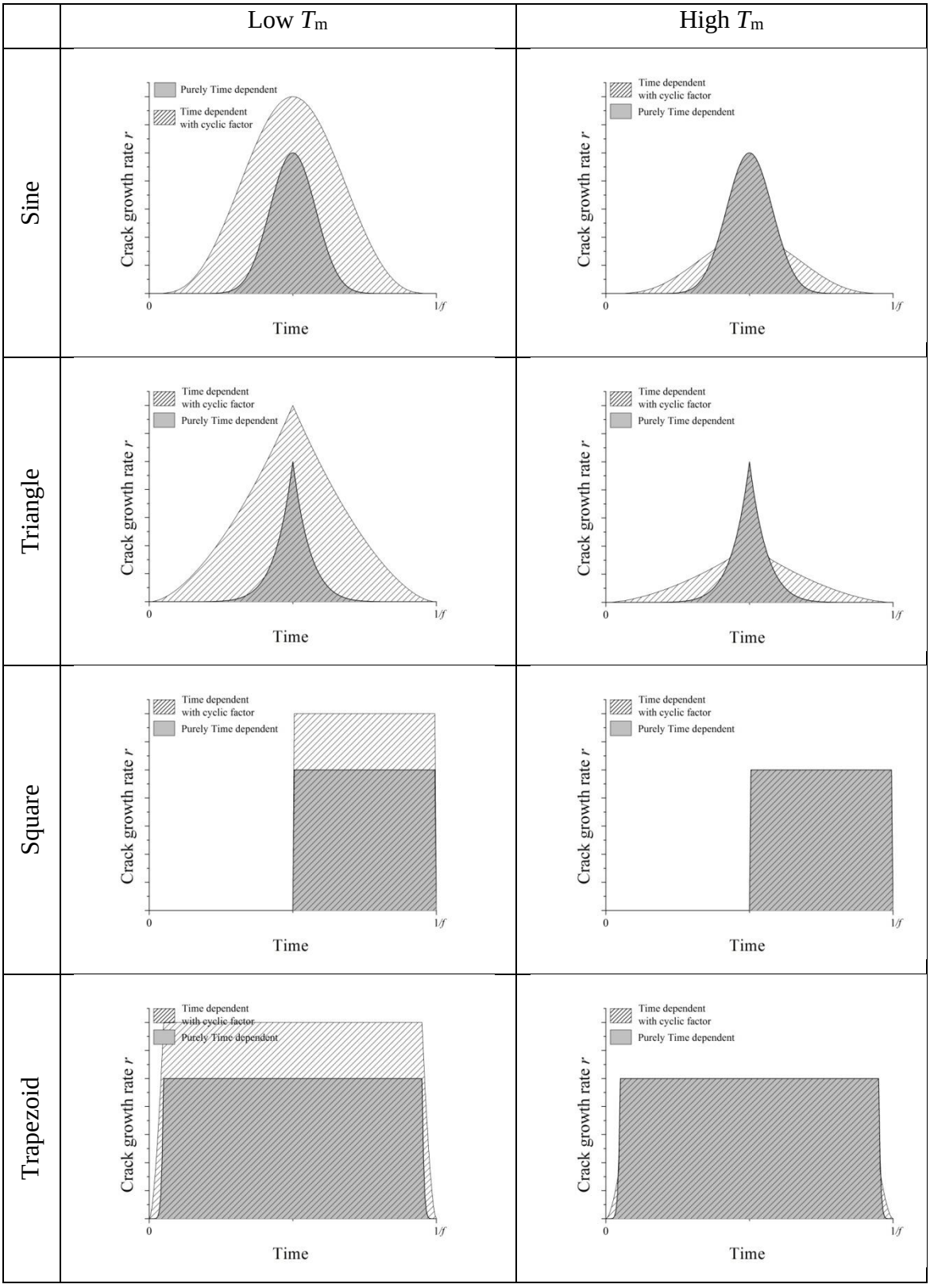

Figure 4-15. The effect of a tearing energy dependent cyclic factor on the total crack growth rate per cycle for the different waveforms. The total crack growth rate per cycle is equal to the area under the curve.

4-4-3. Possible origins and phenomena affecting the cyclic contribution

Progressive damage to the polymer chains ahead of the crack tip

The loading of the rubber ahead of the crack tip in the static test is monotonic and therefore the polymer chains are only loaded once until complete fracture. Conversely the polymer chains network at the crack tip in the fatigue tests are loaded many times before being separated or broken down. The loading may cause breakage of molecular bonds in the polymer network ahead of the crack tip. Upon unloading, the polymer chains may have time to reorganise. This repeated loading and unloading of the rubber at the crack tip might have two effects. First the rubber in the direct vicinity of the crack tip might be weakened by the previous cycles and the breakage of some chains. Second, the reorganisation of the rubber chains might lead to the possibility of further damage to the chains even if the load is maintained constant. The cyclic contribution factor f_{cyclic} would therefore be a consequence of this progressive damage of the chains ahead of the crack tip. It may take the form of a damage function and be introduced in an equation similar to equation (4-5) to calculate the total crack growth per cycle directly.

The variation in the contribution of the cyclic component with frequency may result from the fact that many more cycles are required to reach a particular crack growth length and therefore the rubber in the high strain region is also loaded many times more than their counterpart at lower frequency before being broken apart. The more numerous loadings would result in a higher damage in the rubber at the crack tip.

Permanent deformation at crack tip

Although the bulk material exhibits highly elastic behaviour at relatively small maximum strain and various frequencies, the high deformation experienced by the rubber at the crack tip under loading might create a permanent strain upon unloading. This permanent strain might contribute to the additional crack growth the rubber is subjected to during cyclic loading. Similar to the last paragraph this permanent strain contribution would multiply the time dependent contribution especially in the early and late stage of the cycle. Higher tearing energy would lead to a higher permanent strain as the rubber is being deformed further and therefore would lead to an increase in the cyclic contribution. Similarly to the previous paragraph, higher frequency would mean lower time for the crack to grow although the contribution to the behaviour gets higher because of the higher permanent strain being generated. Relaxation of the strain in the

vicinity of the crack may also play a role in the additional contribution as the relaxation of this permanent strain would diminish the magnitude of the cyclic contribution.

Remarks on loading rate

When the tearing energy during the cycle was calculated with equation (4-2), it was implicitly assumed the rate of loading at the crack tip for all the frequencies and tearing energies was equal to the rate of loading during the static experiments. This assumption originates in the consideration of the maximum tearing energy achieved during one cycle as the governing parameter for the fatigue crack growth. The path to the maximum tearing energy is not considered when using this approach although the viscoelastic properties which are influenced by the rate are believed to play a significant role in the crack growth. The significantly higher rates of loading in fatigue in the region of the crack tip under cyclic loading cause higher energy dissipation in the rubber around the crack tip. The tearing energy necessary to drive the crack forward at a similar growth rate is significantly higher during the fatigue crack growth tests than during the static crack growth tests. The tearing energy calculated with equation (2-53) is the sum of this additional energy to stretch the rubber at the crack tip faster and the energy to drive the crack in the static test. The variation of T with time during one cycle in the fatigue tests should be compensated for this additional energy and only take into account the energy that drives the crack at the same loading rate than in the static tests. This would result in a decrease of the time dependent contribution compared to the values calculated in Section 4-3-1 and by extrapolation an increase in the cyclic contribution.

CHAPTER 5 -PEELING AT INTERFACES

5-1.**Introduction**

The fatigue life of a tyre can be greatly influenced by the properties of the materials it is made of. Figure 2-36 shows tyres are made of various layers bonded together either by physical or chemical interactions. The interfaces formed particularly between the different rubber layers are of potential concern when it comes to predicting the lifetime of the whole structure with cracks likely to initiate or to be driven in the interface regions. In the worst case, catastrophic failure can result from poor bonding properties or adhesion between two layers.

The strength of the interfaces between elastomers has been investigated with different approaches but mainly with unvulcanised compounds mainly because adhesion of vulcanised rubbers may arise for different and additional physical reasons. It has been observed in many studies that interdiffusion of chains has a key role for the resulting strength of interfaces between elastomers (Schach and Creton (2008),Leger and Creton (2008)). Crosslinks resulting from the vulcanisation reduce significantly the mobility of the chains, increase their molecular weight and prevent the chain to move and create covalent bonds across the interface (Gent and Tobias (1984)). Vulcanised rubbers therefore cannot develop molecular bridges across the inferface. Adhesion of crosslinked rubbers therefore relies on different processes related to friction such as deformation and hysteresis of the materials (Gent and Walker (2005)). Although the compounds in a tyre are vulcanised, the strength of the interfaces present in a tyre is mostly due to the physical phenomena occurring before and during the vulcanisation which are similar to those encountered when developing good tack.

Tack is defined as the ability of two materials to resist separation after being brought into contact under a light pressure (Hamed (1981)). Tack is evaluated with the same approach as the tearing energy with a measure of the energy released as a crack grows in the unvulcanised material. Another quantity that relates to unvulcanised material is the green strength which is the ability of an unvulcanised material to resist deformation

and fracture. Therefore, in the case of the bonding of similar compounds, the green strength can be considered as the upper limit of tack, the value at which an interface behaves as bulk the material. Both quantities have important implications in the manufacturing of a tyre. Sufficient tack is required to hold the different layers together before vulcanisation while green strength is required to prevent the tyre from deforming or failing on the racks where the uncured tyres are stocked and to avoid tearing during the first stages of moulding when the green tyre is expanded. The bonding of two surfaces is thought to be the consequence of two main factors: the interdiffusion of chains across the interface and the contact between the two layers. Green strength is also a necessary condition for high tack but is not sufficient to ensure it (Hamed (1981)).

To achieve high levels of bonding, intimate molecular contact must precede interdiffusion. Figure 5-1 shows an interface between two polymers. The scale of this schematic can be chosen from the macroscopic scale where voids are visible with the naked eye to the nanoscale where two molecules interact. On a microscale, the surfaces present a rough topography and therefore contact is only achieved in areas where the peaks and craters of the surface can meet each other. The extent of this area is controlled by the ability of the material to flow and deform under the pressure applied, to the extent of gases and impurities on the surfaces and the ability of these substances to diffuse into the bulk (Hamed (1981)).

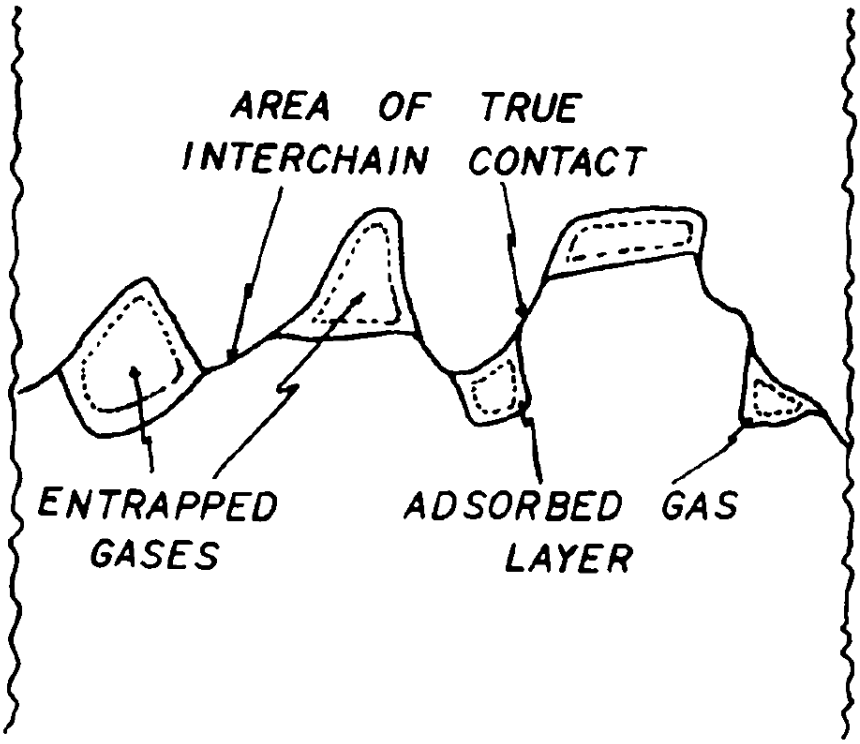

Figure 5-1. Schematic diagram of an interface between two rubbery materials showing partial contact and flaws. Taken from Hamed (1981).

The interdiffusion of the polymer chains and the formation of entanglements across the interface (Willett and Wool (1993)) occurs when two polymers above their glass transition temperature are brought into contact. In order for the chains to move across the interface, the two polymers have to be thermodynamically compatible and present a thermodynamic affinity for the mutual diffusion to be initiated. This interaction is mainly dependent on the Flory interaction parameter χ_{FH} and the degree of polymerisation of the materials brought into contact. If the two polymers are compatible then they will interdiffuse until the interface is healed and spread the stresses throughout the rubber on both sides of the interface. This healing process is dependent on the kinetics of formation of entanglements across the interface and it has been shown an interpenetration of a few entanglements would be sufficient for the interface to attain the same behaviour as the bulk properties of the elastomers (Schach et al. (2007)). The kinetics of interdiffusion have been investigated by many researchers, some of whom have been cited in Chapter 2. The molecular weight (Schach and Creton (2008)), the polymer type (Hamed and Shieh (1986), Davis et al. (2014)) have been shown to directly influence the time required for the chain to interdiffuse which has been directly related to the strength of the interface (Gent and Kim (1990), Hamed (1981)). It is also been proposed the number of chain ends might intervene in the number of chains

crossing the interface and therefore at constant molecular weight, a branched polymer would show higher tack than a linear chain molecular network (Hamed (1981)) because of the higher chain end density. Generally the contact time necessary to reach the green strength are relatively short and have been shown to be in the order of the reptation time of the molecular chains (see Figure 2-34).

Strength of the base elastomers on both sides of the interface also has an influence on tack. The same parameters as for tearing of elastomers have to be taken into account when analysing results of tack. Indeed, in the regions of the interface where intimate molecular contact has been achieved and interdiffusion has taken place, the intrinsic properties of the materials regarding resistance to tearing such as strain crystallisation or any other energy dissipation mechanisms are triggered by the locally healed interface provided a few chains have been able to migrate to the other side of the interface. Higher green strength tends to increase the tack of polymers. With very low green strength the elastomer would behave as a low molecular weight liquid and although molecular contact and interdiffusion would be achieved it would not resist separation. Conversely, highly cohesive molecules present in solid materials are not able to diffuse or deform to allow sufficient molecular contact and therefore cannot achieve bond formation. Elastomers above their glass transition temperature present a good balance between chain mobility and cohesion and therefore both form bonds and resist rupture at an interface.

The kinetics of strength building of interface between elastomers above T_g is therefore controlled by two main mechanisms: the migration of chains across the interface and the progressive establishment of contact between the two materials on a molecular level. The debonding process has been observed in a study by Davis et al. (2014). They developed a device to allow for controllable short contact time combined with a video camera to observe the interfacial failure. The two materials are pressed together with a constant defined force for a duration ranging from 40ms to 10000ms and then separated at the same rate as they were compressed against each other. In this study, SBR with a relatively high molecular weight of 240kg/mol was used to increase the reptation time and therefore the time of contact required in order to reach the plateau strength of the interface. They observed a transition in the debonding behaviour from a defect-driven nucleation (presence of cavities at the interface) to a bulk deformation type of failure (the stresses are transmitted to the bulk rubber and the crack initiates at the interface but

is driven away from it) as can be seen in Figure 5-2. They attributed this change to the ability of the chains to interdiffuse. At very short time (<200ms), the chains did not have time to diffuse and the failure was fragile and driven by the growth of cavities already present at the interface. With longer contact time, the chains are able to diffuse and reinforce the cohesion of the two layers driving the crack away from the interface despite being initiated close to it. This observation is further supported by the fact that this fracture mechanism did not occur when the polymer was pressed against glass where interdiffusion of chains is nonexistent. This study has therefore shown that the time required for the onset of chain diffusion across the interface of a SBR is short. The increase in the strength observed after the initiation of the interdiffusion can be attributed to different phenomena: the further depth of interpenetration, the number of chain crossing or the higher contact area.

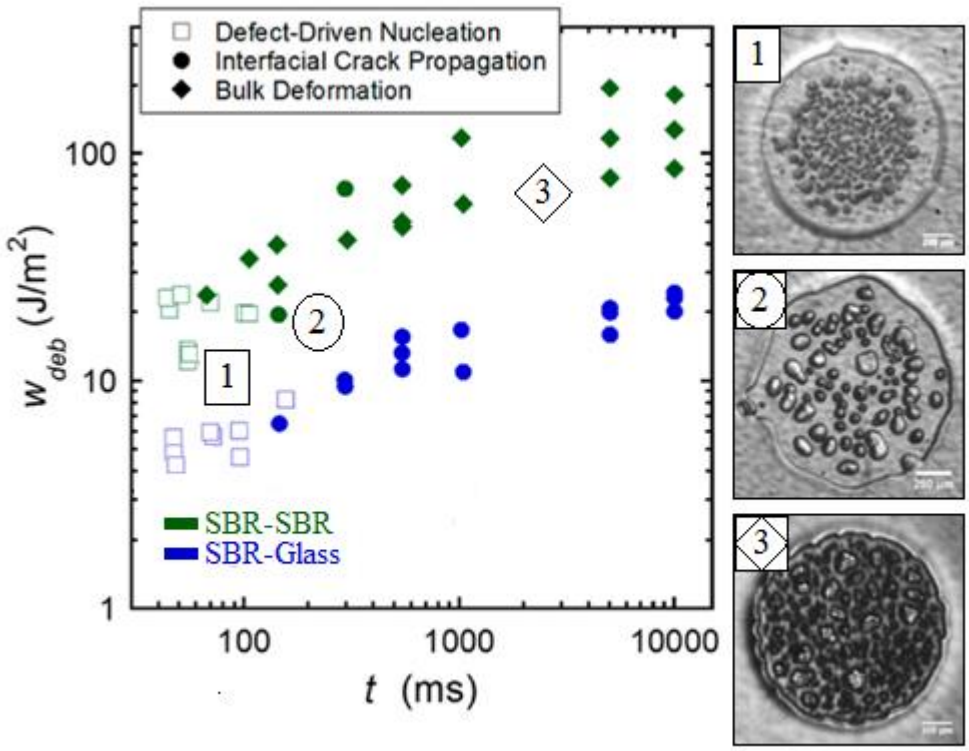

Figure 5-2. Evolution of work of adhesion at short times of contact. Adapted from Davis et al. (2014).

However, it is still unclear which phenomena controls the rate of strength building of an interface. It is broadly accepted the contact pressure does not affect the interdiffusion process (Hamed (1981)). Studies have also shown the contact pressure does not greatly

influence the resulting strength of self adhesion of unvulcanised elastomers (Gent and Kim (1990)). However, the trend of the increase of self adhesion with time is similar to the trend of adhesion with substrates where no interdiffusion can take place (Gent and Kim (1990), Davis et al. (2014)) suggesting the area of contact and the process at the interface plays a crucial role whether by its size that can be significantly influenced over time by the viscous flow of the material or by the diffusion of contaminants into the bulk rubber. To summarise, interdiffusion has been shown to begin shortly after contact, the strength of the resulting interface increases with time and has been linked in studies to the time dependent diffusion process and the time required for a certain length of molecule to diffuse into the other side. However the similarity of the trend of adhesion to cases where interdiffusion is highly unlikely suggest the contact area is also an important factor. One mechanism that could explain this trend is that interdiffusion takes place at relatively short time compared to material flow or diffusion of impurities into the bulk elastomer or is somehow delayed by phenomena at the interface.

In all of the studies above, the strength of the interface has been evaluated for unvulcanised materials. The vulcanising process potentially affects the interdiffusion of the chains as the high temperature would enhance chain motion. Also, the creation of sulphuric links between the chains certainly prevents the segments from moving freely as it is the case with linear chains. During the mixing of the compounds, the force applied is certainly high enough to remove the flaws at the interface. However, a significant question remains. Is this the case when different plies in a tyre are brought into contact under light pressure? The study in this chapter focuses on the strength of interfaces in the vulcanised state and the manufacturing parameters that may have an influence on the resulting strength. Potentially the conditions of contact before vulcanisation influence the resulting resistance to fracture. Both commercial and homemade compounds have been investigated. Moreover, the fracture properties have been evaluated in simple pull out in most studies and the work of adhesion calculated based on the stress versus strain response. It is well known the resulting work of adhesion depends greatly on the size of the initial flaws and that the variation of the strength is quite high under same conditions as the probability of encountering a significant flaw increases with the size of the test specimen. Fatigue fracture in the fracture mechanics framework has therefore been chosen as it provides more reproducible results which eliminate the variations caused by flaw and sample size.

5-2. **Experimental arrangement**

5-2-1. Modification of the geometry

Peeling tests have been widely used before to evaluate the adhesion between two materials or the tear resistance of a thin layer of adhesive. Depending on the material tested and its behaviour at the test temperature, different peel configurations have been adopted previously. Strong interfaces with a wide contact width such as that shown in Figure 3-13 can result in the legs tearing through as a consequence of the high strains developed close to the interface region. Several methods have previously been proposed to overcome this such as introducing a cloth backing to the legs of the test piece or by reinforcing the legs sticking them to a stiffer material. Both techniques prevent the rupture of the legs but do not prevent the crack deviation away from the interface. In fact, the crack often propagates at the interface between the rubber and the backing whether it is introduced in the bulk rubber or on its external face. The technique used in this study is to reduce the contact width between the two layers, making it less than the width of the legs (see Figure 5-3). At a constant force, this reduction keeps the stress in the legs constant while increasing the peeling energy by the ratio of the leg to the contact surface widths. A polytetrafluoroethene (PTFE) film is inserted between the two surfaces where contact is not desired. PTFE has the property to not adhere to rubbery materials and even after the high temperature during the vulcanisation, the film can be peeled off with virtually no deformation of the rubber after curing.

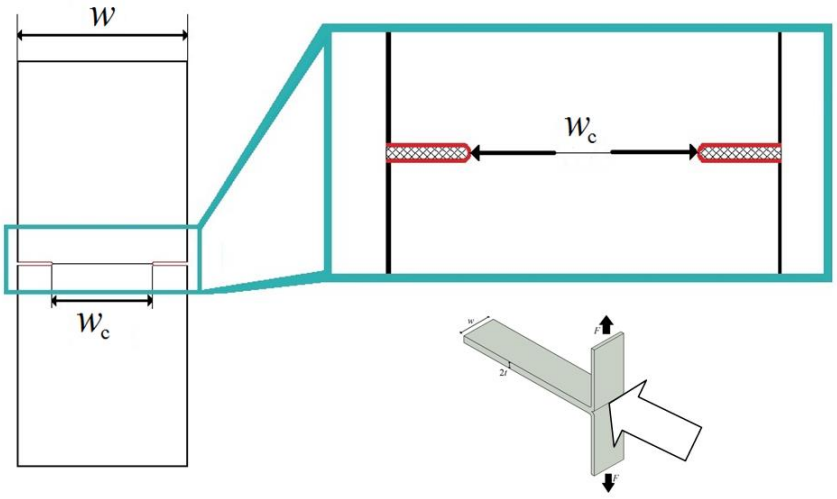

Figure 5-3. Reduction of the surface of contact with a 25µm thick PTFE film. The PTFE is shown as hatched on the drawing.

The peel specimens used in this study were approximately 120mm long, 25mm wide and 2mm thick for each leg. The preparation method is shown in Figure 5-4. Unvulcanised material sheets were cut to the desired dimensions (240mm x 200mm) from calendared pieces prepared on a two rolls mill. A 25µm thick PTFE film was cut to allow contact between the two layers only on the 12mm by 80mm surfaces and this was sandwiched between two sheets. The structure was then cured to optimum conditions under a compressive pressure of 3 MPa and cut on specific lines to obtain peel specimens. After removal of the PTFE film, the samples presented a reduced bonded surface of width w_c. Due to the flow of the rubber at the interface, the PTFE film was slightly pushed away and the width of the bonded area was therefore different from the width of the hole in the PTFE film. The true width of the bonded area w_c was therefore measured after peel testing. The calculation of the peeling energy has to account for the real bonded area. Equations (3-13) and (3-15) which are used to calculate the peeling energy with identical and different materials on either sides of the interface respectfully become

$$P = \frac{2\lambda F}{w_c} - hW\frac{w}{w_c} \tag{5-1}$$

and

$$P = \frac{(\lambda_1 + \lambda_2)F}{w_c} - (h_1 W_1 + h_2 W_2)\frac{w}{w_c} \tag{5-2}$$

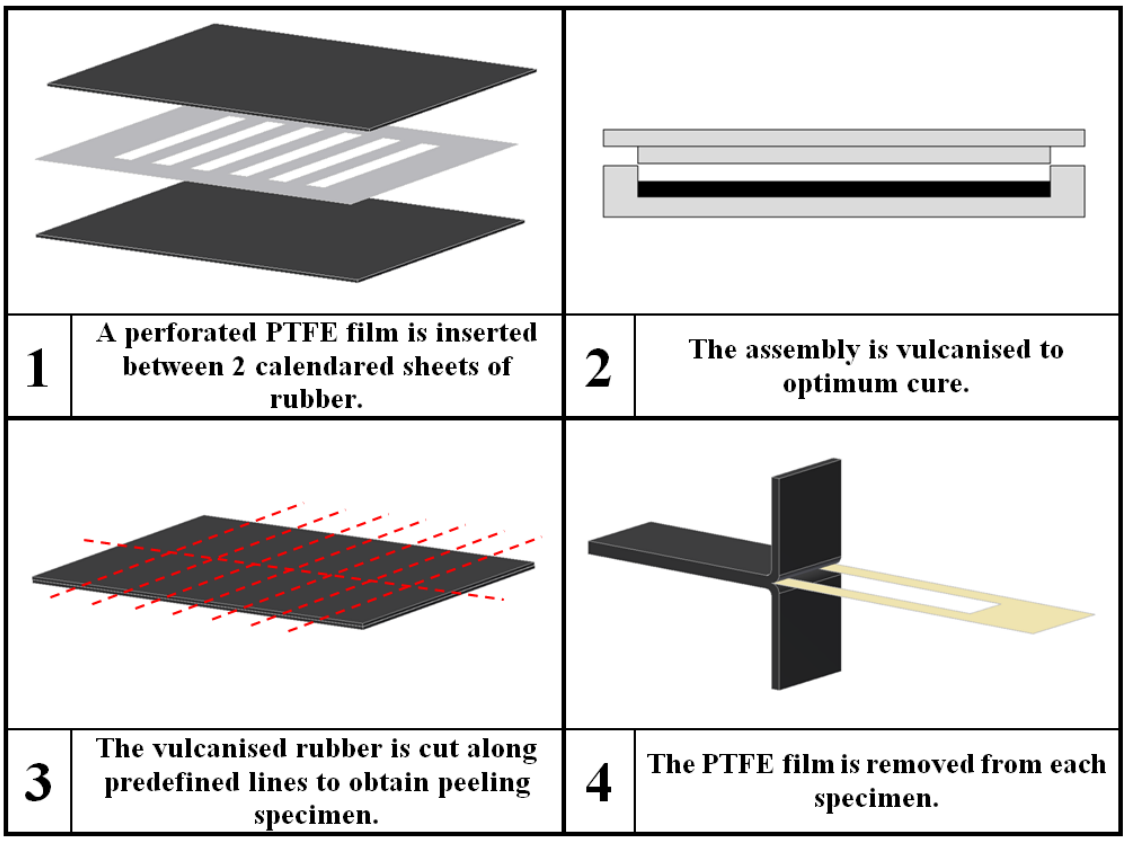

Figure 5-4. Schematic drawing of the process to obtain peeling specimen with reduced bonded area.

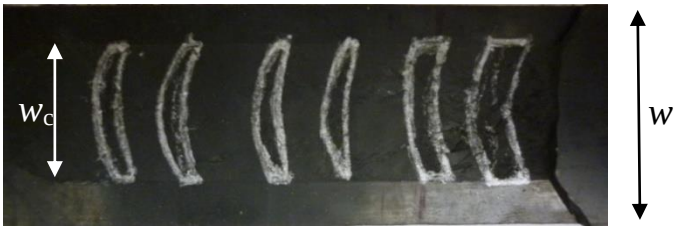

Figure 5-5. Peeled off specimen.

The introduction of a PTFE film at the interface also causes the initial crack tip radius to be set by the shape of the edge of the film. Therefore the crack growth was first initiated manually before each test at a specific force. The two layers were torn apart for an approximate length of 10mm. This procedure was repeated before any subsequent change in the load applied to ensure similar initial conditions between the tests. The crack growth rate was then measured in the steady state regime as mentioned in Section 3-4-2. The change of geometry also has an influence on the crack propagation profile. As can be seen on Figure 5-5 on which a typical crack growth pattern is shown, the crack front is no longer a straight line but is transformed into a semi elliptic pattern resulting from the higher stresses developing at the edges of the crack front. Once the

elliptical pattern is established, it remains similar for the all different peeling energies tested.

5-2-2. Validation of the preparation method

Lake et al. (1969) and many other researchers after them observed the energy release rate is independent of the geometry of the specimen. Therefore, the fatigue behaviour of SBR50 and NR50 evaluated with peeling specimens has been compared to data obtained with the pure shear geometry and trouser test pieces. The results are shown in Figure 5-6. The resistance to fatigue crack growth is similar for the three specimen geometries. The scatter in the crack growth rate per cycle is not unusual in fatigue. The slight difference over the whole range of energy release rate can be attributed to a thickness effect described in Chapter 2 and by Tsunoda et al. (2000) for the SBR50.

In the case of strain crystallising materials such as NR50 shown in Figure 5-6b, the minimum loading has to be carefully controlled to ensure the fully relaxing conditions. In Chapter 2 section 3-6, it has been seen the minimum tearing energy during one cycle could drastically change the resulting resistance to crack growth in fatigue of the material. This has been attributed to the presence of crystals at the crack tip developing upon loading and unable to dissolve above a threshold strain and preventing the crack from growing as much as for fully relaxing conditions. In the case of peeling, the bending of the legs suffices to cause a significant strain in the crack tip region responsible for the development of crystals. The solid line in Figure 5-6b represents a series of tests where the region of the crack tip was not fully relaxed and clearly differs from the behaviour in other modes of loading. Great care has to be taken when choosing the criteria for the minimum of the loading cycle to avoid any contribution of strain crystallisation.

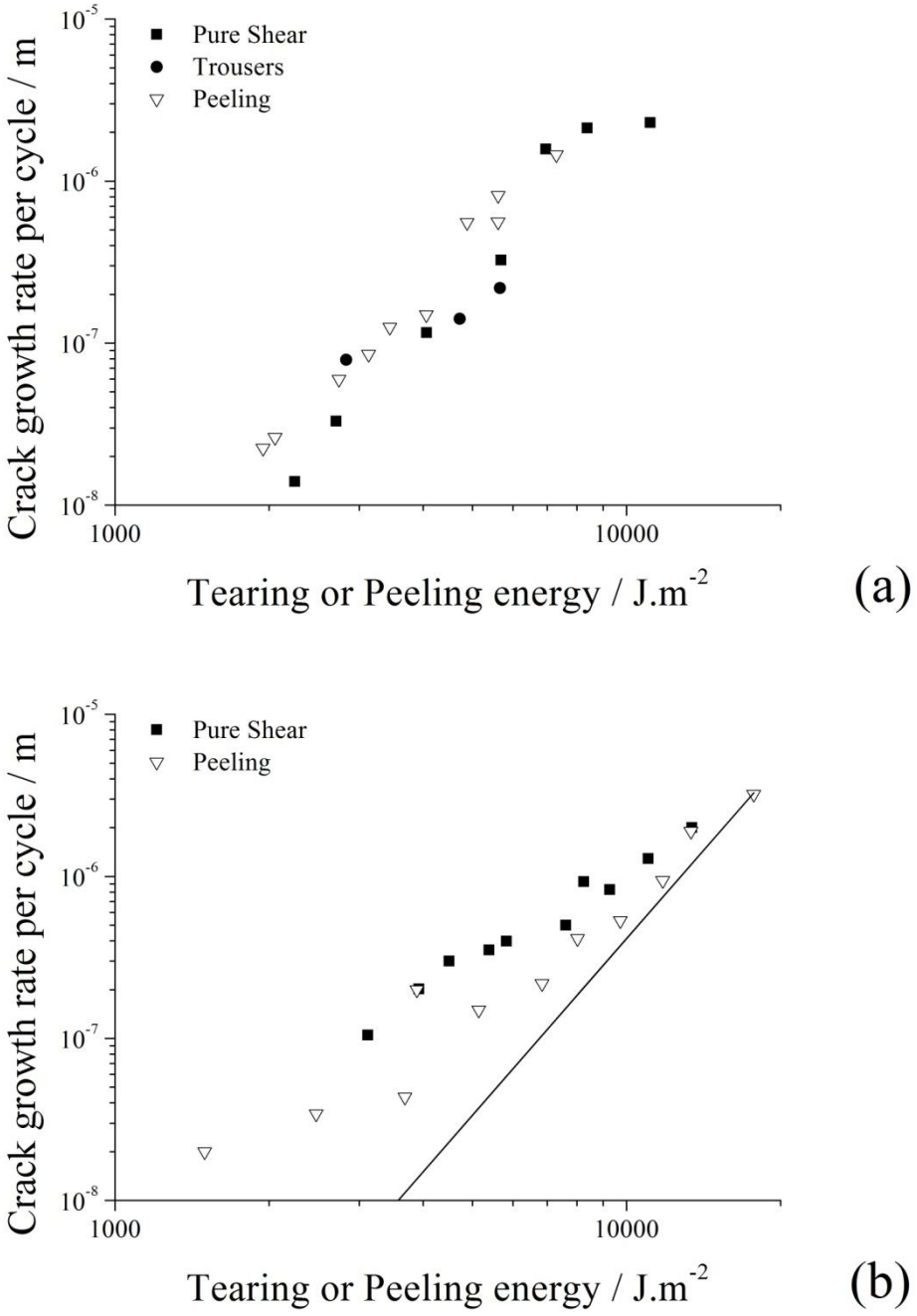

Figure 5-6. Fatigue behaviour of (a)SBR50 and (b)NR50 with different geometries.

5-3. **Strength of interfaces between different materials**

A tyre consists of many different materials. The fatigue behaviour and failure of the structure depends on the behaviour of the interfaces as much as on the behaviour of every single compound. The interface may present initiation site for cracks or resist separation and crack growth less than the materials it bonds together at equivalent loading. The fatigue behaviour of various interfaces between different commercial

compounds has been tested in this study. Some of the results are shown in Figure 5-7. The tear behaviours of the materials bonded together are shown as solid lines as a source of comparison. It can be clearly seen that the interface behaves as the weaker material. Examination of the resulting peeled off surfaces reveals the crack grows mainly in one side of the interface with a rough profile just as it would in the bulk material. This is especially obvious for an SBR0-SBR50 interface where a thin SBR0 film remains on the SBR50 substrate. This suggests the interface is just as strong or stronger that the weaker material itself. However for most of the interfaces tested the roughness of the profile clearly showed that the crack deviated occasionally into the tougher material especially when the mismatch between the materials was not pronounced. Testing the strength of an interface is difficult to achieve as it would require crack growth precisely at the interface at a molecular level. Even though the crack does not propagate exactly at the interface between the two layers, the growth occurs in a close proximity of the interface and this was sufficient to evaluate the adhesion between two surfaces using a fracture mechanics framework.

5-4. **Influence of vulcanising pressure on strength of interface**

In the last section, the resistance to fatigue crack growth at interfaces was similar to the toughness of one of the material making the interface. However failure in heavy duty tyres (truck, airplane) may arise from poor adhesion between the layers superposed during manufacturing. When prepared, the samples were brought into contact, heated up to the curing temperature and left to cure under pressure. The high temperature, high pressure and long curing times are however favourable to the development of strong bonding allowing both good contact and interdiffusion. If the scorch time (the time necessary to reach the onset of crosslinking and therefore chain motion restriction) is considered to be the time available for interdiffusion to occur then the molecular chains have a relatively long period of time to move across the interface as their scorch time is in the region of 15 minutes which has been observed as sufficient to increase the strength significantly (see Figure 2-34) even for large molecular weights. Moreover the elevated temperature at which vulcanisation takes place is helping further interdiffusion and broader contact area by increasing chain mobility while decreasing modulus and viscosity. It is therefore expected to have strongly bonded materials after vulcanisation

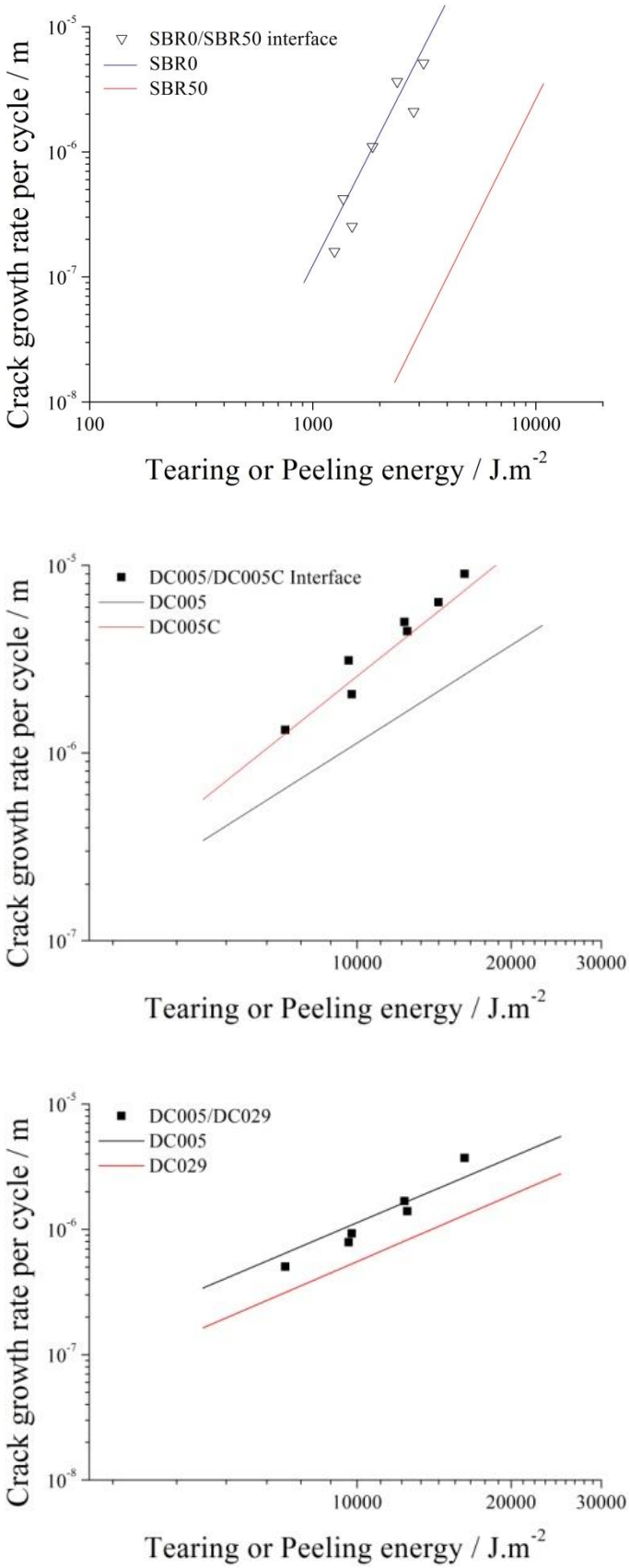

Figure 5-7. Interfaces tested under cyclic loading shows similar behaviour as the weaker material.

under these conditions. The time scale of the diffusion of chains across the interface for elastomers is so short that vulcanisation diminishes the possibility to investigate this easily.

In order to investigate the effect of contact area on the resulting strength of the interface, different compressive pressures were applied during the preparation of the specimens. The formulation of the material was chosen to allow short term interdiffusion and to amplify the influence of contact area. The SBR70 formulation given in Chapter 3 has been used for the following reasons. First, the autoadhesion of SBR increases more slowly with time than NR (Hamed (1981)) which makes it more likely to see a difference with a change of compressive pressure. Moreover SBR does not present effects due to strain crystallisation on the resulting strength. Then the accelerators and initiators have been added at a relatively high content to initiate the reaction early and make the vulcanisation time shorter (see Figure 5-8). This does not prevent interdiffusion from occurring but certainly limits the time the interface has to build strength or widen contact area. Finally, the filler content has been chosen to increase both stiffness and viscosity of the unvulcanised compound to extend the time to develop high surface contact. The elevated temperature reached during the vulcanisation makes the interdiffusion faster than in the literature cited in the introduction of this chapter. The extent of interdiffusion (number of chains and depth of interpenetration) are not evaluated in this thesis.

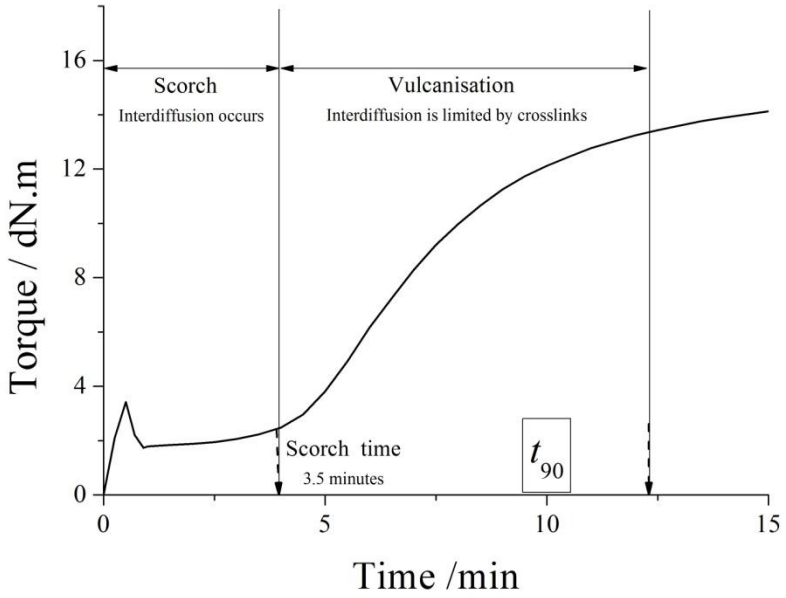

Figure 5-8. Cure curve for SBR70 showing time available for interdiffusion.

The different materials were prepared using a hand press with a digital force display. The compressive stress was obtained by dividing the measured force by the surface area of the whole sheets of rubber brought into contact. The pressure applied ranged from 0.2 MPa to 3 MPa, the maximum pressure available with this moulding configuration. It was carefully done in each case during the first 15s of vulcanisation. The specimens were tested under cyclic loading with fully relaxing conditions at a frequency of 1 Hz. The peeling energy P and the crack growth rate per cycle were calculated using equations (5-1) and (3-14) respectively. The strain rate used to measure the behaviour of SBR70 in tension was similar to the stretching rate of the legs during the peeling tests. Results are shown in Figure 5-9.

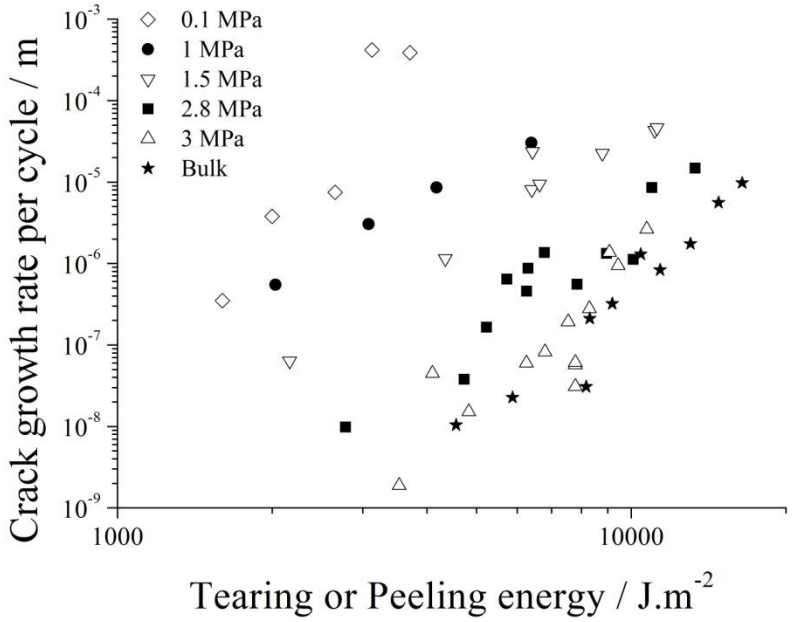

Figure 5-9. Compressive pressure during vulcanisation changes the resistance to crack growth of SBR70.

The effect of pressure in the study by Gent and Kim (1990) is shown in Figure 5-10 for an unfilled and unvulcanised SBR and this was found to be relatively small compared to the effect of the time of contact (see Figure 2-34). A factor of 2 to 3 only in the work of adhesion was observed for large increase in pressure. In this study on fatigue, the effect is much more pronounced and this can be attributed to several factors. The filler content increases the time required to achieve intimate contact over a large area and therefore the role of pressure might be more significant. Unfilled SBR indeed deforms more under small stress than its filled counterpart. The strength of the interfaces in the study was evaluated by separating the two sides rapidly. The size of the flaws at the interface may have a significant influence on the resulting strength as the separation is more likely to begin in one of these flaws. In fatigue the presence of flaws does not affect the magnitude of the peeling energy but increases the crack growth rate. Moreover, the creation of the interfaces was made at room temperature and with relatively small times of contact which may create large flaws as the gases trapped at the interface did not have time to diffuse away.

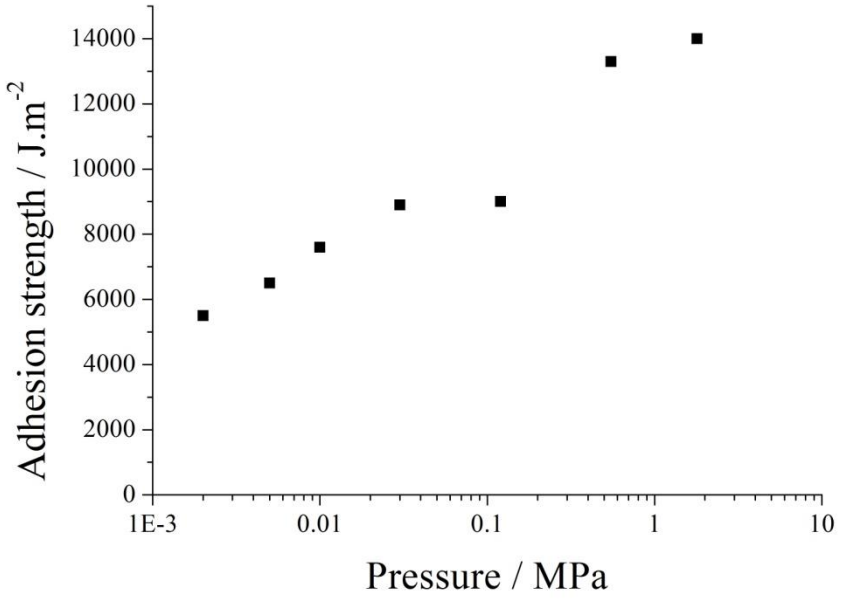

Figure 5-10. Influence of pressure on the adhesion strength of an unvulcanised SBR. Adapted from Gent and Kim (1990).

5-4-1.Observation of peeled off surfaces

The change of fatigue peel behaviour with pressure presented in Figure 5-9 is significant. Several orders of magnitude in the crack growth rate per cycle separate the different pressures at the same peeling energy. Such a high variation is intriguing compared to previous studies. In the literature presented in Chapter 2, it has been seen that the topology of the surface is linked with the resistance to crack growth. Therefore the surfaces created growing the crack in fatigue have been observed at different scales. Pictures of the surfaces resulting from the application of the same peeling energy are shown in Figure 5-11 (a) and (b) at different magnifications. The direction of crack growth is from left to right. The first observation that can be made from these pictures is that a 0.2 MPa pressure is not sufficient to provide full contact even on a microscopic scale. The regions that have not achieved contact with the other side of the interface are darker and present a different topography from the rest of the specimen. The appearance of the surface is reminiscent of the calendered sheets obtained using the two rolls mill. It also shows that the specimens prepared at higher pressures have been deformed enough to ensure contact has been achieved on a microscopic scale. Indeed, the crack surface profile is smoother and craters were completely removed.

From the smallest pressure applied to the highest, the surface topography changes drastically. It is essential to note that the location of the crack remains in the close vicinity of the region where the two sides of the interface have been brought together therefore if crack deviation or branching occur it is does not lead to a sufficient growth in the orthogonal direction to prevent the main crack from growing along the plane of the original interface. As the pressure increases, steps appear on the crack surfaces visible as vertical bright lines on the pictures. The appearance of these steps is seen in most rubbery materials under cyclic loading. Gent and Pulford (1984) and Fukahori and Andrews (1978) linked their numbers and the spacing between them to the strength of the material. Although they attributed the origin of these steps to different mechanisms, they agreed on two main points. First, the strength of the materials increases as the number of steps decreases. Aside from the lowest pressure where the smooth surface and the flaws prevent significant conclusions to be drawn, this assertion is verified when sufficient contact has been achieved. Second, the steps get deeper with higher strength which again can be observed on the pictures. The magnitude of the peaks and craters increases with the pressure applied and seems to exceed the original of the unvulcanised material for high pressure. These observations confirm the resistance to crack growth changes drastically between the low and high pressures.

Additional pictures have been taken from the side of the resulting interface showing the profile of a cut made along the direction of crack growth. The general observations about surface topography made before are confirmed from the view of the cuts. At pressures approaching 3MPa, aside from the significantly rougher profile, additional cracks deviating from the original constrained path are created during crack growth (see Figure 5-12). Branching, the multiplication of crack fronts in the region of the crack tip is a well-known reinforcement process in filled rubbers. As the original unique crack grows, multiple crack fronts are created at its tip. Each of them propagates following a different path until one path dominates and the other cracks remain unchanged by further loadings. The multiplication of crack fronts increases the energy required to grow the whole crack by a certain length due to the higher surface area to be created and therefore leads to an increase in the peeling energy necessary to drive the crack. These pictures provide evidence that additional reinforcement processes are being triggered when the interfaces are created under higher pressures.

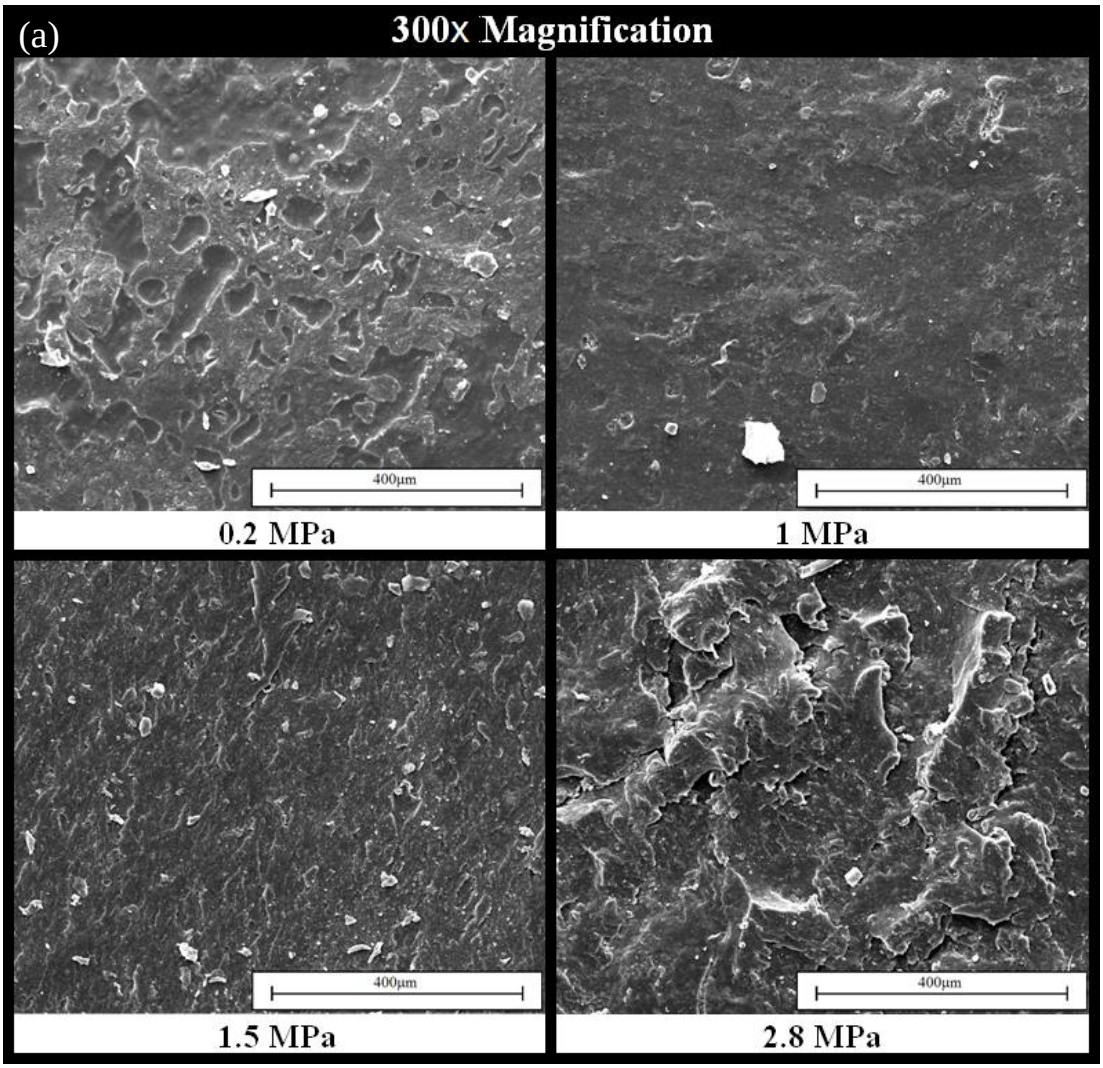
(a)
300x Magnification
400µm
0.2 MPa
400µm
1 MPa
400µm
1.5 MPa
400µm
2.8 MPa

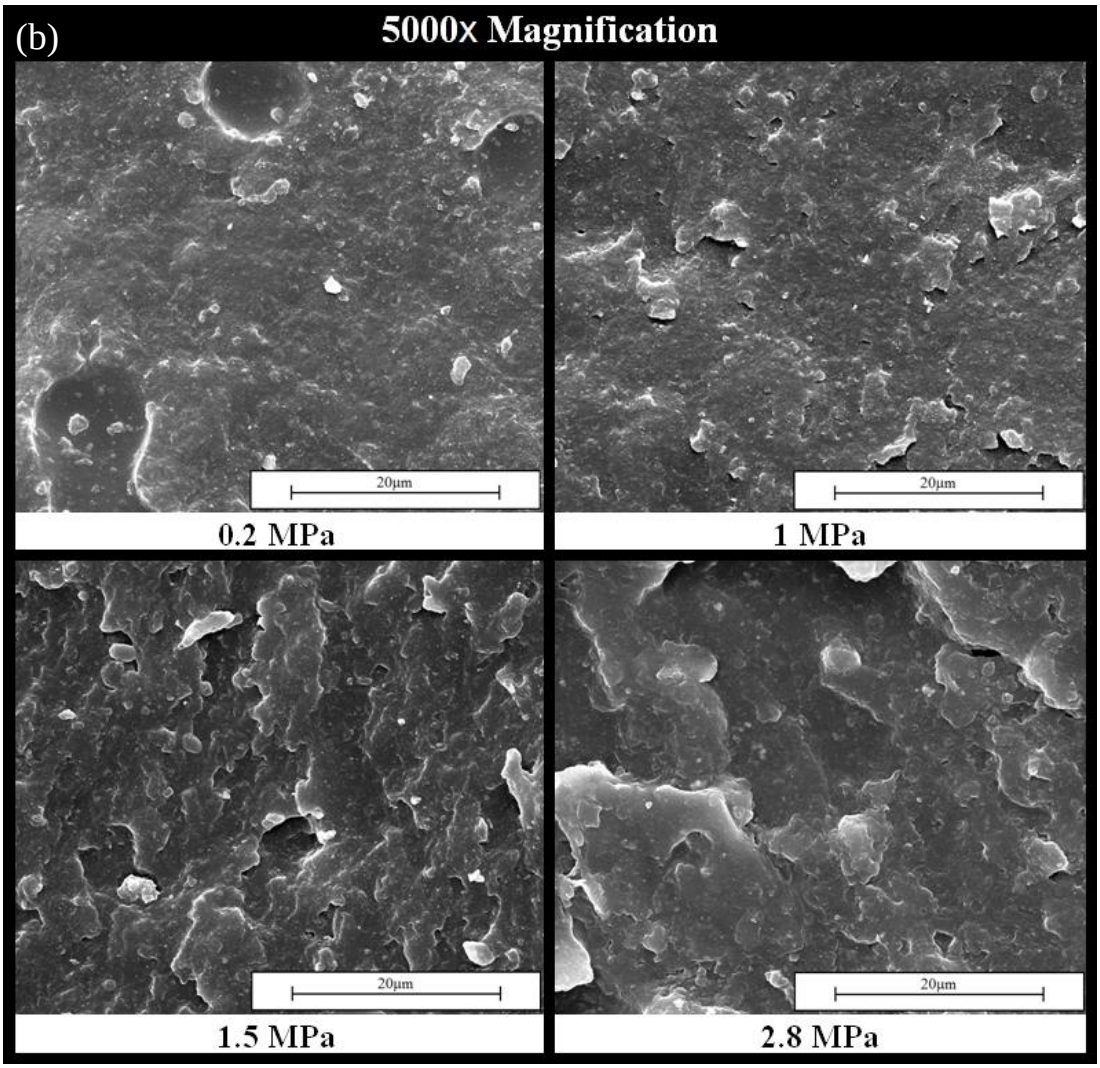

Figure 5-11. SEM images of the separated surfaces magnified (a) 300 times and (b) 5000 times

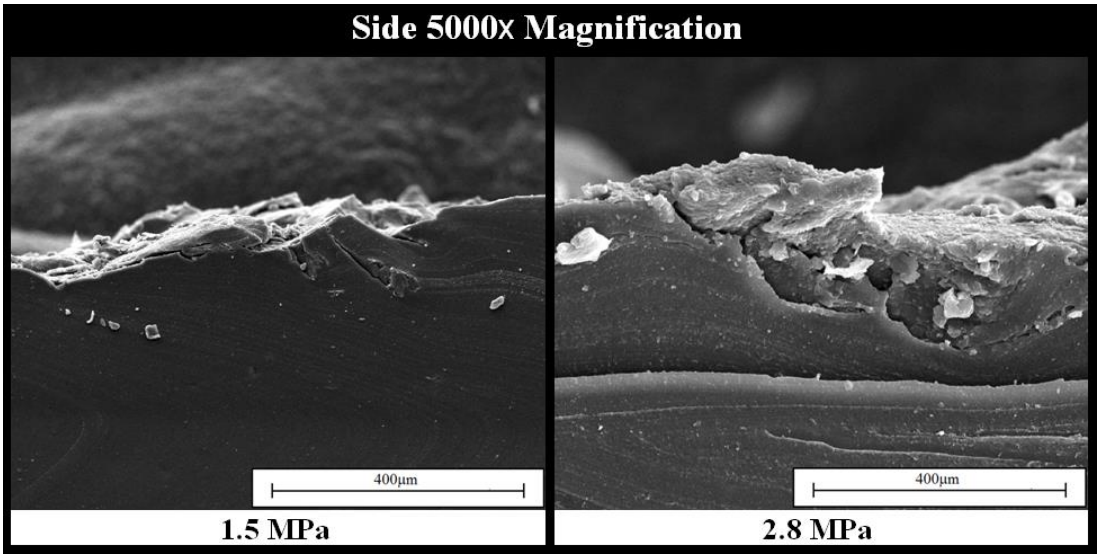

Figure 5-12. SEM images of the sides of the specimen after separation for higher vulcanising pressure. The crack propagates from left to right.

5-4-2. Resulting roughness

Further investigations on the resulting topography were done using a surface profiler. The area of the surfaces analysed were 4mm^2 therefore 4 times bigger than the first pictures in Figure 5-11 at 10 microns spacing in both directions. These intervals are not sufficient to measure the smallest variations of height as in Figure 5-11 (b) but would certainly detect the variations in Figure 5-11 (a). The surface profiles shown in Figure 5-13 look similar to the pictures taken with the SEM but offers a quantitative measure of the variations in height. Therefore further analysis of the surfaces can be made by calculating roughness characteristic R_q based on each of the lines scanned by the probe in the direction of crack growth shown in Figure 5-14.

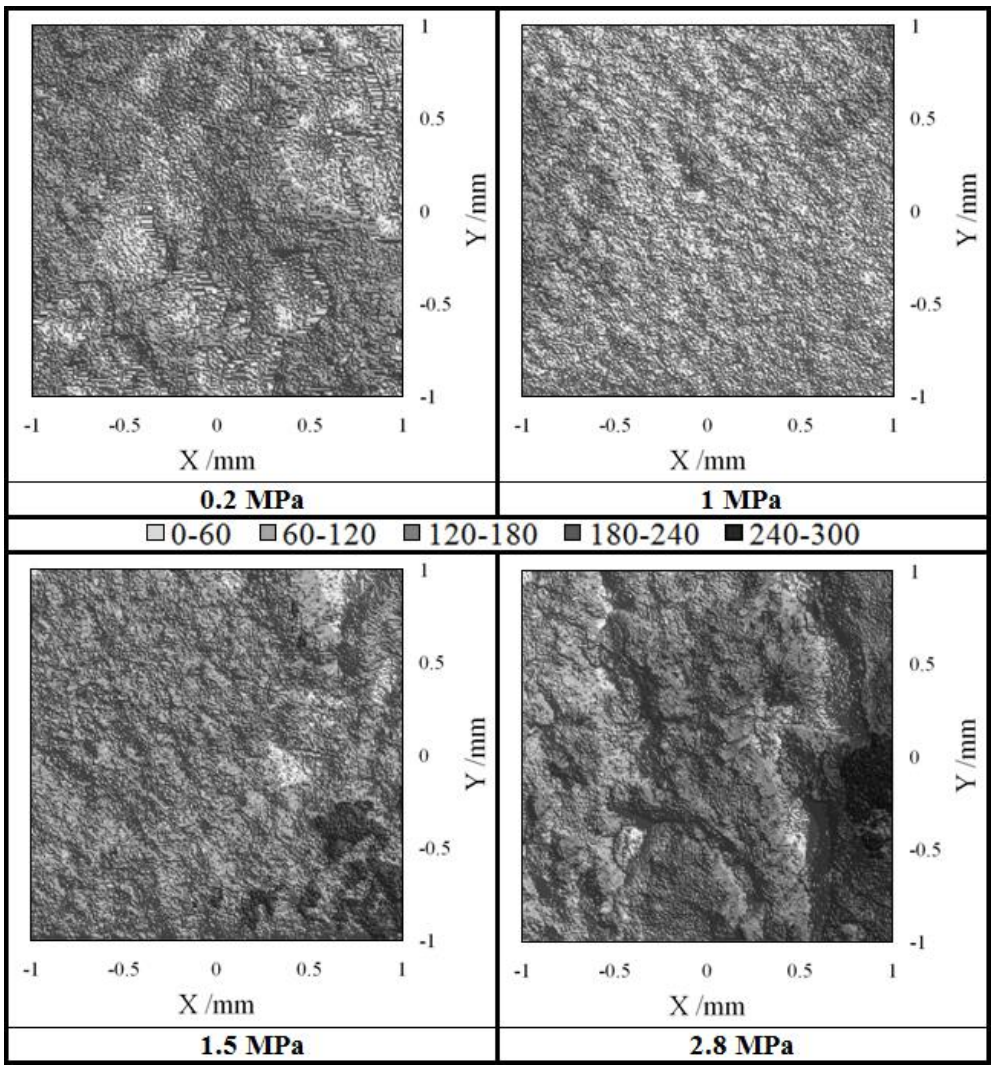

Figure 5-13. Surface topography of the specimen at the same peeling energy. The height is expressed in μm.

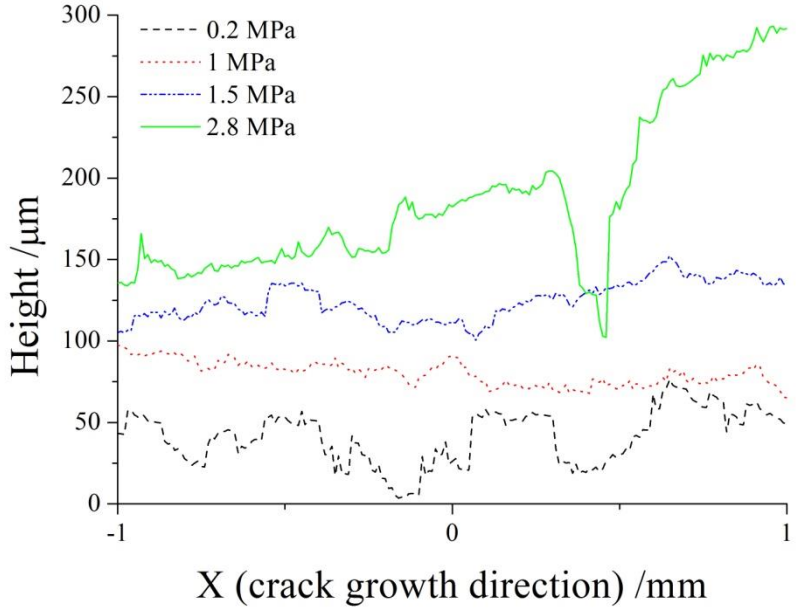

Figure 5-14. Profile lines of the resulting surface after crack growth taken at the same peeling energy.

The results of the roughness calculations are shown in Figure 5-15 and were averaged over the entire sample of lines scanned with the surface profiler. As expected from the observation of the surfaces, the roughness gets significantly higher when the pressure is increased. The voids present at the interface for the smallest pressures results in a higher apparent roughness. The standard deviation of the roughness gets higher which demonstrates the surface also gets more irregular. The change of roughness observed on the crack surfaces further confirms the variation of strength due to the change in pressure when the surface are brought into contact for curing. The origin of this change is unclear. This might be a consequence of a variation in the magnitude of the diffusion either in the number of chains or their depth of penetration but many researchers have pointed out diffusion is independent of the pressure applied (Hamed (1981), Gent and Kim (1990)). Also as the time and temperature of vulcanisation were kept constant for the preparation of the specimens at different pressures, and as the diffusion of the chains occurs at short times for SBR, one could expect the interdiffusion to be similar and fast compared to the establishment of contact.

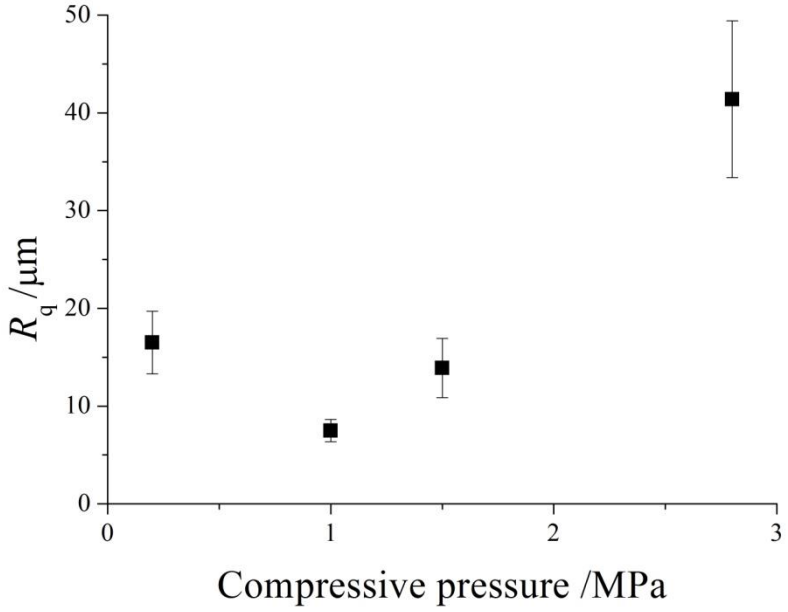

Figure 5-15. Evolution of roughness

5-4-3. Investigations on contact area

To assess the contact area under light pressure, the uncured compound was also pressed against a transparent glass support and observed through a microscope. Square specimens of 5 mm edge length were sandwiched between a glass subtract and an aluminium disc acting as a support for the loading. The load was calculated based on the dimensions of the specimens and applied with. The setup was placed in an oven heated up at 140°C and left for the optimum cure time length. The resulting contact area could be observed through the glass plate under an optical microscope. Although molecular contact could obviously not be observed with this setup it gives an idea of the contact surface at very low pressure and helps to qualitatively evaluate the remaining flows at the interface. Pictures taken with the microscope are shown in Figure 5-16. Observation of the contact area shows that light pressures such as 0.2 to 0.5 MPa are not sufficient to completely remove the flaws. The rubber is pushed against the glass but either the topography of the surface in contact cannot be completely deformed in those conditions to a flat surface or air remains trapped at the interface. At 1 MPa, the flaws have mostly disappeared at the contact area. The percentage of voids observed on the crack surface of the peeling specimens exceeds the amount observed against the glass. On the stiff smooth glass surface the rubber can flow more freely. Also as the specimen are placed in the oven, the temperature rise they are subjected to is not as rapid as

during the vulcanisation and the rubber has therefore more time to flow. The regions where the rubber is in contact with the other half of the peeling specimen are relatively small (less than 50 % in that scale). A further and magnified picture taken with a microscope of the area where contact has been achieved reveals that even in the contact area flaws of smaller size are abundant (see Figure 5-17 (c)). On a side note, the presence of flaws decreases the resistance to crack growth but also acts as stress raisers and initiation point in a structure. Any flaw of more than a few tens of microns can initiate the crack growth. In some areas of the tyre where the compression stress is not properly applied by the inflatable bladder inside the tyre during curing, flaws can be left in the structure which may significantly reduce the lifetime of the structure.

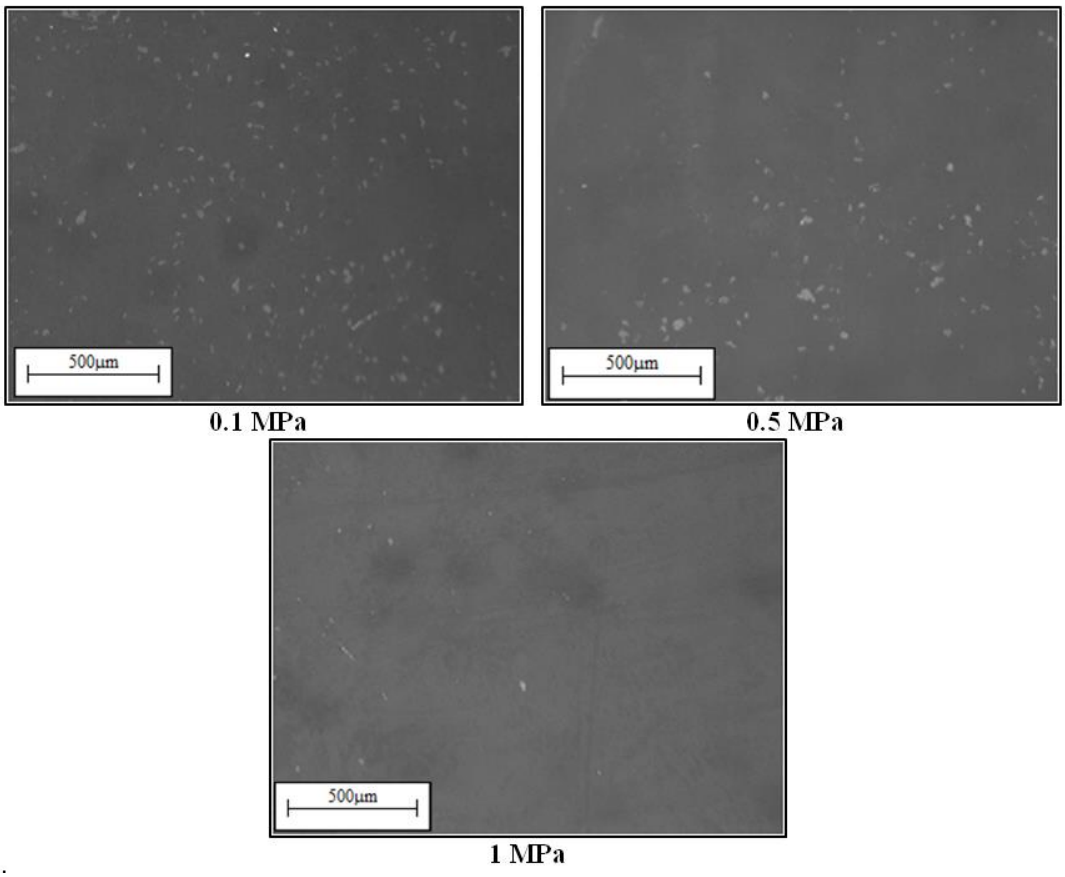

Figure 5-16. Contact area between glass and the rubber under (a) 0.2 MPa, (b) 0.5MPa and (c) 1 MPa.

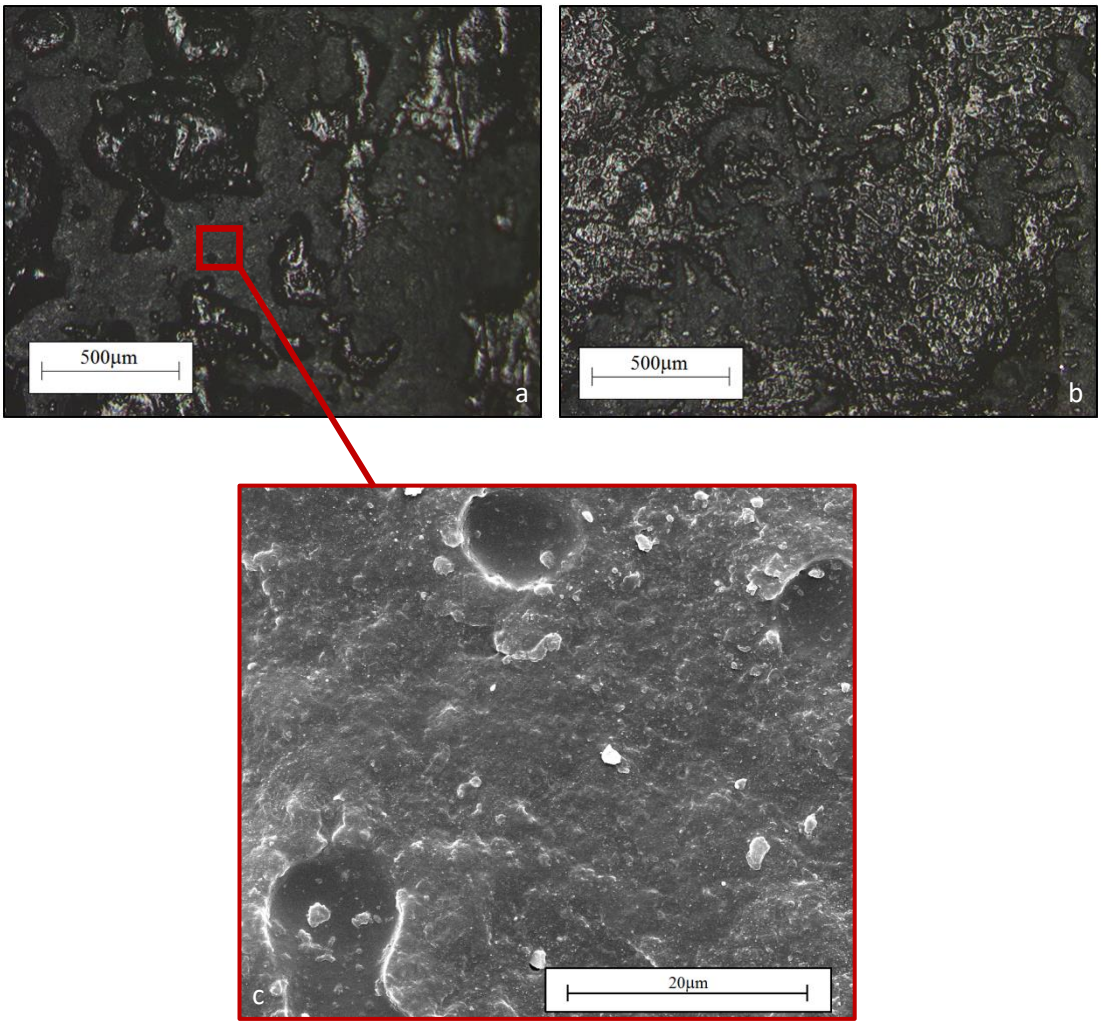

Figure 5-17. Microscope pictures of the cracked surface for the 0.2 MPa specimen. Magnification: (a) and (b) 300x and (c) 5000x.

The presence of flaws can also be attributed to the diffusion of the air trapped between the two layers at the interface into the bulk rubber. The diffusion of gas through rubbery polymers depends on the partial pressure of the gas at the surface of the polymer, its diffusivity and the solubility of the gas in the polymer (George and Thomas (2001)). At a fixed temperature, diffusivity and solubility of the gas into a rubbery polymer are independent of the gas pressure (Matteucci et al. (2006)) and therefore the flux only depends on the pressure of the gas. The migration of air from the interface into the bulk rubber is therefore slower at small pressures. The diffusion of a gas into a rubber is influenced by the segmental mobility of the polymer chains. The diffusion is therefore greatly reduced as the vulcanisation progresses. The rubber transforms from a liquid to a solid during the vulcanisation because the polymer chains get linked to one another and

therefore creates a large network of chains in which the path for the transport of the diffusing molecules is more obstructed.

One way of taking these flaws into account is to calculate the average variation in crack area due to the crack growth. The peeling energy is the ratio of the change in strain energy by the change in crack area. Therefore the peeling energy can be compensated to take into account the flaws at the interface by eliminating the area where contact has visibly not been achieved. The calculations are given in equations (5-3) to (5-5) where P_{comp} is the compensated peeling energy and P_{app} is the apparent peeling energy based solely on the external loading conditions applied to the specimen. P_{app} is calculated based on the experimental conditions from equation (5-1). The observed surface created as the crack growth is designated by A_{obs} while A_{app} is the whole contact surface during curing.

$$P_{comp} = -\frac{dU}{dA_{obs}} \tag{5-3}$$

combined with

$$dA_{obs} = x dA_{app} \text{ and } P_{app} = -\frac{dU}{dA_{app}} \tag{5-4}$$

results in equation (5-5)

$$P_{comp} = -\frac{1}{x}\frac{dU}{dA_{app}} = \frac{1}{x}P_{app} \tag{5-5}$$

The amount of flaws varied with the region of the sample (Figure 17 (a) and (b) for example show the difference) and therefore several pictures were taken in the crack growth region corresponding to different loads to average the surface in contact on a macroscopic scale. Table 5-1 presents the percentage of contact area at the interface at the different apparent peeling energy tested and the compensated peeling energy. The change resulted in the change in the peeling behaviour shown in Figure 5-18. The area compensation for the real contact area gets the low pressure fatigue behaviour closer to the behaviour at higher pressures. This method of compensation shows the assumption of perfect contact for the calculation of the peeling energy creates a significant deviation from the real fatigue behaviour. However the calculations are based on observation of

the surfaces at a large scale (hundreds of microns) compared to the molecular contact (Angstroms) and therefore the values obtained are based on the similar debatable assumption that all flaws are observable at the length scale chosen.

P_{app} /J.m^{-2}	1600	2000	2650	3130	3710
x /%	86	75	67	59	57
P_{comp} /J.m^{-2}	1860	2670	3960	5300	6300

Table 5-1. Compensated peeling energies for 0.2 MPa pressure.

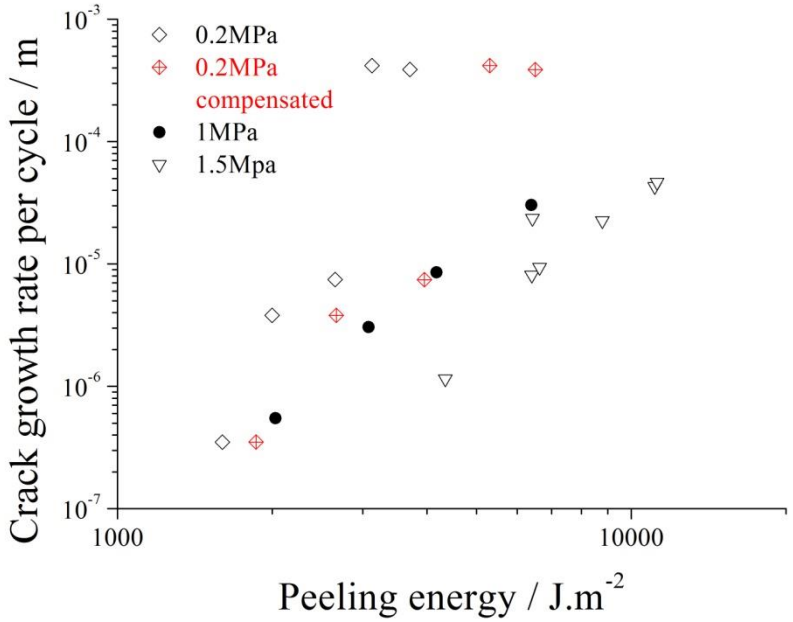

Figure 5-18. Compensated peeling energy at 0.2 MPa

In a similar but inverse approach, the change in contact area required to make fatigue behaviours coincide may be calculated approximately. The variations calculated correspond to the change in contact area which should occur should the fatigue behaviour solely be a function of contact area. This calculation on those curves would not be valid over the whole range of data available because of the variation in the slope of the logarithmic representation. However it can be done for a representative peeling energy or crack growth rate. For a constant crack growth rate, we may consider the pressure at which the interface reaches the strength of the bulk rubber to be sufficient to cause full contact. The change of surface 1/*x* associated with the change of peeling energy can be calculated from the equation above. They are given in Table 5-2 and

represented in Figure 5-19. The values obtained show the contact area would have to change drastically to explain the variation in the fatigue strength of the interface. Even though it is possible to assume the presence of numerous and dense voids at the interface at the nanoscale, attributing the variation of strength exclusively to the variation of contact area seems unreasonable especially for high pressures for which the resulting crack surface exhibits roughness pattern larger both in depth and width than the size of the presumed voids.

Pressure /MPa	**0.2**	**1**	**1.5**	**2.8**	**3**
$1/x$ at 10^{-7}m/cycle	5	5.56	3.03	1.49	1
$1/x$ at 10^{-6}m/cycle	5.88	4.55	2.78	1.43	1
$1/x$ at 10^{-5}m/cycle	7.14	3.70	2.38	1.33	1

Table 5-2. Change in the contact area to fit the bulk material behaviour.

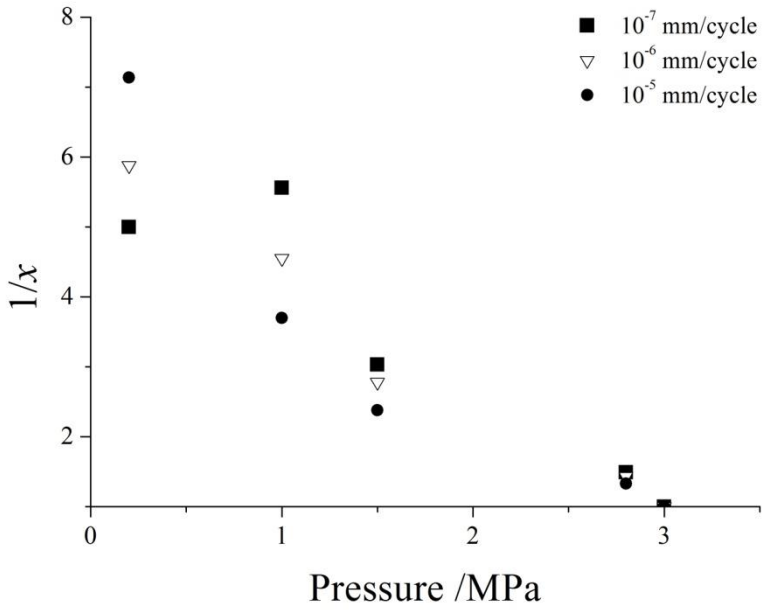

Figure 5-19. Virtual change in surface of contact with pressure to reach bulk properties.

5-5. **Conclusion**

The resistance to fatigue crack growth at interfaces has been investigated using a modified geometry of a commonly used specimen shape. The reduction of the contact area between the two sides of a peeling specimen allows the investigation of a broader range of energies where traditional samples would fail in the bulk rubber as well as the implications of phenomena during vulcanisation on the resulting strength of the cured specimens. Under conditions allowing both interdiffusion and sufficient contact between the two sides of the interface, the resistance to fatigue crack growth is similar to the weakest material forming the interface. Under unfavorable conditions however, the development of strength is greatly reduced and leads to a significantly weaker interface. When the time allowed for diffusion of polymer segments across the interface is limited by a fast creation of crosslinks between the polymer chains, the compressive pressure between the two layers forming the interface plays an important part in the development of the strength. At relatively low pressure, the contact area between the two sides of the interface is limited by the viscosity of the material and the diffusion of the air trapped at the interface into the bulk rubber. The flaws present at the interface contribute to the lower energy necessary to propagate the crack. When the pressure increases and the flaws progressively disappear, the resistance to crack growth approaches the behaviour of the bulk rubber. Attributing the change of strength only to the variation in the contact area, although theoretically possible considering contact on the nanoscale, seems unreasonable as the size of the flaws are negligible compared to the magnitude of the roughness of the separated surface. The crack does not propagate only between the flaws at the interface and their influence is therefore lower. This is further supported by the higher roughness and the branching in the region of the crack tip as the pressure increases which indicates that reinforcement mechanisms are triggered. It appears both interdiffusion of polymer chains and establishment of good contact are involved in the increased resistance to crack growth as the vulcanisation compressive pressure is raised. One possible explanation is the higher the pressure the faster good contact is achieved. In the region in contact, interdiffusion of chains occurs shortly after contact but with time, both the number of polymer chains crossing the interface and interpenetration depth increases until they are stopped by the reduced molecular motion due to crosslinks. The more advanced interdiffusion leads to higher cohesion in the region of the interface and therefore higher energy dissipation as this

region is loaded during crack growth. When the tyres are vulcanised, they are sandwiched between a rigid drum and a membrane inflated to a pressure sufficient to deform the rubber to its final shape. The complex geometry of the tyre however creates interfaces which are not subjected to the same pressure as the one exerted by the membrane on the inside surface of the tyre. This reduction of pressure may lead to a catastrophic effect on the lifetime of the whole tyre (lack of contact area and interdiffusion) as well as create initiation sites for failure (flaws of significant size remaining at the interface).

CHAPTER 6 -PREDICTING TEARING ENERGY IN A TYRE USING A FINITE ELEMENT SUBMODELING APPROACH

6-1. **Introduction**

Fracture of elastomers under cyclic loading is widely discussed throughout. The fracture mechanics approach relates the crack growth rate per cycle to the maximum tearing energy reached during a cycle. Experimental setups used to obtain this behaviour rely on a balance of energy and a transfer from one mode of loading to another to derive the energy released as the crack grows. However, for most components made out of rubber, such an energy balance approach on arbitrary crack geometry has been difficult to obtain in the past. However the advent of finite element analysis has now facilitated the estimation of the tearing energy in a component. Several different methods have been developed to estimate the tearing energy in practice and are described in Chapter 2. Here, they are used and the results evaluated for standard fatigue tests geometries. Even though progress has been made to reduce the computation time and therefore to increase the number of degrees of freedom in a simulation, most FEA software package are still realistically limited to 100,000 elements to give a solution in a reasonable time on a desktop computer. For some components such as tyres, the number of elements is significantly increased above this threshold to describe the complex geometry accurately. The size of the component is also typically very large when compared to the size of the intrinsic crack. A submodelling technique available in Abaqus was used to reduce the number of elements in some simulations. An initial analysis of the entire component such as a tyre with a relatively coarse mesh is performed in order to determine the global deformation in all the main regions of the tyre geometry. The results of this simulation are stored and saved in a file which is then used to drive the

boundary conditions of a much more refined submodel which focuses more fully on the region of interest. The submodelling method was first used on geometries with known analytical solutions to help validate the technique and the results are given in the second part of this chapter. Submodelling was also used to estimate the tearing energy in the bead region of an aircraft tyre where crack growth is often observed. Analysis and results are given in the last part of this chapter.

6-2. **Comparison of FEA techniques to obtain the tearing energy in a component on typical specimens**

6-2-1. Pure shear specimen

The techniques described in the last part of Chapter 2 were used to determine the tearing energy in typical specimen geometries using the finite element software package ABAQUS. A plane stress 2D model of the pure shear crack growth specimen was used and is presented in Figure 6-1. For the virtual crack extension method the change in the tearing energy is obtained from the ratio of the strain energy difference in the specimen divided by the change in crack length as the crack length is increased by the size of an element. Models with different lengths were used to derive the stored energy for different crack lengths. The strain energy in the sample is obtained through the ALLSE output request which sums the strain energy of all the elements in the component. For the Rice J-integral method, a path around the crack tip has to be designated for the software to calculate the energy release rate via a built-in option called *Contour Integral. The integral is calculated on a specified number of contours, the first of which is made of the elements immediately surrounding the crack tip. Each subsequent path adds another row of elements around the crack tip into the contour. Although the J-integral is theoretically path independent, it can be seen in Figure 6-2 to vary until reaching a constant value. This variation is a consequence of discretisation and the numerical error introduced at the crack tip. However, if the contour is taken sufficiently far from the crack tip, the J-integral value is accurately calculated and becomes independent of the contour chosen. In this work, the fifth contour is used unless specified otherwise.

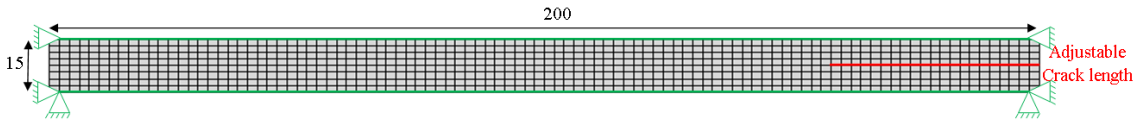

Figure 6-1. Pure shear specimen model.

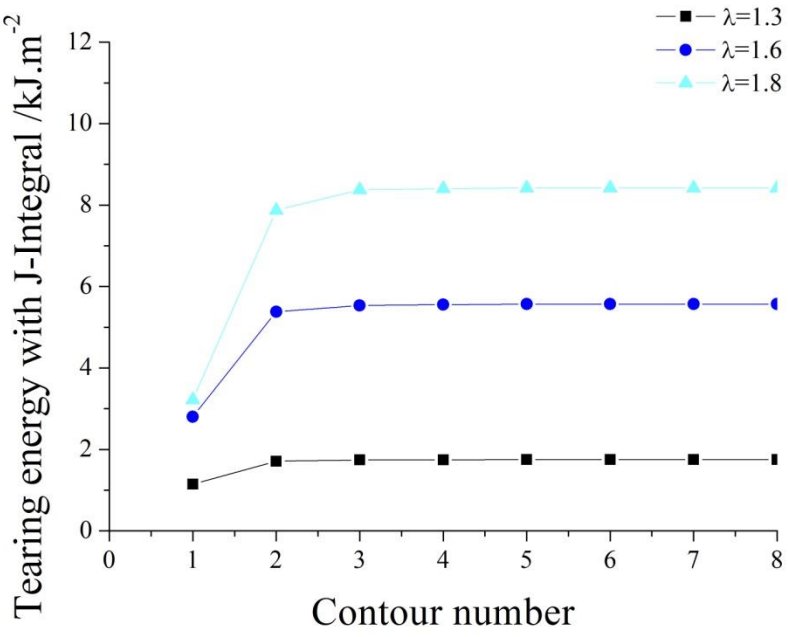

Figure 6-2. Convergence of the tearing energy obtained using the Rice J-Integral method.

Tearing energies were obtained using both methods and compared to the theoretical values obtained from the strain energy function chosen to model the material behaviour and to experimental data for SBR50 and SBR0. The tearing energy in a pure shear tear experiment can be expressed using equation (6-1).

$$T = W_{\text{ph}} l_0 \tag{6-1}$$

As explained in Chapter 3, the Mooney-Rivlin (equation 3-19) and the Yeoh (equation 3-20) strain energy function were chosen to model respectively unfilled and filled elastomers for the finite element analysis. The strain energy density is expressed as a function of the strain invariants of the left Cauchy-Green deformation tensor I_1 and I_2 which are functions of the stretch ratios in the principal directions (see equation (2-28)).

In pure shear, if λ is the extension ratio in the direction of the load, then

$$\lambda_1 = \lambda$$
$$\lambda_2 = \frac{1}{\lambda} \qquad (6\text{–}2)$$
$$\lambda_3 = 1$$

The strain invariants can be expressed in pure shear as

$$I_1 = I_2 = (\lambda^2 + \frac{1}{\lambda^2} + 1) \qquad (6\text{-}3)$$

Combining equations (3-19) and (6-3), the stored energy density in pure shear in the Mooney-Rivlin case can be expressed as

$$W_{\text{ph}} = (C_1 + C_2)(\lambda^2 + \frac{1}{\lambda^2} - 2) \qquad (6\text{-}4)$$

In the Yeoh SEF case, equations (3-20) and (6-3), W_{ph} become:

$$W_{ph} = C_{10}(\lambda^2 + \frac{1}{\lambda^2} - 2) + C_{20}(\lambda^2 + \frac{1}{\lambda^2} - 2)^2 + C_{30}(\lambda^2 + \frac{1}{\lambda^2} - 2)^3 \qquad (6\text{-}5)$$

The results of the simulations are shown on Figure 6-3 (a) and (b) along with the theoretical calculations and the experimental results for the two compounds for a crack of length of 100 mm in a sample test of width 200 mm. Both techniques give similar results and are in good agreement with the theoretical consideration. The departure of the experimental data from the analytical solution is a consequence of the error in the prediction of the pure shear behaviour with SEF coefficients obtained in tension as shown in Figure 3-23. In this range of extension ratio, the simulated stress is lower than the engineering stress measured experimentally. Therefore, the strain energy calculations in a pure shear crack finite element model are affected and these predict a lower tearing energy than the measured experimental data.

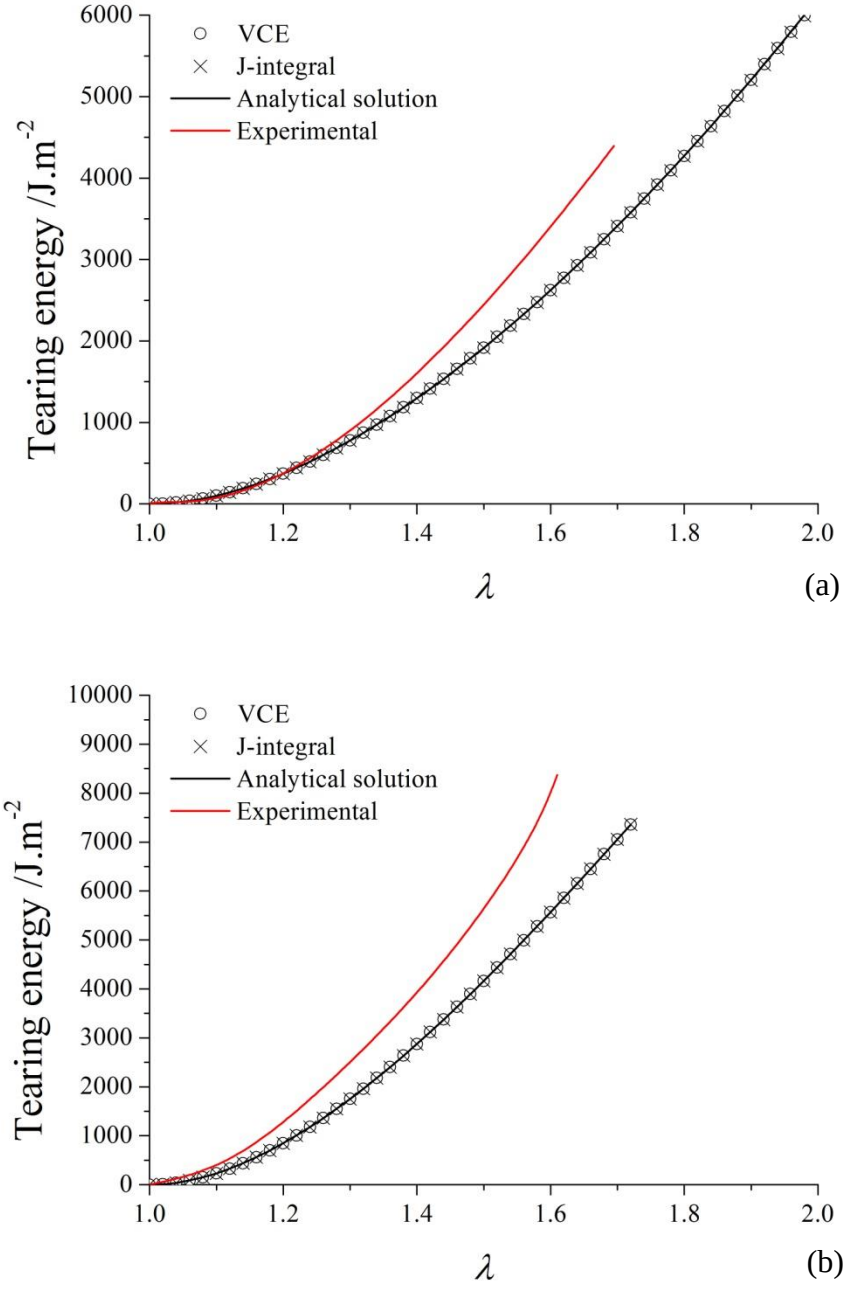

Figure 6-3. The results for the different methods are in agreement with theoretical calculations and in reasonable agreement with experimental data for (a) SBR0 and (b) SBR50.

6-2-2. Edge crack specimen

Similar simulations were done for the edge crack specimen as described in Figure 2-14. The tearing energy can be calculated using equation (2-57). If λ is the extension ratio in the direction of loading in tension, equations (2-28) become:

$$I_1 = \lambda^2 + \frac{2}{\lambda}$$
$$I_2 = 2\lambda + \frac{1}{\lambda^2} \tag{6-6}$$

Inserting these equations into the expression of the elastically stored energy density, the tearing energy can be written as

$$T = 2k\left[C_1(\lambda^2 + \frac{2}{\lambda} - 3) + C_2(2\lambda + \frac{1}{\lambda^2} - 3) \right] c \tag{6-7}$$

for a Mooney-Rivlin strain energy function and

$$T = 2k\left[C_{10}(\lambda^2 + \frac{2}{\lambda} - 3) + C_{20}(\lambda^2 + \frac{2}{\lambda} - 3)^2 + C_{30}(\lambda^2 + \frac{2}{\lambda} - 3)^3 \right] c \tag{6-8}$$

for a Yeoh strain energy function.

Figure 6-4 shows the tearing energy against the crack length for the different approaches with a specimen length and height respectively equal to 40 mm and 100 mm. It can be seen that the theoretical tearing energy calculation is as anticipated valid over a limited range of crack lengths. The balance of energy used to determine the energy release rate can be used only if the unstretched region of the sample evolves as a squared function of the crack length. Once this unstretched region has reached one of the clamped edges of the specimen, the relationship is no longer valid. For a longer specimen, the formula for the tearing energy is valid over a wider range.

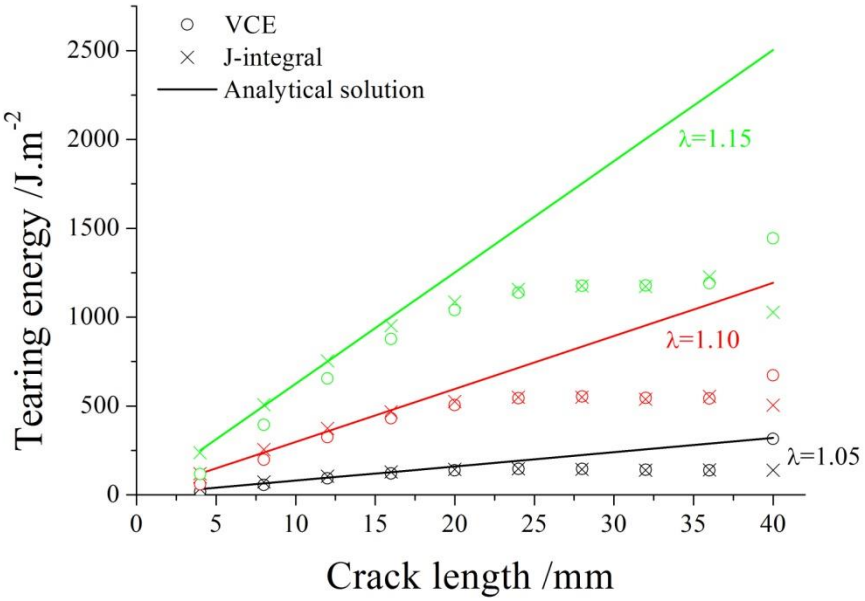

Figure 6-4. Tearing energy calculated for the edge crack sample deviates from theory for higher crack length.

Figure 6-5 shows that for a crack length less than 40% of the sample length, the tearing energies calculated with each method are in good agreement with the theoretical values which has been drawn for a crack of length 12 mm. Values are closer to the measured experimental data than for the previous pure shear case due to the better fit of experimental data in tension than in pure shear. This is especially true for the unfilled material where the behaviour at the low extension ratio is well characterised using the Mooney-Rivlin strain energy function (see Figure 3-20).

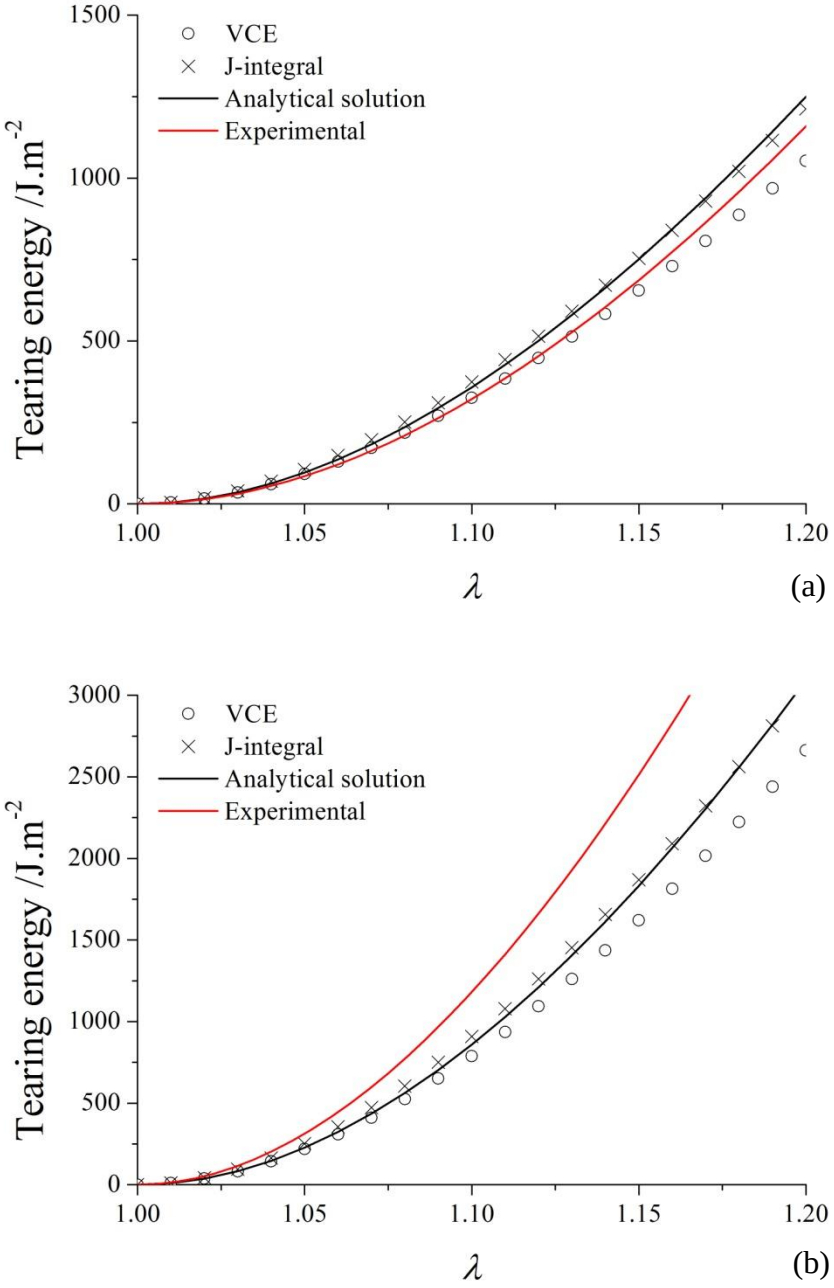

Figure 6-5. Results of simulation are in a reasonable agreement with theory and experimental data for (a) SBR0 and (b) SBR50.

6-3. **Submodelling technique for common geometries**

Submodelling has been used to evaluate the tearing energy in a narrow region of the geometries described above. In this approach, the global model used to drive the boundary conditions of the submodel is crack free. A region of the global model is then remeshed more carefully with a crack introduced into the geometry.

6-3-1. A working example: the pure shear geometry

A model of a pure shear crack growth specimen is shown in Figure 6-6. Initially the global model was analysed without a crack. The region of interest was then reduced to a rectangle in the middle of the sample centred on the location of the crack and a submodel of the same size was created. Then a crack was introduced in the centre of the remeshed submodel and the crack was progressively grown in both directions. The boundary conditions of the submodel were driven by the displacements of the nodes located at the same coordinates in the global model. The tearing energy was calculated using the VCE and J-integral methods respectively and compared to the previous results in Figure 6-7 (a) and (b) for a crack of length 40mm in a global model of length 200mm. It can be seen that the results obtained from both simulations are similar to the tearing energies obtained from the model of the entire geometry. The displacements of the nodes driving the submodel are not affected by the presence of a crack in the whole geometry. If the crack is grown further (see Figure 6-8), a deviation from the results obtained on the whole geometry occurs as we are approaching the edge of the submodel and the displacements of the nodes on the sides of the submodel no longer correspond to the uncracked global model with such a long crack length.

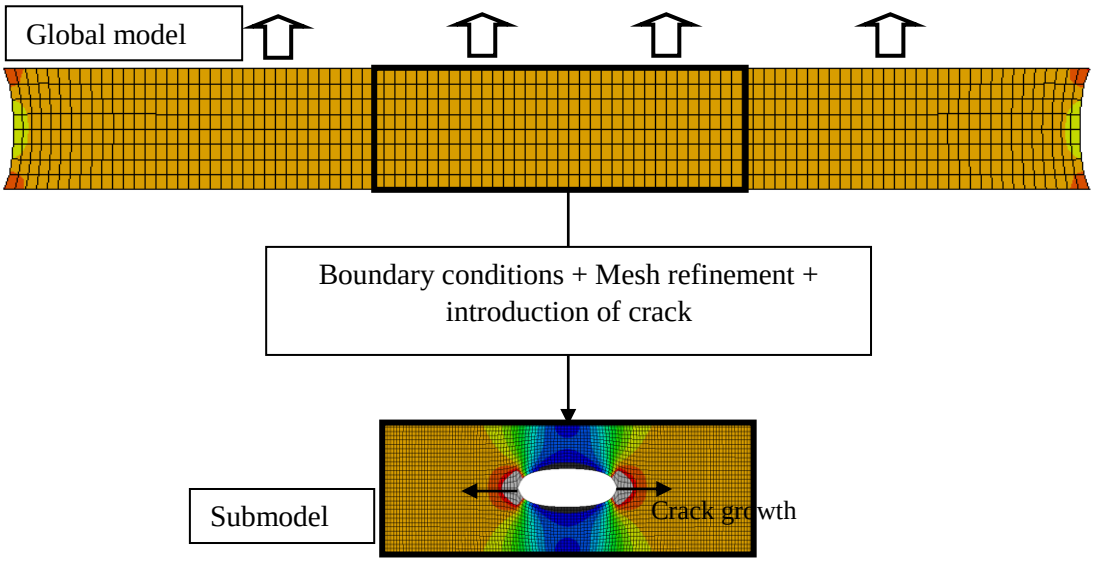

Figure 6-6. The region chosen to assess the submodelling technique.

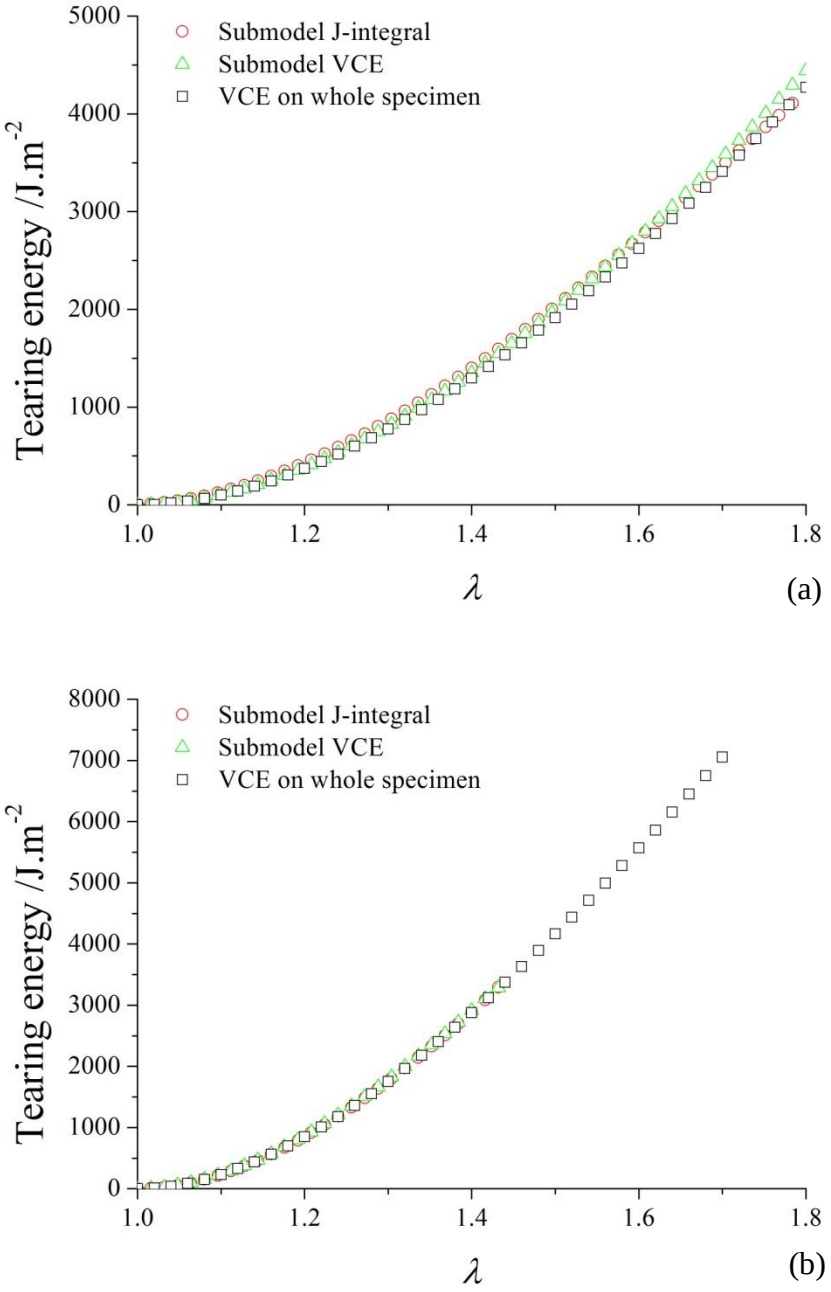

Figure 6-7. Submodelling technique calculates similar tearing energies to the global cracked model of pure shear geometry (a) SBR0 (b) SBR50.

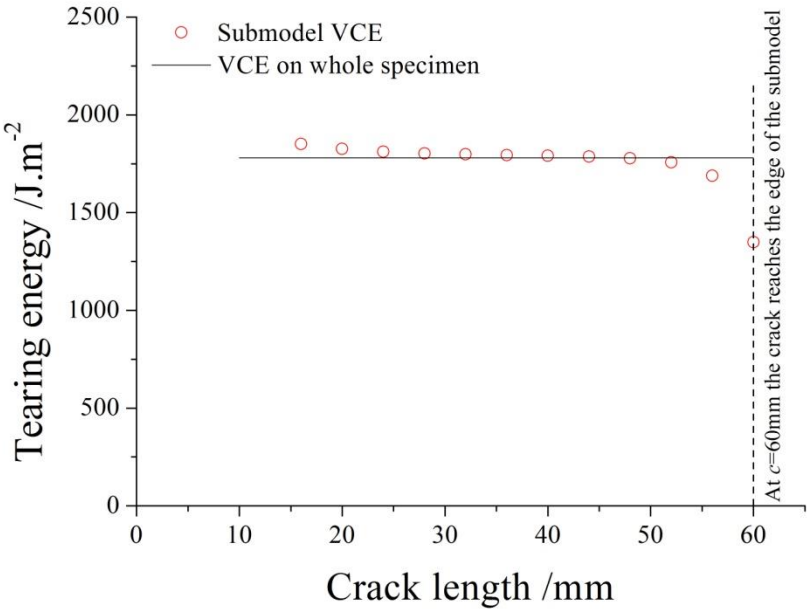

Figure 6-8. The tearing energy deviates from the whole geometry results as the crack approaches the edges.

6-3-2. Limitations of the method: edge crack specimen

A similar study has been performed with the edge crack geometry depicted in Figure 2-57. The nodes for the submodel were taken 20mm away on both sides of the horizontal axis of symmetry of the specimen as can be seen on Figure 6-9. A crack of length 12 mm in a specimen of 40 mm was chosen as it was known to be in the region where the theoretical calculations of the tearing energy are valid.

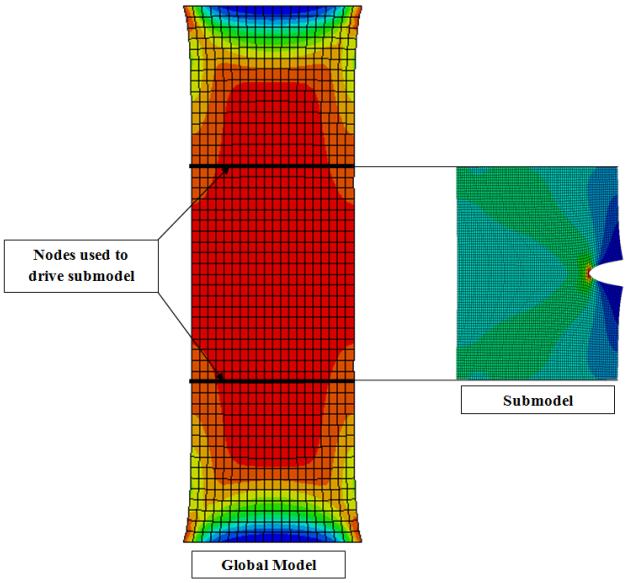

Figure 6-9. Submodelling the edge crack specimen.

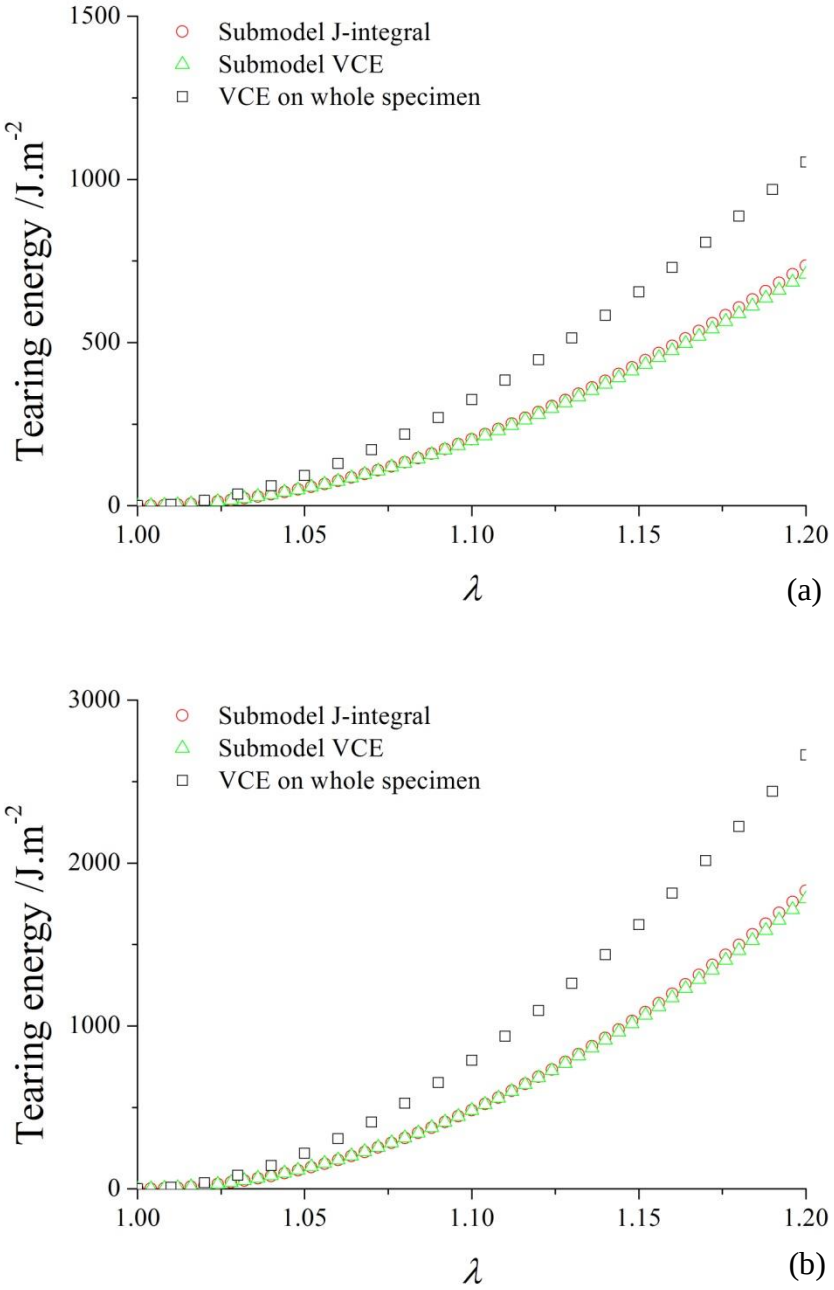

Figure 6-10. Submodelling approach compared with a global crack model. (a) SBR0 (b) SBR50.

The tearing energies obtained with the submodelling approach are shown in Figure 6-10 (a) and (b). It can be seen that the tearing energy calculated with the submodel differs significantly (about 30% less) from the values obtained with the model of the whole specimen obtained earlier in this chapter. The displacements of the nodes in the submodel are driven by the displacements obtained in a whole specimen free of a crack. As this global model is in uniaxial tension, the vertical displacement is constant over the width of the sample. Therefore the displacement of the driven nodes in the submodel is also identical over the width of the sample as can be seen in Figure 6-11. However, if a crack is introduced in the model of the entire specimen, the displacement of the nodes located in a plane perpendicular to the vertical axis no longer have the same displacement. Therefore, the displacements used in the submodel are inappropriate to model the behaviour of the geometry once a crack is introduced. This difference in the displacements explains the discrepancy in the results of the simulations. If the nodes chosen to drive the submodel are taken further away from the crack, the tearing energy tends towards the right value as shown on Figure 6-12 until the submodel eventually is identical in size to the global model with a crack.

The influence of the presence of a crack on the displacements of the nodes greatly depends on the geometry and the location of the crack. Indeed, if the crack was introduced in the middle of the sample instead of the edge, the values obtained would be a better approximation as the displacements remote from the crack would be modified to a lesser extent. The influence of the presence of a crack in the global model on the displacements of the nodes chosen to drive the submodel has to be considered to ensure the application of the submodelling is valid.

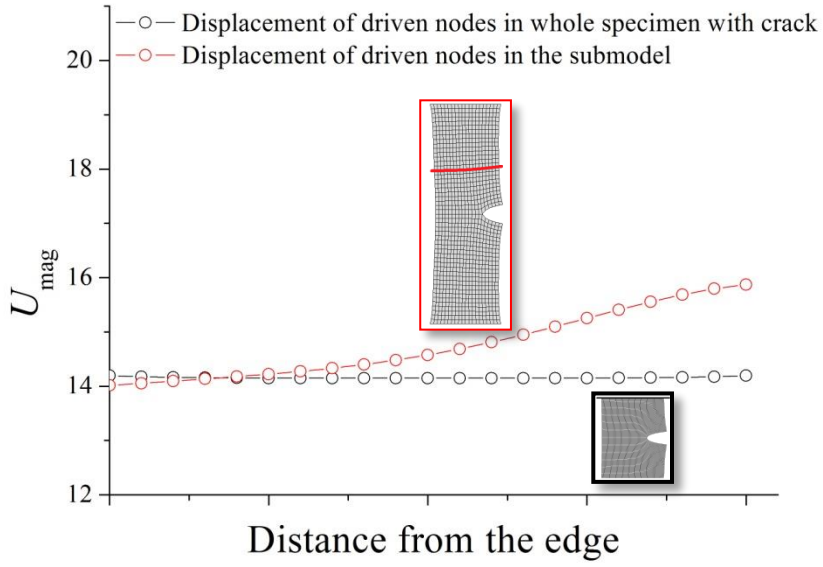

Figure 6-11. The displacements of the driven nodes are modified by the presence of the crack.

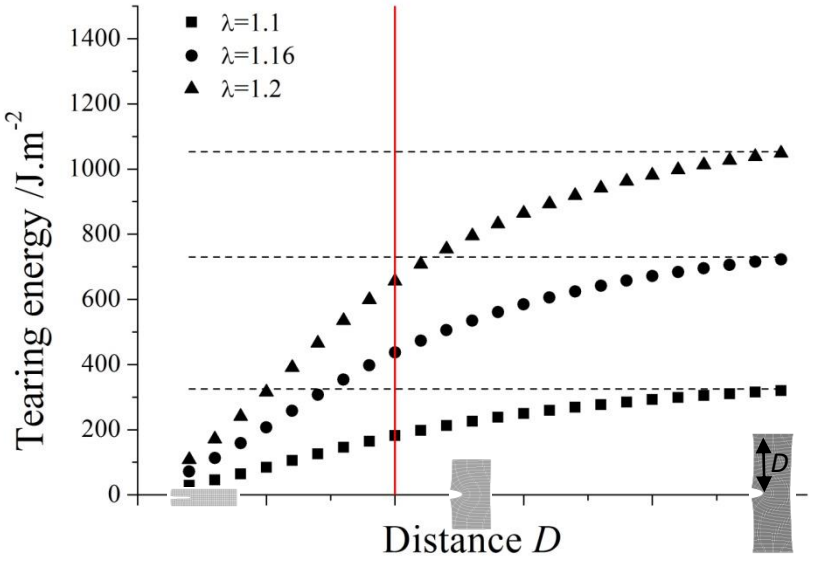

Figure 6-12. Evolution of the tearing energy with size of the submodel. The dashed lines represent the values for the simulations with the whole specimen, the red line is the distance at which the results in Figure 6-10 were obtained.

6-4. **Tyre model used in this study**

6-4-1. Presentation of the model

The model of the tyre used in this study starts as a 2D axisymmetric geometry rotated around the tyre centre (see Figure 6-13) and includes the different relevant parts of a tyre (bead, cords, body plies and rubber compounds). Interpolated strain energy functions derived in Section 3-7 are implemented in the software to reflect the behaviour of the rubber compounds. The steel in the bead is modelled as a linear elastic exhibiting Hooke's law with a modulus of 207 GPa and Poisson ratio of 0.3. Nylon cords are modelled as rebar elements which act as reinforcing layers added to the rubber elements and are characterised by a Marlow strain energy function fitted to uniaxial tensile data. The grooves in the tyre tread were removed as they increase significantly the computing time due to the self contact conditions arising at higher loads and because this geometric simplification does not alter the state of the region of interest in the study which was located close to the bead. The tyre tread was therefore simply considered to be flat.

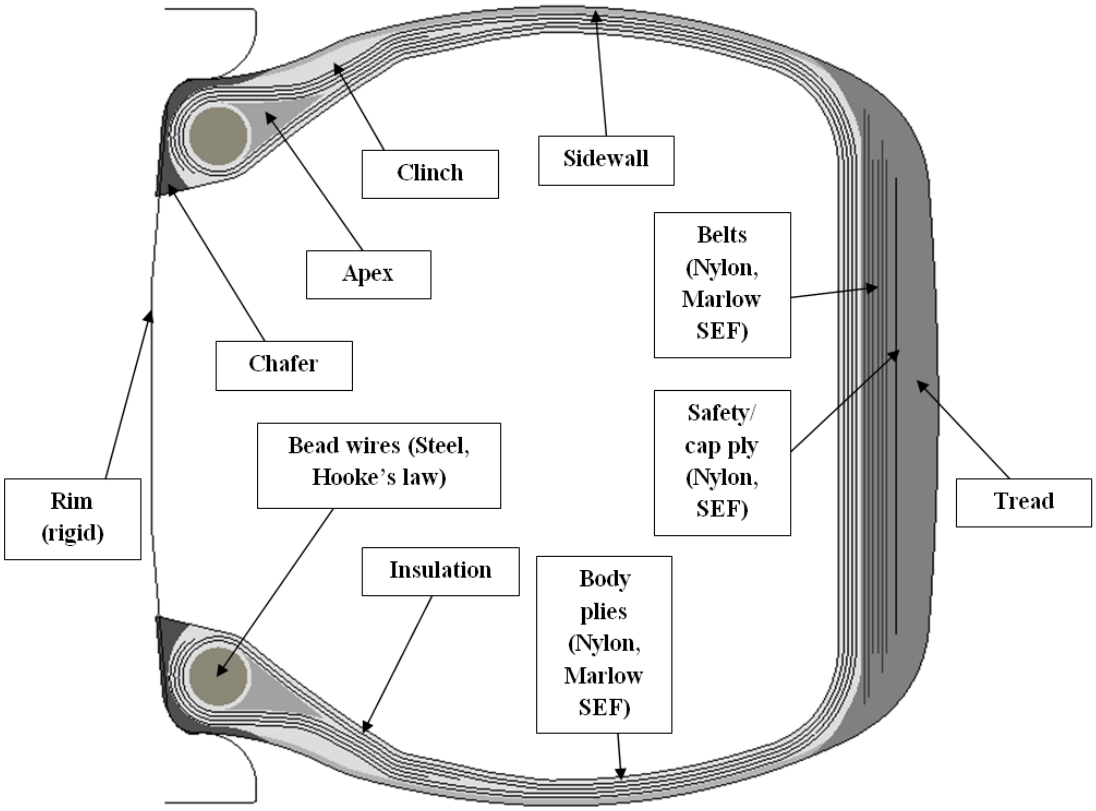

Figure 6-13. Axisymmetric model of the tyre. The materials are rubber compounds unless otherwise stated.

The unloaded 2D model with all axisymmetric external conditions is first revolved around the centre line to generate a 3D model. The contact and the boundary conditions as well as the inflation load are therefore transferred. The size of the elements around the axis can be controlled. The analysis is then divided into three steps. First the contact conditions are applied to fit the tire to the rim, and then the tire is inflated to 1.18MPa by the application of a load over the surface of the innerlayer. Finally a vertical force of 100kN reflecting the contribution of the weight of the aircraft on a single wheel is applied by displacing the road surface.

The results of this global model can then be used to control the boundary conditions of a chosen submodel. The displacements of the nodes in the global model are saved in a file and are applied to selected nodes in the submodel by interpolating their boundary position. This procedure allows the mesh to be refined quite significantly to obtain precise data with a reduced computing demand. Moreover, the mesh can be modified to include a flaw and thus permit the use of the fracture mechanics approach even for relatively large components. An example of a submodel of a reduced portion of the original global model is shown in Figure 6-14.

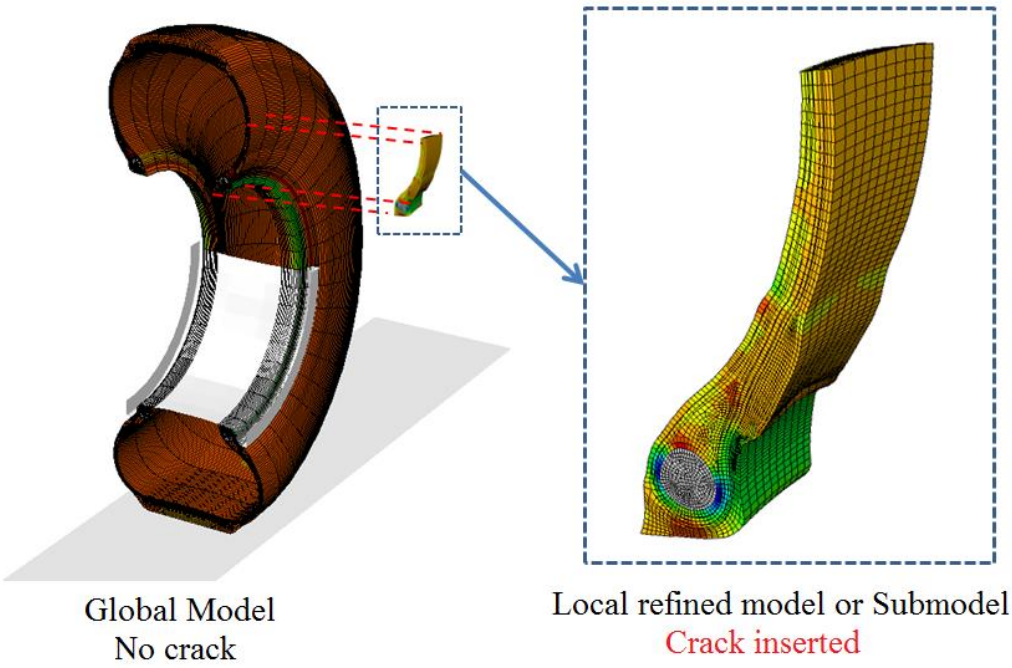

Figure 6-14. The region chosen for the submodel is significantly refined and a crack is introduced.

6-4-2. Selection of the driven nodes in the submodel

As noted previously, the displacements of the nodes used to drive the boundary conditions of the submodel should not be significantly modified by the presence of the crack to obtain accurate results. To select the nodes for the submodel on the tyre, displacements obtained using both crack free and partially torn 2D axisymmetric models were compared. In the axisymmetric simulation, the crack is considered to exist on the whole circumference of the component and the loading is applied to the entire tread. A force ten times higher than on the real tyre was applied in this model and the crack was three times longer than in the real cases modeled in this investigation, higher crack length generally leading to a larger affected area. The axisymmetric case with a crack was therefore a worst-case scenario. Figure 6-15 presents the position of the nodes in both models. For clarity purpose, only the nodes used to drive the submodel are shown. The green error bars represent the deviation of the displacement magnitude between the two models.

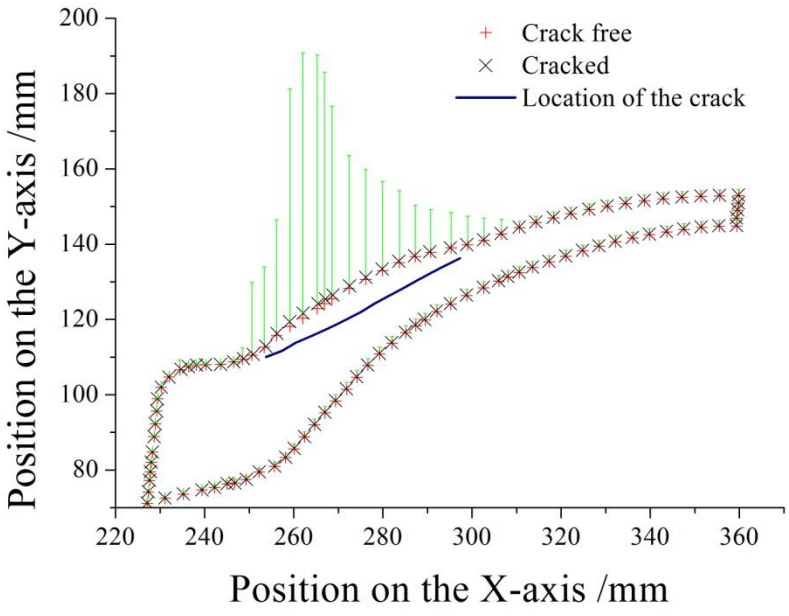

Figure 6-15. Comparison of the position of the nodes in an axisymmetric model with a large crack and 1MN load. The error bars represent the change in the displacement of the nodes amplified by a factor 50 for clarity.

The positions of the nodes on the edge of the region of interest are very similar with or without a crack. The difference is only significant close to the crack location where a change of as much as 30% in the magnitude of the displacement can be observed. The sudden drop on the left of the crack is due to the presence of the rim restraining the motion of the rubber in the vertical direction. Everywhere else, the change in the displacement between the two models is lower than 0.2% in magnitude. This slight change is mainly due to the decrease in stiffness of the region due to the presence of the crack. The application of a compressive force thus shifts the nodes slightly towards the rim. This decrease in stiffness would not be as significant in a model of the whole tyre with a short crack but is the result of the axisymmetry.

In conclusion, the nodes shown in Figure 6-15 seem adequate to serve as reference for the submodel as the introduction of the crack does not significantly alter their position. The nodes on the exterior face were left free to avoid an over constraint if the crack was extended further. In conjunction, all the nodes on the face were used at the first and last set of nodes in the circumferential direction to account for the cyclic symmetry around the tyre. Nodes on the driven surfaces are shown in Figure 6-16.

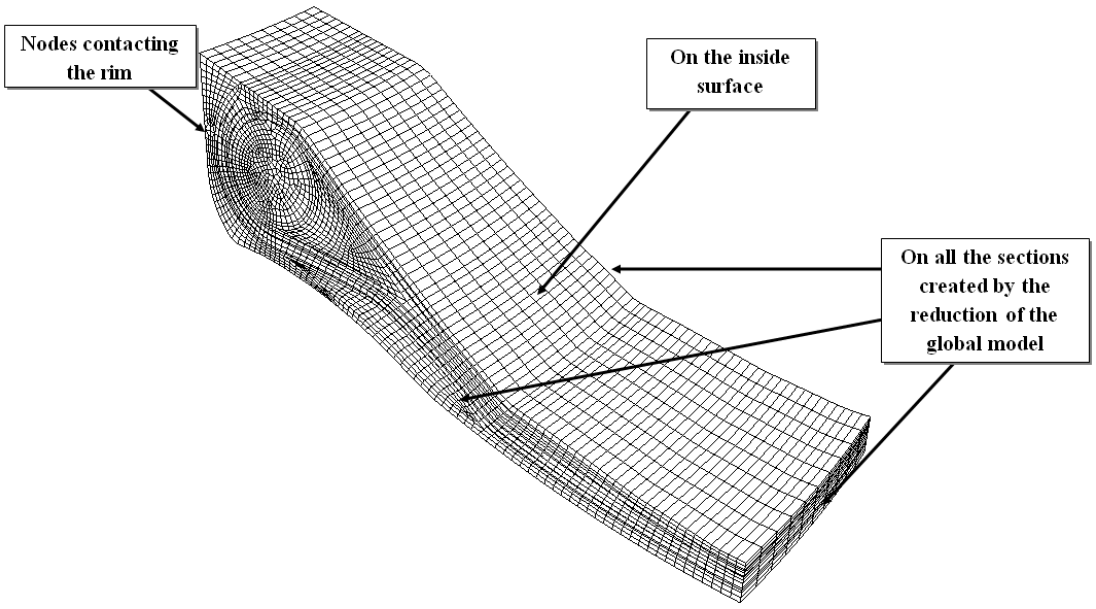

Figure 6-16. Nodes chosen for the submodel of the region close to the bead in the tyre.

6-5. **Evaluation of the tearing energy for various cases**

The tearing energy in the tyre has been evaluated with the VCE approach only. The J-integral approach was initially used but the large modulus mismatch between the materials in the region of the crack tip makes its application unreliable. Taking a contour in the vicinity of the tip of the crack results in error as the fields are not accurately calculated but taking it remote of the tip results in a path dependent integral as the contour and the crack both bridge interfaces between different materials.

Aircraft tyres are subjected to a battery of certification tests before being used in commercial flights including simulations of life cycles such as take-offs, landings and taxiing of an airplane using a large cylinder as a model road surface rotating at different speeds. The structure and the materials inside are therefore fatigued under similar conditions to the real environment of the tyre. The different crack locations and loading cases that were identified in such tests were each investigated closely.

6-5-1. Crack in the vicinity of the clinch

An experimental investigation made on a tyre test rig showed that the typical location of crack growth leading to failure of the tyre was in the neighbourhood of the interface between the clinch and the body plies. A crack introduced between the clinch and the body plies compound was therefore modelled first (Figure 6-17). Two surfaces were created on both sides of the interface and a frictionless contact condition was defined to prevent interpenetration of the two surfaces in compression under load. The size of the crack was varied in the simulations to apply the VCE method to calculate the tearing energy. The crack was extended in both a radial and circumferential directions as shown in Figure 6-18 which identifies both cases.

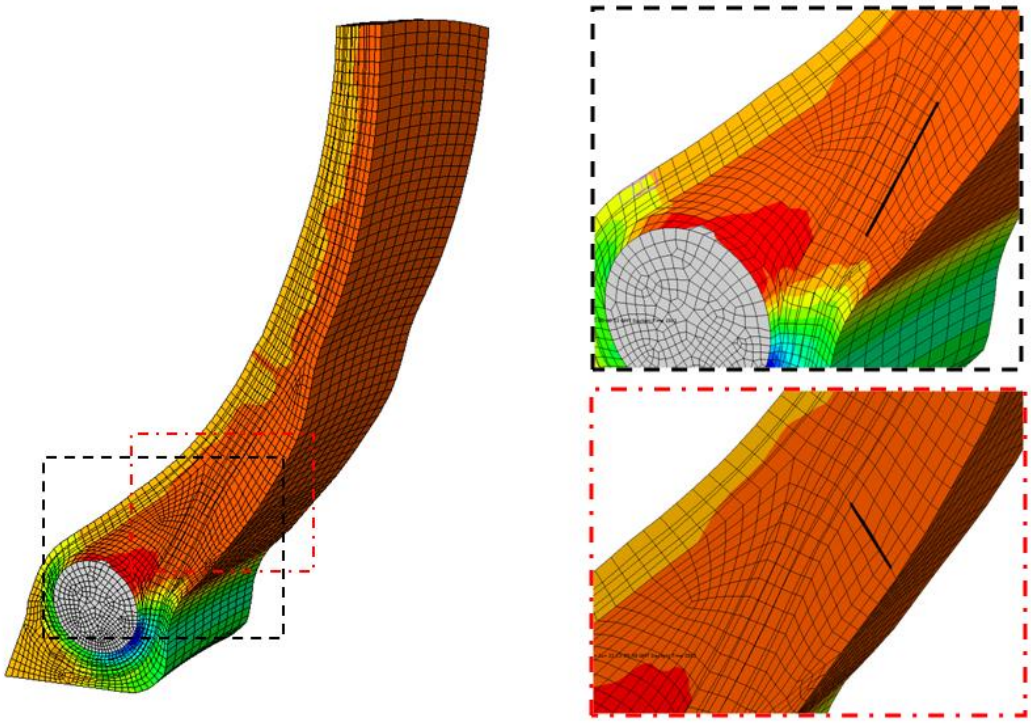

Figure 6-17. Locations of the cracks in the tyre.

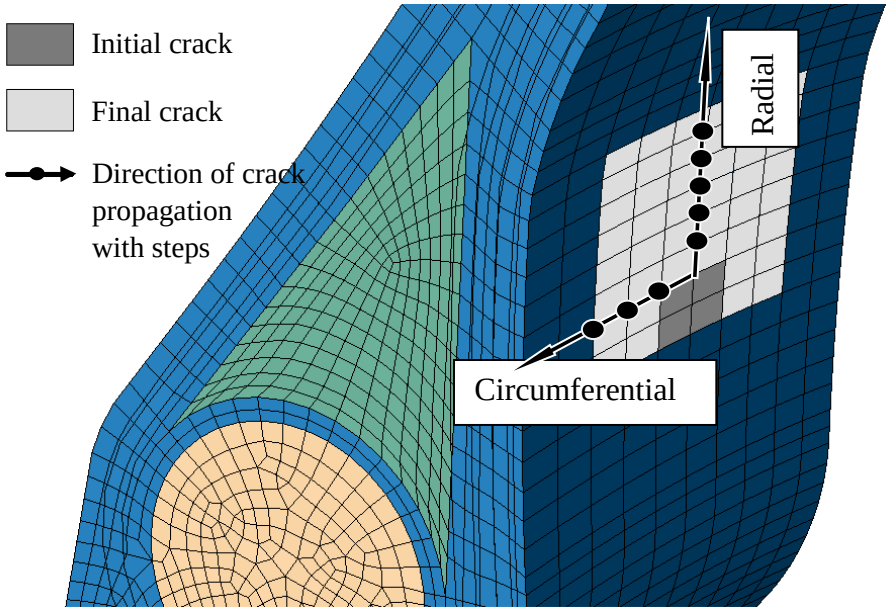

Figure 6-18. Crack growth in the model. The front surface is the surface of the body plies (clinch and sidewall have been removed for clarity).

Results of the model are shown in Figure 6-19 for a crack grown in the radial direction (a) and the circumferential direction (b) after the inflation of the tyre only. In the circumferential case, the crack was grown on both sides of the axis of symmetry for the crack. The loading of the tyre with a vertical load caused the crack to close completely and therefore the tearing energy was considered to be null. In the radial direction, the

trend was the same for moderate width of the crack but a larger increase in the tearing energy was observed when the width approached the edge of the submodel. It was thought likely that the results with 6 elements width might be overconstrained due to the boundary conditions applied on the external surfaces of the submodelling region. The first point of the 2 elements wide curve gives a higher tearing energy than the 4 elements case. This point is obtained with a relatively crude mesh resolution (the dark grey in Figure 6-18) and therefore, the nodes defining the crack are likely to be overconstrained leading to a higher release of energy as the number of elements defining the crack profile are increased. In the circumferential direction, the tearing energy increases with the width of the crack. A 4 elements wide crack with a length of 7.65 mm was used for further examination of this location of the crack.

The submodelling technique only uses the deformation of the nodes in the global model therefore it is straightforward to model how the behaviour of a region changed during all the different phases during the rotation of the tyre. The tearing energies were calculated in the submodel as the region of interest is rotating around the wheel axle both after inflation and the application of the normal loading. Results are shown in Figure 6-20 for a complete rotation under the normal load. It was observed for this specific crack that the maximum tearing energy was achieved as a spike when this region of the tyre initially contacted the road surface and it was reduced to zero whilst in contact with the road. This sharp peak in the energy release rate will also reflect a very rapid rate of loading at the crack tip which might significantly influence the resistance to fatigue crack growth by inhibiting strain induced crystallisation at the crack tip of the natural rubber present in this region (Sakulkaew et al. (2010)).

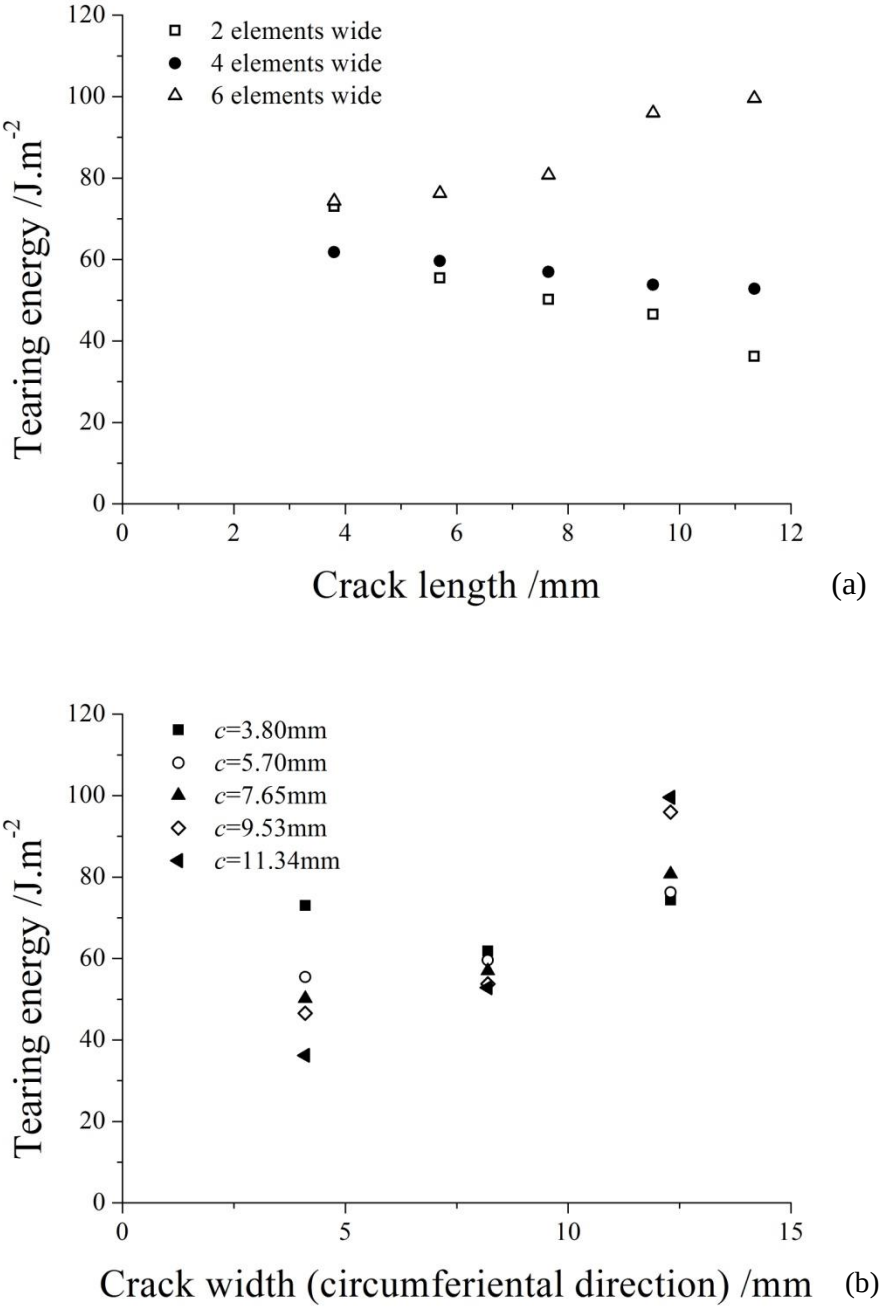

Figure 6-19. Tearing energy for a crack between the clinch and the body plies growing (a) in the radial direction (b) in the circumferential direction.

The tearing energies were relatively modest and should not account for a significant mechanical damage in the tyre. The value of the tearing energy went back to the inflation value as the tyre rotated and the tread region adjacent to the crack was no longer in contact with the road. Due to a limited computing resource, an even finer mesh was not attempted for the global model to examine the spike in the curve more carefully. It would be interesting to see how the tyre behaves around the point of contact

with the road by increasing the number of circumferential elements defining the tyre and the submodel and shifting the position of the crack element by element in the submodel but time constraints prevented this.

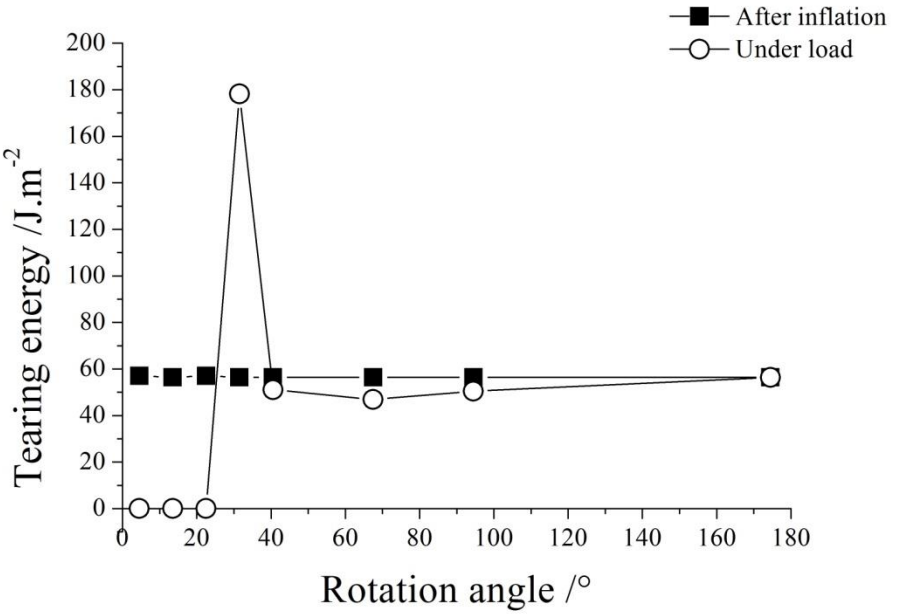

Figure 6-20. Tearing energy obtained through the revolution of the submodel.

6-5-2. Crack growth in the perpendicular direction

Straight rolling

Examining tyres that had failed on the rig test highlighted cracks also grew from the body plies through the clinch until reaching the external surface of the tyre. Although occurring less frequently than the previous case, it was also considered here by growing the crack in the perpendicular direction as shown on Figure 6-17. Initially, a crack in the submodel was modelled for the region where the highest deformation occured under loading (at a rotation angle of 4.5°) and this was inflated only as the road contact loading led to the closure of the crack. The surface towards which the crack was grown was free of constraint (no imposed boundary conditions from the global model) in the submodel so its displacements were not constrained. Figure 6-21 shows the tearing energy increasing significantly as the crack approaches the tyre surface. The inflation of the tyre is critical as it opens the crack while the cyclic loading as the tyre rolls on the track causes crack closure.

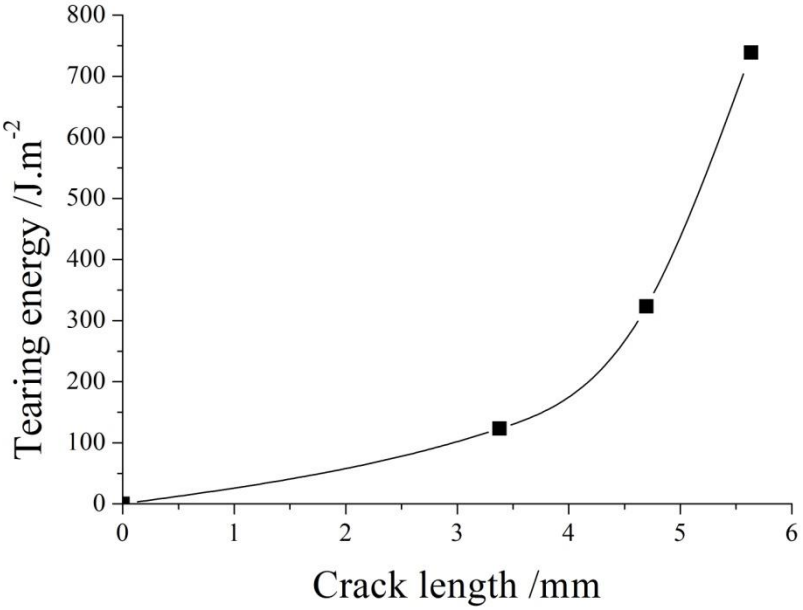

Figure 6-21. Evolution of the tearing energy with crack length for a crack in the clinch.

Cornering conditions

Vertical loading of the tyre causes the closure of the crack. A second lateral shear force was introduced to get its effect on the tearing energy in this region under higher cornering conditions that might open the crack and cause higher crack growth. Figure 6-22 shows that the crack is subjected to much more severe conditions during cornering and that the energy release rate was significantly increased. This type of loading would introduce a significant mechanical damage and adversely affect the lifetime of the tyre. Under cornering conditions, the tearing energy never returns to a fully relaxed condition as the tyre rolls because even under the inflation alone, the tearing energy is positive. Therefore, for a crack in the natural rubber in this specific location, the cornering phase might become less critical for the lifetime of the structure.

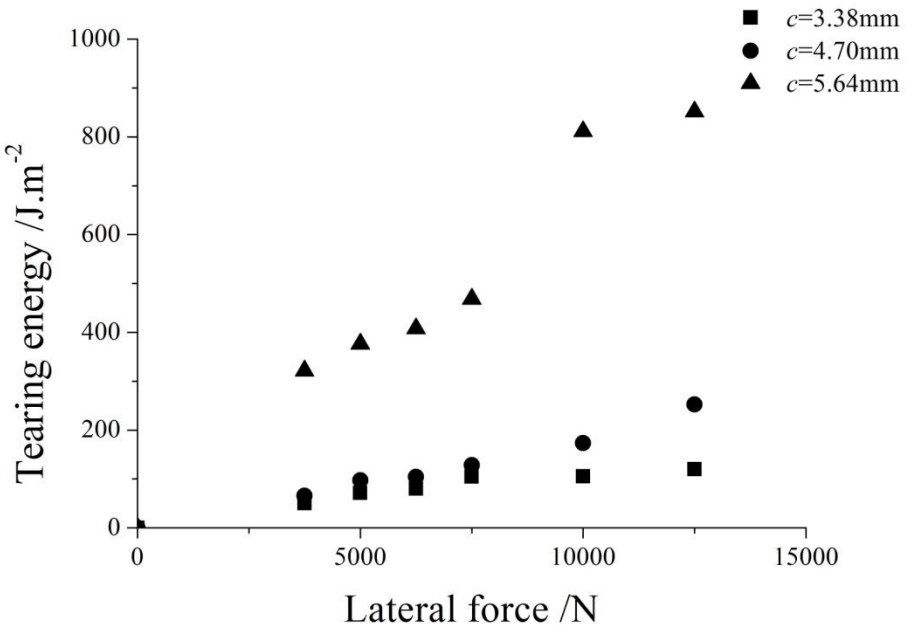

Figure 6-22. Effect of cornering on the tearing energy in the clinch region.

6-6. **Conclusion on using submodelling to calculate tearing energy**

The use of a submodel significantly decreased the computing time and allowed a significant mesh refinement around a small flaw such as a crack in a large structure where an entire model of a suitable mesh size would produce an unfeasibly large number of elements. The precision of the method can be questioned as both the global and the local simulations will generate significant errors that accumulate. The submodelling technique appears to be valid to evaluate the tearing energy as long as the nodes that drive the submodel are carefully chosen and the displacements used as boundary conditions from the global model are not influenced by the modification of the submodel geometry to introduce a crack. The study on the tyre presented in this chapter does not claim to be precise but does represent the conditions found in the tyre during use. The model was, for example, not optimised in terms of material behaviour, the mesh refinement or the method used to obtain the tearing energy. Time dependence and temperature dependence of the materials mechanical properties have not been taken into account for example nor have the imperfect elasticity and viscoelasticity. However, overall the predictions of the tearing energies give reasonable values. It transpires from the simulations that they are not high enough to cause a dramatic or premature failure as for most of the situations accounted for in this study, they are in the range of chemical

degradation of the fatigue behaviour of the materials used in the tyre and therefore the crack growth rate is low. However they could result in a significant crack growth rate for materials presenting low fatigue resistance or poorly bonded interfaces such as those described in Chapter 5. The values obtained appear realistic and allow an estimation of potential lifetimes for specific cracks to be calculated and compared with experimental data obtained on a test rig for validation.

CHAPTER 7 -CONCLUSION AND FUTURE WORK

7-1. **Conclusions**

The most significant conclusions of this thesis can be summarised as follows:

The fatigue crack growth behaviour of a non-strain crystallising rubber such as SBR was found to be the sum of a time dependent and an additional cyclic contribution. The magnitude of these two components were calculated based on the relationship between the static crack growth rate and the tearing energy and the measurement of the fatigue properties at different frequencies. The time dependent behaviour dominates the fatigue tear behaviour at high tearing energies and low frequencies whereas the cyclic component dominates at low tearing energies and high frequencies. The tests conducted in this thesis show that when a constant maximum tearing energy is applied for a major part of the cycle, the rubber behaviour approaches a fully time dependent behaviour although the theory based on the static crack growth fails to predict the correct values for the materials characteristics in fatigue. The various tests made with different waveforms suggest the cyclic component acts as an amplification factor to the crack growth obtained in static crack growth by damaging or irreversibly modifying the material ahead of the crack tip. The cyclic contribution is therefore not seen as an additional term anymore but rather as a factor multiplying the time dependent crack growth at any time of a cycle and it isespecially significant at low values of the tearing energy during the cycle. This effect could originate in the progressive damage of the rubber network in the high strain region at the crack tip.

A peeling specimen geometry with a reduced surface has been developed and gives similar fatigue behaviour to other typical specimen geometries. Relatively strong bonding between two vulcanised rubbers (peeling energy higher than $10kJ.m^{-2}$) have successfully been separated in the region of the interface. The modification of the common peeling geometry allowed the measurement of the fatigue properties at an interface between two vulcanised rubbers brought in contact in the early stages of the vulcanisation. With sufficient time of contact and under conditions favourable to the

establishment of good contact which are a function of the time of curing and the viscoelastic properties of the green material, the resulting fatigue behaviour of the interface was similar to the fatigue properties of the weakest material.

The influence of pressure although obtained in very specific conditions (short contact time and hence a reduced time to allow interdiffusion) is much more significant than on the unvulcanised case reported in the literature. A significant effect of the compressive pressure applied to the interface during vulcanisation was observed for the interface between two sheets of SBR70. The resulting crack surfaces topography show a significant change in their pattern which provides a robust confirmation that the fatigue properties are greatly affected by the vulcanising pressure. The variation of the resistance to fatigue crack growth is attributed to the progressive establishment of contact at the interface due to the high viscosity of the material and potential diffusion of air from the interface to the bulk rubber coupled with the fast interdiffusion occurring in the region where contact has been achieved.

An attempt to determine the tearing energies for particular crack location in a tyre was made using a refined submodel in finite element analysis. Although the tyre model is not optimised, the tearing energies found in this thesis were of the right order of magnitude and could lead to potential failure of the tyre when inherent flaws are present or when the different layers are weakly bonded together such as in Chapter 5. This represents a significant step towards better fatigue life prediction in tyres.

7-2. **Proposition for future work**

In this thesis it is proposed the cyclic contribution occurs at any time during a cycle and is more significant at small values of the tearing energy. Tsunoda (2001) proposed a method to observe the crack growth during one single cycle observing the deformation at the crack tip. This method could be used to see how the total crack growth rate changes with time during a single cycle and the results compared to the predicted values of the theoretical time dependent contribution to observe at what point of the cycle the cyclic contribution affects the crack growth the most.

The cyclic coefficient f_{cyclic} may be approximated by a damage function and inserted back into equation (4-5) to calculate the crack growth rate per cycle directly from a static steady state crack growth experiment. The effect of the damage function would

increase to the value of the tearing energy at any time during the cycle. This function may include the effect of the number of cycle applied as well as the effect of the loading rate. Figure 7-1 (a) and (b) illustrates the state of strain around the crack tip for the static crack growth tests. The rate of loading τ_{load}^{static} of a volume element of rubber approaching the crack tip and initially sufficiently far from the crack tip to be undeformed can be expressed as a function of the static crack growth rate *r*.

$$\tau_{load}^{static} = \frac{d}{r} \tag{7-1}$$

The distance *d* is the crack growth required to load a volume of rubber from the unstrained state to fracture and is related to the radius of the crack tip in the steady state of crack growth. An evaluation of *d* can be made using finite element analysis. For a 0.1 mm crack radius, *d* was found to range between 15 and 25 mm for the range of tearing energies achieved during the tests. In fatigue, a large number of cycles have to be applied to the crack to reach a total crack growth of length *d* which therefore could represent a measure of the number of cycles the rubber is subjected to from the undeformed state to fracture.

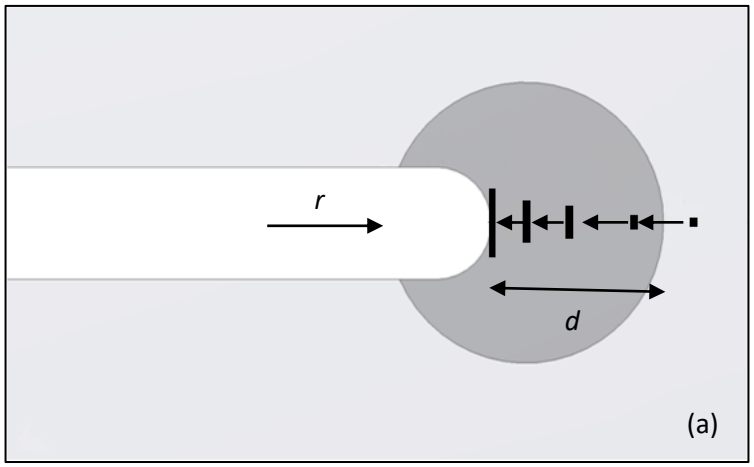

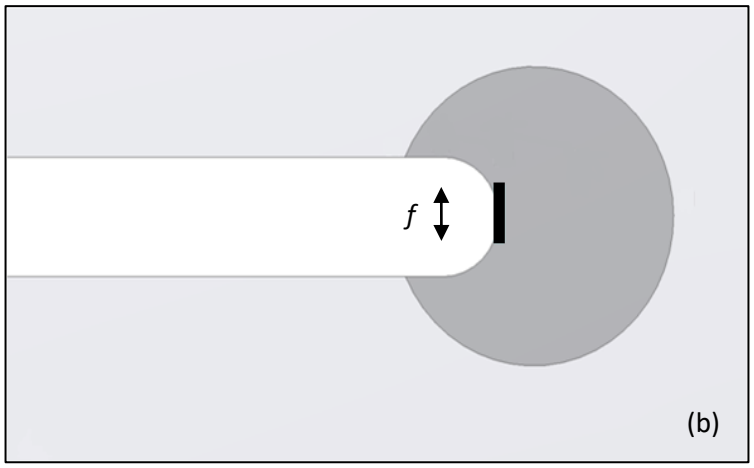

Figure 7-1. Loading of the rubber is (a) slower in the static crack growth tests than in the (b) fatigue tests.

In the cyclic crack growth tests, the rate of loading at the crack tip is imposed by the sinusoidal loading which alternatively opens and closes the crack. Using the frequency *f*, the time of loading can be expressed as

$$\tau_{\text{load}}^{\text{cycling}} = \frac{1}{2f} \tag{7-2}$$

The effect of the loading rate might be considered by the ratio of both times of loading.

The effect of pressure on the resulting strength is only apparent when interdiffusion and contact do not have sufficient time to develop fully. The high temperature of vulcanisation is therefore a significant problem to study how the interfaces get stronger as both contact and interdiffusion are accelerated with temperature. One way to circumvent this problem would be to use alternative vulcanising processes at room temperature such as UV light vulcanisation. Alternatively, the molecular weight of the polymer might be increased to maximise the reptation time of the molecules and therefore increase the time for a chain to cross the interface. A molecular modelling software could be used to analyse the molecular motion across the interface and the dynamics of formation of the interface on the nanoscale to give an indication of how the reinforcement mechanisms at the crack tip might be triggered. The compressive pressure applied to the interfaces between unvulcanised polymers in tyres could be modelled during the moulding phase in order to detect region where pressure is insufficient to ensure good resistance to crack growth.

References

Alexander, H. (1968), "A Constitutive Relation for Rubber-Like Materials." *International Journal of Engineering Science* **6:** 549.

Ali, A., Hosseini M., Sahari B. (2010), "A Review of Constitutive Models for Rubber-Like Materials." *American Journal of Engineering and Applied Sciences* **3:** 232.

Andrews, E. (1961), "Crack Propagation in a Strain-Crystallizing Elastomer." *J Appl Phys* **32:** 542.

Ansarifar, M.A., Fuller K.N.G., Lake G.J. (1993), "Adhesion of Unvulcanized Elastomers." *International Journal of Adhesion and Adhesives* **13:** 105.

Arruda, E.M., Boyce M.C. (1993), "A Three-Dimensional Constitutive Model for the Large Stretch Behavior of Rubber Elastic Materials." *Journal of the Mechanics and Physics of Solids* **41:** 389.

Asare, S., Busfield J.J.C. (2011), "Fatigue Life Prediction of Bonded Rubber Components at Elevated Temperature." *Plastics Rubber and Composites* **40:** 194.

Asare, S., Thomas A.G., Busfield J.J.C. (2009), "Cyclic Stress Relaxation (Csr) of Filled Rubber and Rubber Components." *Rubber Chemistry and Technology* **82:** 104.

Auer, E.E., Doak K.W., Schaffner I.J. (1958), "Factors Affecting Laboratory Cut-Growth Resistance of Cold Sbr Tread Stocks." *Rubber Chemistry and Technology* **31:** 185.

Beatty, J.R. (1964), "Fatigue of Rubber." *Rubber Chemistry and Technology* **37:** 1341.

Bernstein, B., Kearsley E.A., Zapas L.J. (1965), "A Study of Stress Relaxation with Finite Strain." *Rubber Chemistry and Technology* **38:** 76.

Bouasse, H., Carriere Z. (1903), "Courbes De Traction Du Caoutchouc Vulcanisé." *Ann Fac Sci Toulouse* **5:** 257.

Boyce, M.C., Arruda E.M. (2000), "Constitutive Models of Rubber Elasticity: A Review." *Rubber Chemistry and Technology* **73:** 504.

Brenner, S.C., Scott R. (2008), *The Mathematical Theory of Finite Element Methods*, Vol. 15: Springer.

Busfield, J.J.C. (2000), "The Prediction of the Mechanical Performance of Elastomeric Components Using Finite Element Analysis." Queen Mary and Westfield College, University of London.

Busfield, J.J.C., Jha V., Liang H., Papadopoullos I.C., Thomas A.G. (2005), "Prediction of Fatigue Crack Growth Using Finite Element Analysis Techniques Applied to Three-Dimensional Elastomeric Components." *Plastics Rubber and Composites* **34:** 349.

Busfield, J.J.C., Thomas A.G., Ngah M.F. (1999), *Application of Fracture Mechanics for the Fatigue Life Prediction of Carbon Black Filled Elastomers*.

Busfield, J.J.C., Tsunoda K., Davies C.K.L., Thomas A.G. (2002), "Contributions of Time Dependent and Cyclic Crack Growth to the Crack Growth Behavior of Non Strain-Crystallizing Elastomers." *Rubber Chemistry and Technology* **75:** 643.

Busfield, J.J.C.R.C.H.T.A.G. (1997), "Crack Growth and Strain Induced Anisotropy in Carbon Black Filled Natural Rubber." *Journal of Natural Rubber Research* **12:** 131.

Choi, I.S., Roland C.M. (1997), "Strain-Crystallization of Guayule and Hevea Rubbers." *Rubber Chemistry and Technology* **70:** 202.

Cohen, A. (1991), "A Padé Approximant to the Inverse Langevin Function." *Rheologica Acta* **30:** 270.

Criscione, J. (2003), "Rivlin's Representation Formula Is Ill-Conceived for the Determination of Response Functions Via Biaxial Testing." *Journal of Elasticity* **70:** 129.

Darnell, I., Mousseau R., Hulbert G. (2002), "Analysis of Tire Force and Moment Response During Side Slip Using an Efficient Finite Element Model." *Tire Science and Technology* **30:** 66.

Davies, C., De D., Thomas A.G. (1994), "Characterization of the Behavior of Rubber for Engineering Design Purposes. 1. Stress-Strain Relations." *Rubber Chemistry and Technology* **67:** 716.

Davies C. K, L., De D K., Thomas A G. (1996), "Characterisation of the Behaviour of Rubber for Engineering Design Purposes : Stress Relaxation under Repeated Stressing." *Progress in rubber and plastics technology* **12:** 208.

Davies, C.K.L., De D.K., Thomas A.G. (1996), "Characterisation of the Behaviour of Rubber for Engineering Design Purposes : Stress Relaxation under Repeated Stressing." *Progress in rubber and plastics technology* **12:** 208.

Davis, C., Lemoine F., Darnige T., Martina D., Creton C. (2014), "Debonding Mechanisms of Soft Materials at Short Contact Times." *Langmuir* **30:** 10626.

De, D. (1996), "Tear Strength of Carbon-Black-Filled Compounds." *Rubber Chemistry and Technology* **69:** 834.

Diani, J., Fayolle B., Gilormini P. (2009), "A Review on the Mullins Effect." *European Polymer Journal* **45:** 601.

Dizon, E.S., Hicks A.E., Chirico V.E. (1974), "The Effect of Carbon Black Parameters on the Fatigue Life of Filled Rubber Compounds." *Rubber Chemistry and Technology* **47:** 231.

Doi, M., Edwards S.F. (1978a), "Dynamics of Concentrated Polymer Systems. Part 1.- Brownian Motion in the Equilibrium State." *Journal of the Chemical Society, Faraday Transactions 2: Molecular and Chemical Physics* **74:** 1789.

Doi, M., Edwards S.F. (1978b), "Dynamics of Concentrated Polymer Systems. Part 2.- Molecular Motion under Flow." *Journal of the Chemical Society, Faraday Transactions 2: Molecular and Chemical Physics* **74:** 1802.

Doi, M., Edwards S.F. (1978c), "Dynamics of Concentrated Polymer Systems. Part 3.- the Constitutive Equation." *Journal of the Chemical Society, Faraday Transactions 2: Molecular and Chemical Physics* **74:** 1818.

Donea, J., Huerta A., Ponthot J.P., Rodríguez-Ferran A. (2004), "Arbitrary Lagrangian–Eulerian Methods." In *Encyclopedia of Computational Mechanics*: John Wiley & Sons, Ltd.

DSSimulia (2012), In *Abaqus Analysis User's Manual*, Version 6.12 edn.

Fenner, R.T. (1975), *Finite Element Methods for Engineers*: World Scientific.

Ferry, J.D. (1980), *Viscoelastic Properties of Polymers*. New York: Wiley.

Flory, P.J. (1944), "Network Structure and the Elastic Properties of Vulcanized Rubber." *Chemical Reviews* **35:** 51.

Flory, P.J., Erman B. (1982), "Theory of Elasticity of Polymer Networks. 3." *Macromolecules* **15:** 800.

Flory, P.J., Rehner J. (1943), "Statistical Mechanics of Cross-Linked Polymer Networks Ii. Swelling." *The Journal of Chemical Physics* **11:** 521.

Fukahori, Y., Andrews E.H. (1978), "Fracture Surface Roughness in Highly Deformable Polymers." *Journal of Materials Science* **13:** 777.

Fukahori, Y., Seki W. (1992), "Molecular Behaviour of Elastomeric Materials under Large Deformation: 1. Re-Evaluation of the Mooney-Rivlin Plot." *Polymer* **33:** 502.

Gennes, P.G.d. (1971), "Reptation of a Polymer Chain in the Presence of Fixed Obstacles." *The Journal of Chemical Physics* **55:** 572.

Gent, A.N. (1978), "Strength of Elastomers." In *Science and Technology of Rubber*, Mark, J.E., Erman, B., Eirich, R.E. (eds), Vol. Second edition, pp 471: Academic Press.

Gent, A.N. (2001), *Engineering with Rubber: How to Design Rubber Components*: Hanser.

Gent, A.N., Henry A.W. (1967), "On the Tear Strength of Rubber." In *Proceedings of the International Rubber Conference*, Maclaren (ed) p 193, Brighton.

Gent, A.N., Kawahara S., Zhao J. (1998), "Crystallization and Strength of Natural Rubber and Synthetic Cis-1,4-Polyisoprene." *Rubber Chemistry and Technology* **71:** 668.

Gent, A.N., Kim H.J. (1990), "Effect of Contact Time on Tack." *Rubber Chemistry and Technology* **63:** 613.

Gent, A.N., Lindley P.B., Thomas A.G. (1964), "Cut Growth and Fatigue of Rubbers. I. The Relationship between Cut Growth and Fatigue." *Journal of Applied Polymer Science* **8:** 455.

Gent, A.N., Pulford C.T.R. (1984), "Micromechanics of Fracture in Elastomers." *Journal of Materials Science* **19:** 3612.

Gent, A.N., Thomas A.G. (1958), "Forms for the Stored (Strain) Energy Function for Vulcanized Rubber." *Journal of Polymer Science* **28:** 625.

Gent, A.N., Tobias R.H. (1984), "Effect of Interfacial Bonding on the Strength of Adhesion of Elastomers. 3. Interlinking by Molecular Entanglements." *Journal of Polymer Science Part B-Polymer Physics* **22:** 1483.

Gent, A.N., Walker J.D. (2005), *The Pneumatic Tire*. Akron: National Highway Traffic Safety Administration.

George, S.C., Thomas S. (2001), "Transport Phenomena through Polymeric Systems." *Progress in Polymer Science* **26:** 985.

Glucklich, J., Landel R.F. (1976), "Tearing Test as a Means for Estimating Ultimate Properties of Rubber." *Journal of Applied Polymer Science* **20:** 121.

Gough, J., Muhr A.H., Thomas A.G. (1998), "Material Characterisation for Finite Element Analysis of Rubber Components." *Journal of rubber research (Malaysia)* **1:** 222.

Greensmith, H.W. (1956), "Rupture of Rubber. Iv. Tear Properties of Vulcanizates Containing Carbon Black." *Journal of Polymer Science* **21:** 175.

Greensmith, H.W. (1960), "Rupture of Rubber. Viii. Comparisons of Tear and Tensile Rupture Measurements." *Journal of Applied Polymer Science* **3:** 183.

Greensmith, H.W., Mullins L., Thomas A.G. (1960), *Rupture of Rubber*, Vol. 4: SOR.

Greensmith, H.W., Thomas A.G. (1955), "Rupture of Rubber. Iii. Determination of Tear Properties." *Journal of Polymer Science* **18:** 189.

Gregory, M.J. (1979), "The Stress/Strain Behaviour of Filled Rubbers at Moderate Strains." *Plastics and Rubber: Materials and Applications* **4:** 184.

Griffith, A.A. (1921), "The Phenomena of Rupture and Flow in Solids." *Philosophical Transactions of the Royal Society of London Series A* **221:** 163.

Guth, E., Mark H. (1934), "Zur Innermolekularen, Statistik, Insbesondere Bei Kettenmolekiilen I." *Monatshefte fur Chemie und verwandte Teile anderer Wissenschaften* **65:** 93.

Hamed, G.R. (1981), "Tack and Green Strength of Elastomeric Materials." *Rubber Chemistry and Technology* **54:** 576.

Hamed, G.R., Shieh C.H. (1986), "Relationship between the Cohesive Strength and Tack of Elastomers .3. Various Elastomer Types." *Rubber Chemistry and Technology* **59:** 883.

Han, Y.H., Becker E.B., Fahrenthold E.P., Kim D.M. (2004), "Fatigue Life Prediction for Cord-Rubber Composite Tires Using a Global-Local Finite Element Method." *Tire Science and Technology* **32:** 23.

Hart-Smith, L.J. (1966), "Elasticity Parameters for Finite Deformations of Rubber-Like Materials." *Zeitschrift fÃ¼r angewandte Mathematik und Physik ZAMP* **17:** 608.

Harwood, J.A.C., Mullins L., Payne A.R. (1966), "Stress Softening in Natural Rubber Vulcanizates. Part Ii. Stress Softening Effects in Pure Gum and Filler Loaded Rubbers." *Rubber Chemistry and Technology* **39:** 814.

Igarashi, T. (1975), "Mechanics of Peeling of Rubbery Materials .1. Peel Strength and Energy Dissipation." *Journal of Polymer Science Part B-Polymer Physics* **13:** 2129.

Inglis, C.E. (1913), "Stresses in a Plate Due to the Presence of Cracks and Sharp Corners." *Transactions of the Institute of Naval Architects* **10:** 219.

Isihara, A., Hashitsume N., Tatibana M. (1951), "Statistical Theory of Rubber-Like Elasticity. Iv. (Two-Dimensional Stretching)." *The Journal of Chemical Physics* **19:** 1508.

Itskov, M., Dargazany R., Hornes K. (2012), "Taylor Expansion of the Inverse Function with Application to the Langevin Function." *Mathematics and Mechanics of Solids* **17:** 693.

James, A.G., Green A. (1975), "Strain Energy Functions of Rubber. Ii. The Characterization of Filled Vulcanizates." *Journal of Applied Polymer Science* **19:** 2319.

James, A.G., Green A., Simpson G.M. (1975), "Strain Energy Functions of Rubber. I. Characterization of Gum Vulcanizates." *Journal of Applied Polymer Science* **19:** 2033.

James, H.M., Guth E. (1943), "Theory of the Elastic Properties of Rubber." *The Journal of Chemical Physics* **11:** 455.

Jones, R.A.L., Richards R.W. (1999), "Polymer/Polymer Interfaces." In *Polymers Surfaces and Interfaces*, pp 127: Cambridge University Press.

Kabe, K., Koishi M. (2000), "Tire Cornering Simulation Using Finite Element Analysis." *Journal of Applied Polymer Science* **78:** 1566.

Kadir, A., Thomas A.G. (1981), "Tear Behavior of Rubbers over a Wide-Range of Rates." *Rubber Chemistry and Technology* **54:** 15.

Karim, A., Mansour A., Felcher G.P., Russell T.P. (1990), "Short-Time Relaxation at Polymeric Interfaces." *Physical Review B* **42:** 6846.

Kausch, H.H., Tirrell M. (1989), "Polymer Interdiffusion." *Annual Review of Materials Science* **19:** 341.

Kawabata, S., Matsuda M., Tei K., Kawai H. (1981), "Experimental Survey of the Strain Energy Density Function of Isoprene Rubber Vulcanizate." *Macromolecules* **14:** 154.

Kilian, H.-G. (1981), "Equation of State of Real Networks." *Polymer* **22:** 209.

Kim, J.-H., Jeong H.-Y. (2005), "A Study on the Material Properties and Fatigue Life of Natural Rubber with Different Carbon Blacks." *International Journal of Fatigue* **27:** 263.

Kuhn, W. (1936), "Beziehungen Zwischen Molekulgrosse, Statistischer Molekulgestalt Und Elastischen Eigenschaften Hochpolymerer Stoffe." *Kolloid-Zeitschrift* **76:** 258.

Kuhn, W., Grun F. (1942), "Beziehungen Zwischen Elastischen Konstanten Und Dehnungsdoppelbrechung Hochelastischer Stoffe." *Kolloid-Zeitschrift* **101:** 248.

Kuhn, W., Kuhn H. (1946), "Statistische Und Energieelastische Rückstellkraft Bei Stark Auf Dehnung Beanspruchten Fadenmolekeln." *Helvetica Chimica Acta* **29:** 1095.

Lake, G. (1983), "Aspects of Fatigue and Fatigue of Rubber." *Prog Rubber Technol* **45:** 89.

Lake, G. (1995), "Fatigue and Fracture of Elastomers." *Rubber Chemistry and Technology* **68:** 435.

Lake, G.J. (1972), *Mechanical Fatigue of Rubber*, Vol. 45: RUBDIV.

Lake, G.J., Lindley P.B. (1964a), *Rubber Journal* **146:** 30.

Lake, G.J., Lindley P.B. (1964b), "Cut Growth and Fatigue of Rubbers. Ii. Experiments on a Noncrystallizing Rubber." *Journal of Applied Polymer Science* **8:** 707.

Lake, G.J., Lindley P.B. (1964c), "Ozone Cracking, Flex Cracking and Fatigue of Rubber." *Rubber Journal* **146:** 24.

Lake, G.J., Lindley P.B. (1965), "The Mechanical Fatigue Limit for Rubber." *Journal of Applied Polymer Science* **9:** 1233.

Lake, G.J., Lindley P.B., Thomas A.G. (1969), In *Second International Conference on Fracture*, Hall, C. (ed) p 493, Brighton.

Lake, G.J., Thomas A.G., Lawrence C.C. (1992), "Effects of Hydrostatic-Pressure on Crack-Growth in Elastomers." *Polymer* **33:** 4069.

Lake, G.J., Yeoh O.H. (1980), "Measurement of Rubber Cutting Resistance in the Absence of Friction." *Rubber Chemistry and Technology* **53:** 210.

Lake, G.J., Yeoh O.H. (1987), "Effect of Crack Tip Sharpness on the Strength of Vulcanized Rubbers." *Journal of Polymer Science Part B: Polymer Physics* **25:** 1157.

Lectez, A.S., Verron E., Huneau B. (2014), "How to Identify a Hyperelastic Constitutive Equation for Rubber-Like Materials with Multiaxial Tension-Torsion Experiments." *International Journal of Non-Linear Mechanics* **65:** 260.

Leger, L., Creton C. (2008), "Adhesion Mechanisms at Soft Polymer Interfaces." *Philosophical Transactions of the Royal Society a-Mathematical Physical and Engineering Sciences* **366:** 1425.

Legorju-jago, K., Bathias C. (2002), "Fatigue Initiation and Propagation in Natural and Synthetic Rubbers." *International Journal of Fatigue* **24:** 85.

Lindley, P.B. (1972), "Energy for Crack Growth in Model Rubber Components." *The Journal of Strain Analysis for Engineering Design* **7:** 132.

Lindley, P.B. (1973), "Relation between Hysteresis and Dynamic Crack Growth Resistance of Natural-Rubber." *International Journal of Fracture* **9:** 449.

Lindley, P.B. (1974), *Engineering Design with Natural Rubber*: Malaysian Rubber Producers' Research Association.

Marckmann, G., Verron E. (2006), "Comparison of Hyperelastic Models for Rubber-Like Materials." *Rubber Chemistry and Technology* **79:** 835.

Mark, J.E., Erman B. (1994), *Science and Technology of Rubber*: Elsevier Science.

Mars, W., Fatemi A. (2004), "Observations of the Constitutive Response and Characterization of Filled Natural Rubber under Monotonic and Cyclic Multiaxial Stress States." *Journal of engineering materials and technology* **126:** 19.

Mars, W.V., Fatemi A. (2002), "A Literature Survey on Fatigue Analysis Approaches for Rubber." *International Journal of Fatigue* **24:** 949.

Mars, W.V., Fatemi A. (2003), "A Phenomenological Model for the Effect of R Ratio on Fatigue of Strain Crystallizing Rubbers." *Rubber Chemistry and Technology* **76:** 1241.

Matteucci, S., Yampolskii Y., Freeman B.D., Pinnau I. (2006), "Transport of Gases and Vapors in Glassy and Rubbery Polymers." In *Materials Science of Membranes for Gas and Vapor Separation*, pp 1: John Wiley & Sons, Ltd.

Mooney, M. (1940), "A Theory of Large Elastic Deformation." *Journal of Applied Physics* **11:** 582.

Mullins, L. (1948), "Effect of Stretching on the Properties of Rubber." *Rubber Chemistry and Technology* **21:** 281.

Mullins, L. (1959), "Rupture of Rubber Part Ix. Role of Hysteresis in the Tearing of Rubber." *Trans Inst Rubber Ind* **35:** 213.

Mullins, L., Tobin N.R. (1965), "Stress Softening in Rubber Vulcanizates. Part I. Use of a Strain Amplification Factor to Describe the Elastic Behavior of Filler-Reinforced Vulcanized Rubber." *Journal of Applied Polymer Science* **9:** 2993.

Narasaiha, L. (2009), *Finite Element Analysis*: Taylor & Francis.

Obata, Y., Kawabata S., Kawai H. (1970), "Mechanical Properties of Natural Rubber Vulcanizates in Finite Deformation." *Journal of Polymer Science Part A-2: Polymer Physics* **8:** 903.

Ogden, R.W. (1972), "Large Deformation Isotropic Elasticity - on the Correlation of Theory and Experiment for Incompressible Rubberlike Solids." *Proceedings of the Royal Society of London A Mathematical and Physical Sciences* **326:** 565.

Ozupek, S., Becker E.B. (2005), "Finite Element Method for the Study of Belt Edge Delaminations in Truck Tires." *Rubber Chemistry and Technology* **78:** 557.

Pandey, K.N., Setua D.K., Mathur G.N. (2003), "Material Behaviour: Fracture Topography of Rubber Surfaces: An Sem Study." *Polymer Testing* **22:** 353.

Papadopoulos, I.C., Liang H., Busfield J.J.C., Thomas A.G. (2003), *Predicting Cyclic Fatigue Crack Growth Using Finite Element Analysis Techniques Applied to Three-Dimensional Elastomeric Components*.

Papadopoulos, I.C., Thomas A.G., Busfield J.J.C. (2008), "Rate Transitions in the Fatigue Crack Growth of Elastomers." *Journal of Applied Polymer Science* **109:** 1900.

Payne, A.R. (1962), "The Dynamic Properties of Carbon Black Loaded Natural Rubber Vulcanizates. Part Ii." *Journal of Applied Polymer Science* **6:** 368.

Persson, B.N.J., Albohr O., Heinrich G., Ueba H. (2005), "Crack Propagation in Rubber-Like Materials." *Journal of Physics-Condensed Matter* **17:** R1071.

Porter, M. (1967), "Structural Characterization of Filled Vulcanizates Part 1. Determination of the Concentration of Chemical Crosslinks in Natural Rubber

Vulcanizates Containing High Abrasion Furnace Black." *Rubber Chemistry and Technology* **40:** 866.

Previati, G., Kaliske M. (2012), "Crack Propagation in Pneumatic Tires: Continuum Mechanics and Fracture Mechanics Approaches." *International Journal of Fatigue* **37:** 69.

Prince E. Rouse, J. (1953), "A Theory of the Linear Viscoelastic Properties of Dilute Solutions of Coiling Polymers." *The Journal of Chemical Physics* **21:** 1272.

Quek, S.S., Liu G.R. (2003), *Finite Element Method: A Practical Course*: Elsevier Science.

Rice, J.R. (1968), "A Path Independent Integral and the Approximate Analysis of Strain Concentration by Notches and Cracks." *Journal of Applied Mechanics* **35:** 379.

Rickaby, S.R., Scott N.H. (2014), "A Comparison of Limited-Stretch Models of Rubber Elasticity." *International Journal of Non-Linear Mechanics*.

Rivlin, R.S. (1948a), "Large Elastic Deformations of Isotropic Materials. I. Fundamental Concepts." *Philosophical Transactions of the Royal Society of London Series A, Mathematical and Physical Sciences* **240:** 459.

Rivlin, R.S. (1948b), "Large Elastic Deformations of Isotropic Materials. Iii. Some Simple Problems in Cylindrical Polar Co-Ordinates." *Philosophical Transactions of the Royal Society of London Series A, Mathematical and Physical Sciences* **240:** 509.

Rivlin, R.S. (1948c), "Large Elastic Deformations of Isotropic Materials. Iv. Further Developments of the General Theory." *Philosophical Transactions of the Royal Society of London Series A, Mathematical and Physical Sciences* **241:** 379.

Rivlin, R.S. (1956), "Large Elastic Deformations." In *Rheology V1*, Eirich, F. (ed), pp 351: Elsevier.

Rivlin, R.S., Saunders D.W. (1951), "Large Elastic Deformations of Isotropic Materials. Vii. Experiments on the Deformation of Rubber." *Philosophical Transactions of the Royal Society of London Series A, Mathematical and Physical Sciences* **243:** 251.

Rivlin, R.S., Thomas A.G. (1953), "Rupture of Rubber. I. Characteristic Energy for Tearing." *Journal of Polymer Science* **10:** 291.

Sakulkaew, K., Thomas A.G., Busfield J.J.C. (2010), "The Effect of the Rate of Strain on Tearing in Rubber." *Polymer Testing* **30:** 163.

Schach, R., Creton C. (2008), "Adhesion at Interfaces between Highly Entangled Polymer Melts." *Journal of Rheology* **52:** 749.

Schach, R., Tran Y., Menelle A., Creton C. (2007), "Role of Chain Interpenetration in the Adhesion between Immiscible Polymer Melts." *Macromolecules* **40:** 6325.

Sun, C., Gent A., Marteny P. (2000), "Effect of Fatigue Step Loading Sequence on Residual Strength." *Tire Science and Technology* **28:** 196.

Thomas, A.G. (1955), "Rupture of Rubber. Ii. The Strain Concentration at an Incision." *Journal of Polymer Science* **18:** 177.

Thomas, A.G. (1959), "Rupture of Rubber. V. Cut Growth in Natural Rubber Vulcanizates." *Rubber Chemistry and Technology* **32:** 477.

Thomas, A.G. (1960), "Rupture of Rubber. Vi. Further Experiments on the Tear Criterion." *Journal of Applied Polymer Science* **3:** 168.

Thomas, A.G. (1994), "The Development of Fracture-Mechanics for Elastomers." *Rubber Chemistry and Technology* **67:** G50.

Treloar, L.R.G. (1943), "The Elasticity of a Network of Long-Chain Molecules. I." *Transactions of the Faraday Society* **39:** 36.

Treloar, L.R.G. (1944), "Stress-Strain Data for Vulcanised Rubber under Various Types of Deformation." *Transactions of the Faraday Society* **40:** 59.

Treloar, L.R.G. (1948), "Stresses and Birefringence in Rubber Subjected to General Homogeneous Strain." *Proceedings of the Physical Society* **60:** 135.

Treloar, L.R.G. (1975), *The Physics of Rubber Elasticity*, 3rd Edition edn: Oxford University Press.

Tschoegl, N.W. (1971), "Constitutive Equations for Elastomers." *Journal of Polymer Science Part a-1-Polymer Chemistry* **9:** 1959.

Tsunoda, K., Busfield J.J.C., Davies C.K.L., Thomas A.G. (2000), "Effect of Materials Variables on the Tear Behaviour of a Non-Crystallising Elastomer." *Journal of Materials Science* **35:** 5187.

Valanis, K.C., Landel R.F. (1967), "The Strain Energy Function of a Hyperelastic Material in Terms of the Extension Ratios." *Journal of Applied Physics* **38:** 2997.

Van Der Hoff, B.M.E., Buckler E.J. (1967), "Transient Changes in Topology and Energy on Extension of Polybutadiene Networks." *Journal of Macromolecular Science: Part A - Chemistry* **1:** 747.

Westergaard, H.M. (1939), "Bearing Pressures and Cracks." *Journal of Applied Mechanics* **6:** 49.

Willett, J.L., Wool R.P. (1993), "Strength of Incompatible Amorphous Polymer Interfaces." *Macromolecules* **26:** 5336.

Williams, M.L., Landel R.F., Ferry J.D. (1955), "The Temperature Dependence of Relaxation Mechanisms in Amorphous Polymers and Other Glass-Forming Liquids." *Journal of the American Chemical Society* **77:** 3701.

Yeoh, O. (1990), "Characterization of Elastic Properties of Carbon-Black-Filled Rubber Vulcanizates." *Rubber Chemistry and Technology* **63:** 792.

Young, D. (1994), "Effects of Temperature on Fatigue and Fracture." *Rubber Chemistry and Technology* **67:** 137.

Young, D.G. (1986), "Fatigue Crack-Propagation in Elastomer Compounds - Effects of Strain Rate, Temperature, Strain Level, and Oxidation." *Rubber Chemistry and Technology* **59:** 809.